All-inorganic White Light Emitting Devices Based on ZnO Nanocrystals

Von der Fakultät für Ingenieurwissenschaften
Abteilung Elektrotechnik und Informationstechnik
der Universität Duisburg-Essen

zur Erlangung des akademischen Grades

Doktor der Ingenieurwissenschaften

genehmigte Dissertation

von

Ekaterina Nannen
aus
Vologda

1. Gutachter: Prof. Dr. rer. nat. Gerd Bacher
2. Gutachter: Prof. Dr. rer. nat. Roland Schmechel
Tag der mündlichen Prüfung: 21.09.2012

Dein Führerin die Natur sey, welch'r du must folgen von weiten,

Williglich, anderst du irrst, wo sie dich nicht thut leyten,

Die Vernunfft sey dein Stab, und es muß stärcken die Erfahrnheit

Dein Gesicht, daß du könnst sehen, was gelegt ist weit und breit,

Daß Lesen sey wie ein Lamp im Finstern leuchtend hell und klar,

Dadurch du mögst verhüten der Sachn und Wörter Gefahr.[1]

Table of contents

Table of contents iii
Introduction 1
1 Nanocrystal-LEDs and Mechanisms of Their Operation 5
1.1 AC and DC Driven Devices 6
1.1.1 AC driven devices 6
1.1.2 DC driven devices 8
1.2 Electroluminescence Mechanisms in NC-LEDs. 11
1.2.1 Direct charge injection 11
1.2.2 Exciton energy transfer 12
1.2.3 Ionization mechanisms 13
1.3 Current Transport Mechanisms in NC-LEDs 15
1.3.1 Ideal p-n junction 15
1.3.2 Charge transport mechanisms in NC-LEDs 17
2 Optical and Electronic Properties of ZnO: Background 31
2.1 Emission Properties of ZnO 33
2.1.1 Near-band-gap-related (NBR) emission in ZnO 34
2.1.2 Defect related optical transitions in ZnO 37
2.2 Electronic Properties of ZnO 43
3 Structural and Optical Properties of ZnO Nanocrystals: Experiment 49
3.1 Synthesis of ZnO Nanocrystals 50
3.1.1 Liquid phase synthesis methods 50
3.1.2 Gas phase synthesis methods 51
3.1.3 Structural analysis of the nanocrystals 52
3.2 Absorption Spectroscopy 55
3.3 Photoluminescence Spectroscopy 58

3.3.1 Excitation power dependent behavior 60
3.3.2 Atmosphere dependent behavior 64
3.3.3 Size dependent behavior 65
3.4 Temperature Dependent Spectroscopy 67
3.4.1 Near-band-gap transitions at low temperature 67
3.4.2 Temperature dependent behavior 68
3.5 Thermal Treatment 73
3.6 Assignment of the Luminescent Transitions 78
3.6.1 Near-band-gap related transitions 78
3.6.2 Red transitions 79
3.6.3 Green transitions 79
3.6.4 Violet and blue transitions 80
4 Archetype All-Inorganic ZnO NC-LED 83
4.1 Design and Fabrication 85
4.2 ITO-based Archetype ZnO NC-LED 87
4.2.1 Impact of the ITO substrate on the layer morphology 87
4.2.2 ITO-based archetype device characteristics 88
4.3 FTO-based Archetype ZnO NC-LEDs 92
4.3.1 Impact of the FTO substrate on the layer morphology 92
4.3.2 FTO-based archetype device characteristics 93
4.3.3 Annealing of FTO-based archetype devices 96
4.3.4 FTO archetype devices based on aged nanocrystals 100
4.4 Study of the I-V Behavior 105
4.5 Proposed Emission Mechanism 109
5 Si/ZnO Heterojunction NC-LEDs 113
5.1 Si Nanocrystal Layers 115
5.2 Si/ZnO Bilayer NC-LEDs 118
5.2.1 I-V behavior of the Si/ZnO bilayer devices 119
5.2.1 Emission properties 122

5.3 Si/ZnO Multilayer NC-LEDs 127
6 WO_3/ZnO Heterojunction NC-LEDs 131
6.1 Fabrication of a WO_3/ZnO Heterojunction 133
6.2 WO_3/ZnO NC-Heterojunction LED 135
7 Summary and Conclusions 141
Bibliography 145
Appendix 163
A1 Characterization Techniques 163
A2 Fabrication Details 169
A3 Contributions Associated with the Thesis 174
A4 Further Contributions 176
Acknowledgment 177

Introduction

Nowadays, the demand for low-cost light emitters is high, covering a wide range of different applications in advertisement and give-away industry, low-cost indicators and displays for e.g. consumer electronics, mobile phones, toys, and many more. In addition, cost-efficient large area emitters are highly desired in automotive industry as well as in architecture, urban development, and interior for innovative design and ambient lightning applications. Additional profitable market segments could be created by introducing emitters on flexible substrates. So far, these demands are mostly fulfilled by organic light emitting devices (OLEDs).[2–5] In order to cover these market segments and develop new ones, nanoparticle based emitters are regarded as an attractive alternative to OLEDs with potential of improvements in lifetime, power consumption and fabrication costs. Nanocrystal based light emitting devices (NC-LEDs) are expected to combine the robustness, long-term stability and efficiency of traditional semiconductor material systems, known from epitaxially grown LEDs and laser diodes, [2, 6, 7] with flexible low-cost large area fabrication techniques of OLEDs [2–5].

Historically, the first nanocrystals used for NC-LEDs [8] were so-called quantum dots (QDs) [9, 10], synthesized chemically using solution-based processes. QDs show color tunability due to the quantum confinement effect. Additionally, they also exhibit a high photoluminescence (PL) quantum efficiency (QE) approaching 1 and pure color-saturated emission.[11] Due to their luminescent properties as well as more-or-less established synthesis routes for monodisperse QDs in stable and processable dispersions, these materials remain up to now the primary choice for nanoparticle LED fabrication. The most efficient monochrome NC-LEDs to date incorporate Cd-based II/VI QDs sandwiched between organic charge injection and transport layers.[12] Their external quantum efficiency (EQE) thereby approaches a theoretical limit of 20% considering the limit of light extraction efficiency.[13] However, the brightness of such organic /inorganic hybrid QD-LEDs usually remains limited to the order of several

hundred cdm^{-2}, owing to the poor confinement of the excitons in the active QD region between the organic support layers.[12, 14] Furthermore, high drive current densities, required for high brightness values, often can not be sustained by the delicate organic support layers. As an approach to improving the robustness of the device and increase the operation current densities, the substitution of organic support layers (hole OR electron transport and injection layers) by inorganic metal oxides was introduced.[15–20] The implementation of ZnO nanocrystalline layer for electron injection and transport [16] recently resulted in the record luminance value of 218.800 cdm^{-2} for green QD-LED with a maximum external quantum efficiency (EQE) of 5.8%.[20] This rapid improvement of QD-LED performance during the past 5 years as well as progress in their fabrication techniques enabling large-area patterning and printing [13, 18, 21–23] has attracted high attention from industrial side with the first prototype QD-LED-based mono- and full-color active matrix displays being recently presented by QD Vision and Samsung Electronics.

While monochrome light emission is highly desirable for display applications, the requirements for ambient lighting are quite different. In this case, broad band white light emission with a color rendering index approaching 100 (sun, black body radiator) and correlated color temperatures between ~2500 K ("warm white" of incandescent light bulbs) and ~5000 K ("cool white" of horizon daylight) is required. The combination of efficient red, green and blue (RGB) monochrome QDs in a QD-LED in analogy to the RGB-approach of epitaxial LEDs [2, 6] results however in color rendering indices typically below 90.[24, 25] Since in this case the organic support layers can no longer be tailored to the corresponding type of the QDs, as in case of monochrome QD-LEDs, the highest EQE values for white NC-LEDs achieved to date are in the range of 0.3%.[25] The strategy to combine broad band, defect-related emission in ultrasmall CdSe nanocrystals with the blue emission of the organic support layer results in high CRI values of up to 96.6 [26], however, with a maximal EQE of $1.3 \cdot 10^{-4}$%.

The incorporated organic support layers are usually sensitive to thermal stress and exhibit degradation by oxygen and moisture. This limits the fabrication techniques and operating lifetime of devices, making a fabrication under controlled environment as well as an appropriate encapsulation crucial for good device performance. Therefore, the development of efficient all-inorganic NC-LEDs is highly desirable. Nevertheless, a major concern retarding QD-LEDs from widely spread commercialization is the application of toxic heavy metals such as Cd.

ZnO offers a high potential as the luminescent active layer in hybrid emitting devices because this material is widely available, non-toxic and robust against oxidation.[27–33] This should make large-area applications under ambient air conditions possible. Its direct band gap and high exciton binding energy at room temperature enables efficient emission for laser and LED applications in the ultra violet (UV) spectral range.[34–37] Most important, the variety of natural defects and doping impurities enables efficient emission across the whole visible spectral range [27, 38–40] with photoluminescence quantum yields of 45% and higher [41–43]. Theoretically, this enables stable, efficient, balanced white emission from one and the same heavy metal(Cd)-free material. This potential has triggered intense research into ZnO based white light emitting devices (WLEDs).[38, 44–47]

One of the main drawbacks of implementing ZnO in WLEDs is the fact that ZnO is a natural n-type semiconductor with an energetically low lying valence band edge and efficient p-doping of ZnO is still an open issue.[48] Therefore, the realization of cost-effective nanostructure ZnO light emitting devices remains challenging. ZnO nanowires in hybrid systems is one of the concepts that showed large area electroluminescence (EL) in the visible and UV spectral range.[49–56] The nanowire growth process, unfortunately, makes low-cost production, e.g. by printing techniques, of such large area emitters on flexible substrates in most cases inconvenient. The unbeatable advantage of the nanocrystal implementation into the LEDs remains the fact that the synthesis of the active material is separated from the fabrication of the device. In addition, ZnO NCs can be produced by gas phase synthesis on a tons scale at very low costs.[31] Such particles are commercially available in both hydrophilic and hydrophobic stable dispersions and are widely applied in cosmetic and paint industries.[31, 57]

ZnO nanoparticles in hybrid devices with organic support layers showed visible and near-band-gap EL at room temperature in the DC regime.[29, 58–60] Unfortunately, organic hole injectors are very sensitive to humidity, oxygen and UV irradiation, which inherently limits the operating lifetimes of such devices. A possible solution is to combine ZnO with rigid p-type substrates, such as p-Si and p-GaN. Several research groups have already demonstrated light emission from ZnO layers or nanowires grown on such rigid substrates.[38, 44, 61–66] In addition, a combination between p-type metal oxides NiO, [54, 55] $CuAlO_2$ [51] and $SrCu_2O_2$ [67] with ZnO layers and nanowires has been demonstrated.[38, 44] Despite all these efforts, no efficiency values were reported so far for any kind of inorganic ZnO WLEDs, emphasizing fundamental challenges for the above mentioned device designs.[68]

The main focus of this work is to explore the implementation of commercially available ZnO NCs as an active light emitting material in all-inorganic white NC-LEDs as a possible environmentally safe and ambient-air-compatible alternative to conventional QD-LEDs.

In the first chapter, the main NC-LED concepts are introduced with the emphasis on their design and the underlying emission mechanisms. The charge transport mechanisms typically considered in DC-operated NC-LEDs and the corresponding mathematical models are presented as well.

In the second chapter, the optical and electronic properties of ZnO crystals are summarized. The main focus of the chapter is on the origin of the near-band-gap and defect-related emission in ZnO.

The third chapter is dedicated to the properties of ZnO NC, implemented in the NC-LEDs within this work. First, their synthesis route in the gas phase is introduced and their structural properties are discussed. The focus of the chapter is on the absorption and emission properties of the ZnO NCs, studied using absorption and photoluminescence spectroscopy.

The fourth chapter introduces all-inorganic ZnO archetype NC-LEDs. Their simple and straightforward design enables extensive study of the I-V behavior of the ZnO NC layers and its correlation with the luminescent properties of the NCs and NC-LEDs. Thereby, a model for the emission mechanism in all-inorganic ZnO NC-LEDs is suggested.

In the fifth chapter, an advanced device design incorporating p-doped Si NCs and ZnO NCs in a solution processible heterojunction is developed. The performance of the NC-multilayer LED is further improved by the introduction of an additional intermixed layer within the active region of the device.

The sixth chapter introduces all-inorganic, metal oxide white NC-LEDs. The luminescent ZnO NCs are thereby combined for the first time with WO_3 NCs in an intermixed approach. The resulting devices demonstrate highly homogeneous large-area white light emission with the highest EQE reported to date for an all-inorganic ZnO based LED.

Finally, the results of the work are summarized and the conclusions on the implementation of ZnO NC in all-inorganic NC-LEDs are drawn.

Chapter 1

Nanocrystal-LEDs and Mechanisms of Their Operation

This chapter gives an overview of the two main concepts of nanocrystal (NC) -LEDs currently discussed in literature. The design of the LEDs varies significantly within the two possible operation regimes namely direct (DC) and alternating (AC) current driven devices. The main AC and DC NC-LED design concepts as well as their evolution during the past decade are discussed below. Furthermore, the electroluminescence mechanisms, typically suggested to be involved in the operation of the corresponding NC-LEDs are introduced. Further focus of the chapter lies on the charge carrier transport mechanisms in NC-LEDs under DC operation. The mathematical models, describing these mechanisms, enable the introduction of characteristic "smart plots" of the I-V behavior. These "smart plots" can help to identify the contribution of different mechanisms to the current transport in case they dominate the I-V behavior in a certain voltage range.

1.1 AC and DC Driven Devices

Like other electrically driven light emitting devices, NC-LEDs can be as well divided into those operated at direct (DC) and at alternating (AC) currents. Typically, the light emission processes differ in these two cases, demanding different device architectures and involved material systems, which are discussed below. The research into these new device concepts and their development started in 1994 [8] and has rapidly proceeded since then. First, light emitting devices based on nanoparticles and operated under DC were presented historically prior to AC devices, mainly pushed by the OLEDs technology and the development of quantum dots with high room temperature quantum efficiency and the availability of processable stable dispersions.

1.1.1 AC driven devices

Alternating current thin-film electroluminescent (AC-TFEL) devices are well known as efficient and robust large area emitting devices with low power consumption and are already in wide-spread use in the flat panel market. AC-TFEL devices consist of an emissive phosphor layer, e.g. manganese-doped zinc sulfide (ZnS:Mn), sandwiched between insulating layers that are electrically contacted by the electrodes. One of the electrodes is typically metallic, another is a transparent conductive oxide (TCO) to enable the light emission through it. At high voltages, charge carriers trapped at the interfaces between the layers are injected into the phosphor. They can be trapped within the phosphor and recombine (bipolar field-emission model) or become accelerated by the applied electric field and excite the luminescent centers of the phosphor by impact excitation and ionization mechanisms.[69] The development of multicolor-displays remains challenging since most different-colored phosphors comprise different material systems and therefore require different treatment (e.g. annealing under different conditions) and deposition techniques.[69, 70]

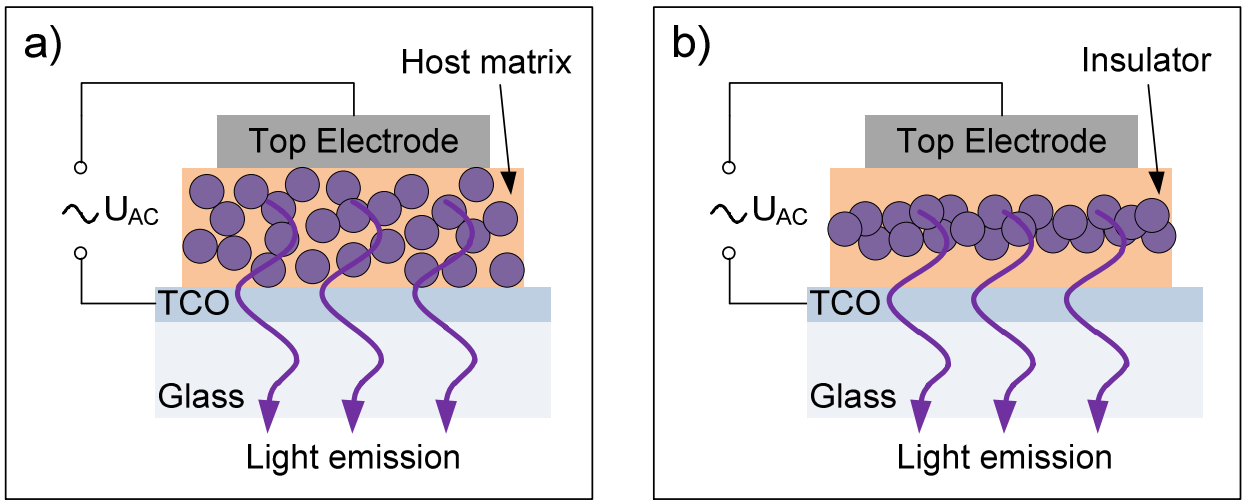

Figure 1.1: Different designs of NC-LEDs operated by alternating current. The light emitting nanocrystals are embedded between two electrodes within an insulating host matrix (a) or in between two insulating layers (b). The light emission can be observed through one of the electrodes, which has to be transparent (TCO).

It is expected that the standard AC-TFEL devices can be improved by replacing the mostly used micro-powders by nanoparticles, allowing easy fabrication of multicolor displays and lowering material costs. Thereby, design and functionality remain generally the same as in case of micro-powder devices. The basic possible designs are shown in Figure 1.1. Thereby, the nanocrystals are either embedded in an insulating host matrix (design (a)) or sandwiched between insulating layers (design (b)). In 2003, Manzoor and colleagues demonstrated the successful fabrication of nanoparticle-based AC-TFEL devices according design (b) with blue, green and orange-red colored light emission using doped ZnS nanocrystals. The EL emission was observed at low AC voltages of 10 V and a frequency of 100 Hz.[71] Design (a) was used in 2007 by Adachi and co-workers.[72] First steps towards large-area printable AC-displays were made by Toyama and colleagues. They demonstrated EL of a printed nanocrystal layer of ZnS:Mn with a luminance of almost 3 cdm^{-2} using a 200 V AC, 5 kHz sinusoidal voltage.[73] A luminance of 2 cdm^{-2} was demonstrated by Wood and co-workers in an all-transparent light emitting device, operated at 170 V peak to peak at 30 kHz frequency.[74] AC-driven blue, green and red QD-LEDs were also recently demonstrated.[75] These findings present first steps towards printable, transparent multicolor AC-driven displays, based on direct band gap semiconducting nanoparticles.

1.1.2 DC driven devices

The typical structure of NC-LEDs operated under direct current was adopted from the OLED technology. The schematic of a typical design is shown in Figure 1.2. Usually, a TCO coated glass is used as a substrate and as a transparent electrode. The most frequently used TCO is indium tin oxide (ITO), utilized in touchscreens and liquid crystal displays as a standard. An alternative is fluorine-doped tin oxide (FTO), frequently used in solar-energy conversion applications [76] because of its stable mechanical and chemical properties [77, 78]. Recent developments uncovered new substitutes for ITO like aluminum (AZO) and gallium (GZO) doped zinc oxides [79–81] and many others. The other electrode typically consists of metals with a low work function. When using barium (Ba), magnesium (Mg) or calcium (Ca), an additional layer of aluminum (Al) or silver (Ag) on top is needed to passivate the reactive electrode and to protect it from oxidation. Because of their easy handling, Al electrodes are most frequently implemented. The active light emitting layer consisting of either pure nanoparticles (design (b)) or organic/nanoparticle compounds (design (a)) is sandwiched between the two electrodes. When forward biased, holes are supposed to be injected into the active layer from the TCO and electrons from the top metallic electrode, subsequently recombine and emit light. This is the reason why usually a TCO with a high work function and a cathode metal with a low work function value are preferred to lower the energy barriers for hole and electron injection, respectively.

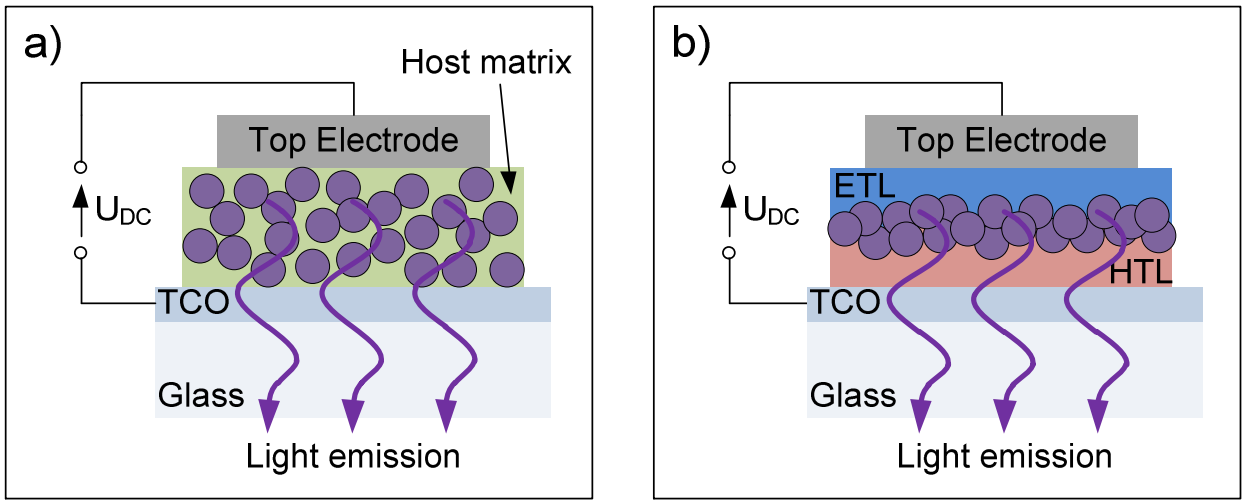

Figure 1.2: Different device designs of NC-LEDs, operated under constant voltage. Nanocrystals are sandwiched between the electrodes, whereby they can be (a) incorporated within an organic matrix or (b) assembled as a tight layer with possible additional hole (HTL) and electron transport layers (ETL).

The first QD material system introduced in electroluminescent devices was CdSe, presented by Alivisatos and co-workers in 1994.[8] A p-paraphenylene vinylene (PPV) layer, covered by a multilayer structure with closely packed disordered sheets of CdSe nanocrystals, separated by organic spacers, was sandwiched between indium doped tin oxide (ITO) and magnesium (Mg) electrodes. A subsequent publication from two groups at MIT [82] demonstrated a single-layer CdSe-QD-LED with the nanocrystals incorporated into an organic polymer matrix. In this case, the QDs were blended with a hole and an electron conducting polymer and spin casted on an ITO-substrate in one fabrication step, followed by the top Mg/Ag evaporation. Although these first devices showed quite low external quantum efficiencies (EQEs) of 0.001-0.01% [8] and 0.0005% [82], they demonstrated the principle application potential of QDs and quantum confinement effects in light emitting devices. The device design, as sketched in Figure 1.2 (a), with a QD / organic polymer blend sandwiched between two electrodes was also further developed by other groups using hole-conducting [24, 83–90], electron-conducting [91], isolating [92–94], and semiconducting [95] organic polymers as a host matrix. The successful implementation of other semiconducting QDs for applications in the visible (CdTe [95]) and the near-infrared (InAs [84], PbS [96], PbSe [90]) spectral range using this device concept have been demonstrated. Never the less, external quantum efficiencies of these devices remained quite low mainly due to the charge imbalance, caused by inhomogeneous charge transport characteristics, since most QDs exhibit poor conductivity. Additionally, close proximity of the particles to the electrodes can lead to electroluminescence (EL) quenching.[97]

A significant increase in the external efficiency (factor 20) and lifetime (factor 100) with respect to the first devices was achieved in 1997 by introducing core/shell QDs, consisting of a CdSe core coated with a CdS shell.[98] In addition, the QDs were assembled in a separate layer on top of the organic PPV layer, introducing an alternative design of the QD-LED, in which the QDs are no longer incorporated into an organic host matrix, but deposited as a self-contained layer from the dispersion. The active luminescent QD layer is sandwiched between the TCO and the top electrode with additional organic layer(s) between the electrode(s) and the QD-layer to enable and enhance injection and transport of charge carriers to the QDs, as schematically shown in Figure 1.2 (b).

In 2002, a further 25-fold improvement in luminescence efficiency of QD-LEDs was achieved by Coe-Sullivan and co-workers by modifying the deposition technique of the active luminescent QD-layer.[99] The developed phase-segregation approach enabled a precise deposition of a single QD-monolayer between two organic charge injection /

transport layers. ITO and Mg:Ag were used as a transparent anode and a cathode, respectively. A peak EQE of 0.52 % was achieved by this device structure. The main improvement of the QD-LEDs was achieved by separating the luminescence function of the QDs from their participation in charge conduction, which was not the case in earlier devices. Here, the charge carriers were transported to the vicinity of QDs only by the organic layers. The exciton generation on QDs was attributed to two parallel processes: direct charge injection into the QDs and exciton energy transfer from organic molecules. The fine-tuning of this design resulted in an EQE of 2.7 % (at 13 cdm^{-2}) for an orange QD-LED, which is about 1000 times higher than the EQE of the first hybrid QD-LED devices.[12] Recently, QD Vision Inc. announced red, green and blue QD-LEDs with EQE exceeding 6 %.[13]

Though the best EQE values and the lowest turn-on voltages so far were reached by the combination of organic support layers with a monolayer of efficient QDs, their brightness usually remains limited to the order of several hundred cdm^{-2}, owing to the poor confinement of the excitons in the active QD region.[12, 14] Also, high driving current densities, required for high brightness values, often can't be sustained by delicate organic support layers. As an approach to improving the robustness of the device and increasing the operation current densities, the substitution of the organic support layers (hole OR electron transport and injection layer) by inorganic metal oxides was introduced.[15–20] The implementation of ZnO nanocrystalline layer for electron injection and transport [16] resulted recently in the so-far record luminance value of 218.800 cdm^{-2} for green QD-LED with a maximum external quantum efficiency (EQE) of 5.8%.[20]

The substitution of both organic electron and hole transport and injection layers by sputtered metal oxides resulted in an all-inorganic QD-LED exceeding the brightness of 1900 cdm^{-2} and still supporting current densities of 3.5 Acm^{-2}.[100] Such all-inorganic devices demonstrated robust operation in ambient air for 20 h without additional encapsulation.[101] Unfortunately, these all-inorganic devices typically require higher operation voltages and, more importantly, more than one order of magnitude lower EQE (0.15 % as a maximum), compared to state-of-the-art monochrome QD-LEDs.[13, 100, 101]

1.2 Electroluminescence Mechanisms in NC-LEDs.

Light emitters based on nanocrystals is a quite new and fast developing field of research with many different device architectures and fabrication techniques and still more to come. The understanding of the processes behind the electroluminescence (EL) in different devices needs to be deepened. The origin of the light emission is still under discussion and can be attributed to different processes. In case of nanocrystals embedded in conductive or semiconducting polymer matrices, as well as devices with organic support layer(s), the EL is most frequently attributed to two processes, taking place at the same time: direct charge carrier injection into the particles and energy transfer from the host matrix or from organic support layers to the particles. Both processes result in formation of excitons on the nanocrystals and their defect states, which recombine and emit light.[102, 24, 88, 86, 103–105] In case of nanoparticles embedded in an isolating host matrix [72, 92–94] or pure inorganic LEDs without additional organic support layers [106–108], the exciton formation may not purely be attributed to direct charge carrier injection, but impact ionization has to be considered as well [72, 106]. The possible EL mechanisms in NC-LEDs are briefly introduced in the following sections.

1.2.1 Direct charge injection

Direct charge injection is a proposed mechanism for most of the DC-operated hybrid and inorganic nanocrystal LEDs.[8, 15, 24, 25, 83, 85–88, 92, 100, 102, 104, 105, 109–115] When operated in forward direction, i.e. when positive voltage is applied to the anode (here TCO) and consequently the negative bias is applied to the cathode (here metallic contact), holes are injected from the TCO into the hole injection and transport layer and the electrons from the metallic electrode into the electron injection and transport layer, respectively. The injected carriers subsequently travel through the transport layers to the nanocrystals and can form the excitons, which can recombine radiatively. This process is schematically illustrated in Figure 1.3.

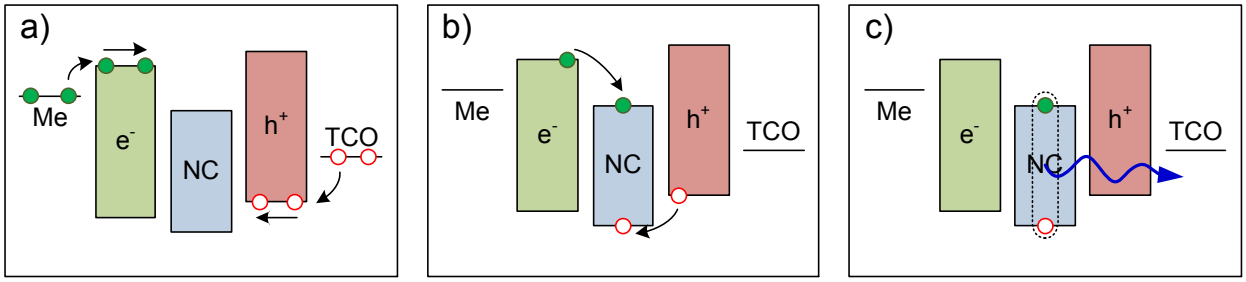

Figure 1.3: Schematic diagram of the direct charge injection mechanism in a simplified band diagram of the organic hybrid or inorganic-nanocrystal LED. (a) shows the charge carrier injection into charge injection and transport layers, followed by the charge injection into the nanocrystals (b) and exciton formation and recombination on nanocrystals (c).

The resulting efficiency of the LEDs depends very much on a careful alignment of the charge injection layers according to the valence and conduction band position of the active light emitting nanocrystals as well as balanced hole and electron injection.[15, 84, 85, 100, 110, 113, 116] The non-radiative recombination of the charge carriers, QD charging and the shunt currents through the device are mainly limiting the efficiency of the LEDs, based on this mechanism.[13, 15, 113, 117] On the other hand, the NC-LEDs with the highest so-far reported brightness operate via the direct charge injection.[13, 20]

1.2.2 Exciton energy transfer

Exciton energy transfer typically contributes to the nanocrystal light emission in DC-operated hybrid organic-nanocrystal LEDs in addition to the direct charge injection.[8, 13, 24, 25, 82, 102, 104, 105, 109, 110] In most organic hole and electron injection and transport layers, excitons can also be formed on the involved organic molecules. In case they are formed in close proximity to the embedded nanocrystals, their energy can be radiationlessly transferred to QDs. Afterwards, the formed excitons recombine radiatively.[102, 118] This process, frequently referred as Förster resonance energy transfer (FRET) [119], is illustrated in Figure 1.4. The efficiency of this process depends mainly on the distance between donor and acceptor (typically below 10 nm), the spectral overlap of their emission (donor) and absorption (acceptor) spectra and the relative orientation of their emission (donor) and absorption (acceptor) dipole moments.[102, 120–122]

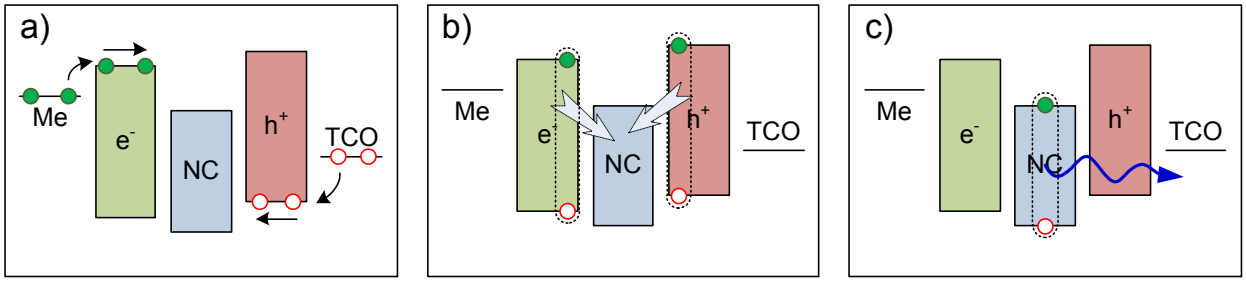

Figure 1.4: Schematic diagram of the exciton energy transfer mechanism in a simplified band diagram of the organic-nanocrystal hybrid LED. (a) shows the charge carrier injection into organic layers, followed by (b) exciton formation on the organic molecules and the energy transfer and (c) exciton formation and recombination on the nanocrystals, after [118].

The exciton energy transfer process was proposed to be the dominating effect in case of some organic-inorganic hybrid QD-LEDs, though the direct charge injection is present as well.[105] By optimizing the design of hybrid QD-LEDs to support the energy transfer, the EQE could be increased by 50% resulting in the monochromatic nanocrystal LEDs with the highest external quantum efficiency to date.[13, 105, 109]

1.2.3 Ionization mechanisms

Electron-hole pairs in nanocrystals can be also generated by ionization processes, which can occur not only during AC [71–74] but also during DC [72, 93, 101, 107] operation of the device. Two main ionization processes can be considered: impact excitation by hot electrons [69, 123] and field induced ionization [101].

In case of impact excitation by hot electrons, shown in Figure 1.5 (a), electrons in the conduction band of the light emitting crystal, injected from the interface states of the isolator or from the electrode, are accelerated by the high electric field (so-called hot electrons). At the impact event, they lose their energy and in case their energy is high enough they can thereby excite an electron-hole pair, which can recombine radiatively. This process is well-studied in case of microscopic phosphors with commercially available devices based on it.[69] When it comes to nanocrystal phosphors, the theoretical framework with according experiments need to be developed, since so far only very few nanocrystal devices, which were suggested to operate on the basis of this mechanism, have been demonstrated.[72, 106]

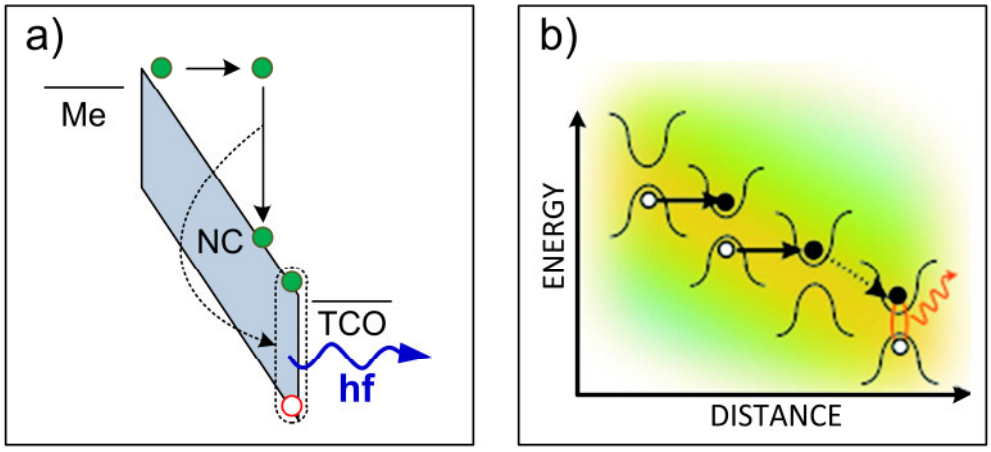

Figure 1.5: (a) Schematic diagram of the impact excitation mechanism in a simplified band diagram of the all-inorganic NC-LED: electron is accelerated by the applied electrical field, becoming hot and exciting an electron-hole pair by an impact with the subsequent radiative recombination of the latter one. (b) Schematic diagram of the field-driven ionization mechanism in a simplified band diagram of the nanocrystal LED: electron extraction from the VB of one NC to the CB of the neighbor one, resulting in hole formation and the radiative recombination, from [124].

The model of another ionization mechanism, the so-called field-driven ionization sketched in Figure 1.5 (b), was recently presented by Wood et al.[101, 124] It was suggested that if the field over a stack of nanocrystals is high enough, an electron can be extracted from the valence band of a nanocrystal and transferred into the conduction band of a neighboring nanocrystal, as shown in Figure 1.5 (b), creating an electron and a hole that are spatially separated onto neighboring nanoscale entities. Electrons and holes from the multiple ionization events that arrive at the same QD can form excitons, which then radiatively recombine, contributing to the thin film luminescence.[75, 101, 124] The suggested electric field-driven ionization process can locally generate these charge carrier pairs, needed to achieve the EL and thereby removes the design constraints of charge injection and carrier transport that are typically the dominant considerations in selecting the materials, deposition methods and architecture of nanostructured LEDs.[124]

1.3 Current Transport Mechanisms in NC-LEDs

Several charge carrier transport mechanisms can be considered to explain the I-V behavior of the nanocrystal LEDs. The most prominent ones encounter the drift, diffusion and recombination-generation of the charge carriers (Shockley equation), the overcoming of the metal-semiconductor contact potential barrier by tunneling or thermionic emission and the formation of a space charge region, leading to space-charge-limited currents. All of them can theoretically contribute to the charge transport within complex NC-LED structures, possibly dominating at certain voltage ranges. On the other hand, determining the dominant mechanism can give a route for the efficiency improvement of the device performance, since the limiting factors can then be identified and influenced. The mathematical description of the mentioned mechanisms offers a chance to identify the dominant one by a smart plot of the measured I-V characteristic on the corresponding modified scales. For this purpose the mathematical models to describe the mechanisms as well as the resulting "smart plots" are going to be introduced within the following sections.

1.3.1 Ideal p-n junction

The I-V behavior of an ideal p-n junction can be described by the Shockley diode equation [125]:

$$I = I_S\left(\exp\left(\frac{U}{nU_T}\right)-1\right), \quad (1.3.1)$$

with I being the current trough the diode, U the applied voltage, I_S the reverse bias saturation current, U_T the thermal voltage and n the ideality factor (also known as a quality factor or emission coefficient) respectively. This ideal equation is derived under the assumption of charge carrier diffusion, drift (due to the applied electrical field) and thermal recombination-generation influencing the charge transport, without accounting

for the processes of the breakdown of the diode under the reverse bias and photon-assisted charge carrier generation and recombination.

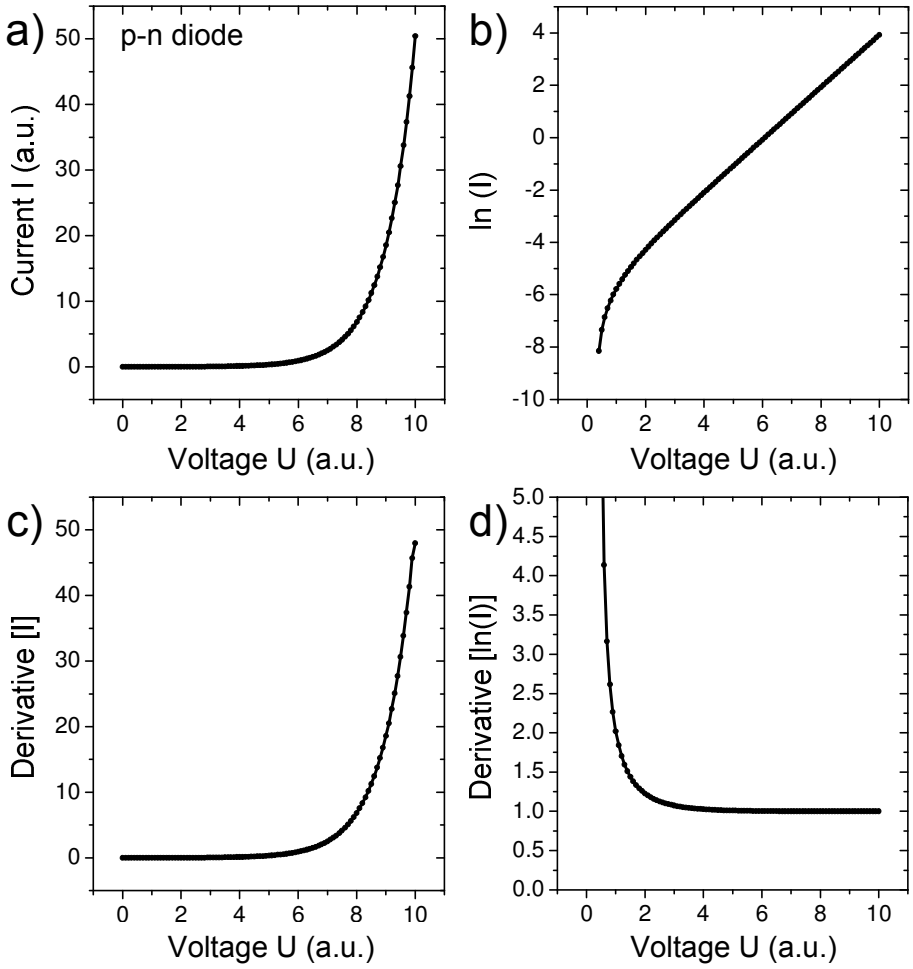

Figure 1.6: Linear plot of the diode I-V characteristic (a) and its derivative (c) as well as its semi-logarithmic plot (b) with the corresponding derivative (d).

Figure 1.6 shows an exemplary plot of the diode I-V curve (a) and its derivative (c) on a linear scale. At higher operating voltages, the impact of the saturation currents becomes negligible and the current trough the diode has an exponential dependence on the applied bias, as shown in equation (1.3.1). Therefore, when the natural logarithm of the measured current through the diode is plotted as a function of the applied bias, a linear dependence is observed in the high voltage range, as shown in Figure 1.6 (b). The corresponding slope of the curve (Figure 1.6 (d)) approaches consequently a constant value in the high voltage region. Therefore the drift and diffusion based contributions to the I-V behavior are typically identified by the semi-logarithmic plots of the I-V characteristics.

1.3.2 Charge transport mechanisms in NC-LEDs

The transport properties of the nanocrystal layers are also determined by the presence of defects, interfaces and discrete states, [126] which is quite similar to the properties of the organic layers in OLEDs. Also, most of the NC-LEDs are based on organic (semi-) conductors with very thin NC layers between organic layers or organic layers doped with NC so that the I-V-behavior is mainly defined by the involved organic materials and electrical contacts. Therefore, the charge transport models applied to explain the I-V behavior of the OLEDs are often applied to the NC-LEDs.[15, 116] In most cases, the current through the device can be explained and fitted in different ranges of applied voltages by different mechanisms and curves, but typically due to the design of the OLEDs and NC-LEDs two main operation regimes are considered: [116, 127–129]

1) the injection limited regime where the layers within the device can support the whole current injected by the electrodes and therefore the current density is limited by the charge injection properties of the electrodes, which dominate the I-V behavior.

2) the "bulk regime", which occurs when the electrodes can supply more charges than can be transported through the layers. Hence, the current density is limited by the "bulk" properties of the involved materials.

These both cases present more or less the limiting boundaries of the I-V behavior. In this part of the chapter, the main mechanisms that are considered to explain the injection and transport of the charge carriers within nanocrystal LEDs are introduced.

1.3.2.1 Injection limited current

When the current through the device is limited by the injection of the charge from the electrode rather than the bulk properties of the involved materials, it is called injection limited current (ILC).[127] The spatial distribution of the electric field E under the ILC conditions is assumed to be uniform:

$$E(x) = E(x = 0) = \frac{U}{d}, \quad (1.3.2)$$

with U being the applied voltage and d the distance between the electrodes.

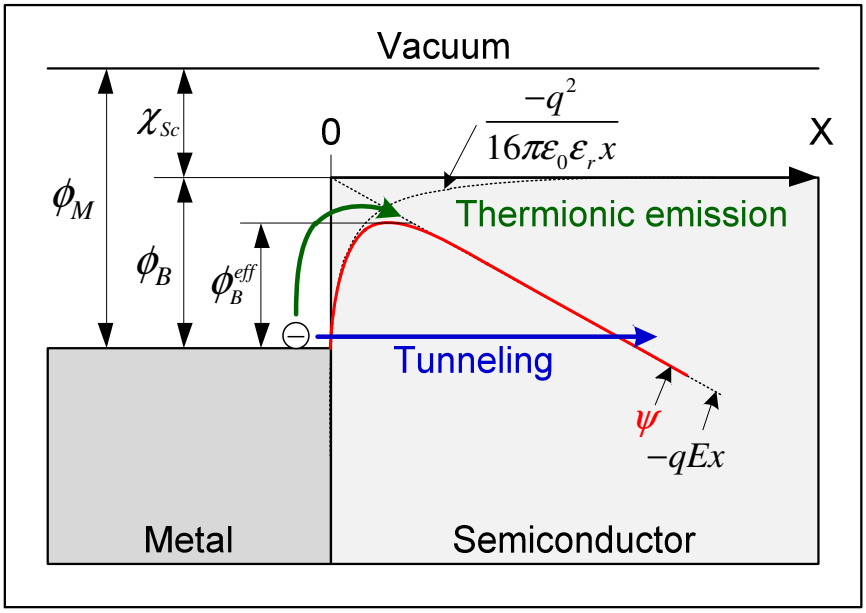

Figure 1.7: Simplified energy band diagram representing the Schottky-effect between the metal surface and the n-type semiconductor. ψ shows the resulting form of the potential barrier, lowered by the external field $-qEx$ (red). The injection of the electrons over / through the energy barrier takes place via the thermionic emission (green) and tunneling (blue) processes.

The most commonly used injection models for ILC are derived based on thermionic emission and Fowler-Nordheim tunneling effects.[69, 127, 130, 131] The schematic of both mechanisms is presented on the example of the metal-semiconductor barrier in Figure 1.7. Thereby, according to the Schottky-Mott model, the metal with the work function of ϕ_M is in an ideal contact (i.e. absence of interface states) with the semiconductor with an electron affinity of χ_{Sc} forming a potential barrier for the electrons to enter the n-type semiconductor with a height of $\phi_B = \phi_M - \chi_{Sc}$. The form of the potential barrier is derived by the induced positive image charge q at the distance x resulting in the attractive image force $F = \frac{-q^2}{16\pi\varepsilon_0\varepsilon_r x}$, with ε_0 and ε_r being the permittivity of vacuum and semiconductor respectively. When the external electric field E is applied, the total barrier height will be reduced to ϕ_B^{eff} (the so-called Schottky-effect).

Thermionic Emission (TE)

The thermally activated hopping of the electron (charge carrier) over the energy barrier (whereby the actual shape of the energy barrier is not important) is called thermionic or Richardson-Schottky emission (TE). The process is schematically shown

in Figure 1.7 in green. The temperature dependent current density J_{TE} in this case can be described as [131]

$$J_{TE} = A^* T^2 \exp\left(-\frac{\phi_B}{k_B T}\right), \quad (1.3.3)$$

where T is the Temperature, k_B is the Bolzmann constant, m^* is the effective electron mass, h is Planck's constant and $A^* = \frac{4\pi q k_B^2 m^*}{h^3}$ is the Richardson constant. Under consideration of the field induced barrier lowering, the field dependent current density can be expressed by [131]

$$J_{TE} = A^* T^2 \exp\left(-\frac{\phi_B^{eff}}{k_B T}\right) = A^* T^2 \exp\left(-\frac{\phi_B - \beta_{SC}\sqrt{E}}{k_B T}\right), \text{ with } \beta_{SC} = \sqrt{\frac{q^3}{4\pi\varepsilon_0\varepsilon_r}}. \quad (1.3.4)$$

The typical I-V curve based on the ideal TE mechanism is shown in Figure 1.8 (a) with its derivative (c) on a linear scale.

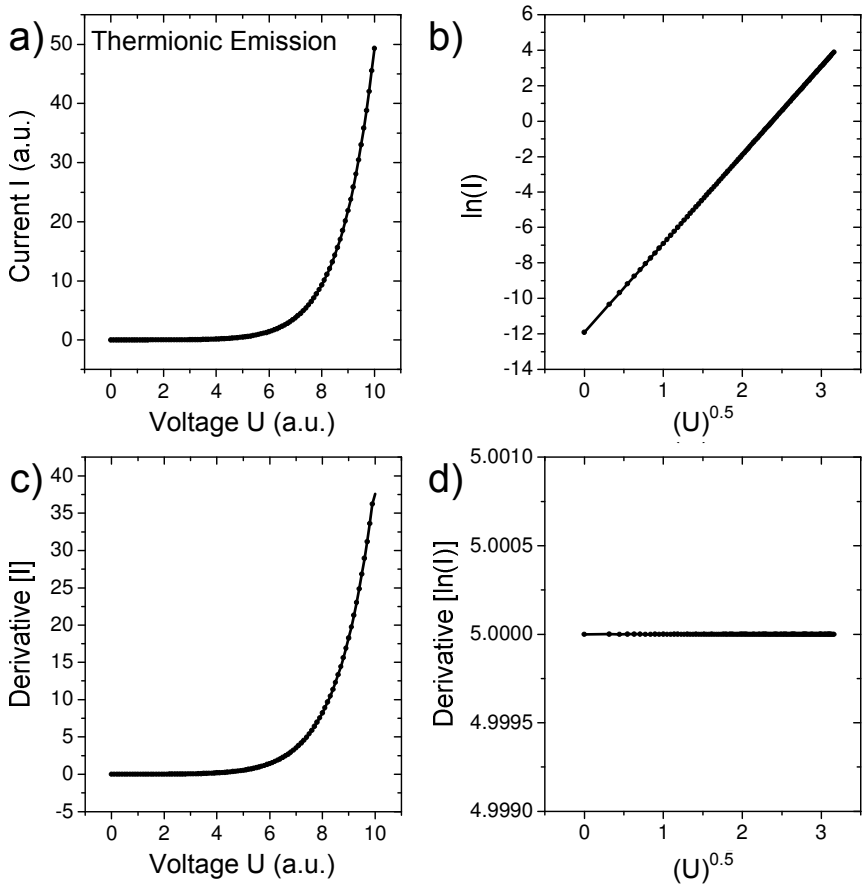

Figure 1.8: Linear plot of the ideal thermionic emission (TE)-characteristic (a) and its derivative (c) as well as its characteristic "smart" plot of $\ln(I)$ vs. $\sqrt{U}$ (b) with the corresponding derivative (d).

The main characteristic of the TE model is the high temperature dependence of the resulting current density. Practically, the evidence for the TE dominating the I-V behavior can be also identified by the linear characteristic of the $\ln(J)$ vs. $\sqrt{E}$ or the $\ln(I)$ vs. $\sqrt{U}$ plot, as shown in Figure 1.8 (b). The constant slope can be identified by the corresponding derivative plot, as shown in Figure 1.8 (d).

Tunneling Injection (TI)

When the applied electric field is high enough, the charge carriers can tunnel directly to the conduction band through the potential barrier. The process is schematically shown in Figure 1.7 in blue. Classically, the resulting current density can be described as tunneling through the barrier according to Fowler and Nordheim: [132]

$$J_{FN} = \frac{q^3}{8\pi h \phi_B} E^2 \exp\left(-\frac{\kappa}{E}\right), \text{ with } \kappa = \frac{8\pi\sqrt{2m^*}\phi_B^{3/2}}{3qh}. \quad (1.3.5)$$

In this case the current density does not depend on the temperature, but only on the barrier height and the applied electric field, resulting in

$$J_{FN} \propto E^2 \exp\left(-\frac{\kappa}{E}\right) \Leftrightarrow J_{FN} \propto U^2 \exp\left(-\frac{b}{U}\right), \text{ where } b \text{ is constant.} \quad (1.3.6)$$

Figure 1.9 shows a typical I-V characteristic of the ideal tunneling diode on the linear scale (a) with its derivative (c).

The Fowler-Nordheim tunneling dominating the I-V behavior can be ideally identified by the independence of the I-V characteristics of the device on temperature (temperature-dependent measurement series) and by the dependence of the I-V curve on the applied field (thickness-dependent I-V measurement series). Another indication for the tunneling is revealed by the linear characteristic of the $\ln\left(\frac{I}{E^2}\right)$ vs. $\frac{1}{E}$ or the $\ln\left(\frac{I}{U^2}\right)$ vs. $\frac{1}{U}$ plot (the so-called Fowler-Nordheim, FN-plot), as can be seen from Figure 1.9 (b). The slope of the curve is constant (Figure 1.9 (d)) and depends on the height of the potential barrier.

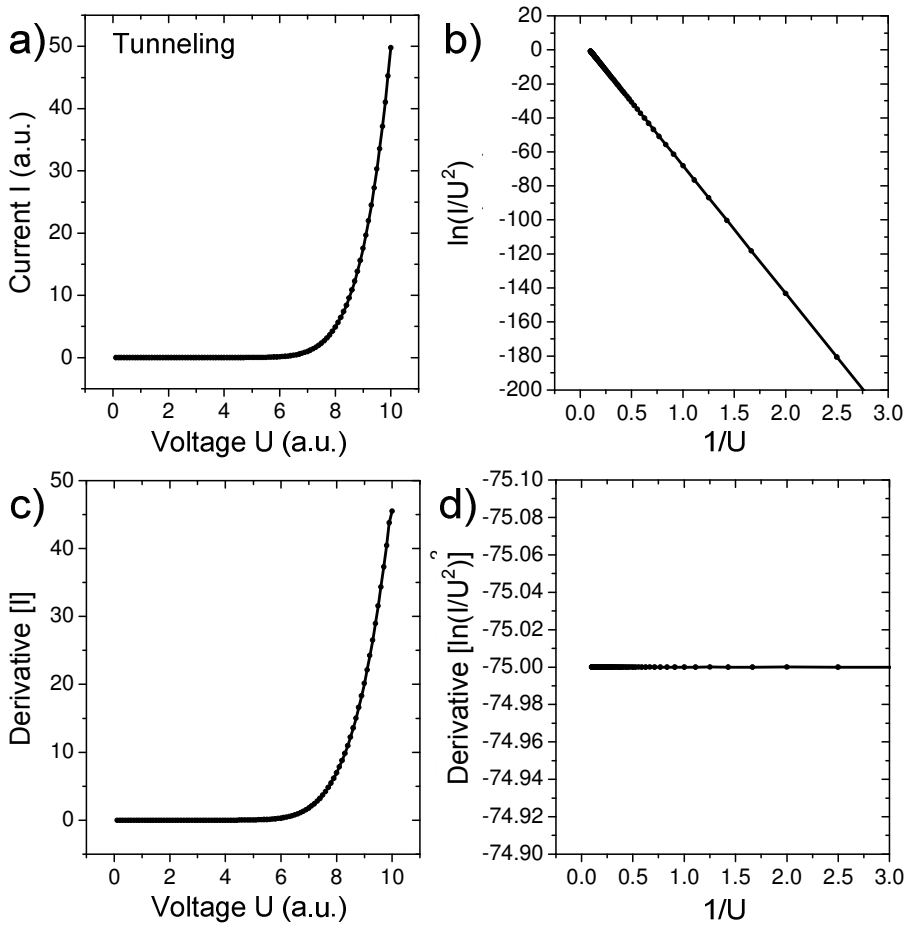

Figure 1.9: Linear plot of the ideal tunneling I-V characteristic (a) and its derivative (c) as well as its characteristic Fowler-Nordheim-plot (b) with the corresponding derivative (d).

The lowering of the potential barrier as well as diffusion effects are not considered by the classic Fowler-Nordheim relation. The more general relation can be obtained under the consideration of the energy distribution of the electrons on the Fermi-edge of the metallic contact.[130, 133]

$$J_{TI} = \frac{q^2 \pi k_B T}{h^2} \sqrt{\frac{m^*}{2\phi_B}} \sin^{-1}\left(\frac{1}{E} \cdot \frac{4\pi^2 \sqrt{2m^*} k_B T}{qh}\right) \cdot E \exp\left(-\frac{8\pi\sqrt{2m^*}\left(\phi_B\right)^{3/2}}{3qh} \cdot \frac{1}{E}\right) \quad (1.3.7)$$

The Fowler-Norheim relation (1.3.5) can be derived from the equation (1.3.7) as a special low temperature case.

1.3.2.2 Space-charge limited current (SCLC)

When the electrodes supply more charge carriers than can be transported by the material, the charge accumulates in the material (space charge is created), inhibiting further injection until an equilibrium is reached with a uniform current and a non-uniform electric field $E(x) \propto \sqrt{x}$ inside the material [128, 134]. The current in this case is called space charge limited (SCL) current. The models of the space charge limited conduction were developed in the middle of the 20th century by solving Poisson's equation, which relates the local electric field to the local charge density, and continuity equation, which states that the steady-state current density must be divergenceless [135–138, 128]. The SCL conduction models were originally developed for the description of the charge transport through polycrystalline and amorphous isolators [135–138] and later adapted to describe the I-V behavior of organic materials [129], which became a common practice in the field of organic electronics.[128, 139] The I-V behavior typical for the SCL currents was also observed for many nanocrystal LEDs. [15, 16, 85, 89, 100, 106, 116, 140]

The unipolar SCL current density through the ideal trap-free isolator without intrinsic carriers, under the assumption of a perfect ohmic contact to it, is described by the Mott-Gurney law [134, 135]:

$$J_{SCL} = \frac{9}{8}\varepsilon_0\varepsilon_r\mu\frac{U^2}{d^3}, \quad (1.3.8)$$

where μ is the field independent mobility.

This power-law dependence on voltage was first demonstrated in CdS crystals [137] and has been frequently observed in many organic materials and nanocrystalline devices.[100, 116, 141, 142] The typical I-V curve for the case of ideal SCL conduction is schematically shown in Figure 1.10 (a). In this case, the characteristic double-logarithmic plot results in the linear dependence with a slope of 2.

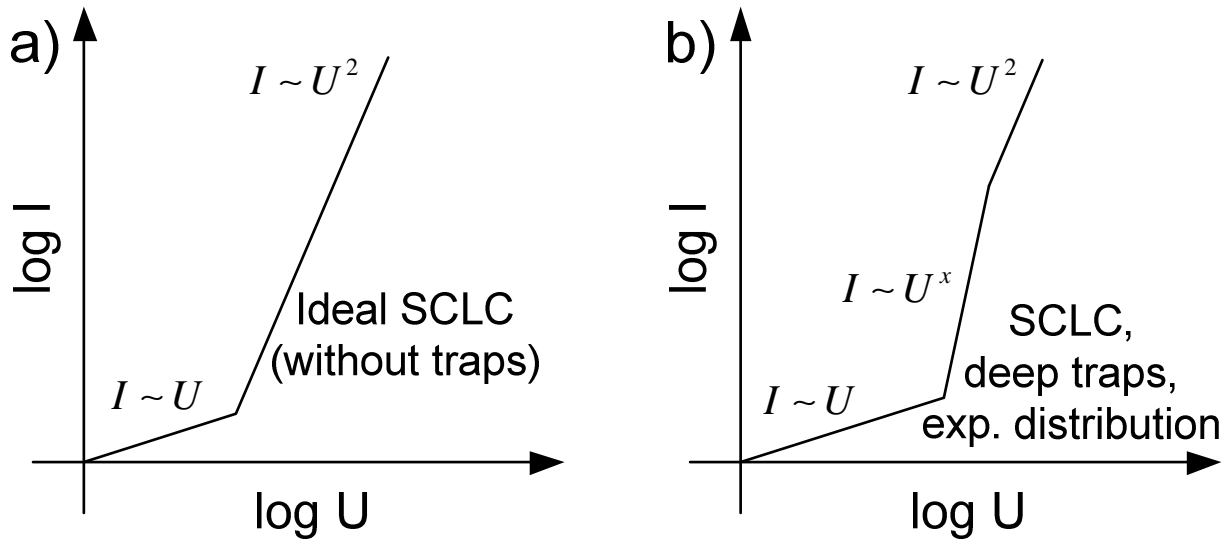

Figure 1.10: Schematic of the I-V curve corresponding to the SCL conduction within an ideal trap-free isolator (a) and an isolator with an exponential distribution of trap states (b).

In order to include the effects of trap states within the band gap of the isolator, the model was extended.[143] The so-called trap limited current (TCL) density can be derived from equation (1.3.8) under consideration of an exponential energy distribution of the trap states $f(W)$ [143], which is (in case of electron transport) defined as

$$f(W) = \frac{N_T}{k_B T_T} \exp\left(\frac{W - W_C}{k_B T_T}\right), \quad (1.3.9)$$

where N_T is the density of the traps, T_T is the characteristic temperature of the distribution (higher than the measurement temperature) and W_C is the edge of the conduction band. The resulting TCL is then described as [143]

$$J_{TCL} = q^{l-1} \mu N_C \left(\frac{2l+1}{l+1}\right)^{l+1} \left(\frac{l \varepsilon_0 \varepsilon_r}{(l+1) N_T}\right)^{l} \frac{U^{l+1}}{d^{2l+1}}, \quad (1.3.10)$$

with N_C being the effective density of states in the conduction band and $l = \frac{T_T}{T}$ being a parameter reflecting the relation between the average trap energy $k_B T_T$ and the thermal energy $k_B T$. The more convenient notation of this relation is

$$J_{TLC} \propto \mu \frac{U^{l+1}}{d^{2l+1}}. \quad (1.3.11)$$

In case of TCL, the total current density is reduced, compared to trap-free SCL current, due to the charge capture in the traps. Increasing the applied voltage results in an increase of injected charge carriers, which fill the limited number of traps. The reduction of empty traps results in a rapid, power-law $I \propto U^{\alpha}$ increase in current. At sufficiently high applied bias, all the traps are filled (the so-called traps-filled-limit, TFL [138]) and consequently, the current becomes SCL, as schematically sketched in Figure 1.10 (b). The possible contribution by space charge limited effects can be identified in a double logarithmic plot of the I-V curve. In this case, the I-V characteristic would follow a linear fit, whereby the slope of the curve equals the coefficient $\alpha = l + 1$ of the typical power law dependence.

In cases of typical SCL and TCL currents at very low electric fields, the I-V-behavior typically exhibits first linear ohmic ($\alpha = 1$) or super-ohmic ($1 < \alpha < 1.5$) conduction,[15, 106, 116, 142] before the applied field is sufficient enough to populate the trap states, so that SCL / TCL conduction becomes dominant[144], as sketched in the low-voltage regime in Figure 1.10.

Charge carrier transport in nanoparticle systems can, in most cases, be described by the introduced space-charge-limited current model assuming hopping of electrons, whereby in most cases the TFL is not reached within the range of the operation voltage, so that TCL conduction dominates the I-V behavior.[8, 15, 95, 106, 116, 140, 145, 146] In some cases, a transition between different trap states takes place when the applied bias is increased. This causes a change of the corresponding slope on the double-logarithmic plot.[29, 113]

To model such an I-V behavior, a function

$$I_{TCL}(U) = a \cdot U + b \cdot U^{4} + c \cdot U^{13} \quad (1.3.12)$$

defined as the sum of the linear ohmic and two power-law (~U^4 and ~U^{13}) contributions (with constants a, b and c) was chosen and plotted in Figure 1.11 (green) on a linear (a) and double-logarithmic (b) scale with the corresponding derivatives (c and d). On the double-logarithmic plot, the single components (black, red and blue curves) represent the asymptote of the resulting function within the voltage range, where their contribution is dominant (Figure 1.11 (b)). The derivative of the components, shown in Figure 1.11 (d) is constant, corresponding to the slope of the linear asymptote in Figure 1.11 (c). The derivative of the resulting curve approaches a constant value only at very low voltages, where the ohmic contribution is very dominant. At higher voltages, where the power-law dependence with the exponent of 4 dominates the

conduction (0.5 to 0.8 on the X-axis in Figure 1.11 (b)), no distinct approaching of the derivative to the constant value of 4 (Figure 1.11 (d)) can be observed.

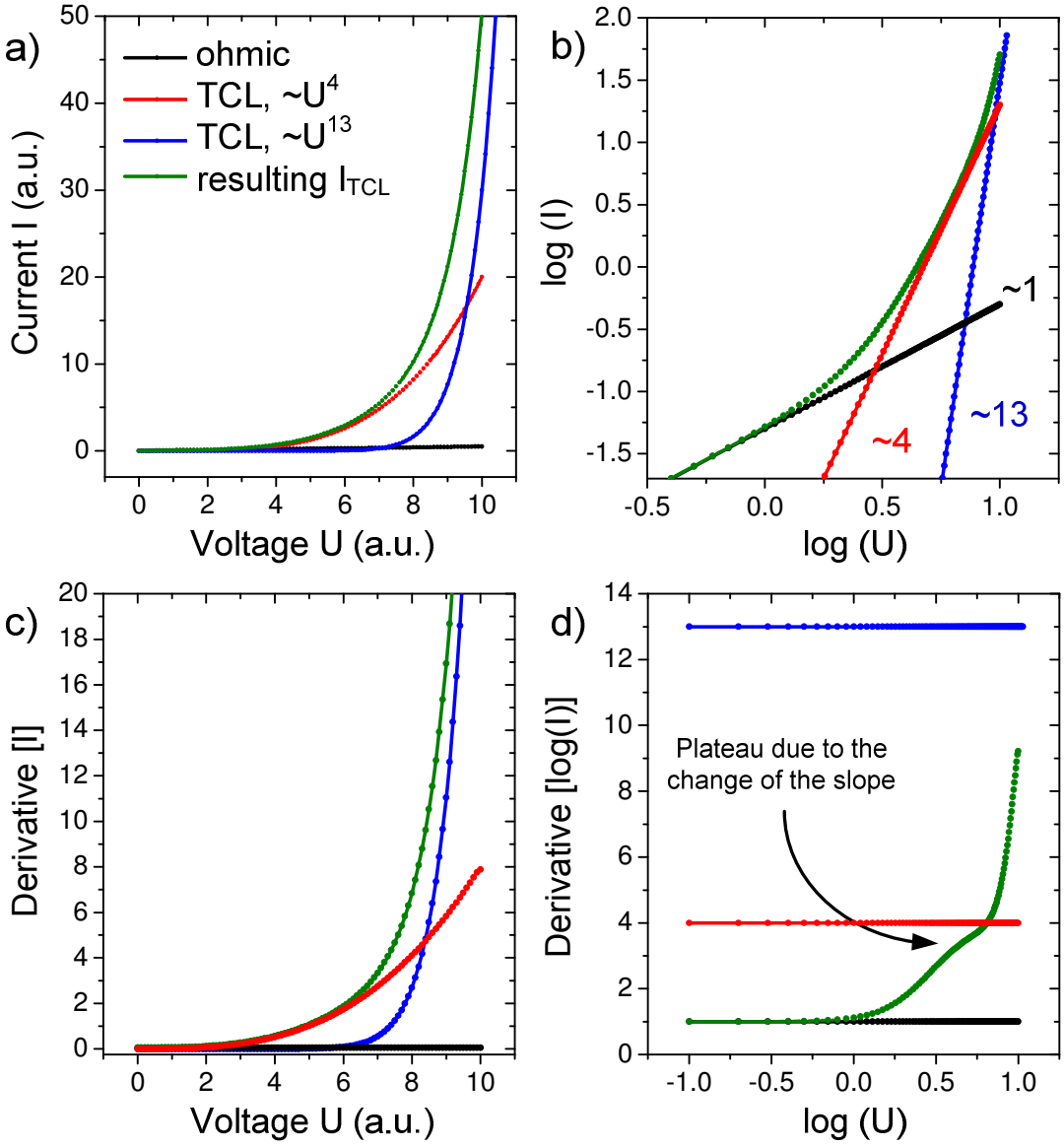

Figure 1.11: Ohmic (black), and power law contributions with the exponent of α=4 (red) and α=13 (blue) as well as the resulting sum of the functions (green) on a liner (a) and double-logarithmic (b) scale with the corresponding derivatives (c,d).

Instead, a "plateau" is formed due to the change of exponent from 4 to 13. The height of the plateau is below the value of 4 and at higher voltages the final value of the exponent (13) is by far not yet reached, although according to the plot in Figure 1.11 (b) the higher exponent contribution becomes dominant. Therefore, it is quite speculative to draw conclusions on the trap density or the position of its energy within the higher voltage range when at least two different defect states distributions are active and the final saturation limit is not yet reached.

1.3.2.3 Intermediate regimes

All discussed conduction mechanisms can contribute, though more or less intense, to the charge transport through a nanocrystalline device. The range, where the contribution of at least one additional mechanism can no longer be neglected and becomes even comparable to the initial one, is called the intermediate regime.[127, 128] The voltage range of this intermediate regime, typically between ILC and SCL/TCL conduction, strongly depends on device design and dimensions and can cover a very wide range of operating voltages, sometimes even the whole operating range.[127] Therefore, the quantitative fitting of the I-V curves, especially within the intermediate regime, can be highly speculative, since different additional experiments are required for clear interpretation of the I-V behavior as well as for the extraction of the important parameters of the involved materials such as mobility, built-in potential, injection barrier height, average energy of the trap states and others.[127, 128]

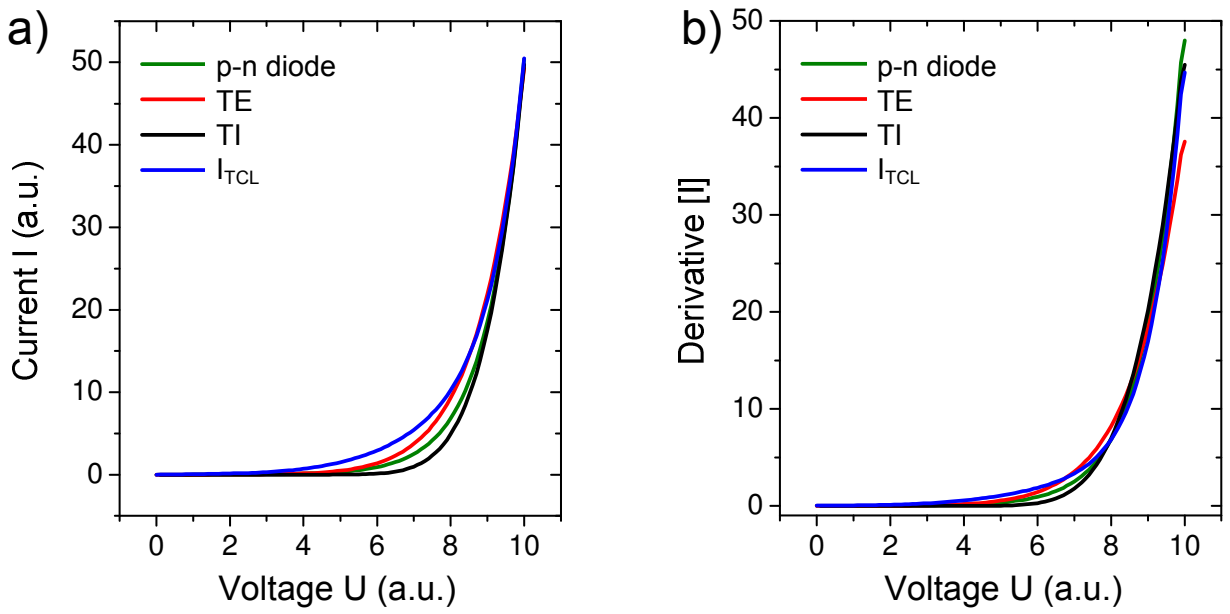

Figure 1.12: Linear plot of the I-V curves (a) based on the Shockley-equation (green), thermionic emission (red) and tunneling (black) through the energy barrier as well as trap-charge-limited conduction (blue) and the corresponding derivatives (b).

As can be seen from Figure 1.12, showing sample I-V curves based on the equations (1.3.1), (1.3.4), (1.3.6) and (1.3.12), there is no obvious difference between neither the I-V curves of the mechanisms (a) nor their derivatives (b) under forward bias on a linear scale. Nevertheless, the I-V-curves can be analyzed qualitatively. Characteristic features

of the different mechanisms on the different "smart"-plots of the I-V curve can help deduce and identify the involvement of a particular mechanism within the voltage range where it plays a significant role among the others. For this purpose, sample curves corresponding to the different mechanisms, as introduced above (Figure 1.12 (a)), are plotted on each of the "smart"-plots with the corresponding derivatives below.

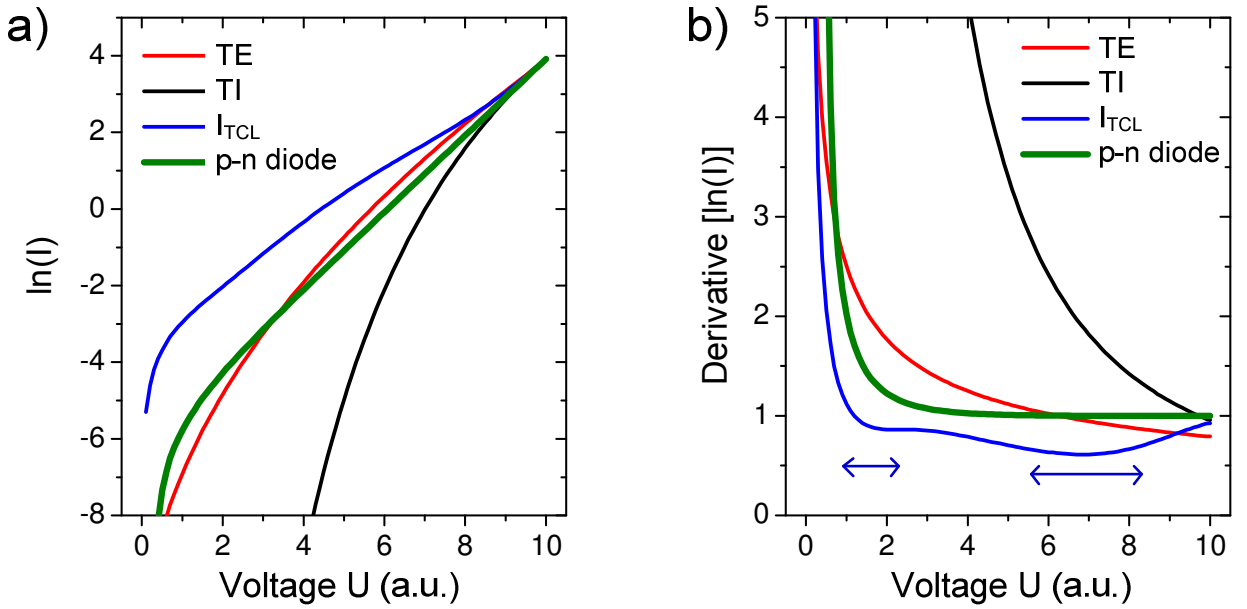

Figure 1.13: Semi-logarithmic plot of the I-V curves typical for the thermionic emission (red), tunneling injection (black), trap-charge-limited conduction (blue) and p-n diode (green) (a) with the corresponding derivatives (b).

Figure 1.13 shows a semi-logarithmic plot of the typical I-V curves of the introduced transport mechanisms (a) and their derivatives (b). No clear difference between the different I-V-curves is evident from Figure 1.13 (a), with all of the curves showing a constant, monotonically increasing behavior, approaching a linear (p-n diode) or an almost linear (others) behavior in the high voltage range. On the other hand, the behavior of the derivatives (Figure 1.13 (b)) is clearly different. While the derivative-curve of the p-n-diode approaches a constant value with increasing voltage, TE and TI exhibit a monotonous decrease over the entire voltage range. TCL is the only mechanism showing a monotonous increase in the high-voltage range, whereby the modeled TCL-conduction of the NC-layer (Figure 1.11) also shows two local minima in the transition range between the ohmic and TCL ($\sim U^4$) and the two different TCL ($\sim U^4$ and $\sim U^{13}$) regimes, as indicated by the blue arrows.

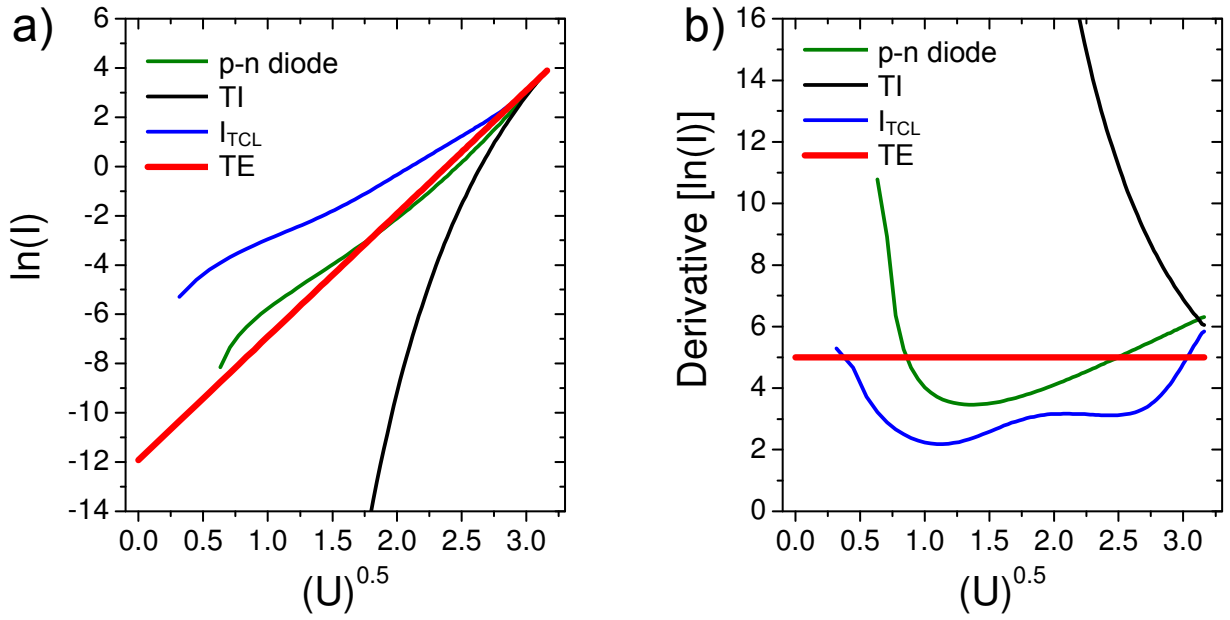

Figure 1.14: Plot of the natural logarithm of current (a) and its derivative (b) as a function of the square root of the voltage for thermionic emission (red), tunneling injection (black), trap-charge-limited conduction (blue) and p-n diode (green).

Figure 1.14 plots the natural logarithm of current vs. the square root of the voltage for the typical I-V curves (a) of the introduced transport mechanisms and their derivatives (b), usually introduced to identify the TE contribution to the I-V characteristic. Only TE results in a linear behavior on a plot (a) over the whole voltage range, while the other mechanisms superficially approach a linear behavior as the voltage increases. The plot of the corresponding derivatives (b) clearly shows a constant for the TE over the whole voltage range. The curves corresponding to p-n diode and TCL behavior show an increase of their slopes for the high voltage range, while the slope of the TI curve monotonously decreases over the whole voltage range.

Figure 1.15 shows a double-logarithmic plot of the typical I-V curves (a) of the introduced transport mechanisms and their derivatives (b), usually introduced to identify the space-charge / trap-charge limited conduction. The slopes of the TE, TI and TCL curves (Figure 1.15 (b)) increase monotonously with increasing voltage, while the TCL curve shows a typical plateau, discussed above. Tunneling is the only mechanism resulting in a continuous decrease of the slope with increasing voltage throughout the whole voltage range. This characteristic implies a possible contribution of tunneling to the overall I-V characteristics.

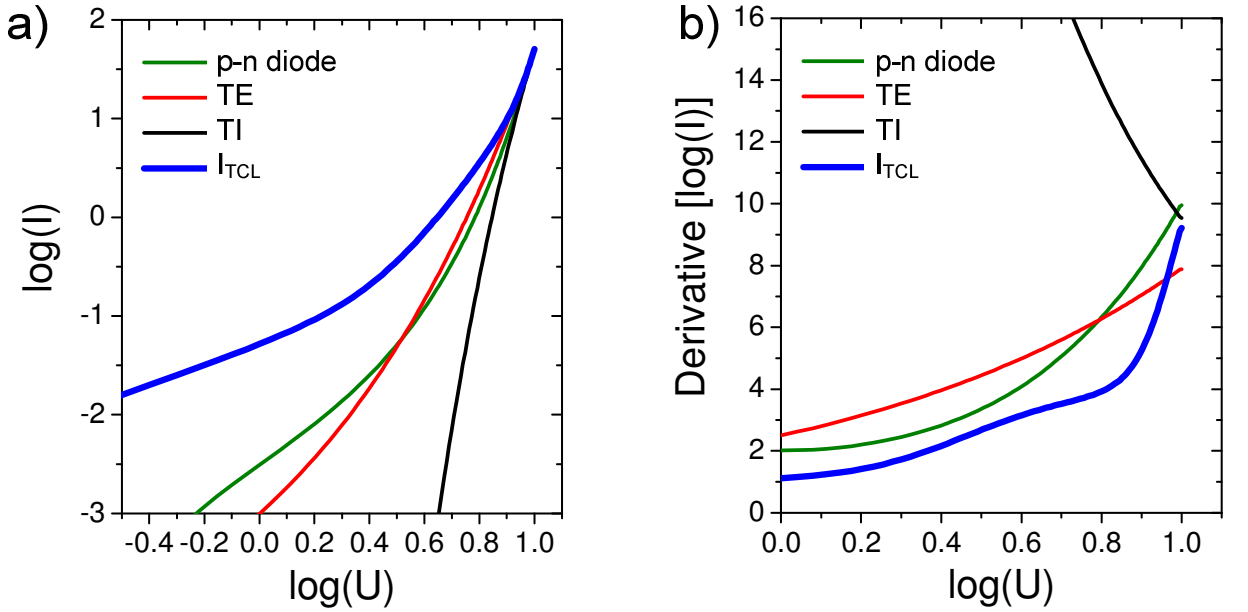

Figure 1.15: Double-logarithmic plot of the I-V curves typical for thermionic emission (red), tunneling injection (black), trap-charge-limited conduction (blue) and p-n diode (green) (a) with the corresponding derivatives (b).

Another method to identify tunneling is to plot the I-V curve and the corresponding derivative as Fowler-Nordheim plots, as shown in Figure 1.16. The curves, related to p-n diode and thermionic emission, exhibit a continuous decrease of the slope, whereby the slope remains negative throughout the whole voltage range.

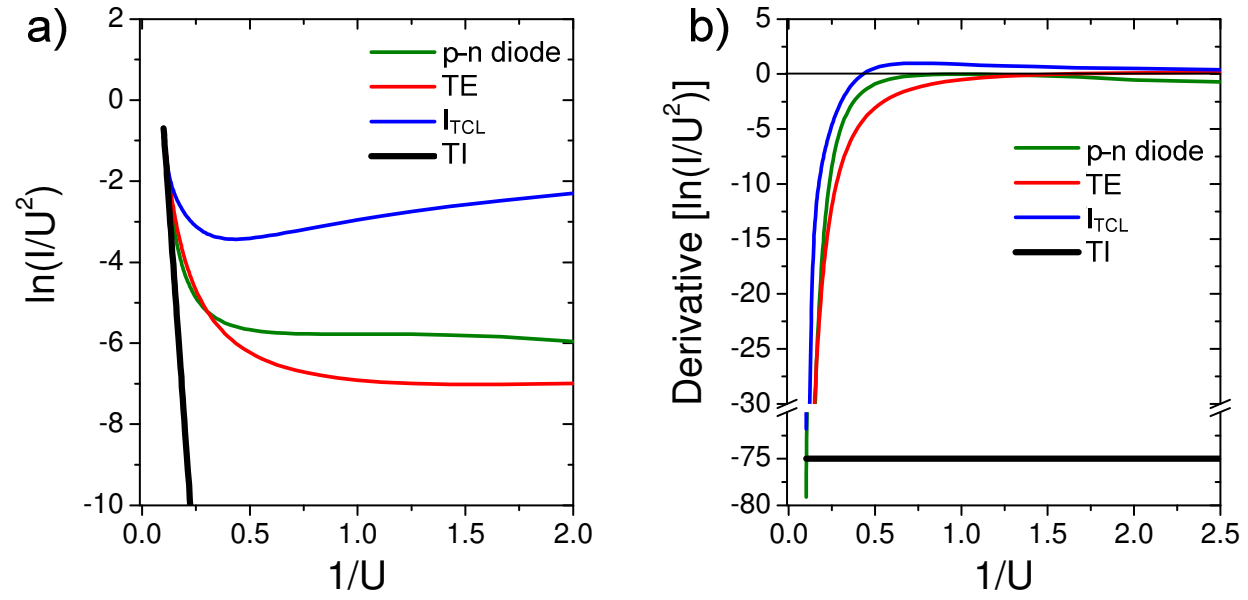

Figure 1.16: Fowler-Nordheim-plot of the I-V-curves typical for thermionic emission (red), tunneling injection (black), trap-charge-limited conduction (blue) and p-n diode (green) (a) with the corresponding derivatives (b).

Only the modeled TCL-behavior shows first an increase of the slope (the slope becomes positive) due to the ohmic contribution in the low-voltage range, followed by the fast decrease of the slope accompanied by the reversal of the sign of the slope due to the power law contribution becoming dominant as the voltage is increased. The tunneling mechanism results in a constant slope, corresponding to the height of the potential barrier (Figure 1.16 (b), black curve). While the standard Fowler-Nordheim-plot (Figure 1.16 (a)) superficially shows a linear behavior for all of the discussed mechanisms in the high-voltage range, the corresponding plot of the derivatives is far more conclusive when it comes to the identification of the possible tunneling contribution to the total I-V characteristic of the device.

Chapter 2

Optical and Electronic Properties of ZnO: Background

The following chapter gives a short introduction to ZnO and its electronic and optical properties with a focus on the emission properties of ZnO crystals, since their knowledge as well as the potential of their modification is very important for the design of the efficient LEDs with the desired electroluminescent properties.

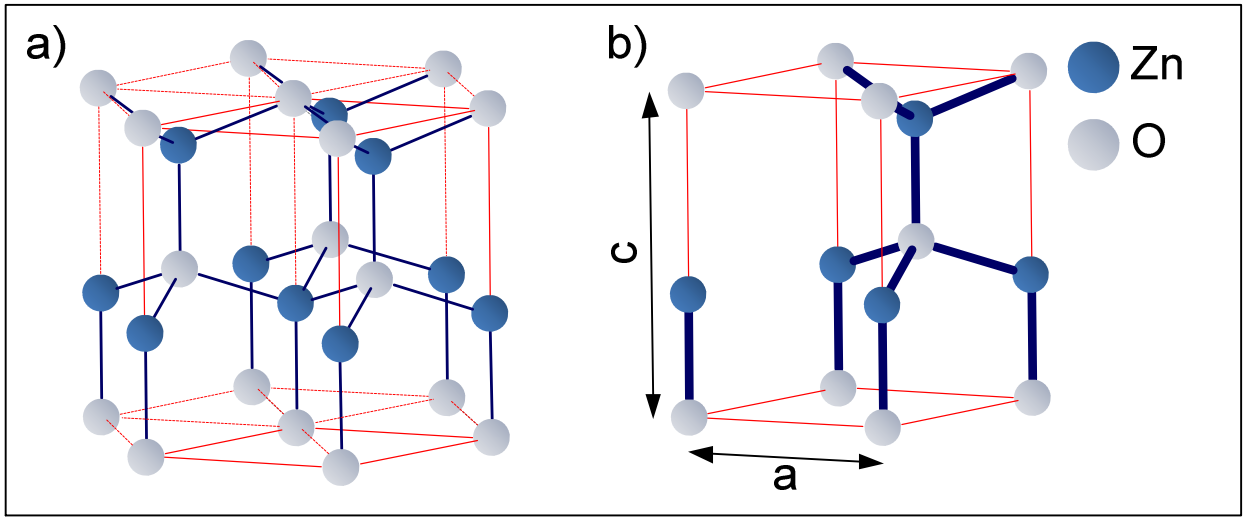

Figure 2.1: Schematic of the wurtzite-type crystal structure of ZnO. (a) shows the hexagonal symmetry of the structure. (b) shows a unit cell of ZnO with corresponding lattice constants a and c. Blue lines represent the tetrahedral coordination between neighboring atoms. The dark blue spheres correspond to zinc atoms and the grey ones to oxygen.

ZnO belongs to the group of II-VI compound semiconductors, which comprise the binary compounds of Zn, Cd, and Hg (group II in the periodic system of elements) with O, S, Se, and Te (group VI) and their ternary and quaternary alloys.[147] While at high

pressure ZnO can be stabilized in the rock salt structure and the cubic zinc blende-type structure can be grown epitaxially on suitable cubic substrates, [27, 36, 147–151] ZnO preferably crystalizes in the hexagonal wurtzite–type structure, sketched in Figure 2.1 (a). The structure is composed of two interpenetrating hexagonal close-packed sublattices of each type of atom, displaced along the threefold *c*-axis by 3/8 (ideal crystal) with respect to each other.[27, 36, 147]

The two lattice parameters *a* and *c* of the wurtzite-type ZnO unit cell are shown in Figure 2.1 (b). Typical values for *a* and *c* are reported to be in the range of 3.2475 to 3.2501 Å and 5.2042 to 5.241 Å, respectively.[36] The ratio c/a of the lattice constants is around 1.6 and deviates only slightly from the ideal value of $c/a = \sqrt{8/3} \approx 1.633$.[36, 147] Within the crystal, one oxygen atom is tetrahedrally arranged with four zinc atoms and vice versa. This type of arrangement is typical for covalent chemical bonding with sp^3 hybridization. Furthermore, the Zn-O bond also shows strong ionic character. Therefore ZnO is classified as both ionic and covalent compound with an iconicity of $f_i = 0.616$ on the Phillips scale.[152] The partial ionic bonding and the lack of center of inversion gives rise to the piezoelectrical properties of ZnO.

The magnetic, thermal and anisotropic properties of ZnO [27, 36, 147] are not going to be discussed here. Instead, the focus of this chapter lies on the electronic and emissive properties of ZnO, most relevant to the fabrication of LEDs, which are going to be introduced below.

2.1 Emission Properties of ZnO

In order to understand such optical properties of ZnO crystals as transmission characteristics and near-band-gap and defect related emission, an introduction to the electronic band structure of ZnO is needed first. ZnO is a direct band gap semiconductor, which means that the global minimum of the conduction band and the global maxima of the valence bands (CB and VB respectively) are situated at the same $k = 0$ point of the Brillouin zone (so-called Γ-point), as schematically shown in Figure 2.2.

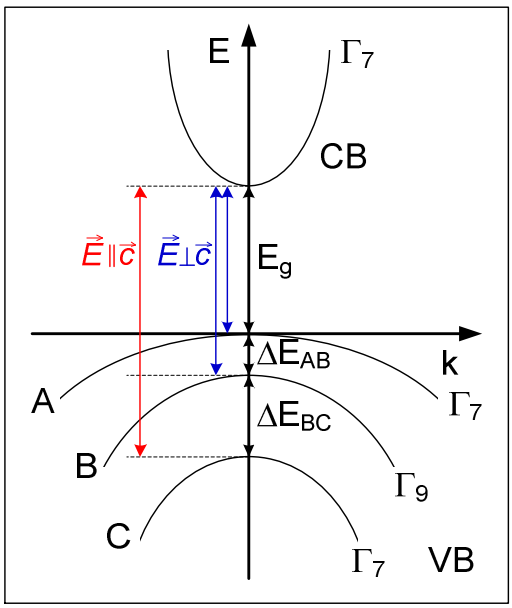

Figure 2.2: The conduction band (CB) and the valence band (VB) of ZnO in the vicinity of the fundamental band gap. The polarizations of the dominant transitions are indicated. After [37].

The lowest CB is formed by the empty 4s states of Zn^{2+} or the antibonding sp^3 hybrid states and its bottom has a Γ_7 symmetry.[147] The VB is formed from the occupied 2p orbitals of O^{2-} or from the bonding sp^3 orbitals. Due to the crystal field and the spin-orbit coupling, the VB of ZnO is spit into 3 closely spaced valence bands, referred to as the A, B and C bands. The A and C subbands are known to have Γ_7 symmetry, while the B subband has a Γ_9 symmetry.[27, 36, 147, 153] The distance between the A and the B band (ΔE_{AB}) is in the order of 5 meV and between the B and the C band (ΔE_{BC}) in the order of 40 meV at low temperatures.[27, 36, 147, 153, 154] With increasing temperature, the band gap shrinks due to the change in the lattice constants and lattice

vibrations, which results in the reduction of the transition energy following the empirical Varshni relation [155]

$$E_g(T) = E_0 - \frac{\alpha T^2}{T+\beta}, \quad (2.1.1)$$

with E_0 [eV] being the extrapolated band gap energy at a temperature of 0 K and α [eVK^{-1}] and β [K], being the material specific temperature constants. The typical values of the constants for single crystal ZnO band gap are $\alpha = -0.55 \cdot 10^{-3}$ eVK^{-1} and $\beta = -900$K for temperatures up to 300K.[36] The excitonic transition energies associated with the A, B and C valence bands also follow this relation with $\alpha = -0.72 \cdot 10^{-3}$ eVK^{-1} and $\beta = -1077$K [27], although slightly different values have also been reported.[156, 157] In case of nanostructures, experimentally β remains in the range of 900 K to 920 K while α shows slightly lower values, compared to bulk, in the range of about $-0.95 \cdot 10^{-3}$ eVK^{-1} to $-1.2 \cdot 10^{-3}$ eVK^{-1}.[158–161] The room temperature direct band gap of ZnO is reported to be between 3.365 eV [37] and 3.377 eV [27, 36, 162, 163].

2.1.1 Near-band-gap-related (NBR) emission in ZnO

ZnO was historically probably the first semiconductor, which demonstrated excitonic features at room temperature.[37, 164] Excitons are quasiparticles formed by the Coulomb attraction between (mostly photo-excited) holes in the VB and electrons in the CB. These quasiparticles can move through the crystal and thereby transport the energy until electron and hole recombine. The energy E_X, which is released by this process is the band gap energy E_g of the semiconductor, reduced by the binding energy of the free exciton $E_{b,X}$.[36]

$$E_X = E_g - E_{b,X} \quad (2.1.2)$$

The binding energy of the exciton can be described with good accuracy by a hydrogen-like series: [37]

$$E_{b,X} = \frac{\mu e^4}{8\varepsilon^2 h^2} \cdot \frac{1}{n_B^2} = R_y^* \cdot \frac{1}{n_B^2}, \quad (2.1.3)$$

with n_B being the main (or Bohr) quantum number of the exciton state, μ the reduced effective exciton mass, $\varepsilon = \varepsilon_0 \varepsilon_r$ the effective dielectric constant, e the elementary charge, h the Planck constant and R_y^* the excitonic Rydberg energy.

The exciton binding energy in most bulk semiconductors is well below or, in case of GaN, close to the value of the thermal energy at 300 K (≈26 meV) [165], which leads to thermal dissociation of the excitons at room temperature. In case of ZnO, the exciton binding energy $E_{b,X}\,(n=1) \approx 60$ meV [166] is significantly higher than the thermal energy at 300 K, resulting in excitonic features of the near-band-gap transitions at room temperature.[36, 37, 154] This high exciton binding energy makes ZnO a very promising material for efficient light emitting and lasing applications.[27, 36, 37, 147, 167–169] The corresponding excitonic Bohr radius α_B^X of ZnO is reported to be in the order of 1.8 nm [37, 147, 156, 170] to 2.34 nm [27, 36, 38, 163].

Free excitons, especially at low temperatures, can be bound to some radiative or nonradiative centers, caused by different structural defects and impurities, which results in the formation of the so-called bound exciton complexes (BEC). Depending on whether electron or hole are coupling to the neutral (or ionized) defect state, the BECs are called neutral (or ionized) donor- (DX) and acceptor- (AX) bound excitons respectively.[36, 37] The emission energy of these BECs is the energy of the corresponding free exciton (mostly A), reduced by the characteristic binding energy of the exciton complex $E_{b,BEC}$.[36, 37]

$$E_{BEC} = E_X - E_{b,BEC} \quad (2.1.4)$$

The ionized donor bound excitons (D^+X) have the smallest binding energy to the complex of about 5 meV, followed by neutral bound excitons (D^0X) with binding energy typically above 10 meV. The neutral acceptor bound exciton (A^0X) binding energy can be as high as 50 to 120 meV.[37, 38, 147] The typical energy ranges where a particular donor and acceptor bound excitons may be found is shown in Figure 2.3.

Additional characteristics, which can be observed in low temperature ZnO PL spectra in the UV spectral range, are the two electron satellites (TES) of the D^0Xs and the longitudinal optical phonon replicas (LO) of the free and bound excitons. TES transitions involve radiative recombination of a neutral donor bound exciton, leaving the donor in the excited (2s, 2p instead of 1s) state. The separation between the D^0X and the corresponding TES can be approximated by $3/4$ of the donor binding energy.[37, 171] The typical energy range of TES transitions [36, 37] is also shown in Figure 2.3.

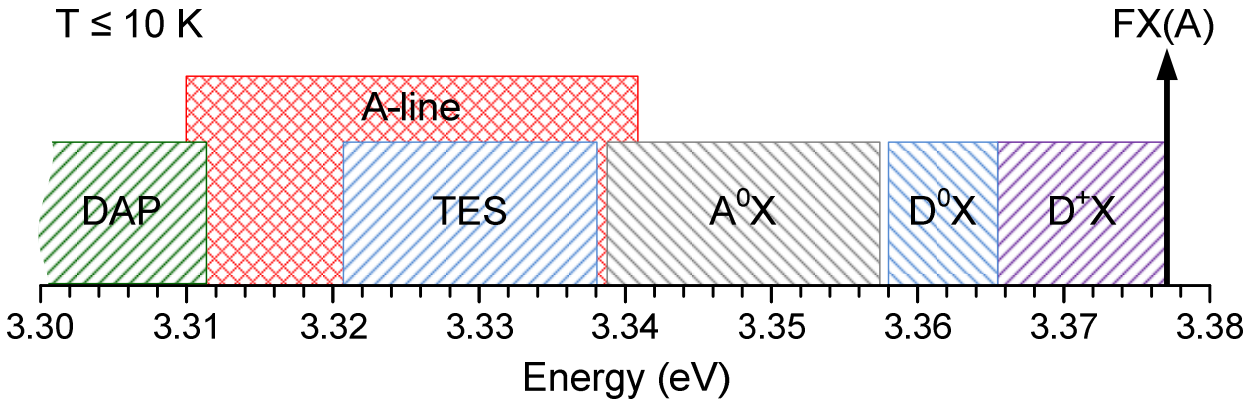

Figure 2.3: A schematic drawing of the energy ranges where the various bound exciton transitions may occur.

Free and bound exciton transitions can occur with the emission of one or more optical phonons at the cost of a lower transition probability, resulting in the LO-phonon replica of the free ($E_{LO,X}$) and BEC ($E_{LO,BEC}$) excitons. The energy of these transitions is given by [36]

$$E_{LO,X} = E_g - E_{b,X} - m \cdot E_p;\ E_{LO,BEC} = E_X - E_{b,BEC} - m \cdot E_p,\ (m = 0,1,2,3...) \quad (2.1.5)$$

with m being the number of the phonons emitted per transition (typically 1 to 4). In general, the transition probability and the emission intensity decrease with the increase of m. The energy separation between the free (E_X) or bound exciton (E_{BEC}) transition and the corresponding LO-phonon replica ($E_{LO,X}, E_{LO,BEC}$) is in the range of $E_p \approx 71$ to 73 meV (phonon energy).[27, 36, 37, 147, 167]

The discussed BECs have no translational degree of freedom, therefore they form very narrow absorption and luminescence bands at low temperatures with a width down to 1 meV.[147, 172] ZnO nanostructures, such as rods, nanocrystals or quantum dots, typically exhibit a larger linewidth at low temperatures with values between 10 and 170 meV [159, 167, 168, 173], although values of 3.7 meV and below were also achieved by annealing.[173, 174] The large linewidths, compared to bulk ZnO, result from typical wide size and shape distribution of the nanostructures as well as high amount of defects stemming from the synthesis routes and increased surface to volume ratio. Also, the number of the observed BEC peaks in ZnO nanostructures is typically lower than in ZnO single crystals.[167] The temperature dependent behavior of the BEC transitions in both bulk ZnO and nanostructures is the same: with increasing temperature their intensity decreases progressively compared to the intensity of free excitons due to thermal dissociation. The BEC lines disappear at temperatures between

50 and 150 K, depending on their binding energies to the corresponding defects.[36, 37, 167] Consequently, the free exciton emission becomes by far the dominant one at room temperature, whereby the separation between A and B excitonic peaks usually can not be spectrally resolved at temperatures higher than 160 K.[167] The exception is the observation of so-called A- (or Y-) line with its corresponding LO-phonon replica in different ZnO nanostructures with enhanced surface to volume ratio [159, 173–177], which can clearly be traced from low temperatures (at ~3.31 to 3.34 eV) up to room temperature.[174, 175] Although the exact origin of this line, most frequently observed at ~3.333 eV [178] is still controversially discussed in literature [36, 37, 160, 168, 178], the most established explanation for this transition are free excitons bound to the surface states or extended structural defects at the surface of the nanostructures.[168, 173–178]

In addition to the introduced transitions, donor-acceptor-pair-related (DAP) transitions can also be observed in the near-band-gap spectral range in ZnO. The corresponding typical energy range of these transitions is between ~3.1 and 3.27 eV at low temperatures [36, 37] with only few reports of DAP transitions slightly above 3.31 eV.[179, 158] The schematic drawing of the energy ranges for different discussed NBR-related transitions in ZnO at low temperature in Figure 2.3 is therefore completed by the upper part of the energy range for the possible DAP transitions.

2.1.2 Defect related optical transitions in ZnO

Room temperature PL spectra often contain not only excitonic near-band-gap emission but also pronounced emission throughout the whole visible spectral range, stemming from different defect-related transitions within the band gap of ZnO. This defect related emission can strongly dominate the overall emission characteristics or even completely suppress excitonic emission of ZnO with quantum yields at room temperature up to 0.2 and 0.45.[41, 42]

In general, defect-related transitions in semiconductors can be classified as free-to-bound (FB) and bound-to-bound (BB) transitions. FB, or band-impurity transitions, are those from the donor level to the valence band (VB), $\left(D^0, h\right)$, or from the conduction band (CB) to the acceptor level $\left(e, A^0\right)$, as schematically shown in Figure 2.4 by the transitions 1 and 2 respectively. The emission energy (E_1 / E_2) of these transitions depends on the band gap E_g of the semiconductor, the ionization energy of the

corresponding impurity (E_D / E_A) and the mean kinetic energy of free carriers in the CB or VB, respectively.[180–182]

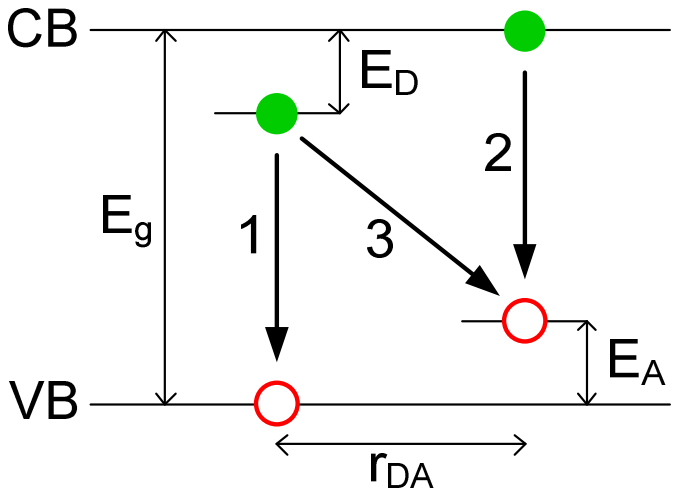

$$E_1 = E_g - E_D - E_{kin} \quad (2.1.6)$$

$$E_2 = E_g - E_A + E_{kin} \quad (2.1.7)$$

$$E_3 = E_g - (E_D + E_A) + E_C, \quad (2.1.8)$$

$$E_C = \frac{e^2}{4\pi\varepsilon r_{DA}}. \quad (2.1.9)$$

Figure 2.4: A schematic drawing of the energy ranges where the various bound exciton transitions may be positioned.

The BB or donor-acceptor-pair (DAP) recombination energy E_3 is given by the band gap of the material and the ionization energies of the involved donor and acceptor levels as well as the Coulomb interaction energy E_C between them. E_C therefore depends on the static dielectric constant $\varepsilon = \varepsilon_0 \varepsilon_r$ of the material and the distance r_{DA} between donor and acceptor in the pair. For smaller r_{DA} values (typically below 40 Å), the emission line of each DAP is separated, resulting in a series of sharp emission lines in the PL spectrum. For larger values of r_{DA} (so-called distant DAP), the intervals among the emission lines are small leading to the observation of a broad emission band.[69]

Contrary to FB transitions, the DAP transitions typically show a shift towards higher energies (blue shift) with increasing excitation power density, which can be approximated by [180]

$$E_{DAP}(P_{exc}) = E_{DAP,0}(P_0) + \beta \log(P_{exc}/P_0). \quad (2.1.10)$$

$E_{DAP,0}$ is thereby the energy of the DAP transition at the initial excitation power P_0 and β represents the energy shift of the transition per decade of the excitation power increase. Typical values of β for conventional DAP transitions are in the range of 5 meV per decade and below, [183–186] which usually increases with increasing impurity doping level (above $5 \cdot 10^{18}$ cm^{-3}).[183, 187] Another possibility to distinguish

DAP transitions from the FB ones is by their temperature-dependent behavior: contrary to FB, DAP transitions exhibit almost no line broadening with temperature with a very slight blue-shift of the emission.[188]

Although defect-related transitions in the visible range have been studied for decades, there is still no consensus in the literature on the positions of the peaks in the PL spectrum of ZnO nanostructures and thin films and their origin.[27, 36, 162, 163, 167, 168, 173, 189, 190] Partly, this is due to the strong dependence of the predominance of different transitions on the growth conditions of the nanostructures and layers (e.g. method, temperature, partial pressures of oxygen and zinc, etc.) and their post growth treatment, especially annealing under different atmospheres.[162] In addition, it was also observed that in spite of the similarities of the defect emission between different ZnO samples, they may not contain the same types and concentration of the defects.[173] Also, the recombination properties of ZnO nanostructures are expected to be different to the bulk due to the larger surface to volume ratio, [159, 167] so the conclusions made for the transitions in ZnO bulk crystals may not be completely applicable to ZnO nanostructures. As a consequence, different defect levels and their concentrations were observed for structures with different surface to volume ratios.[167, 191] Still there are some systematic observations and proposed theories on the origin of the different natural point defect-related transitions in ZnO. Therefore, in general following types of point defects can be considered: Zn and O vacancies (V_{Zn}, V_O), interstitials (Zn_i, O_i) and antisites (Zn_O, O_{Zn}). These defects can also be singly or doubly ionized (indicated by * and ** respectively) and form further complexes with each other. The emission resulting from the natural point defects in ZnO is briefly discussed below, not taking into account transitions caused by intentionally incorporated luminescent centers like copper, lithium and others [37]. Typically, ZnO emission in the visible range can be divided into violet-blue, green-yellow and red-near-infrared emission groups due to their similar origins.

Violet-blue emission is often less pronounced.[190] Its origin is typically attributed to interstitial Zn defects (Zn_i) and, in most cases, it is observed when crystals were synthesized or post-treated under Zn-rich conditions. The most frequent observation of blue emission was in layers or bulk crystals of ZnO [192, 157, 193], while in case of nanostructures like nanowires and rods, this emission is very rare, weak [194, 195] and quenched at room temperature [173]. Only recently, few methods of nanoparticle synthesis, which resulted in distinct blue emission, were introduced.[163, 190, 196] The observed transitions with according references for bulk ZnO or layers (structure type

3), different nanostructures as wires, rods, etc. (structure type 2) and ZnO nanocrystals (type 1) and quantum dots (QDs) are summarized in Table 2.1.

	Peak Position		Behavior, proposed origin of the peak	Reference	Type
	(eV)	(nm)			
	3.1	400	after annealing, Zn_i, VB or CB are involved Zn_i to VB transition	[162] [165]	1 2
	3.09-3.03	402-410	Zn_i to VB transition	[157]	3
	3.03	410	related to acceptor defects	[193]	3
	3.0	415	Zn_i to VB transition	[190]	1
	2.95	420	CB to Zn_i (deep acceptor), surface	[189]	1
	2.85	436	related to acceptor defects	[193]	3
	2.81	440	weak, only in CL, Zn_i to V_{Zn} or VB	[197]	1
	2.78	446	shallow donor (V_O or Zn_i) to VB	[192]	3
	2.82-2.59	440-480	Weak	[194]	2
	2.82-2.54	440, 455, 488	strong, emission shift by annealing, extended Zn_i states to VB,	[190]	1
	2.7	460	Zn_i	[198]	2
	2.7-2.67	460-465	intensity ~ excitation power	[199]	3
	2.67	465	Weak	[195]	2
	2.64	470	shallow donor (V_O or Zn_i) to VB	[192]	3
	2.61	475	Zn_i? V_O	[200]	3

Table 2.1: Position and proposed origin of violet and blue transitions of ZnO at room temperature.

In most cases the violet and blue emissions are attributed to transitions involving CB or VB and Zn_i, whereby Zn_i was controversially claimed to be either a shallow donor [190] or a deep acceptor [189]. However, due to its rareness there is a lack of systematic studies on blue emission and its origin in ZnO.[190]

Green and green-yellow emissions are the most frequently observed defect-related emissions in ZnO with the highest so-far reported room temperature PL quantum yield among all other ZnO point defects up to 0.2 and 0.45.[41, 42] At the same time these defects are the most controversially discussed.[36, 167, 168] As can be seen from Table 2.2 (which shows only a small fraction of the reports on green emission in ZnO), the positions of "green" differ quite a lot from one study to another. Often, there are different observations and consequently different explanations for spectrally identical transitions or the same explanation for different transitions. Also, it should be considered that the green emission bands are quite wide and often multiple transitions overlap, making the identification difficult. In addition, surface morphology (bulk and layers vs. nanostructures with high surface to volume ratio) and the resulting surface effects, such as formation of the depletion zone and its impact on the transitions [158, 191, 201–203] should be considered as well.

	Peak Position		Behavior, proposed origin of the peak	Reference	Type
	(eV)	(nm)			
	2.53	490	formation of V_O	[189]	1
	2.5	497	formation of V_O	[198]	2
	2.5	497	V_O to VB (without depletion zone)	[191]	1
	2.48	500	Zn_i V_O	[200]	3
	2.48	500	V_O to VB	[197]	1
	2.76-2.3	450-540	quantum size effect, deep donor (V_o^*) to VB	[163]	QDs
	2.43	510	DAP (probably V_O & V_{Zn}) DAP at surfaces or grain boundaries isolated V_o^* to VB, surface depletion surface defects, defect complexes	[199, 204] [173] [201] [205]	3 2 1 2
	2.42	513	V_o^*	[206]	2
	2.48-2.41	500-515	isolated V_O to VB	[207]	1
	2.4	517	broad, V_o^* to VB V_O to VB	[208] [209]	3 QDs
	2.39 2.38	520 522	V_O and Zn_i O_{Zn}	[210] [162] [211]	2 1 3
	2.36	525	V_O V_o^* complex to VB, surface depletion	[200] [201]	3 1
	2.34	530	O_{Zn} antisite	[189]	1
	2.3	540	DAP shallowly trapped e^- with deeply trapped h^+ (V_o^{**}) Zn_i to O_i	[212] [213] [197]	2 QDs 1
	2.28	544	at least 2 peaks are contributing	[193]	3
	2.27	548	O_i	[206]	2
	2.24	554		[198]	2
	2.22	560	surface defects	[214]	2
	2.2	564	CB to V_o^{**} (deeply trapped hole) CB to V_o^{**} (in the depletion zone)	[215] [191]	QDs 1

Table 2.2: Position and proposed origin of the green and green-yellow transitions of ZnO at room temperature.

There are 3 main hypotheses about the origin of green emission all related to oxygen vacancies: transition from the CB to the singly ionized oxygen vacancy (V_O^*) [201], from the CB to the double ionized oxygen vacancy V_O^{**} [215] since V_O^* can be considered as unstable [216], and from the neutral oxygen vacancy to the VB [163]. The latter two can take place at the same time as yellow and green emissions, respectively, whereby the domination of the one of both depends on e.g. the formation of the depletion zone.[191] Other defects like Zn_i and interstitial oxygen (O_i) as well as oxygen antisite (O_{Zn}) were also proposed. Recently, also some evidence for donor-acceptor pair recombination

(DAP) was observed for ZnO nanospheres.[173] It is also feasible that multiple different transitions are responsible for the green emission in ZnO depending on the shape, size, synthesis and post-treatment of the structures, so further studies are needed to reach a better understanding especially of the origin of green transitions.

	Peak Position		Behavior, proposed origin of the peak	Reference	Type
	(eV)	(nm)			
	2.18	570	broad, defect produced traps	[55]	2
	2.15	576	OH- or $Zn(OH)_2$ groups	[173]	2
	2.14	580	DAP	[207]	1
	2.1	590	DAP Hydroxyl groups	[212] [161]	2 2
	2.1-2.07	590-600	broad, OH-groups on the surface, defect complexes	[54]	2

Table 2.3: Position and proposed origin of the yellow transitions of ZnO at room temperature.

Yellow transitions are less controversial, being observed mostly in nanowires and nanorods and attributed to defect complexes involving the presence of $Zn(OH)_2$ and/or hydroxyl groups on the surface of nanostructures.[173, 217] DAP transitions were considered as well [207, 212], as can be seen from the summary in Table 2.3.

	Peak Position		Behavior, proposed origin of the peak	Reference	Type
	(eV)	(nm)			
	2.07	600	O_i or its complexes	[162]	1
	2.07-1.91	600-650	Defects related to excess O, possibly involving V_{Zn}-complexes	[173]	2
	1.98	626	O_i, oxygen-rich	[210]	2
	1.94	640	Oxygen-related defects	[218]	2
	1.9-1.8	640-680	CB to acceptor	[212]	2
	1.78	697	O_i	[206]	2
	1.7	730	CB to acceptor-like center	[219]	3
	1.66	750	Oxygen-related defects	[218]	2

Table 2.4: Position and proposed origin of orange, red and near-infrared transitions of ZnO at room temperature.

Orange, red and near-infrared emissions in ZnO (summarized in Table 2.4) are usually observed when the structures are synthesized or post-treated under oxygen-rich conditions. Therefore, they are typically associated with defect complexes related to the excess oxygen (e.g. O_i). Although the transition is proposed to involve the CB and the deep defect level, the identification of the possible candidate from the energy level calculations (see the summary in [38]) remains challenging.[173]

While green emission in ZnO has been excessively studied for years with no obvious consensus on its origin, blue and red emissions remain rare with more experimental framework work required for the clear identification of the involved transitions.[168]

2.2 Electronic Properties of ZnO

ZnO is known to be a natural n-type material. While n-type doping concentrations beyond 10^{20} cm^{-3} are easily possible,[147] stable p-type doping is hardly achievable.[36, 37, 220] In the nominally undoped case, wurtzite ZnO also shows n-type semiconductor behavior, attributed to natural shallow donors with activation energies in the range of 20 to 45 meV formed by intrinsic defects such as Zn interstitials and O vacancies or hydrogen impurities.[36, 221, 222] The clear consensus on the exact origin is not reached to date [221], although some recent reports favor interstitial Zn as a shallow donor and reduce the role of oxygen vacancy as a source for n-type conductivity since it acts as a deep trap.[223–225]

The exact electronic properties of ZnO are hard to quantify experimentally due to a large variation thereof depending on the fabrication route, treatment and quality of different samples.[36] Room temperature electron mobility for bulk ZnO is typically in the range of 120 to 205 $cm^2V^{-1}s^{-1}$. The corresponding background carrier concentration varies from $1 \cdot 10^{16}$ to $5 \cdot 10^{15}$ cm^{-3}.[36] The largest reported n-type doping level is in the order of 10^{20} cm^{-3}.[154]

Even higher background carrier concentration values compared to bulk ZnO can be achieved when reducing the crystal size of epitaxial layers over nanowires and nanorods down to nanocrystals. The reduction of the size leads to additional defects and facets on the crystal surface, acting similarly to point defects in the single crystal and resulting in carrier concentrations of up to 10^{18} cm^{-3} and higher for single ZnO nanostructures.[222, 226] For comparison, the conduction band density of states N_c is determined to be ~$3.7 \cdot 10^{18}$ cm^{-3} [227] and the critical carrier concentration for the metal-insulator (Mott) transition in ZnO is evaluated to be $n_c \approx 5 - 6 \cdot 10^{18}\,\mathrm{cm}^{-3}$, which is the most accepted value in literature.[221, 222, 228–230] It should be noted though that different approaches estimating the Mott concentration are available in literature, resulting in values between ~10^{17} cm^{-3} and 10^{20} cm^{-3}.[227, 230]

Such a high amount of charge carriers is also expected to influence the optical behavior of the nanostructures resulting e.g. in the red shift of the band gap (band gap narrowing) due to many-body effect and the blue-shift of the absorption edge caused by the filling of the conduction band states, the so-called Burstein-Moss shift.[37, 231]

In this case, the overall onset of the absorption is the result of the delicate interplay between both effects.[37, 232–234]

When discussing the electronic and optical properties of ZnO, especially those of ZnO nanostructures with high surface to volume ratio, the formation of the charge accumulation region on the surface and grain boundaries of ZnO should also be considered. ZnO has a rich surface chemistry and, depending on surface treatments, and change of its termination (adsorbed and desorbed species), as well as environment (atmosphere, pressure, solvents, etc.), both downward and upward band bending on the surface of ZnO can occur.[37, 169] Also, it is well established that an electron depletion region is formed on the untreated surface of ZnO crystals under ambient air, resulting in the upwards surface band bending and Fermi-level pinning,[37] as schematically shown in Figure 2.5 (a). Both, adsorbed species (e.g. oxygen) and surface defects act as acceptor-like surface states and trap donor electrons of the naturally n-type ZnO.[201, 235] The negative surface charge at the grain boundary interface is compensated for the positive charge in the depletion layer in the grain, resulting in an upward bending of the bands and ionization of traps (see an exemplarily energy level of a trap in Figure 2.5 (a), red dotted line) close to the surface of a ZnO crystal.[235] The width d of the depletion layer can be obtained by [201]

$$d = \left(\frac{2\varepsilon \cdot \Phi_B}{e^2 N_D} \right), \quad (2.1.11)$$

where $\varepsilon = \varepsilon_0 \varepsilon_r$ is the static dielectric constant of ZnO, Φ_B is the barrier height at the boundary, e is the elementary charge and N_D is the donor density. In ZnO crystals the barrier height Φ_B is typically estimated to be $\Phi_B \approx 1$ V, [201, 236, 237], although values of 0.8 V [238], 0.5 eV [158] as well as those above 1.5 eV [202, 239] were also considered. On an absolute scale, the value of ~1 eV is large, but when it is related to the band gap energy of ZnO, Φ_B / E_g corresponds to a typical value for polycrystalline semiconductors.[236, 240] Under the assumption of a donor concentration of ~10^{17} to 10^{18} cm^{-3}, which is a typical value for nominally undoped ZnO crystals at room temperature [158, 201, 203, 236–238], the depletion width is estimated to be ~50 to 100 nm.

Figure 2.5 (b) schematically shows the band alignment at the grain boundary between two ZnO crystals at zero bias. It describes the boundary between two ZnO grains in a polycrystalline film [203, 238] or between two ZnO nanostructures [241]. Thereby a double Schottky barrier of the height Φ_B is formed. The width of the negative surface

charge layer is typically below 1 nm [237] and is therefore sometimes neglected in the schematic illustration of the energy band diagrams.[236, 237, 242]

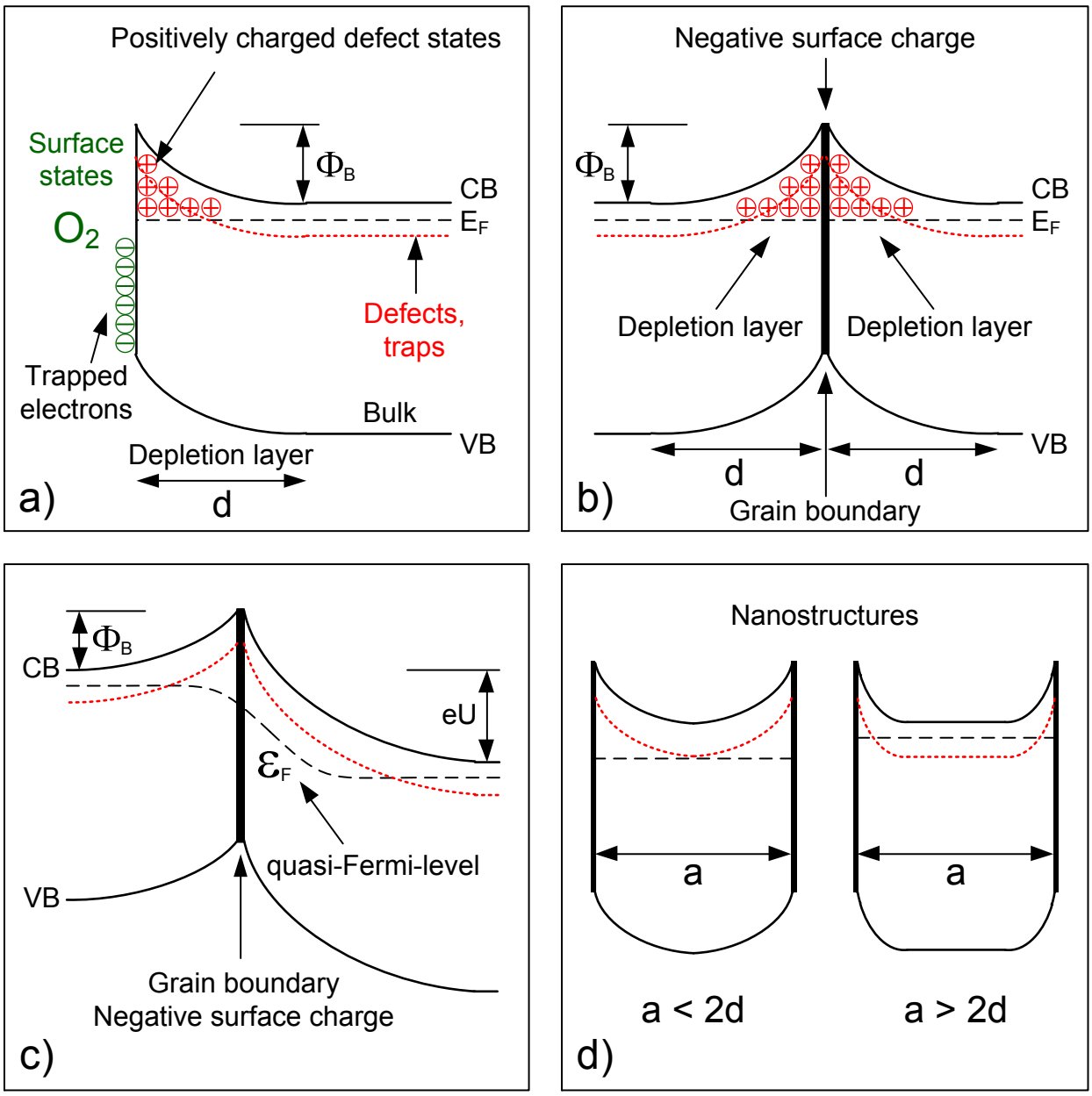

Figure 2.5: (a) Upward band banding on a grain boundary of ZnO in presence of acceptor-like surface traps. (b) Schematic of the band alignment at the grain boundary between two ZnO crystals. (c) Schematic of the band alignment at a voltage drop of U V across the grain boundary between two ZnO crystals. (d) Sketch of the energy band diagram of a ZnO nanostructure with (left part) wide and (right part) narrow depletion region.

Figure 2.5 (c) shows the case where a voltage U is applied across the ZnO grain boundary, after Ref. [236] The dashed line schematically shows the course of the quasi-Fermi-level ε_F across the double Schottky barrier. The height of the barrier changes thereby with applied voltage [236]: At moderate voltages (below 2 V per grain

boundary) the barrier height Φ_B decreases, whereby its decrease is slowed down by the interface charge, which counteracts its lowering by pinning the potential barrier by the interface states. To some extent it can stabilize the barrier for moderate voltages, until all interface states are filled. Further increase of the applied voltage leads to a rapid decrease of Φ_B (breakdown of the barrier). The typical voltages at which the breakdown takes place are known from ZnO varistors to be in the range of ~3.2 – 4 V.[235, 236, 243] Several mechanisms of high non-linearity can in addition contribute to the breakdown at the same time such as hole creation [238] and impact ionization [236] in the depletion region as well as tunneling.[243]

Figure 2.5 (d) illustrates the case when the depletion length d becomes comparable to the grain size of the ZnO crystal, which is relevant in nanostructures.[158, 201, 242] When the size of the nanostructure is larger than twice the width of the depletion layer on its surface (right part), the nanostructure is only partly depleted, forming a core-shell structure with higher carrier concentration inside the core compared to the shell. When the size of the nanostructure is below double the width of the depletion layer (left part), the nanostructure is completely depleted with the Fermi-level moving away from the conduction band. Thereby traps are ionized and their amount increases, resulting in a change of the emission and charge transport properties of the nanostructures.[158, 201, 242] The surface depletion layer controls the density and mobility of the electrons in the nanostructure as well as its emission properties, while the contact barrier influences the charge carrier transport between the nanostructures. [158, 191, 201, 241, 242]

Due to their large surface to volume ratio, nanostructures are very sensitive towards changes of the surface chemistry. For example, adsorption or desorption of oxygen can turn the nanostructure from a completely depleted state over a partly depleted to an almost undepleted state, respectively.[241] The pronounced effect of the photoconductive response in ZnO nanostructures has a similar origin.[37, 169] In the depleted (by adsorbed oxygen from the atmosphere) state under above-band-gap UV excitation electron-hole pairs are created in the ZnO. These dissociate due to the electric filed resulting from the depletion layer. Holes diffuse towards the surface and electrons are gathered in the core of the nanostructure. The holes neutralize the oxygen adsorbed on the nanostructure surface and initiate its desorption. This results in the decrease of the energy barrier height and reduction of the depletion layer width, which together with the free electrons generated by optical absorption, increases the conductivity of the nanostructure and through the nanostructure network by several orders of

magnitude.[36, 37, 244] Similar effects can be also induced by adsorption or desorption of other gases (e.g. H_2, NH_3, CO, ethanol, etc.) [242, 245], making the application of ZnO nanostructures as cost-effective high performance gas and UV sensors particularly very promising.[36, 37, 242, 245]

The change between the depletion states in nanostructures also has significant impact on their luminescent properties, since the balance between the different shallow/deep ionized and neutral (luminescent) trap states is changed resulting in e.g. significant increase/suppression [201, 202, 241, 246] or change of the color [158, 191] of the defect-related luminescence.

Chapter 3

Structural and Optical Properties of ZnO Nanocrystals: Experiment

It is essential to utilize nanocrystals with high crystalline quality and excellent luminescent properties for light emitting devices (LEDs). Especially white LED applications require nanocrystals with pronounced broad defect related emission and as few non-radiative (structural) defects as possible. The synthesis route has the strongest influence on the electrical and optical properties of the nanocrystals. The prominent synthesis paths (liquid and gas phase) as well as the way commercial ZnO nanocrystals were fabricated, are going to be briefly introduced within this chapter. The resulting ZnO nanocrystals were studied by means of scanning- (SEM) and transmission electron microscopy (TEM) as well as by absorption spectroscopy. The luminescent properties of the nanocrystals were studied by photoluminescence spectroscopy (PL). To gain a deeper understanding of the origin of the luminescent transitions as well as the way they can be tailored / improved for the later devices, additional PL experiments were introduced. The proposed luminescent transition diagram is going to be presented in this chapter.

3.1 Synthesis of ZnO Nanocrystals

Great diversity of amazing ZnO nanostructures such as nano- particles, rods, wires, tubes, spheres, tetrapods, rings, belts, etc., can be produced by different synthesis routes.[36, 167, 168] Besides top-down approaches such as milling, which are of low energy efficiency and result in a high inhomogeneity of the produced particles [247, 248], the bottom up synthesis routes can be mainly divided in liquid and gas phase synthesis methods. The main advantages and disadvantages of these routes are going to be presented in the following two sections, whereas the details on the different synthesis routes of ZnO nanostructures can be found elsewhere.[36, 167, 168, 249]

3.1.1 Liquid phase synthesis methods

ZnO nanocrystals can be chemically grown at low temperatures in aqueous solutions, therefore the hydrothermal (using water as a solvent) growth method is the most frequently used one. The hydrothermal growth can be additionally supported by an applied electric field for higher growth rates (electrodeposition).[168] The solution based synthesis in other solvents (solvothermal growth) is also possible, but rare. Zinc nitrite and hexamethylenetetramine are applied most commonly among other precursors, although simple reaction between pure Zn and water can be also used.[168]

The relatively slow chemical reaction rates enable precise control of the experimental conditions and the physical formation processes of the nanostructures. Also, different additives may be intoduced throughout the synthesis to influence the shape, size and the properties of the resulting functional nanostructures. This exact control of the shape and size of the resulting uniform / monodisperse nanostructures is the main advantage of the liquid phase synthesis routes. Another advantage is the fact that the reactions take place at very moderate temperatures (often below 100°C or even at room temperature) and can be easily performed and modified in a laboratory setup.

On the other hand, the slow chemical reactions in solutions result in low production rates.[247] The complex precursors and additional chemicals are often expensive and can introduce additional (sometimes significant) impurities into the ZnO nanostructures, which are difficult or impossible to be removed afterwards. Also, the

separation of the synthesized nanostructures from the wet phase is quite challenging and requires multiple filtration and washing steps.[247]

3.1.2 Gas phase synthesis methods

During this synthesis route, the Zn precursor (in form of a chemical compound or pure Zn) is transformed into the gas phase and carried through the reactor by the carrier gas. The Zn molecular nuclei are formed either by condensation or by chemical reaction (decomposition of the precursor compound). The nuclei are oxidized and grow by collision and coalescence in high temperature regions of the reactor. The temperatures required for the gas phase synthesis of ZnO nanocrystals are typically in the range of 500°C to 1000°C and sometimes above.[248, 250, 251] The synthesis routes (and the corresponding reactor designs) differ by the nucleation source and the way the energy is introduced to the system, which can be e.g. by furnaces (chemical vapor deposition (CVD), chemical vapor synthesis (CVS) [249, 250]), flame (pyrolysis [57, 251]), microwave (plasma [251]) or laser-based processes.[168, 248] The growth and aggregation of the particles can be controlled by the time spent within the high temperature zone of the reactor. The growth processes are stopped by very high cooling rates of typically > 1000 K/s.[248] The whole synthesis time from the injection of the precursors to the formation of the particles is typically in the range of milliseconds. Subsequently the synthesized particles are collected by different kinds of separators like filters, washers, cyclones etc., so the whole process of nanoparticle synthesis and separation rarely exceeds one second.[248]

Due to the synthesis at high temperatures, the resulting nanocrystals typically demonstrate high crystalline quality and environmental stability. Other advantages of the synthesis in the gas phase are the easy upscaling of the reactors, cost efficiency and high production rates enabling mass production of the particles on the tons scale.[247, 248]

Contrary to the possible variety of shapes in case of solution-based synthesis, the gas phase synthesis usually results in spherical nanocrystals with large size distribution, compared to wet synthesis, but significantly smaller, than after the milling processes.[248]

Recent modifications of the traditional gas phase reactors [248] demonstrated that ZnO nanocrystals can be also in-situ functionalized or coated by an additional shell [249, 252], which earlier was a privilege of the solution-based synthesis routes.

ZnO nanocrystals (VP AdNano® ZnO20), used in this work, were fabricated by the gas phase synthesis in a flame reactor by Evonik Degussa GmbH. During this process Zn powder was first evaporated and subsequently cooled down and oxidized to ZnO nanocrystals in a flame reactor.[57] The synthesis is characterized by temperatures above 500°C (typically between 1000°C and 2400°C) and Zn-rich conditions. The retrieved ZnO powder consists of nanocrystal aggregates of different shape with a logarithmic-normal distributed size and a typical mean diameter of 40 nm, formed by primary particles with 20 nm size. The ZnO nanopowder produced on a large scale at low costs following this route is widely used in cosmetics, particular in sunscreen formulations as well as in paints, coatings, resins and fibers.[57]

3.1.3 Structural analysis of the nanocrystals

The structural properties of the ZnO nanocrystals used in this work were studied by means of scanning and transmission electron microscopy (SEM and TEM respectively). Statistics on the size and shape distribution of the crystals were obtained by SEM analysis of more than 1000 nanocrystals (see Appendix A1). The particles were found to crystallize in three dominating shapes: spherical, square-shaped nanocrystals and nanorods. Spherical particles (Figure 3.1, light blue bars) with a typical diameter of 20 to 30 nm are in good agreement with the size of the primary particles. Squared particles (Figure 3.1, blue bars) are in the range of 80 nm and the rods (Figure 3.1, dark blue bars)were found to have a diameter of the primary particles of 20 to 30 nm and lengths from 100 nm to 300nm and higher. The assignment of the discussed shapes is indicated in the inset of Figure 3.1 on the SEM picture of the nanocrystals by the rings of the corresponding colors.

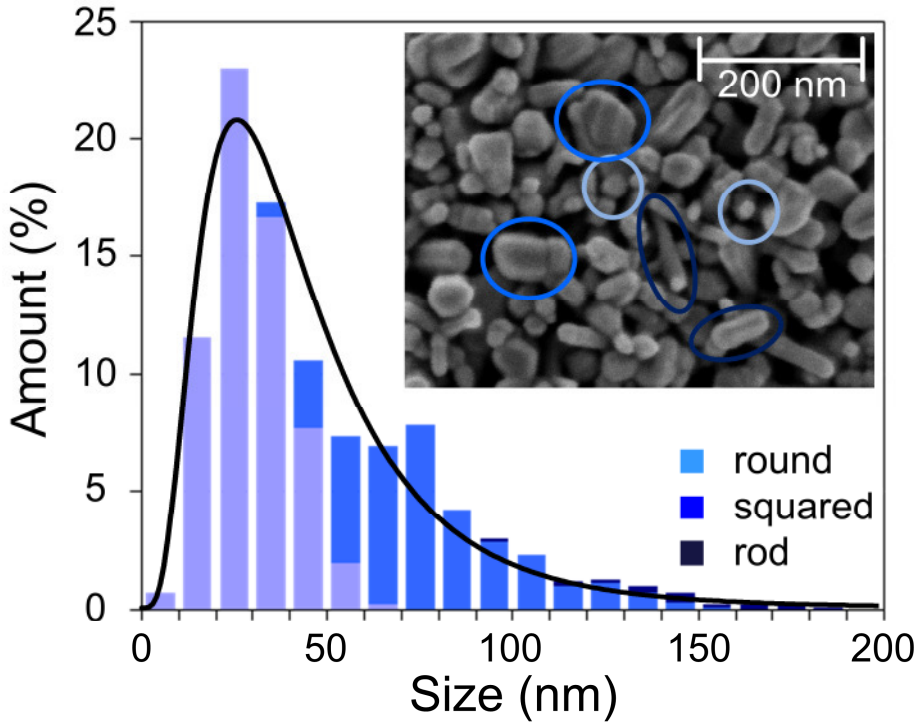

Figure 3.1: Size and shape distribution of VP AdNano® ZnO nanocrystals. The black solid line shows the log-normal fit to the size distribution. Three different dominating shapes (spherical, squared and rods) are indicated by the different colors of the bars (light blue, blue and dark blue, respectively). The inset shows the SEM image of the nanocrystals, pointing out the different shapes.

The size of the nanocrystals from the gas phase follows the log-normal distribution $y(x)$ [253]

$$y = \frac{A}{\sqrt{2\pi}\cdot wx}\exp\left[\frac{-\left(\ln\frac{x}{x_c}\right)^2}{2w^2}\right], \quad (3.1.1)$$

with A being a coefficient, corresponding to the total area under the curve and w being the standard deviation from the mean value x_c. The log-normal fit to the size distribution (black solid line in Figure 3.1) gives a mean value of $x_c = 38.4$ nm and the standard deviation of $w = 0.6$.

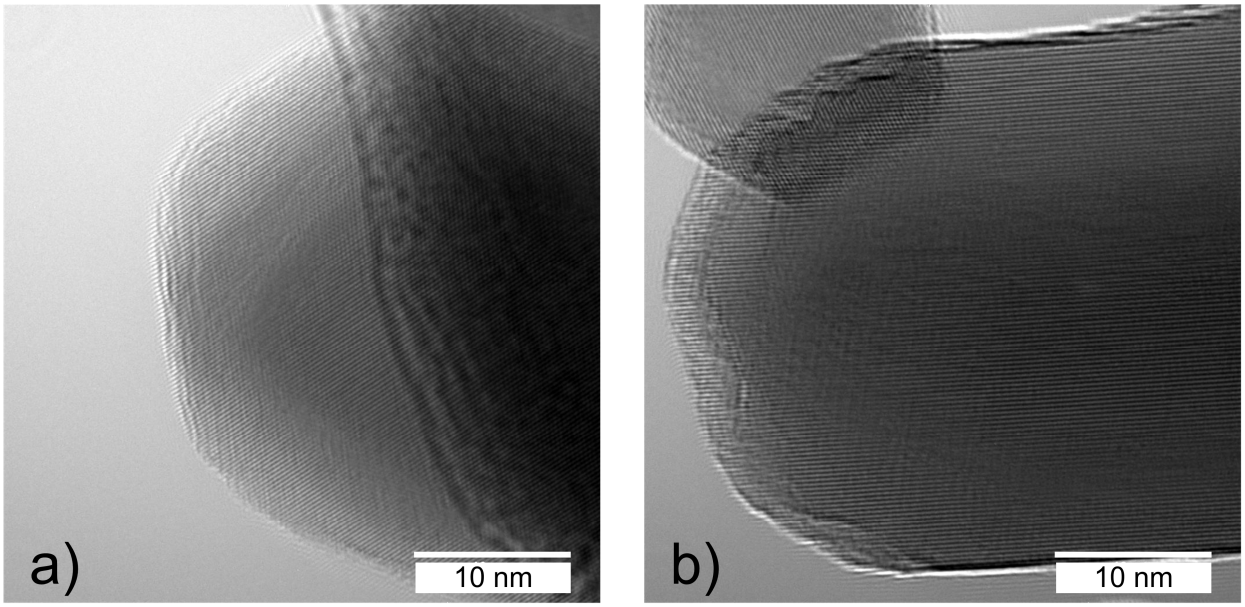

Figure 3.2: Exemplary high resolution TEM images of a (a) small spherical and (b) a middle-sized rod-shaped VP AdNano® ZnO nanocrystal.

The high resolution TEM study of the nanocrystals revealed that the inner part of the crystals consists of a single crystal phase without any line or planar defects. Figure 3.2 shows exemplary the TEM images of a small spherical nanocrystal (a) and a larger rod-shaped one (b), impressively demonstrating the high crystalline quality of the material. Unfortunately, the surface region of the crystals can not be analyzed in detail due to superposition of the crystal structure with the diffraction artifacts.

The high crystalline quality of the selected ZnO nanocrystal (NC) system can be also cross-checked by optical studies of the particles. Especially excitons in ZnO provide a sensitive indicator of the material quality since they get easily quenched or influenced (broadening, shift of the optical resonances) by crystal defects.[167, 254] Also, the knowledge of the luminescent behavior (both band gap and defect related) is essential for the LED performance and design, as going to be demonstrated in Chapter 4. Since the origin and the behavior of the different defect states as well as their exact position within ZnO band gap is still an open issue [36, 37, 167, 168], it is also important to gain a better understanding of the defect structure of the selected material for possible correlations with the electroluminescent properties of the device. Therefore in the following sections the absorption (3.2) and photoluminescent properties (3.3 – 3.5) of the ZnO NCs are going to be discussed in detail.

3.2 Absorption Spectroscopy

For the absorption measurements of the selected material, an approximately 300 nm thick ZnO NC layer was spin-coated from a butyl acetate dispersion (see Appendix A2) on top of a quartz substrate. An equal uncoated quartz sheet was used as a reference in the double channel Cary 5000 UV-Vis spectrometer. The absorption coefficient was estimated by transmission measurements of the layer using the following formula: [255, 256]

$$\alpha(\lambda) = -\ln\left(\frac{I(\lambda)}{I_0(\lambda)}\right)\cdot\frac{1}{d}, \quad (3.2.1)$$

with α being the absorption coefficient, I the transmitted and I_0 the incident light intensity, and d the thickness of the nanocrystal layer. The resulting absorption characteristic is shown in Figure 3.3. One can clearly observe the typical transparency of ZnO in the visible range, as also demonstrated by the photo of the ZnO dispersion in the inset of the Figure 3.3. In addition, a distinct excitonic contribution to the absorption spectra is observed at room temperature.

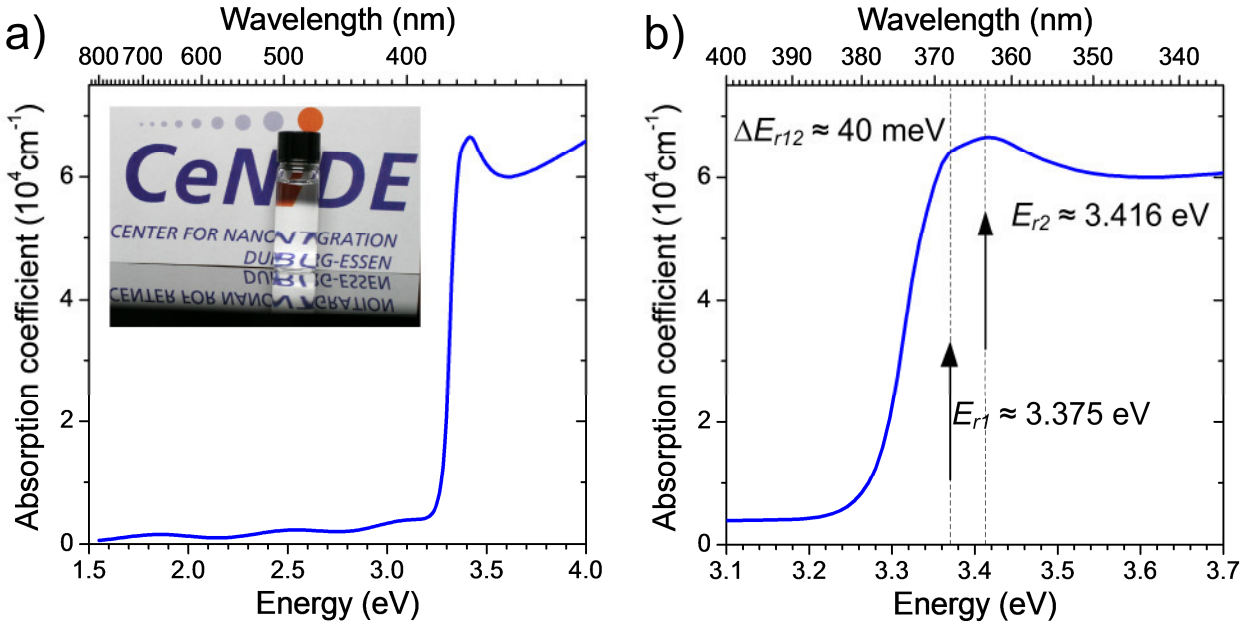

Figure 3.3: (a) Room temperature absorption of the ZnO NC layer with the photograph of the dispersion in the inset. (b) Enlarged excitonic absorption resonance of the ZnO NCs.

The estimated absorption coefficient values are in good agreement with values reported in literature.[36, 147, 254, 255, 257] Moreover, by considering the typical absorption coefficient of the free exciton transition energy at room temperature of $\alpha_0 \approx 2 \cdot 10^5 \,\mathrm{cm}^{-1}$ [36] one can estimate the packing density P_D of the nanocrystal layer by [258]

$$P_D = \frac{\alpha}{\alpha_0}, \quad (3.2.2)$$

which, for the NC layers studied in this work, results in a packing density of $P_D = 0.33$. This value is reasonable for spin-coated nanocrystal layers from commercial dispersions [259] and is in excellent agreement with other reports on NC layers from the same material system.[258]

A closer look at the excitonic absorption peak reveals at least two different absorption resonances E_{r1} and E_{r2}, separated by $E_{r12} \approx 40$ meV, as shown in Figure 3.3 (b). A similar near-band-gap room temperature absorption characteristic was observed earlier in epitaxial ZnO films [254, 260]. In Ref. [260], the first, low-energy peak situated at ~3.324 eV was attributed to the free exciton absorption resonance. The second broad peak at higher energy (shifted by 72.5 meV) was less pronounced and attributed to strong exciton-LO phonon coupling process. This interpretation is not suitable for the present case, since the separation between both peaks is significantly smaller than the typical values for the LO phonon energies of 72 meV [36]. Also, the intensity of the first peak observed in Ref. [260] was higher than the phonon related one, which is not the case for the present absorption spectrum. The peak intensities in case of [254], situated at ~3.4 eV, show very similar results compared to our findings. The origin of the transitions was explained in terms of A and B excitons, separated by 50 meV. However, this interpretation might not be correct compared to literature [36]. At room temperature the A and B resonances merge to a single peak [147] so consequently the peaks are more likely due to B- and C-excitonic transitions [36]. The same interpretation can also be supported in our case by considering the separation energy of 40 meV, which is close to the reported values of $E_{BC} \approx 37$ to 43.7 meV.[27, 36, 147, 153, 154]

Under the assumption of resonances E_{r1} and E_{r2} corresponding to free B and C excitonic transitions, the value of the band gap E_g can be estimated by (2.1.2) to be [37]

$$E_g = E_{X,B} - \Delta E_{AB} + E_{b,X} \approx 3.375 \text{ eV} - 0.005 \text{ eV} + 0.06 \text{ eV} = 3.43 \text{ eV}$$

This value is significantly higher compared to typical values of the ZnO band gap at room temperature of 3.365 eV to 3.377 eV [36, 37, 162, 163]. Such a blue shift of the band gap by ≈ 60 meV can in principle result from a confinement effect [261] or from a Burstein-Moss shift (see also Section 2.2) of the absorption edge due to high amount of free charge carriers [37, 233, 234]. The confinement effects can be excluded, since the particle size (diameter) is significantly above 4.6 nm [163] (twice the excitonic Bohr radius α_B^X, see Chapter 2.1.1). Assuming the origin of the blue shift to be due to the excess charge carriers, the concentration of the free electrons can be estimated to be between ~10^{19} cm^{-3} [227] and ~5-8·10^{19} cm^{-3} [233, 234] under the consideration of both the red shift due to the band gap narrowing effect and the Burstein-Moss shift. On the other hand, the fact that excitonic resonances are clearly observed at room temperature (i.e. not dissociate due to the screening) indicates that the free charge carrier concentration in ZnO nanocrystals is below the critical Mott concentration, [229, 230] which for ZnO is estimated to be between ~10^{17} cm^{-3} and 10^{20} cm^{-3} [227, 230] with $n_c \approx 5-6\cdot 10^{18}\,\mathrm{cm}^{-3}$, being the most accepted value in literature.[221, 222, 228–230] Besides, excitonic resonances in absorption spectra have been observed in highly doped ZnO:Al films as well.[227] It should also be noted that the possible impacts of the depletion region on the surface of the nanocrystals, as well as the formation of Mahan excitons [229] are not considered in the free electron density estimations above. Therefore the exact determination of the free charge carrier concentration in the studied ZnO NCs from the absorption spectra is not appropriate, while the assumption of a high natural n-type doping level of the ZnO nanocrystals resulting in free charge carrier concentrations of the order of 10^{18} to 10^{19} cm^{-3} inside the core of the nanocrystals at room temperature is realistic.

3.3 Photoluminescence Spectroscopy

The emission properties of the commercially available ZnO nanocrystals were studied in the standard macro photoluminescence (PL) setup (see Appendix A1) at room temperature. When analyzing the optical properties of especially ZnO nanostructures and comparing different samples with each other, several typical limitations need to be considered for a correct interpretation of the photoluminescence spectra.

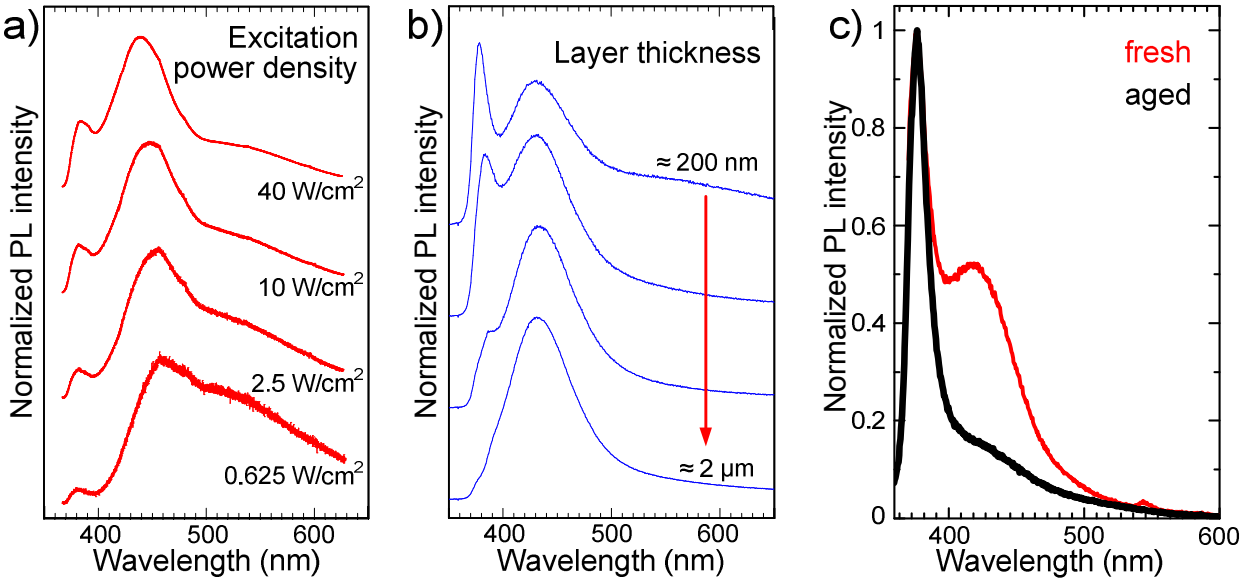

Figure 3.4: (a) Normalized PL spectra of fresh ZnO NCs, spin-coated in a homogeneous, ca. 500 nm thick layer on Si-substrate, at different excitation densities (1200 mm^{-1} grating). (b) Normalized PL spectra of the fresh ZnO nanocrystals spin-coated in a layer with continuously increasing layer thickness at the constant excitation density of 6.4 mW/cm^2 (150 mm^{-1} grating). (c) Normalized PL spectra of the homogeneous ZnO NC layers, spin-coated from the same dispersion and measured fresh (red) and after 3.5 years (black) at the same excitation density of 64 mW/cm^2.

Photoluminescence spectra of ZnO typically show a near-band-gap related (NBR) contribution in the UV and a defect-related contribution in the visible (VIS) spectral range, as discussed in Chapter 2. The observed UV to VIS ratio can not be used as the absolute determining factor of the crystalline quality of ZnO since the PL spectra of ZnO may exhibit very prominent NBR and negligible VIS contribution even in presence of considerable defect concentrations in the material.[167, 168, 262] In addition, the shape of the PL spectra strongly depends on the excitation power density [159, 199, 209, 262] as shown in Figure 3.4 (a). The contribution of the NBR typically increases at higher excitation densities compared to defect related emission, significantly changing

the shape of the PL spectra, as will be discussed in detail in section 3.3.1. This behavior results also in a high sensitivity of the shape of the resulting PL spectra to the experimental conditions, such as characteristics of the focusing lens (effects of chromatic and spherical aberration), the exact position of the sample and the lens, and the alignment of the PL setup. Hence, it is crucial to ensure the identical optimized setup alignment and the excitation power density for the comparative PL measurements of different samples.

Figure 3.4 (b) illustrates another limitation. An inhomogeneous nanocrystal layer on the plane glass substrate was prepared in a way that its thickness gradually changes from above 2 μm down to 200 nm and below. The excitation spot was continuously moved from the thin side to the thick one and the PL emission spectra were collected. The relative contribution of the NBR to the overall spectrum continuously decreases as the thickness is increased. In this case, the dominant role in the change of the detected emission shape is played by the reabsorption effects. Due to higher porosity of the nanocrystal layers compared to bulk ZnO layers and high scattering by the nanocrystals [262], the excitation light can rather deeply penetrate the nanocrystal layer. While the NBR is reabsorbed by the nanocrystals, the defect-related PL is predominantly transmitted through the layer [263] changing the overall shape of the PL spectra. Hence, for comparing the PL of different ZnO samples one needs to ensure the same thickness and packing density in case of nanocrystalline layers or the same nanocrystal concentration in the solvent in case of nanocrystalline dispersions.

While Figure 3.4 (a) and (b) show the PL spectra of the nanocrystalline layers spin-coated from the freshly received ZnO butyl acetate dispersions, Figure 3.4 (c) shows the change of the PL spectra of the ZnO nanocrystals, spin-coated soon after their synthesis ("fresh") compared to the layer from the same ZnO nanocrystal dispersion 3.5 years later ("aged"). Both layers are ca. 350 nm thick and were excited at the same excitation power density. Due to slightly different emission intensities, both spectra were normalized to their UV-peak for comparison. The intensity of the defect-related emission, especially in the blue spectral range, reduced significantly over the time. This can be attributed to the self-annealing properties of the ZnO nanocrystals as well as their aging.[197, 200, 264] Hence, for the study of the influence of different treatments and / or environments on the PL properties of the particles (e.g. annealing under different conditions), it is important to start with nanocrystals of the same origin (batch) and complete the treatment and the measurement of all particles within the same short period of time to exclude the influence of the ageing effects.

It can be concluded that for comparison of the PL characteristics of different nanocrystalline ZnO samples and the correct interpretation of the corresponding PL spectra, one needs to ensure identical excitation conditions, origin (batch) of the nanocrystals and their layer thickness or concentration.

3.3.1 Excitation power dependent behavior

The excitation power density dependent PL behavior of ZnO nanocrystals, introduced for the fresh particles (Figure 3.4 (a)) is going to be discussed here in more detail for the case of the aged ZnO nanocrystals. Figure 3.5 shows the PL of the ZnO nanocrystal layer formed by spin-coating on a Si-substrate from the butyl acetate dispersion of aged ZnO nanocrystals.

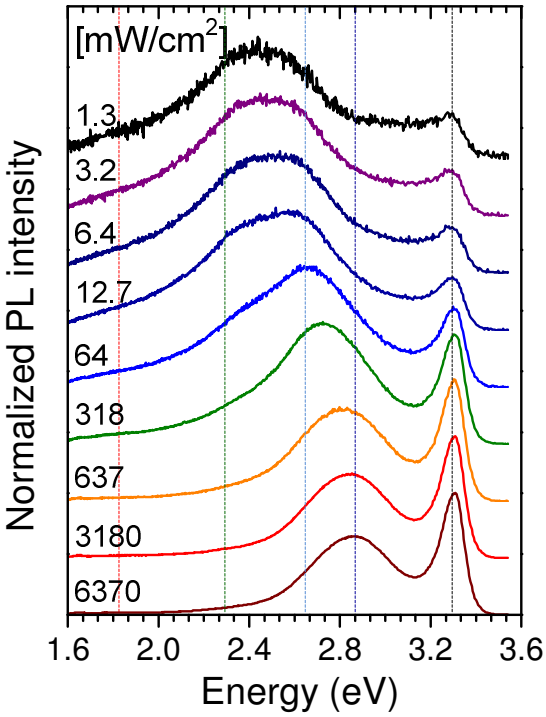

Figure 3.5: Normalized PL intensity of the aged ZnO nanocrystal layer at different excitation densities.

The PL spectra at low excitation densities are dominated by the broad visible emission at ~2.44 eV and show a very weak NBR contribution. At high excitation densities a pronounced peak in UV range dominates the emission together with a defect-related peak in the blue range at ~2.84 eV. While the NBR shows an almost negligible blue-shift with excitation power, the defect-related emission demonstrates a blue shift of ~600 meV accompanied by a narrowing of the emission full width at half maximum

(FWHM) from ~670 meV to ~450 meV within the excitation range between ~1 mW/cm² and ~6 W/cm².

The blue shift of defect related emission with increasing excitation power can have two possible reasons: the peak stems from a donor acceptor pair (DAP) related transition [265] or the emission is a result of multiple transitions, whereby the emission shift is due to a change in the carrier occupation of different states at higher excitation powers.[209]

The blue shift of the DAP transition is typically within the range of several tens of meV (see Chapter 2.1.2, equation (2.1.10)) when the excitation intensity is changed by 3 to 10 orders of magnitude.[173, 187, 265] This value is at least one order of magnitude lower than the observed blue shift of the defect-related peak in the present case. So it can be concluded that the resulting defect related contribution to the PL spectra stems from a superposition of multiple defect related transitions, as indicated by the dashed lines in Figure 3.5. A higher excitation density results in a higher occupation of the luminescent defect states with higher energies, causing the overall blue shift of the defect related emission. A closer look at the PL spectra at different excitation densities helps to deduce the position and width of the involved transitions.

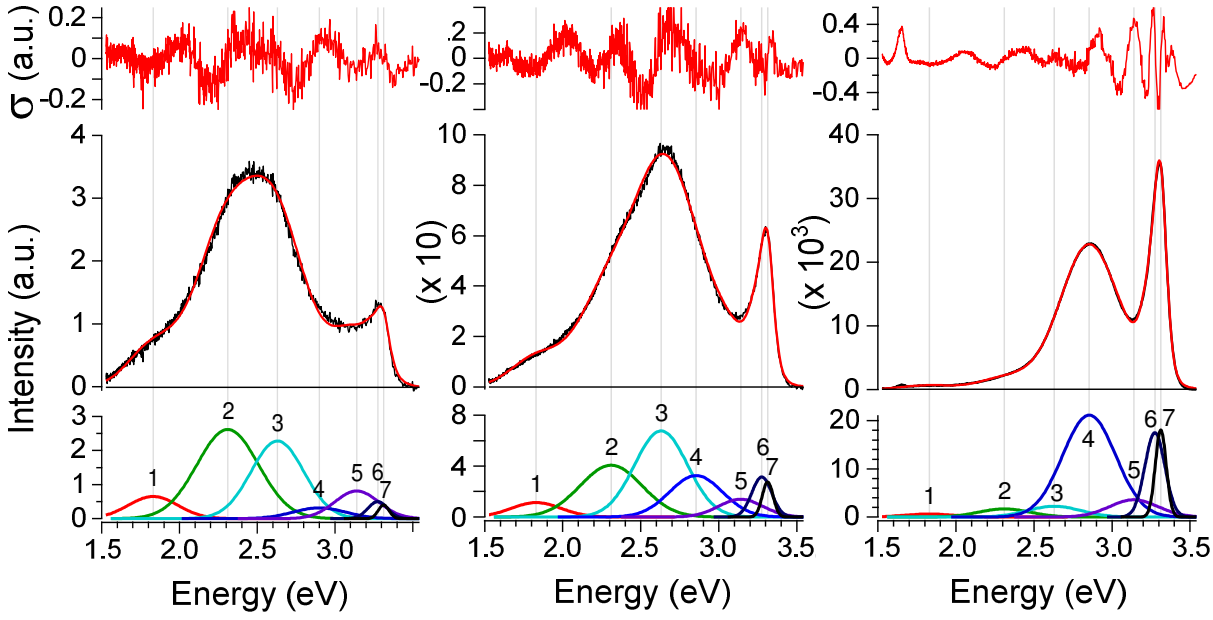

Figure 3.6: PL spectra of ZnO NC layer (black) at 3 different excitation densities, as well as their fit (red) by the proposed transitions (middle part), the deviation of the fit from the original spectra (upper part) and the corresponding transitions (lower part).

Figure 3.6 shows the PL spectra at low (a), ~3 mW/cm²), middle (b), ~60 mW/cm²) and high (c), ~6 W/cm²) excitation power densities. At low excitation density, the

energetically low transitions in the red (~1.85 eV) and the green (~2.32 eV) spectral range can be deduced. At moderate excitation, the shape of the first blue peak at ~2.64 eV becomes pronounced. At high excitation power, the second energetically higher blue transition at ~2.84 eV dominates the emission spectrum in addition to the NBR emission.

In order to study the behavior and origin of different defect-related transitions, their contributions need to be separated from each other e.g. by fitting of the PL spectra, as exemplarily showed in Figure 3.6. Here, following simplifications were necessary to fit all of the PL spectra with one and the same set of parameters: all of the transitions were assumed to have a Gaussian peak profile with the width and the spectral position remaining constant for all excitation power densities at the same temperature.

The contributions of the defect related transitions in the visible range appear quite obvious at different excitation densities: the "red" one at ~1.85 eV with a corresponding width of ~220 meV, the "green" one at ~2.32 eV (~270 meV), and the blue defect-related contribution, consisting of at least two transitions [190] of the "blue 2" at ~2.64 eV (~220 meV) and "blue 1" at ~2.84 eV (~180 meV).

The NBR peak shows an almost negligible blue shift at high excitation densities as well as highly non-symmetric shape on high and low energy sides. This shape can be only fitted by at least 2 Gaussian peaks: the sharper one at ~3.313 eV (width of ~50 meV) and a wider one at ~3.27 eV (width of ~95 meV). The assignment of the NBR emission to two different transitions was confirmed by the temperature dependent PL study in Chapter 3.4.

Due to a large deviation of the overall fit in the sub-UV range, which could not be corrected by combinations of defect and NBR transitions, discussed above, an additional background "violet" peak at ~3.12 eV (~120 meV) needed to be introduced to the overall fit, although it does not show a contribution, pronounced enough to clearly separate this peak from the others at the studied excitation densities. The existence of this transition was verified by electroluminescence spectra of the ZnO NC-LEDs (see Chapter 4.3.4).

The excitation power dependent PL measurements can also give useful information about the origin of the involved transitions. It is well-known that the PL intensity I is correlated with the excitation power density P by a power law:[159, 262]

$$I \sim P^k \quad (3.3.1).$$

In case of the excitation above the band gap, the power factor k is in the range $1 \leq k < 2$ for the free and bound exciton emissions and in the range of $0 < k \leq 1$ for the free-to-bound (FB) and bound-to-bound (BB) radiative recombinations.[159, 262, 266, 267] The possible origin of the superlinear behavior of the excitonic transitions can be explained by the consideration of the competition between different excitonic and defect-related recombination paths [267] as well as by a model suggesting the formation of excitons from free electrons and holes.[266] The observation of the superlinear dependence of the transition intensity on the excitation power can be interpreted as the excitonic origin of this transition. [159, 262, 267]

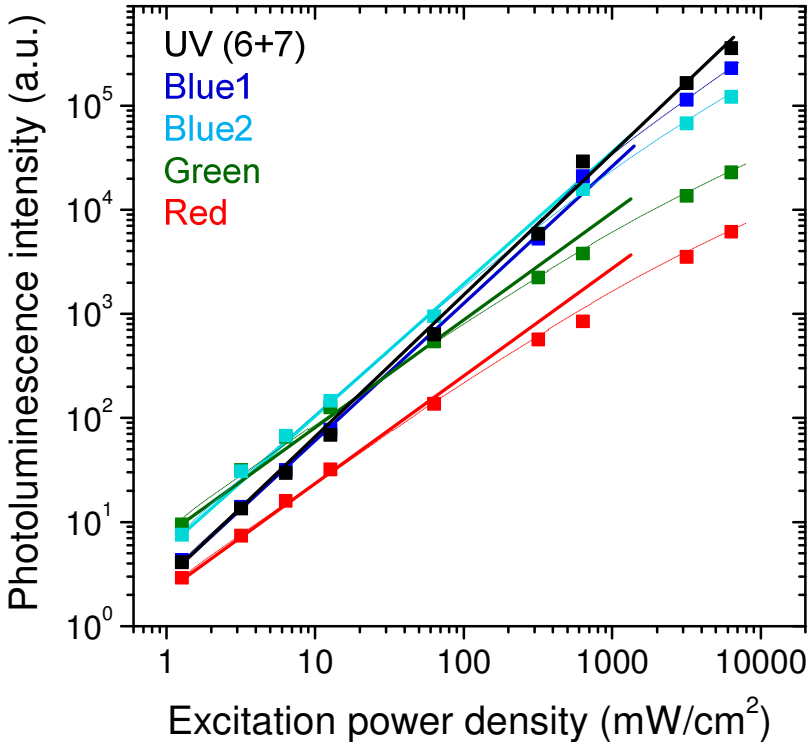

Figure 3.7: Double logarithmic plot of the intensity of the PL in the range of the proposed transitions in the corresponding color. Dotted lines are guides to the eye.

Figure 3.7 (a) shows the peak intensity of the PL in the spectral range of the corresponding proposed transitions (from the Gaussian fit) as a function of the excitation density on a double logarithmic plot, so that the power factor k can be easily identified by the slope of the corresponding curves (solid lines). The power factors for the red (0.82), green (0.8), and blue 2 (0.98) transitions are below 1 and support the assignment of these recombinations to defect-related transitions. The power factor for the blue 1 transition (1.04) is marginally above 1, which might be due to light scattering by the particles, in case that the concentration of the corresponding defects is very high.[262] The power factor for the UV intensity is higher than 1 (1.34), which is a sign of bound or free excitons.

3.3.2 Atmosphere dependent behavior

The electronic and emission properties of ZnO nanostructures are known to react sensitively to the changes in atmospheric conditions, which can be utilized e.g. in gas sensors.[36, 37, 168, 169] These changes are mainly due to the formation of the depletion zone on the surface of the nanostructures and its change (see Chapter 2.2) depending on the humidity, pressure and concentration of other gases in the atmosphere, surrounding the nanostructures.[158, 191, 201] Changes of the defect-related emission properties such as intensity or color of ZnO structures were also observed.[158, 173, 189, 191, 201] ZnO nanocrystals studied in this work also showed changes in the PL properties at room temperature in different atmospheric conditions.

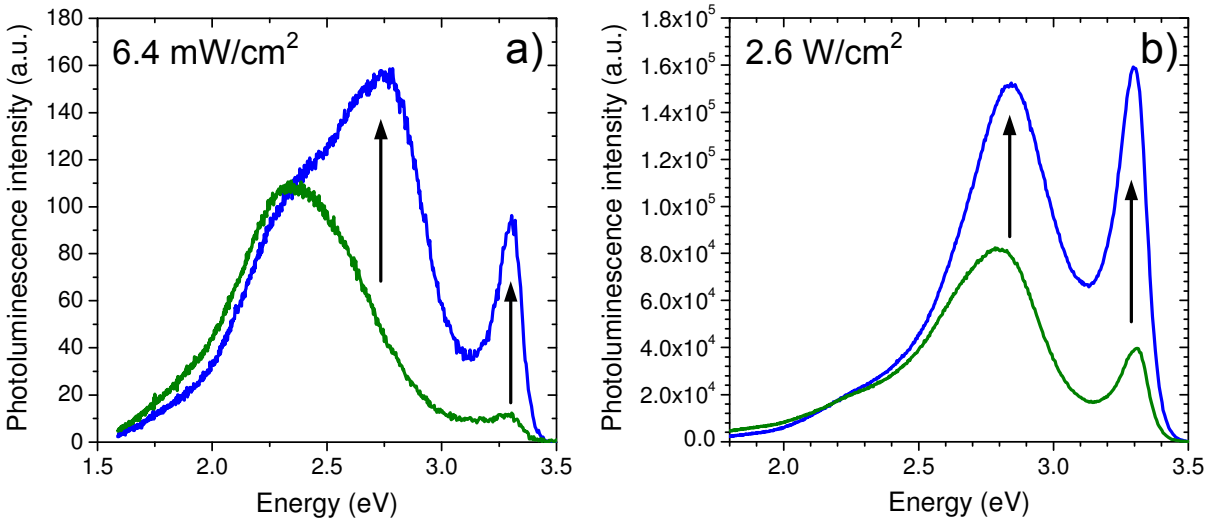

Figure 3.8: PL spectra of the ZnO nanocrystal layer at low (a) and high (b) excitation power density. Green spectra correspond to the PL under ambient air, while blue ones to the PL under vacuum.

Figure 3.8 shows the PL spectra of the ZnO NC layer in ambient air (green) and under 10^{-5} mbar vacuum (blue) at low (6.4 mW/cm², a) and high (2.6 W/cm², b) excitation power densities. While under both excitation conditions the intensity of the red emission slightly reduces and of the green one almost does not change, the contributions in the blue and UV spectral range increase significantly if the ambient air is removed by vacuum. Though to clearly identify the reason for such behavior, further experiments (e.g. PL under different atmospheres) are needed, some useful conclusions can be made. First, the emission intensity in the blue and UV range is obviously partly quenched under normal atmospheric conditions by components of the ambient air (oxygen, water, OH-groups, etc. [173, 189]) or by some components of the dispersion inside the layer (solvent residues, dispersion additives, etc.). Second, these quenching

substance(s) can be successfully removed by the evacuation of the nanocrystal layer, which results in the increase of the emission intensity. Consequently there might also be other ways to achieve the same effect e.g. by annealing of the particles. And third, the defects, responsible for the blue 1 and 2 transitions are most probably situated close to the surface of the nanocrystals, since they react so sensitive on the changes of the atmosphere around and inside the nanocrystal layer.

3.3.3 Size dependent behavior

The experiments in part 3.3.2 showed that the defects inducing the emission in the blue spectral range might be situated close to the surface / on the surface of the ZnO nanocrystals. To clarify this assumption, the original mix of the ZnO nanocrystals was centrifuged for 2 minutes at 20.000 rpm, extracting the small ZnO nanocrystals from the mix.

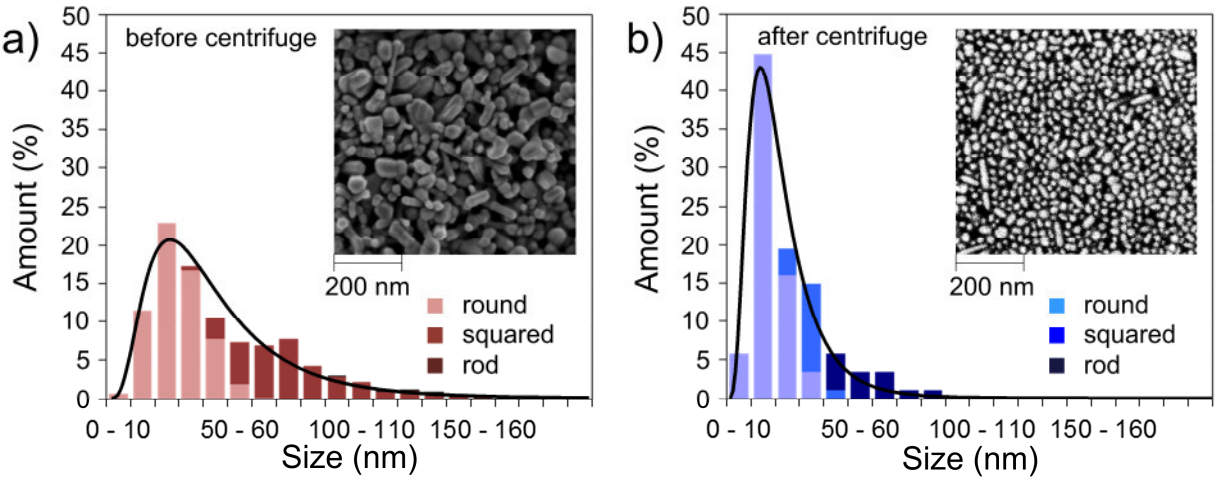

Figure 3.9: Size and shape distribution of the ZnO nanocrystals, fitted by a log-normal distribution (black curve), with the SEM image of the corresponding NC layer as an inset before (a) and after (b) the centrifuge step.

Figure 3.9 compares the original size and shape distribution (a), discussed in Chapter 3.1 to the size and shape distribution of the nanocrystals in the ZnO layer, spin-coated from the centrifuged dispersion. The modified size of the NCs can as well be fitted by the log-normal size distribution after equation (3.1.1). The standard deviation of the NC size distribution was reduced by the centrifuge step from 0.6 to 0.56 and the mean value of the NC size from 38.4 nm to 19.3 nm. The SEM image of the centrifuged layer on the inset of Figure 3.9 (b) illustrates the reduction of the ZnO size by the centrifuge step, making the round shape of the crystals dominating.

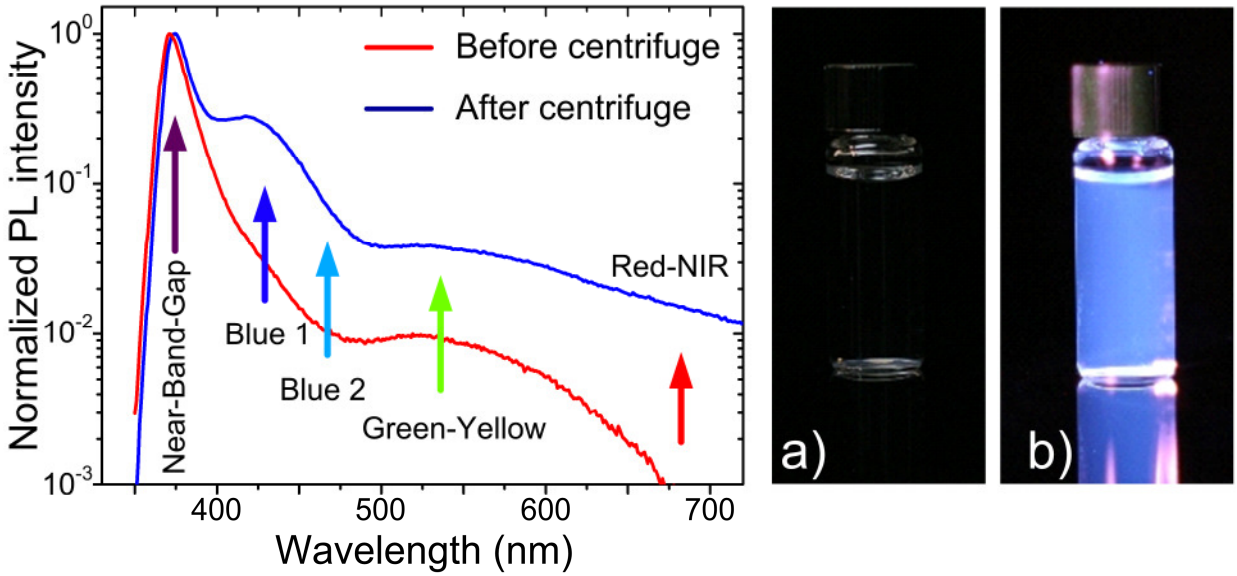

Figure 3.10: (left) Normalized PL spectra of the aged NC layers from the initial (red) and centrifuged (blue) dispersions. (right, a) Image of the centrifuged dispersion under daylight illumination, demonstrating high transparency in the visible range. (right, b) Image of the same dispersion under UV lamp illumination, demonstrating the bluish-white emission color of the centrifuged ZnO nanocrystals.

The impact of the size selection by the centrifuge step on the luminescent properties of the crystals is illustrated by Figure 3.10. The PL spectra of the NC layer from the initial (aged) dispersion and the NC layer from the centrifuged (aged) dispersion were normalized to their NBR contribution. The peak intensity of the NBR emission in both cases was in the similar range, although the resulting thickness of the centrifuged layer was significantly lower (ca. 50-100 nm), compared to the layer from the initial dispersion (ca. 300 nm). The comparison between both spectra shows the increase in green emission by a factor of 3 to 4, whereas the blue and red emissions increased by almost one order of magnitude. This supports the assumption that the most luminescent defects (especially the blue ones) are situated on the surface of the nanocrystals or close to it. As the size of the nanocrystals was reduced by the centrifuge step, the surface to volume ratio of the nanocrystals increased, which lead to the increased contribution of the luminescent defects close to the surface of the NC compared to the NBR emission. In addition, the NBR emission peak showed a red shift of ~25 meV with decreased size distribution. This is most probably due to the increased contribution from the second NBR peak (6) at 3.27 eV, which can result from the high amount of the exciton recombination centers near the surface of the nanocrystals.[159] The origin of the NBR transitions 6 and 7 can be clarified by PL measurements at low temperatures, where the phonon broadening and defect-related transitions are suppressed. The results of the temperature dependent measurements are going to be discussed in the following section.

3.4 Temperature Dependent Spectroscopy

PL spectroscopy of the aged ZnO nanocrystal layer was performed at temperatures between 5 and 300 K in a closed-cycle cryostat within a standard PL setup (see Appendix A1). At low temperatures, the broadening of the transitions due to phonons is significantly reduced. This can help to identify the different transitions, which merge to a single peak at room temperature. In case of defect related transitions, temperature dependent measurements can help clarify if conduction or valence band states are involved in the defect-related transition.

3.4.1 Near-band-gap transitions at low temperature

A typical PL spectrum of the ZnO NC layer at 5 K is shown in Figure 3.11 (a). The first peak on the high energy side at 3.377 eV and a corresponding FWHM of ~30 meV can be clearly attributed to the free A-Exciton (FX_A) due to its peak position.[171, 173, 268, 269] The transition line width is well within the range between 10 and 170 meV, typical for ZnO nanostructures (see Chapter 2.1.1).[159, 167, 168, 173]

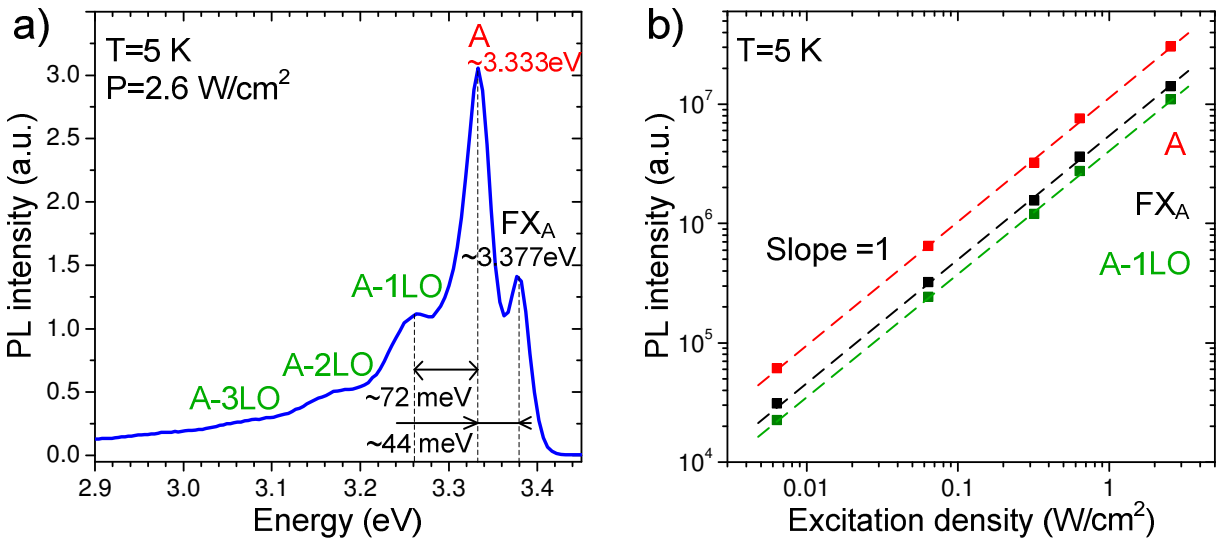

Figure 3.11: (a) PL spectrum of the aged ZnO NC layer at 5 K and 2.6 W/cm² excitation power density. (b) Double logarithmic plot of emission intensity of the A-line (red), free A-exciton (black) and the 1st-order LO-phonon replica of the A-line as a function of excitation power density.

The second, most intense peak at 3.333 eV exhibits a FWHM of ~34 meV. This peak is situated in the energy range below the typical transition energies of donor-bound excitons (DX) (see Chapter 2.1, Figure 2.3). It is separated by ~44 meV from FX_A, consequently it can not be attributed to the LO-phonon replica of the free A-exciton. Due to the spectral position of the peak, it can be assigned to either the so-called A-(or Y-) line, the acceptor bound exciton (AX) or the two electron satellite (TES) of the DX line.[178] Since no DX could be observed, the origin of this transition is very unlikely to be due to TES. Here, the peak at 3.333 eV (also due to its temperature dependent behavior, see 3.4.2) can be assigned in excellent agreement of its spectral position [178], to the free exciton, bound to the surface states or extended structural defects on the surface (A-line), which is frequently observed in nanostructures.[159, 173–177]

The weak transitions on the low energy side can be attributed to the 1^{st}, 2^{nd} and 3^{rd}–order LO-phonon replica of the A-line due to their separation by ~72 meV.

Figure 3.11 (b) shows the excitation dependent behavior of the FX_A, A-line and its 1^{st}-LO-phonon replica. All transitions show a linear dependence of the emission intensity on the excitation power density, typical for both the FX_A and A transitions as well as their LO-phonon replicas at low temperatures.[160]

3.4.2 Temperature dependent behavior

The A-line, assigned to structural defects at the surface or extended surface states can be typically traced from low temperatures up to room temperature in different nanostructures [160, 174, 175] as opposed to other BEC transitions. This is also the case in the studied ZnO nanocrystals, supporting the assignment of the 3.333 eV peak to the A-line. Figure 3.12 (a) shows the PL spectra at 2.6 W/cm^2 excitation power density normalized to the corresponding maximum at different temperatures from 5 to 300 K. While the contribution of the LO-phonon replicas can be disregarded at 200 K and above, both FX_A and A-line can be followed up to room temperature, forming the NBR peak in the UV range at 300 K. Also, both transitions exhibit a temperature dependent red-shift of the emission due to the shrinking of the band gap with increasing temperature. The peak positions of the transitions (plotted as a function of sample temperature in Figure 3.12 (b)) were determined by Gaussian fitting of the PL spectra. Both transitions show a red shift of ~60 meV from 5 K to room temperature. The red-shift of the peak energy can be fitted by the Varshni relation (2.1.1) with

$\alpha = -0.77 \cdot 10^{-3}\,\mathrm{eVK^{-1}}$ and $\beta = -1077\,\mathrm{K}$. These values are in good agreement with values reported for bulk ZnO [36] and other ZnO nanostructures [165]. The slight deviations from the fit at higher temperatures were also observed in literature.[171] A careful look at the energy position of the FX_A transition at 5 and 50 K reveals a blue shift of the emission by ~8 meV, which can not be explained by any fitting uncertainties. The blue shift of the excitonic emission is followed by the known red-shift, with peak position at 100 K being still ~3 meV blue-shifted as compared to the FX_A position at 5 K. Such blue shift in excitonic emission with increasing temperature, following then essentially the dependence of the band gap (red-shift) is often called the S-shaped behavior and was frequently observed in heavily doped GaAs, InGaP, GaInNAs/GaAs quantum wells, as well as in epitaxial layers of InGaN, AlGaN, InN and ZnMgO.[37, 270–273] This behavior is caused by the high amount of localized states below the free exciton energy.[37] Recently, the S-shaped behavior was also observed for free A-exciton transition in ZnO nanorods [274] and nanocrystals [159]. The observation of this behavior is, besides the blue shift of the absorption edge (see Chapter 3.2), additional evidence of heavy n-type doping with concentrations between typically 10^{18} and 10^{20} $1/cm^3$.[273, 275]

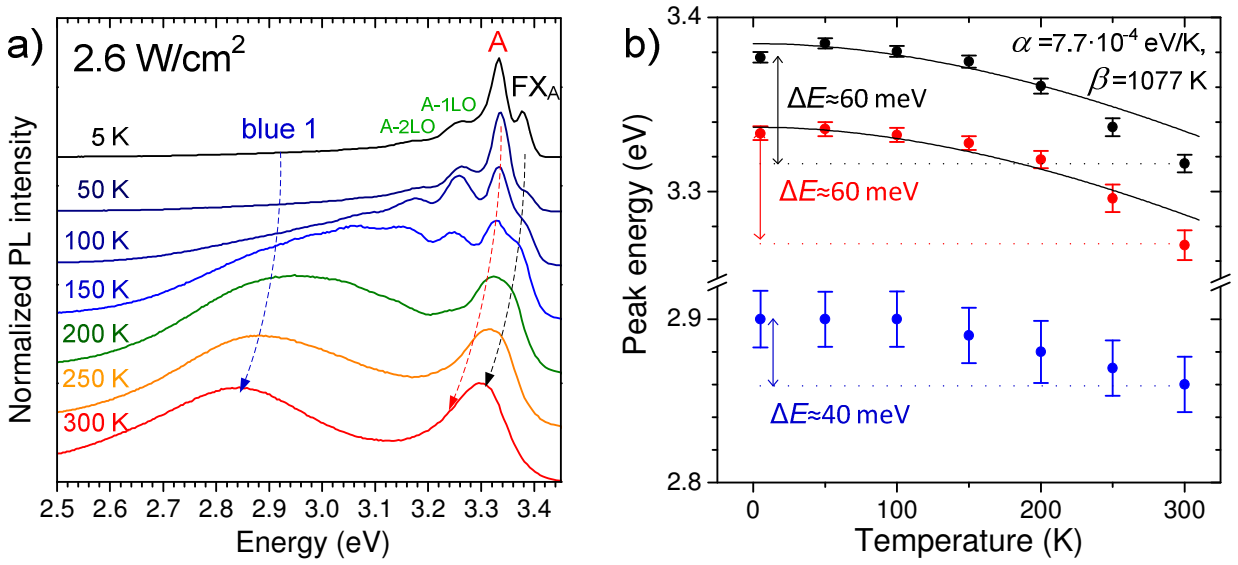

Figure 3.12: (a) PL spectra of the aged ZnO NC layer, normalized to the corresponding maximum intensity, at different temperatures. (b) Energy shifts of the free A-exciton (black), A-line (red) and blue 1 (blue) transitions as a function of temperature.

The increase of the band gap with decreasing temperature should result in a blue shift of those defect-related transitions, which involve CB or LB, under the assumption that the energy levels arising from defects, do not move significantly with the bands. This case is realistic, since the energy levels, associated with the visible emission are in general deep donor or acceptor levels, so they are less influenced by the movement of

the band energy.[41, 163, 276] This assumption can be also supported by other reports.[41, 163, 215, 276] On the other hand, in case of the DAP transition no significant blue shift of the emission peak with decreasing temperature is expected.[173, 188]

Figure 3.12 (a) demonstrates a red shift of the blue 1 transition with increasing temperature. At 5 K and 2.6 W/cm² excitation power density, the contribution of the blue 1 transition with a peak intensity above 10.000 counts is distinct enough compared to the background signal of 50 ± 10 counts to be fitted by a Gaussian profile with a peak position at ~2.9 eV. The expected red shift of the band gap up to 100 K is within few meV, which is almost negligible compared to the width of the blue 1 transition. Thus, the spectral position of the fitted blue 1 peak was intentionally left constant up to 100 K. The spectral position of the peak at 150 K was determined to be 2.88 eV and from there on a pronounced red shift can be traced up to room temperature. On the other hand, it should be noted that due to the large width of the blue 1 defect related transition, compared to excitonic transitions, the fitting inaccuracy of its spectral position is quite high. Consequently, the energy shift of the blue 1 transition, shown in Figure 3.12 (b), can not be used to determine if the CB or the VB is involved in the transition.[163] Nevertheless, the overall energy shift of ~40 meV is pronounced enough to be detected, so it can be concluded that either the VB or the CB are involved in the blue 1 transition.

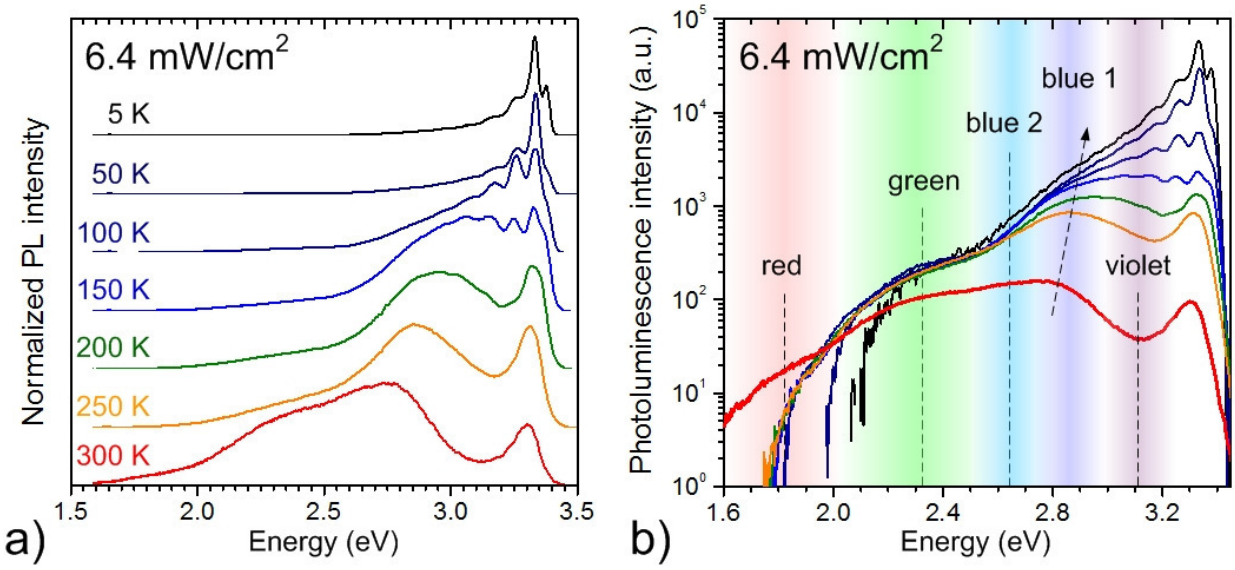

Figure 3.13: (a) Normalized PL spectra of the ZnO NC layer at temperatures between 5 and 300 K. (b) Logarithmic plot of the PL intensity, the color of the spectra correspond to the different temperatures. (b)

The blue 1 transition dominates the PL at high excitation densities. Therefore, the lowest excitation density was used to study the temperature-dependent behavior of

other defect-related transitions. Figure 3.13 (a) shows the normalized PL spectra at different temperatures. Figure 3.13 (b) depicts the PL spectra at different temperatures, indicated by the corresponding colors from (a) on a logarithmic plot. The red transitions are quenched at low temperatures. The blue 2 transition with a peak intensity of ~1000 counts at 5 K is pronounced enough compared to the background of ~10 ± 5 counts (at 6.4 meV excitation power density) to be fitted by the Gaussian profile, though the corresponding emission shoulder is not distinct enough to clearly trace the spectral position of this transition, so no conclusions can be made on its temperature dependent shift. On the other hand, the green transition shows no significant energy shift with temperature. This behavior is typical for DAP transitions.[173]

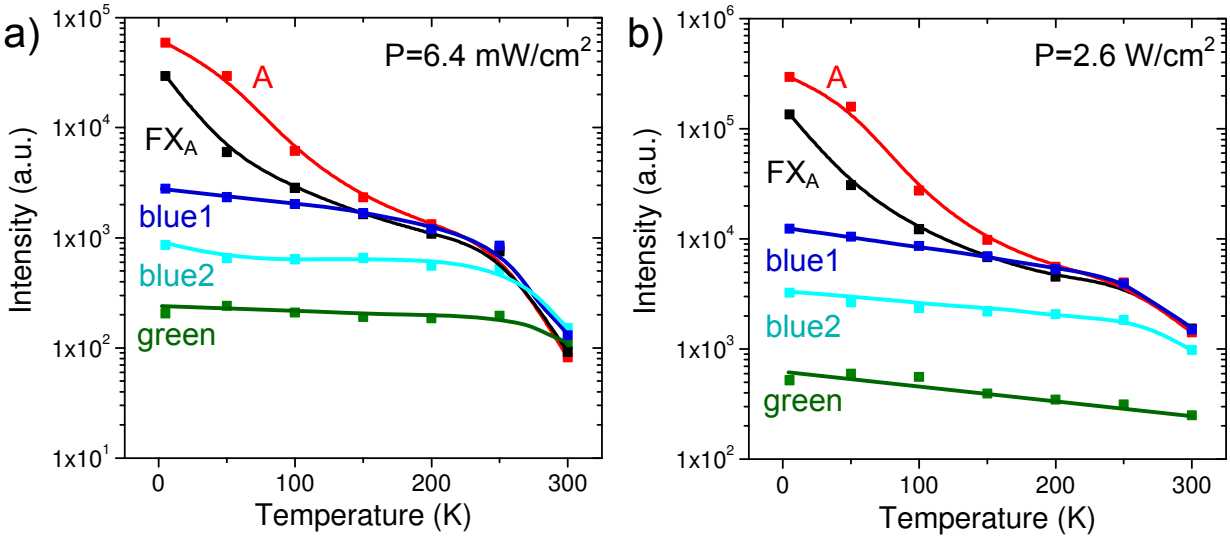

Figure 3.14: Temperature dependent behavior of the identified transitions at low (a) and high (b) excitation power densities.

The emission intensity of different transitions as a function of temperature at low (a) and high (b) excitation power density is shown in Figure 3.14. The intensity of the green emission shows a very moderate increase by a factor of 2-3 if the temperature is decreased down to 5 K, which is another strong evidence of the DAP-transition.[173, 277] The fact that the broad width (~270 meV) of the corresponding fitted Gaussian peak remains almost constant over the whole temperature range also supports this assignment.[173, 188, 277] The intensity of the blue 1 transition increases by more than one order of magnitude, when the ZnO NC layer is cooled down to cryogenic temperatures, supporting the involvement of either CB or VB (FB transition). [173, 277]

The intensity of the NBR transitions decreases by over two orders of magnitude from 5 to 300 K. This can be interpreted in terms of non-radiative defect centers, quenching the emission efficiency at room temperature.

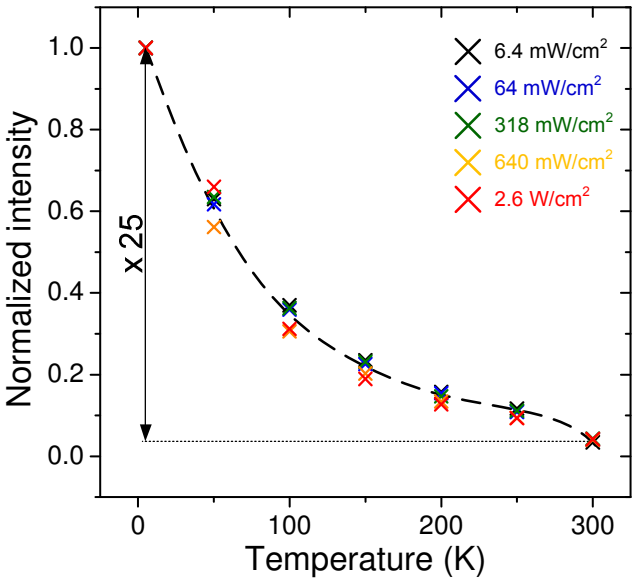

Figure 3.15: Temperature dependent behavior of the overall integrated PL intensity at different excitation power densities.

Figure 3.15 shows the temperature behavior of the overall (integrated) PL intensity of the nanocrystals at different excitation power densities. The overall intensity at room temperature is reduced by a factor of 25 compared to the low temperature intensity, which is comparable to other reports on ZnO nanocrystals and can be attributed to a thermally activated quenching. The nonradiative pathways become more probable at higher temperatures, which leads to the overall quenching of the emission.[213] Particularly, Klingshirn and co-workers observed a temperature dependent reduction of the PL quantum yield (QY) of ZnO nanocrystals by more than one order of magnitude from ~11% at cryogenic temperatures down to ~0.6% at room temperature.[170] For the ZnO studied here, the room temperature QY of the crystals was measured using the comparative method [41, 42] with anthracene- and 9,10-diphenyl anthracene- solutions as references to 0.2%. This low value is not surprising, since the particles were not optimized for their luminescent properties during the synthesis. In recent contributions, values of 20% and even 45% at room temperature were reported [41, 42], demonstrating high potential of ZnO nanocrystals as a luminescent material.

3.5 Thermal Treatment

The PL measurements under different atmospheric conditions showed that the emission intensity, especially in blue and UV spectral range, can be sufficiently increased in vacuum, probably by removal of luminescence quenching species from the surface of the ZnO NCs. Therefore, there might be a certain potential to improve the luminescent properties of the as-synthesized nanocrystals, e.g. by thermal treatment [174], which is going to be explored in this section. Also, it has been demonstrated that the overall emission color of ZnO nanostructures can be influenced by annealing [173, 190, 198, 200], which is important for tailoring the emission color of the later devices. Moreover, annealing experiments can provide additional evidence for the origin of the different defect-related transitions. For example, annealing in air or oxygen was found to decrease the amount of Zn_i and V_O [200] and can result in additional O_i causing orange-red luminescence [173], whereas annealing in nitrogen or Zn-vapor can result in additional transitions in the blue spectral range.[198]

Soft, 30 minutes long annealing under different atmospheres in a quartz tube furnace was applied to NC layers with identical thicknesses. To study the long-term impact on their luminescent properties, which is particularly important for the device fabrication, the annealed samples were stored in air after annealing together with the untreated control sample for ca. 2 months prior to the PL measurements.

In the first step, ambient air was chosen as an atmospheric condition during the annealing of the freshly synthesized NC layers. Figure 3.16 (a) shows the PL spectra of the ZnO layers, annealed in ambient air at different temperatures. The peak intensity of the NBR emission, shown as a function of annealing temperature in Figure 3.16 (b), reveals a constant decrease with increasing annealing temperature. Only above 500°C a slight increase is observable, which can be attributed to the improvement of the crystalline quality by annealing at elevated temperatures.[174] The impact of annealing on the peak intensity of the blue 1, blue 2 and green transitions is shown in corresponding colors in Figure 3.16 (c). In case of the blue transitions, there are two temperature regimes: the intensity increases in the range of $0°C < T \leq 200°C$ and decreases at temperatures above 200°C. The intensity of the green emission remains almost constant throughout the whole temperature range.

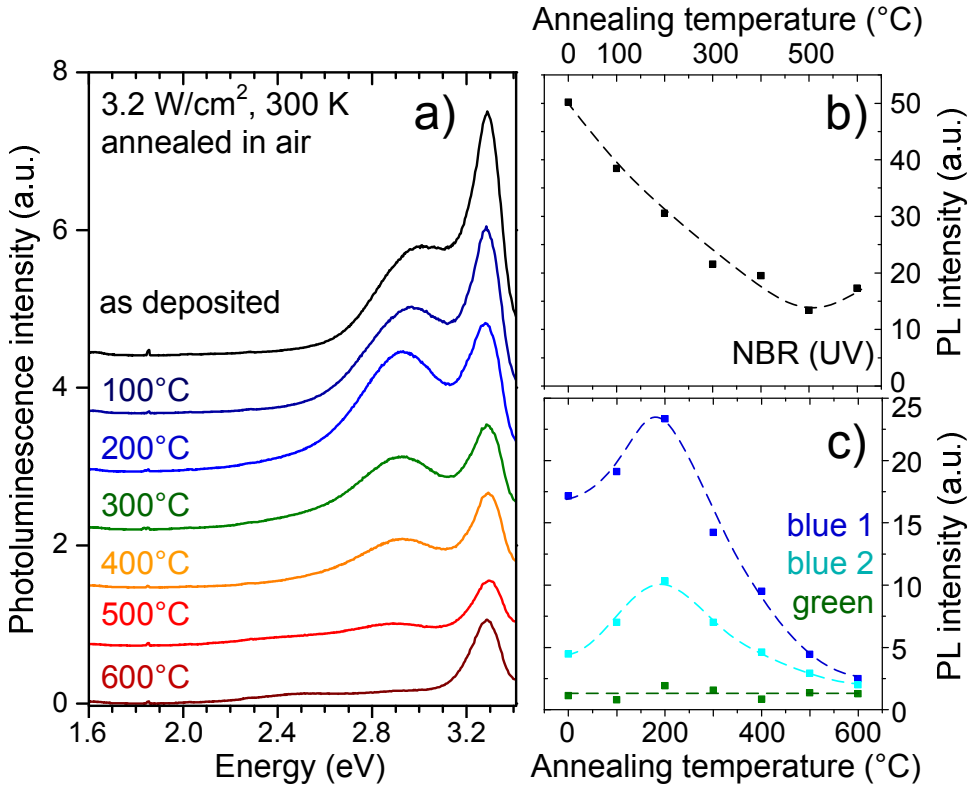

Figure 3.16: (a) PL spectra of the fresh ZnO NC layers, annealed at different temperatures under ambient air. (b) The intensity of the NBR and (c) defect-related emission intensities as a function of the annealing temperature.

To clarify the influence of oxygen and water vapor, which are both present in ambient air, on the temperature dependent behavior of the defect-related transitions, an additional experiment was performed. ZnO NC layers (aged) were annealed for 30 minutes at the same temperatures under nitrogen flow with the control group, annealed in ambient air. The resulting PL spectra are shown in Figure 3.17. The annealing behavior of the aged NCs in air (Figure 3.17 (a)) is very similar to the behavior of the fresh ones (Figure 3.16 (a)). The annealing under nitrogen flow (Figure 3.17 (b)) also shows mainly the same trend: increase of the blue emission at moderate annealing temperatures followed by a rapid decrease of its intensity at annealing temperatures above 300°C. For better analysis of the temperature-dependent behavior in different atmospheres, the peak intensity of the visible and NBR transitions were studied separately.

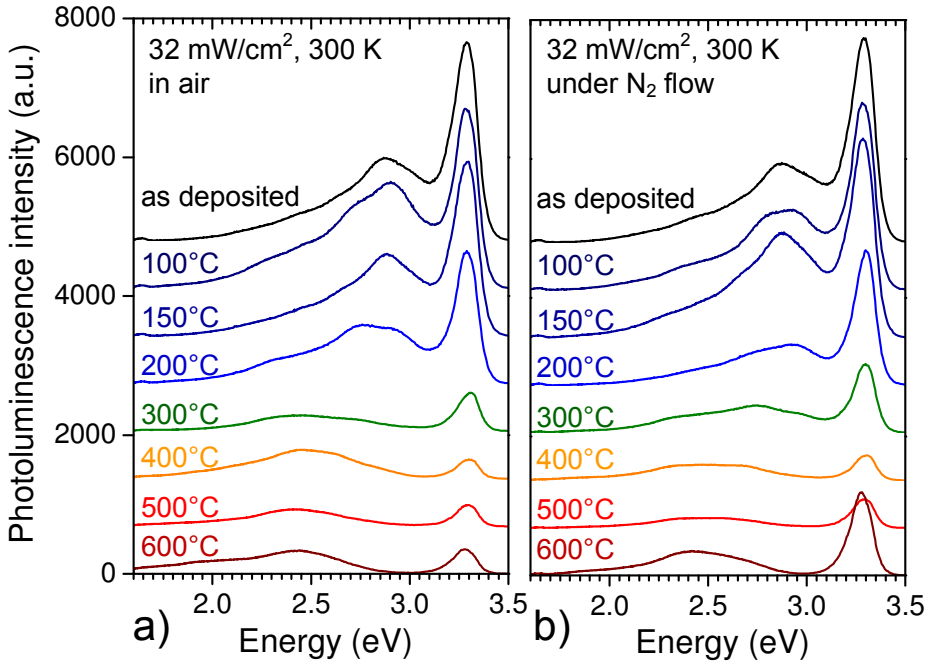

Figure 3.17: Photoluminescence spectra of the aged ZnO NC layers, annealed in ambient air (a) and under nitrogen flow (b) at different temperatures.

Figure 3.18 shows the intensity of the involved transitions as a function of the annealing conditions. The annealing behavior of the aged NCs in air is very similar to the behavior of the fresh ones. The NBR emission intensity continuously decreases with temperature, with only a slight increase above 500°C (Figure 3.18 (a)). Blue transitions show an increased intensity, compared to the untreated sample, in the range between 0°C and 200°C. Thereby, the maximum intensity of the blue emission was achieved at a lower temperature of 100°C, compared to fresh particles (200°C), which might be due to ageing effects (see discussion in Chapter 3.6). The annealing in air at temperatures above 200°C results in a decrease of the blue emissions by almost one order of magnitude (Figure 3.18 (c)). The green emission shows, as in case of the fresh particles, a stable intensity behavior without significant changes with temperature (Figure 3.18 (e)).

Comparing the impact of the annealing atmosphere on the luminescent properties of the ZnO NCs reveals some interesting details. The intensity of the NBR transitions decreases upon annealing up to 400°C by about one order of magnitude under both atmospheres (Figure 3.18 (a) and (b)). While in air only a very slight intensity increase can be noticed after the annealing at higher temperatures, the NBR intensity increases by a factor of more than 3 upon annealing at 600°C in nitrogen. This behavior might be explained in terms of a superposition of two different effects: the annealing at elevated temperatures improves the crystalline quality, leading to the increased NBR

contribution [174], at the same time additional defects are introduced to the lattice by a component of the ambient air (e.g. oxygen), obviously not present under N_2-flow, which quenches the NBR emission.

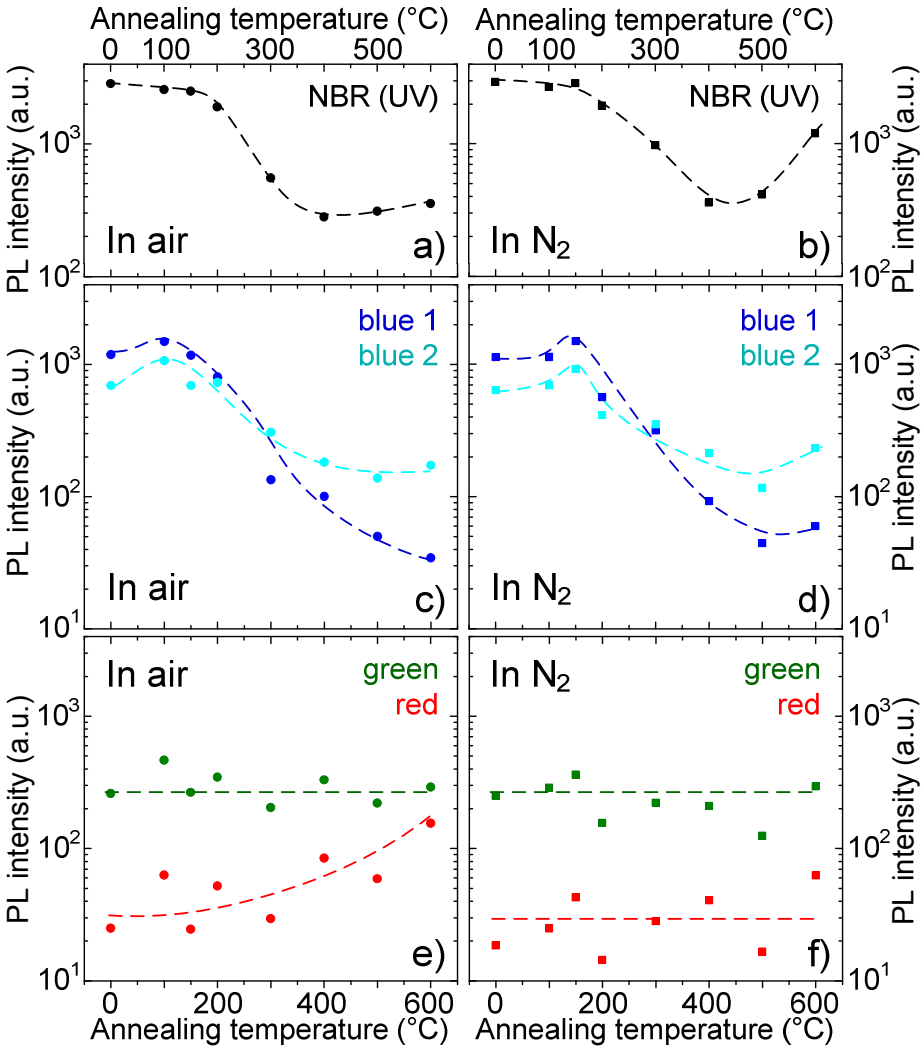

Figure 3.18: PL intensity of the involved transitions in the UV (a,b), blue (c,d) red and green (e,f) spectral range as a function of annealing temperature, depending on the atmosphere.

The behavior of the blue transitions is essentially the same for both cases (Figure 3.18 (c) and (d)), with the maximum intensity being reached in case of nitrogen at slightly higher temperatures. Consequently, the blue transitions and their intensity changes upon annealing are not induced by the components of the atmosphere (e.g. oxygen, humidity, etc.), rather than by the temperature-dependent changes within the existing, as synthesized defect distribution within the crystals, since both batches were stored and measured under identical conditions in air.

The intensity of the green emission is in both cases stable, without any influence by the annealing (Figure 3.18 (e) and (f)). The intensity of the red emission shows an

almost negligible increase after the annealing at 600°C in nitrogen, whereas it shows a continuous increase when NC are annealed at temperatures above 400°C in air. This behavior was also observed in literature and clearly can be attributed to the excess oxygen, incorporated during the annealing.[173, 190] This interpretation correlates well with the observed quenching of the NBR emission, which might be due to the introduction of additional defects to the NC lattice by oxygen during the annealing at temperatures above 400°C in air.

The focus of this work lies on the fabrication of white LEDs based on ZnO nanocrystals, therefore an efficient defect-related emission of ZnO is desired. The behavior of the overall, integrated PL intensity as a function of annealing temperature and atmosphere is shown in Figure 3.19.

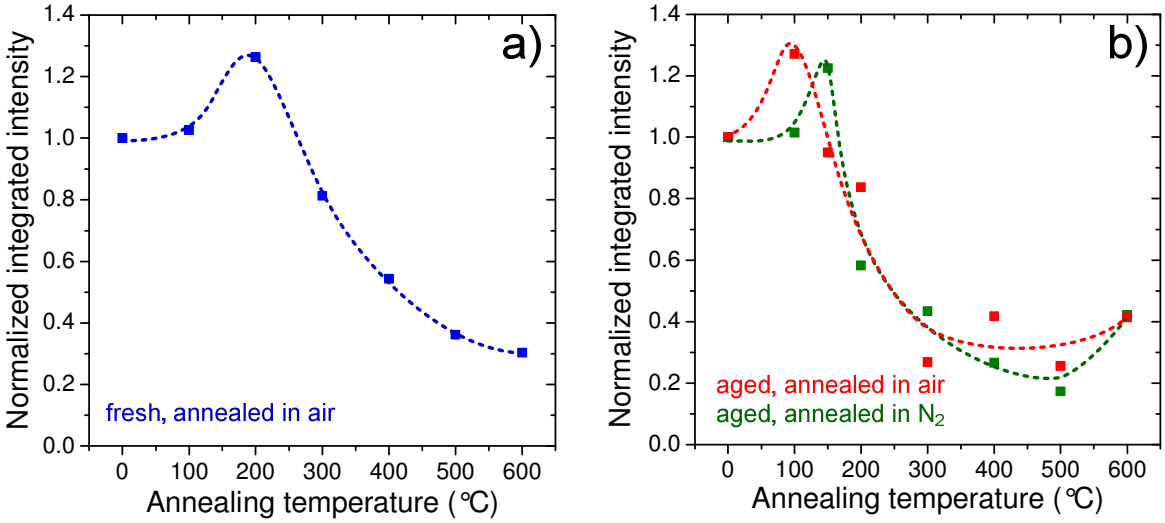

Figure 3.19: The integrated PL intensity of the fresh ZnO NCs (a) and the aged ones (b) at different annealing temperatures.

For both fresh and aged particles, two main temperature regimes can be identified. During the soft annealing regime in air and nitrogen at temperatures between 0°C and 200°C, the total intensity of the PL emission increases by a factor of ~1.3. This can be attributed to desorption of solvent residues and water from the layer as well as to the rearrangement of the defect states, which can be mobilized by these low temperatures. In the annealing range between 200°C and 400°C the intensity of the PL emission drops down followed by slight decrease / saturation at higher temperatures. Technically, it can be concluded that the PL efficiency of the as-synthesized ZnO NC can be increased by the soft annealing step, while the relative contribution of the blue, red and NBR transitions to the overall emission spectrum can be tuned by annealing at different temperatures under different atmospheric conditions.

3.6 Assignment of the Luminescent Transitions

The photoluminescence properties of the NCs depending on the excitation conditions, temperature, atmosphere and post-synthesis treatments were studied. The wide defect related contributions in the red, green and blue spectral range were identified, as well as defect related contribution in the near-UV range and pronounced excitonic near-band-gap emission. In the following section, the findings are summarized, analyzed and possible emission origins are proposed, as schematically shown in Figure 3.20.

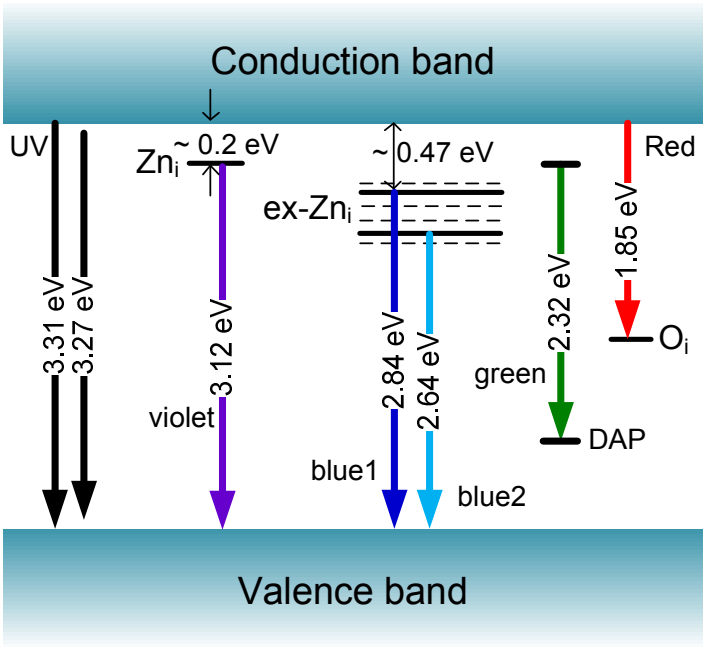

Figure 3.20: Proposed simplified energy diagram of the identified radiative transitions of ZnO NCs.

3.6.1 Near-band-gap related transitions

NBR emission was found to be mainly caused by two excitonic transitions, merged together to a single peak at room temperature. Based on the low temperature photoluminescence study, their spectral position at 3.313 eV and 3.27 eV (3.377 eV and 3.333 eV at 5 K) could be identified and followed up to room temperature. These transitions can be attributed to the free A-exciton (FX_A) [171, 173, 268, 269] and the A-exciton bound to surface states or extended structural defects on the NC surface (A-line) [159, 173–178] respectively. The size-selection experiment at room temperature

(see Figure 3.10) supports this assignment: the contribution of the A-line compared to FX_A is increased in case of smaller NCs with higher surface to volume ratio, which results in a ~25 meV red shift of the NBR peak compared to the assembly of NCs with bigger size (lower surface to volume ratio).

3.6.2 Red transitions

Red emission at ~1.85 eV is the least pronounced, but its contribution increases when the crystals are annealed at temperatures above 400°C in oxygen-rich conditions. This observation is in agreement with literature, where the excess oxygen is clearly correlated with orange-red emission [162, 173, 210, 218] and can be attributed to the formation of oxygen interstitials or antisites.[162, 206, 210] Several groups suggested a transition from the CB to the deep acceptor levels [212, 219] in agreement with theoretical predictions.[168] Therefore the red emission band here can be attributed to the transition from the CB to the O_i defect level. This assignment is also in agreement with the observed EL properties of the ZnO NC devices. (see Chapter 4) Interestingly, the change of the red emission is correlated with the variation of the emission intensity in the NBR and the blue/green spectral range, as observed by the changes in PL spectra at increasing temperature (from 250 K to 300 K), change of the atmosphere (from vacuum to ambient air) and annealing conditions (N_2 vs. air at annealing temperatures above 400°C). A possible explanation for this correlation might be an increased formation of non-radiative defects by excess oxygen in addition to the radiative (orange-red) ones. However this assumption needs further systematic studies.

3.6.3 Green transitions

The green emission at ~2.32 eV shows no temperature dependent spectral shift and no significant intensity decrease (increase) with increasing (decreasing) temperature. This behavior is typical for DAP-transitions [173, 277], therefore similar to observations in Ref. [173, 197, 199, 212, 213], this transition can be attributed to a DAP. The intensity of this transition showed to be quite insensitive towards the atmospheric conditions, as well as towards annealing up to 600°C in different atmospheres. Therefore the most frequent assignment of the green emission in ZnO to oxygen-related defects, involving either the VB or the CB is quite unlikely in the present case. The possible reason for this transition might be due to stable defects within the crystal lattice, with shallowly

trapped electrons and deeply trapped holes.[212, 213] Further experiments are needed though for the final determination of the origin of this DAP transition.

3.6.4 Violet and blue transitions

The blue emission in the studied ZnO nanocrystals is the most intense defect related contribution to the overall PL spectra. The blue emission centers were found to be located close to the nanocrystal surface and showed high sensitivity towards atmospheric conditions. The emission in the blue spectral range was found to consist of at least two transitions at higher (~2.84 eV) and lower (~2.64 eV) energy sides. Interestingly, the temperature and atmosphere behavior of both transitions is strongly correlated. In addition, these lines seem to be frequently observed together.[190, 192] The intensity of both transitions showed two different behavioral regions when annealed at different temperatures. In the low-temperature annealing regime ($0°C \leq T \leq 200°C$) both transitions show an increase in luminescence intensity resulting in an overall intensity increase by the factor of 1.3. At temperatures above 200°C the blue emission bands are rapidly quenched. Similar behavior was also observed by Zeng et al.[190]

In literature, the blue and violet emissions are often attributed to the presence of Zn_i defects.(see Table 2.1) It has been theoretically predicted and practically demonstrated that the formation of stable Zn_i defects requires highly non-equilibrium conditions: Zn-rich atmosphere and high synthesis temperatures.[190, 224, 225, 278] These conditions do not apply for the most (chemical, liquid phase) synthesis routes of nanostructures, which can explain the rareness of the blue emission.[190] The required conditions, however, perfectly match with the synthesis route of the ZnO NCs studied here [57], making the formation of Zn_i very probable.

To explain the annealing temperature dependent behavior of the blue transitions, Zeng et al. [190] suggested a model of the Zn_i transitions, whereby the violet and blue emissions result from the transition from the neutral (initial) and so-called extended, charged Zn interstitial states or their complexes to the VB, respectively. The highly non-equilibrium processes produce a high concentration of Zn_i with different charge, including neutral (initial state), single and double charged species. The low temperature annealing provides enough ionization energy and increases the concentration of the extended Zn interstitials (charged Zn_i or/and their complexes),

strengthening blue emissions. The high temperature annealing might induce the outward diffusion of Zn_i and quenching of the emission in the blue spectral range.[190]

Indeed, Zn_i are known to be fast diffusors, being already mobile at temperatures below room temperature.[173, 225] The outward diffusion of Zn_i was also identified as the main mechanism of ZnO varistor degradation.[235] Thereby, positively charged Zn interstitials can rapidly migrate towards the negatively charged grain boundary interface. At the interface these charged defects react with the negatively charged defects in the grain boundary, whereby both are neutralized. The loss of the charges results in a reduction of the energy barrier height. This process is typically facilitated by annealing or electrical stress of the varistor, leading to the breakdown of the varistor functionality.

The experiments presented here support the model of Zeng et al.[190] The temperature-dependent PL experiments revealed the participation of either VB or CB in the blue 1 transition. The observed temperature regimes as well as the spectral position of the blue transitions are in good agreement with those of Ref. [190]. The violet emission, corresponding to the transition from the neutral Zn_i to VB [157, 162, 165, 190], could be observed only as a pronounced background contribution to the PL spectra due to dominant blue and excitonic emissions, but it shows a prominent contribution to the EL spectra, as going to be discussed in Chapter 4. Besides, Zn_i is known to be a shallow donor [224, 225] and both the low-temperature PL behavior and the blue shift of the absorption indicate a high natural n-type doping of the ZnO NCs, which can be correlated with the Zn_i defects, since they were suggested to be the origin of the high n-type conductivity in ZnO.[224, 278]

Experimentally, the PL emission in the blue spectral range could be attributed to the defects close to the surface of the NCs. Assuming the origin of the blue emission due to extended Zn_i states (charged Zn_i and /or their luminescent complexes) and considering the possible formation of the depletion layer on the surface of the NCs, the following luminescence model can be suggested on the basis of Ref. [158, 191, 201, 246]. The interstitial Zn defects can be ionized and transformed to the extended Zn_i states close to the surface of the NC, where thereby donated electrons are trapped by the defects on the grain boundary. Another explanation might be an increased concentration of the Zn_i close to the surface of ZnO NCs.

In summary, based on the structural, absorbance and photoluminescence study of the ZnO nanocrystals, the energy diagram of the involved radiative transitions, shown in

Figure 3.20 can be proposed. The pronounced defect-related contributions in red, green and especially blue spectral range make the selected ZnO nanocrystals promising candidate for all-inorganic white nanocrystal LED.

Chapter 4

Archetype All-Inorganic ZnO NC-LED

Electroluminescent devices with nanostructures as an active layer are expected to combine reliability, long operating lifetime and high optical quality of semiconductor material systems with low cost, easy handling and flexible large-area technology of OLEDs.[98, 100, 110] ZnO reveals a high potential as the luminescent active layer in hybrid emitting devices because this material is widely available, non-toxic and robust against oxidation.[27–30] This should enable large-area applications under ambient air conditions. Besides, its direct band gap and high exciton binding energy at room temperature enable efficient emission for laser and LED applications in the visible and ultra violet (UV) spectral range.[34, 35]

However, the realization of cost-effective nanostructure ZnO light emitting devices remains challenging. ZnO nanowires in hybrid systems is one of the concepts that showed large area electroluminescence (EL) in the visible and UV spectral range.[49–56] The nanowire growth process, unfortunately, makes low-cost production, e.g. by printing techniques, of such large area emitters on flexible substrates in most cases inconvenient. The unbeatable advantage of the nanocrystal implementation into the LEDs remains the fact that the synthesis of the active material is separated from the fabrication of the device.

ZnO nanoparticles in hybrid devices with organic support layers showed visible and near-band-gap EL at room temperature in the DC regime.[29, 58–60] However, additional organic charge injection support layers are quite sensitive against humidity, oxygen and UV exposure, and therefore limit the lifetime of these devices. An alternative approach is to renounce the organic support layers. In this case, only defect related EL in ZnO nanopowders was observed so far at several hundred volts.[279, 280]

A distinctive near-band-gap contribution to the EL signal at low voltages remained so far challenging for all-inorganic ZnO nanoparticle devices. Also, the EL mechanism behind such simple ZnO structures remains a puzzle [281] with no systematic studies correlating the defect structure of the ZnO with its electrical, photoluminescent and electroluminescent properties.

In this chapter, organic free ZnO archetype nanocrystal (NC) electroluminescent devices are presented. The LEDs showed defect related EL as well as near-band-gap emission in the UV spectral range at voltages below 10 V under ambient air conditions. The influence of the transparent conductive oxide (TCO)-work function and thermal treatment on the device performance is studied, finally resulting in large area EL emission with a distinctive near-band-gap contribution. In addition, the simple device design enables for the first time a direct correlation between the defects in ZnO nanocrystals and the I-V, PL and EL properties of the corresponding devices. The experimental observations allow a suggestion of the emission model, which is also consistent with different reports from the literature on the not yet well understood behavior of ZnO-based devices.

4.1 Design and Fabrication

The basic concept of the archetype ZnO-NC light emitting device is shown in Figure 4.1 (a). The transparent conducting oxide (TCO)-coated glass is used as a substrate and transparent contact electrode, while a layer of ZnO nanocrystals acts as an active light emitting layer and a top Al electrode as another electrical contact layer.

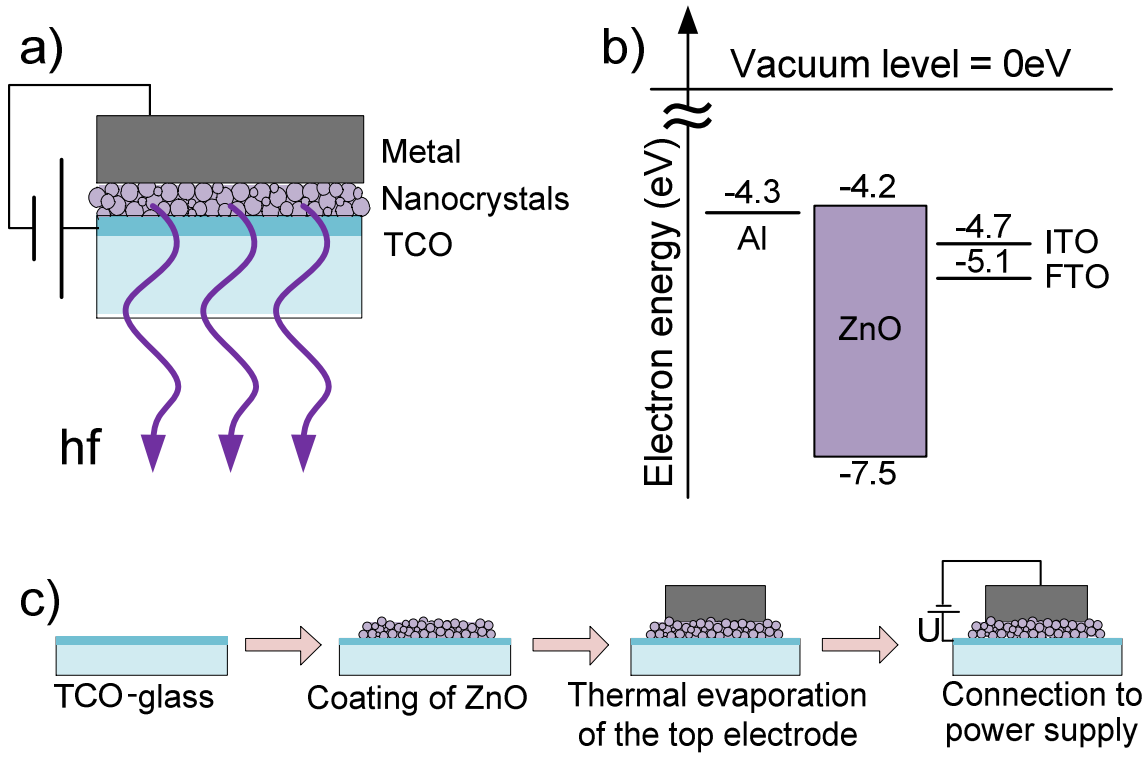

Figure 4.1: (a) Device structure (under forward-bias operation). (b) Simplified energy band diagram of the involved materials. (c) Schematic of the device fabrication steps.

Figure 4.1 (b) shows the simplified energy band diagram of the involved materials, based on the values known from literature.[50, 105, 282] Under forward bias, the electrons are expected to be injected from the Al electrode into the conduction band (CB) of ZnO, while the electrons from the deep traps and valence band (VB) are expected to be extracted by the TCO (ITO, FTO), leaving a hole behind (hole injection), which can then radiatively recombine with the electron from the CB.

The fabrication process is schematically shown in Figure 4.1 (c). The TCO-coated substrates are first cleaned and dried by nitrogen. Subsequently, a commercially available butyl acetate dispersion of the nanoparticles is spin coated on top of the

substrate. It should be noted that all archetype devices, discussed in this chapter, were fabricated with "fresh" nanoparticles (see Chapter 3). Finally, an approximately 250 nm thick Al layer is deposited on top of the nanoparticle layer by thermal evaporation through a shadow mask. The whole process, except the Al evaporation, is carried out at room temperature and under ambient air conditions. Therefore it is easy and in principal suitable for industrial upscaling and printing techniques. More details on the fabrication procedure can be found in Appendix A2.

One of the main preconditions for the fabrication of a luminescent device is a closely packed luminescent layer of nanoparticles. By varying the spin coating parameters and the dilution of the dispersion, it was possible to achieve tight, homogeneous layers on different substrates and change their thickness between 200 nm and several μm.

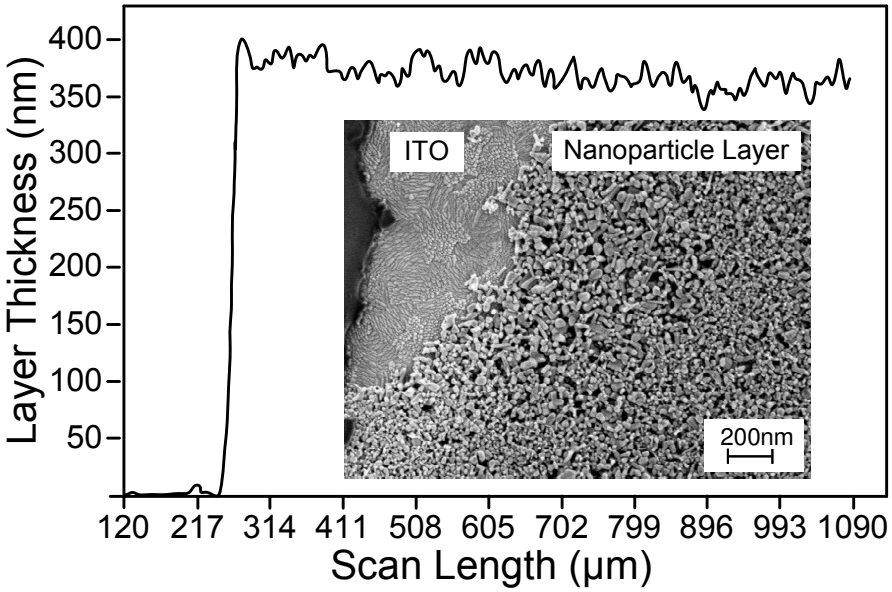

Figure 4.2: Surface profile of a typical ZnO nanocrystal layer. The inset shows a typical SEM image of the edge of a NC layer on an ITO substrate.

Figure 4.2 shows a typical surface profile of a ~350 nm thick nanoparticle layer, which is obtained by a KLA-Tencor P15 surface profiler. The scan reveals a homogeneous layer with a thickness deviation of less than 40 nm, which is within the range of the nanocrystal size. The thickness is stable across the whole scan regime of about 1 mm. No extended trenches within the layer, which might later result in shortcuts from the top electrode to the substrate, could be detected. The inset of Figure 4.2 shows a typical SEM image of the nanocrystal layer, supporting the result of the surface profile measurements that the layers are tightly packed and homogeneous. The typical packing density of the ZnO NC layers was estimated by absorption spectroscopy to be 0.33 (see Chapter 3.2).

4.2 ITO-based Archetype ZnO NC-LED

In the first straight forward approach, indium tin oxide (ITO) coated glass substrates were chosen as a TCO contact to the nanocrystal layer due to its high electrical conductivity and smooth surface. The electrical and luminescent behavior of such ITO-ZnO-Al archetype devices is presented in this section.

4.2.1 Impact of the ITO substrate on the layer morphology

Indium tin oxide (ITO, In_2O_2:SnO_2, typically in 90:10 wt% ratio) is the most prominent TCO, where carrier densities above 10^{21} cm^{-3} and resistivities below 10^{-5} Ωcm have been demonstrated.[283] It is used as a transparent conducting substrate in organic LEDs, LCD displays and novel hybrid LEDs as a standard due to its superior electrical behavior and very smooth surface. ITO coating is usually deposited on top of glass substrates by DC or RF magnetron sputtering, which results in films with very low roughness, down to an atomic monolayer.[284] The main disadvantage of the ITO is revealed by its high production cost due to scarceness of indium and expensive fabrication process of the required sputtering targets as well as the costly deposition process itself. A possible alternative to ITO for low-cost white NC-LEDs is going to be discussed in Chapter 4.3.

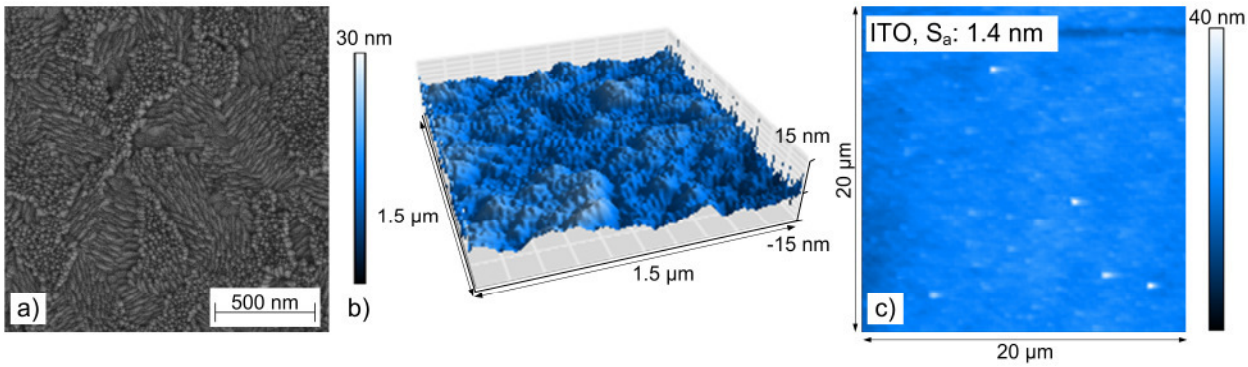

Figure 4.3: (a) SEM image of the ITO substrate, applied in ZnO NC-LEDs. (b) 3D and (c) top AFM images of the ITO substrate revealing 1.4 nm average surface roughness.

In this work, ITO with a sheet resistance of 20 Ω/sq from Merck was chosen in a first step as a transparent electrode. The transmission of the ITO at 380 nm and the average transmission in the visible spectral range were measured to be about 73 % and 92 %,

respectively. Figure 4.3 (a) shows the SEM image of the ITO substrate. The atomic force microscopy (AFM) measurements on the cleaned substrates revealed an average surface roughness (see Appendix A1) of 1.4 nm, as can be seen from the 3D (b) and topography (c) AFM images in Figure 4.3.

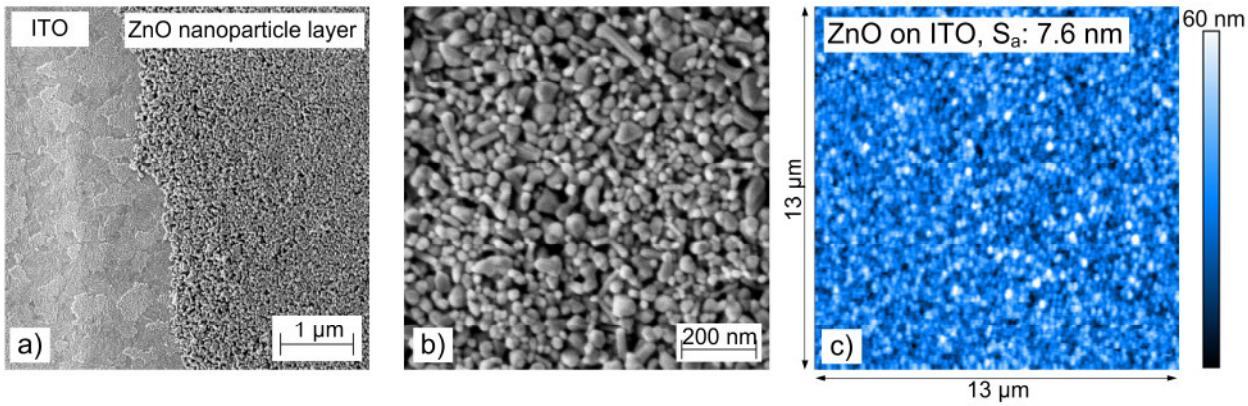

Figure 4.4: (a) SEM image of the ZnO NC layer on top of the ITO substrate, (b) close-up on the ZnO NC layer and (c) AFM image of the ZnO NC layer with the resulting average surface roughness of 7.6 nm.

The morphology study of the spin-coated ZnO NC layers is depicted in Figure 4.4 with (a) and (b) showing typical SEM-images of the NC layers on top of the ITO substrate. The resulting layers are densely packed and reveal an average surface roughness of 7.6 nm, as shown in an AFM image of the layer in Figure 4.4 (c).

4.2.2 ITO-based archetype device characteristics

The first all-inorganic ZnO NC devices, based on a ~350 nm thick particle layer, sandwiched between ITO and Al electrodes showed Electroluminescence (EL), while being operated under forward bias (electrons are injected into the NC layer from the Al electrode). The EL signal from the device was collected through the ITO substrate in a standard luminescence setup, also used for the PL measurements. Figure 4.5 shows the normalized EL spectra of the device (a) and the corresponding emission intensity (b) as a function of the applied voltage.

The first EL spectra could be detected at voltages as low as 4 V, as shown in Figure 4.5 (a), lower part. The corresponding spectrum shows a peak at ~670 nm with contributions from the red to near-infrared (NIR) spectral regions, indicating that at low applied voltages low energy defects within the band gap are accessed.

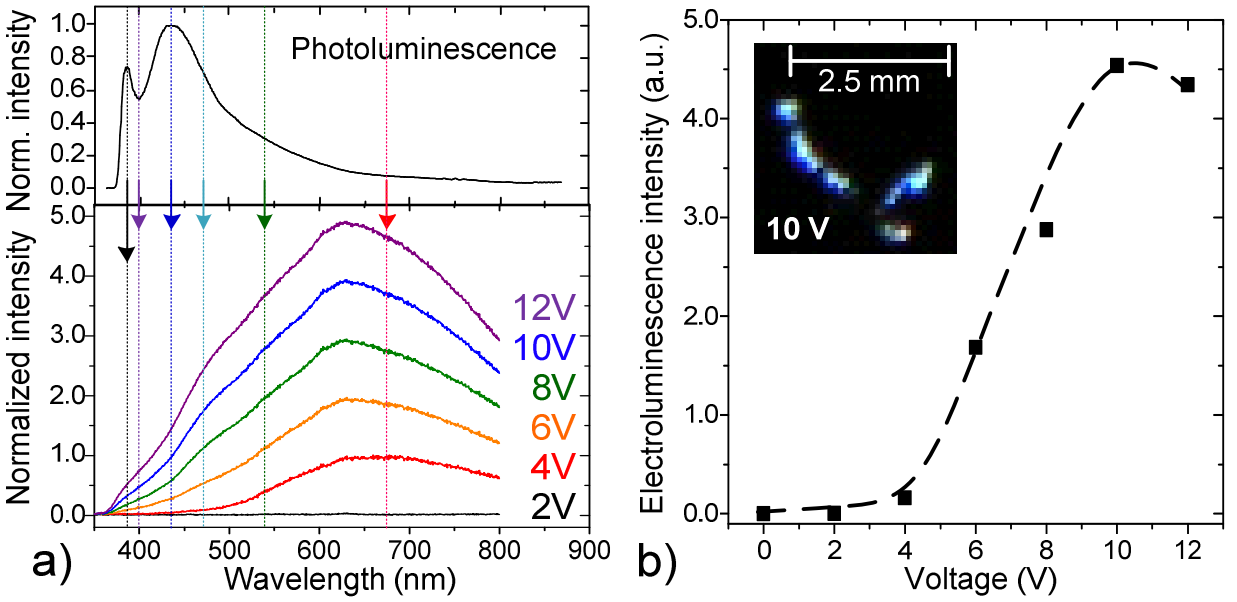

Figure 4.5: (a) PL of the ZnO NC layer (upper part) with identified NBR and visible transitions (indicated by the arrows with corresponding color) compared to the normalized EL spectra of the ITO-based ZnO NC-LED (lower part). (b) Corresponding EL intensity of the device as a function of the applied voltage. The inset in (b) shows an image of light emission at 10 V

The comparison to the PL of the nanocrystal layer (upper part of Figure 4.5 (a)) reveals a correlation with the red defect-related transition (red arrow) at ~1.85 eV (~671 nm), attributed (see Chapter 3) to excess oxygen (probably a transition from the CB to the O_i level). An increase in applied voltage leads to a broadening of the EL spectrum toward the high energy side. Most of the visible spectrum is covered at 6 – 8 V with increasing green and blue contributions. The characteristic ZnO near-band-gap emission (black arrow) below 400 nm is quite weak and less pronounced, compared to the emission in the visible range. Nevertheless, it can be observed at voltages above 8 V. Though all defect related transitions, identified by the PL measurements (marked by colored arrows in the upper part of Figure 4.5 (a), see also Figure 3.6 and Figure 3.20 (a)), can also be observed in EL, the intensity ratio among them is quite different, significantly changing the shape of the spectra. Apparently, defect states responsible for low energy transitions are easily populated during electrical carrier injection, while the high excess energy in case of optical excitation favors short wavelength emission in photoluminescence. Such voltage dependent behavior of the EL as well as deviations in shape from the PL spectrum is quite common for ZnO LEDs and was observed in layer [285, 286] and nanowire / nanorod [49, 53, 54, 168] devices. The overall intensity of the emission increases by a factor of more than 20 as the applied voltage is increased to 10 V (Figure 4.5 (b)). At higher voltages, the intensity first starts to decrease slowly, followed by the breakdown of the device at voltages above 13 V.

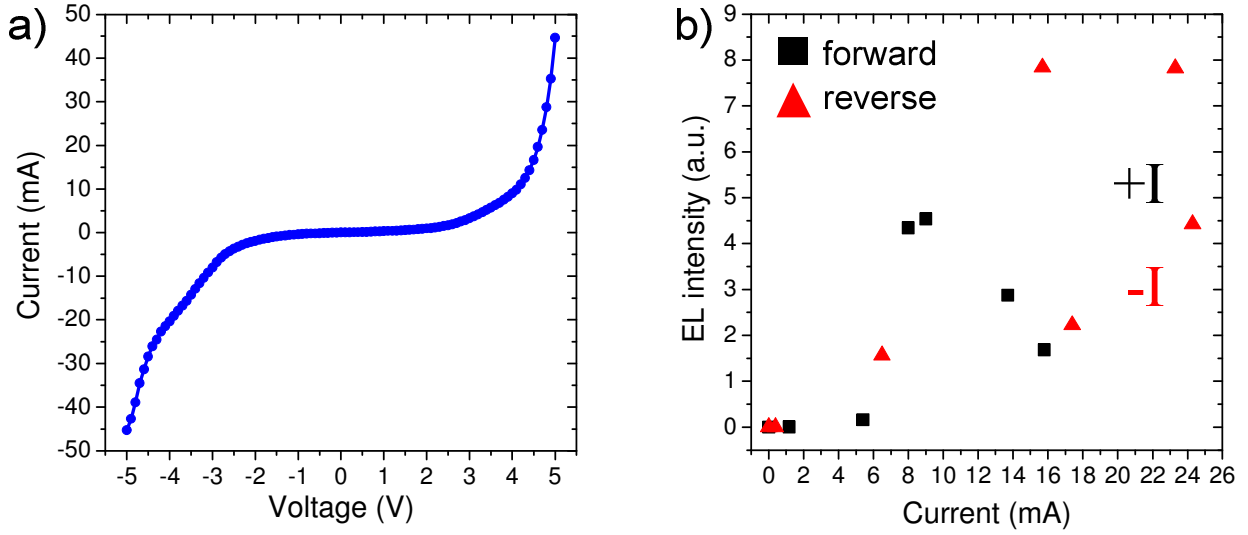

Figure 4.6: (a) Typical I-V-behavior of the ITO-archetype device under forward (positive) and reverse (negative) bias. (b) Intensity of the EL under forward (black squares) and reverse (red triangles) bias as a function of the current through the device.

The device showed an almost symmetric, non-linear I-V behavior under both forward (positive, electrons are injected from the metallic contact) and reverse (negative, electrons are injected from the TCO contact) bias, as shown in Figure 4.6 (a). The non-linear I-V behavior under both biases was also frequently observed in case of ZnO-only devices [281, 287–290], as well as in case of single-active-layer organic/inorganic NC hybrid devices [89, 94, 96, 111, 116, 140, 145, 291] and NC-LEDs with unipolar device architecture.[101] Such an I-V curve is a typical sign of unipolar current transport [101], i.e. the I-V behavior is dominated by one species of charge carriers [116, 142] as proposed by Parker et al.[292] According to his model, the I-V behavior is controlled by the current density of the majority injected charge carriers [292], which are electrons in case of ZnO archetype devices. A closer look at the first-principle energy diagram in Figure 4.1 (b) for the case of ITO (work function of 4.7 eV) as a transparent electrode reveals very similar conditions for the electron injection and extraction under forward and reverse bias due to similar work functions of the electrodes, which results in almost symmetric I-V characteristics. This was also observed in other NC-LEDs with similar work functions of the electrodes.[89, 94, 116, 291, 292]

For NC-LEDs, the non-linear I-V behavior under both bias directions typically also results in light emission under both polarities.[89, 94, 96, 101, 111, 116, 291] According to the operation model suggested by Parker et al. [292], the EL emission can be expected under both forward and reverse bias conditions, whereby its efficiency is determined by minority charge carriers. The emission intensity as a function of the current through the device under forward (black squares, +I) and reverse (red triangles,

-I) bias is shown in Figure 4.6 (b). The device showed fast degradation under operation, resulting in the unstable current / intensity behavior. Besides, neither bias directions was clearly favored, as can be seen from Figure 4.6 (b). This is in agreement with the model proposed by Parker et al. [292], since it can be concluded from the band alignment (Figure 4.1 (b)) that none of the bias conditions is clearly favored.

4.3 FTO-based Archetype ZnO NC-LEDs

The challenging issue of hole injection into (electron extraction from) the valence band of the ZnO NC-LEDs can be expected to be improved by using TCOs with a higher work function, in analogy to the electron injection into the CB of organic semiconductors in OLEDs.[292] While ideally no substantial change in the I-V-behavior under forward bias can be expected (the conditions for the electron injection remain the same), the electron extraction efficiency from the VB and deep trap states is expected to increase with increasing work function of the TCO, as well as the overall device efficiency.[292]

4.3.1 Impact of the FTO substrate on the layer morphology

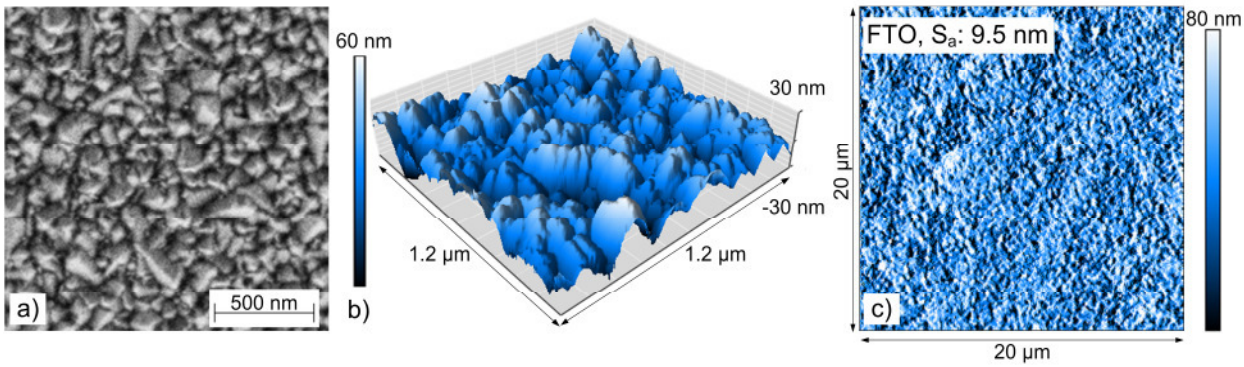

Figure 4.7: (a) Typical SEM image of the FTO substrate, applied in ZnO NC-LEDs. (b) Topographical 3D and (c) top AFM images of the FTO substrate revealing an average surface roughness of 9.5 nm.

A promising and by far less expensive TCO candidate to replace ITO and to improve the device performance is fluorine doped tin oxide (FTO, SnO_2:F) with a typical work function of ~4.9 eV [50, 293]. Usually it is deposited directly on freshly fabricated hot glass sheets (3.2 x 6 m^2) at atmospheric pressure conditions in a CVD-process.[294] Thereby, the typical coating thickness of 320 – 450 nm results in a sheet resistance between 8 and 15 Ω/sq. Due to large-area and very cost-effective deposition technique of FTO compared to ITO (CVD vs. magnetron sputtering) as well as the wide availability of the precursor material, the fabrication costs of the FTO are quite low. On the other hand, the fabrication process of the FTO always results in a principally higher roughness of the coating, compared to ITO [295], as can be seen from Figure 4.7. It

shows typical SEM and AFM images of the Pilkington TEC-15 FTO-coated glasses (15 Ω/sq), implemented in this work, demonstrating a high average roughness of 9.5 nm and the "pyramidal" surface structure with local height deviations up to 60 nm. The transmission of the FTO at 380 nm and the average transmission in the visible spectral range were measured to be about 61 % and 77 %, respectively. In order to additionally increase the work function of the FTO [282], the substrates were treated by the UV-ozone (UVO)-cleaner for 10 minutes after the standard cleaning procedure and directly prior the NC layer deposition. Therefore the work function of the FTO can be assumed to be 5.1 eV.[282] (see Figure 4.1 (b))

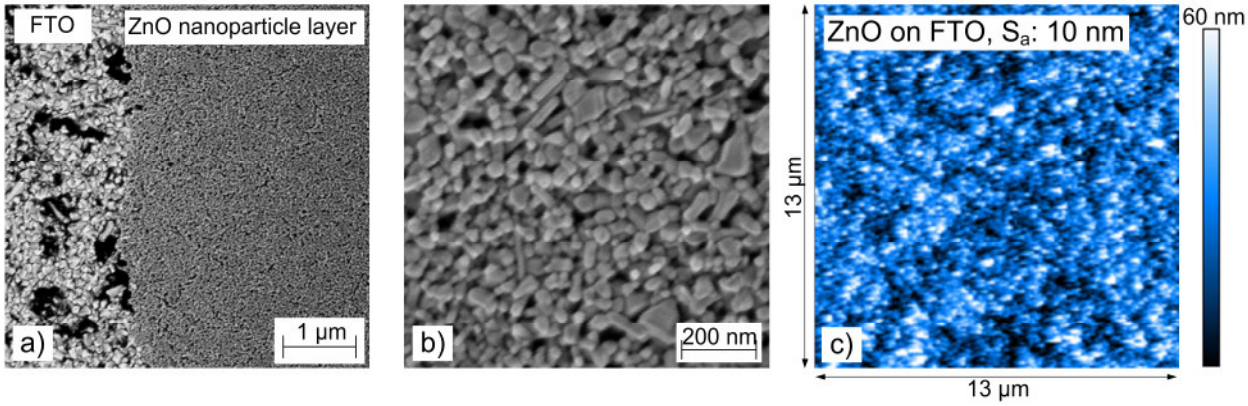

Figure 4.8: (a) SEM image of the ZnO NC layer on top of the FTO substrate, (b) close-up on the ZnO NC layer and (c) AFM image of the ZnO NC layer with the resulting average surface roughness of 10 nm.

ZnO NC layers were deposited on top of the FTO substrates from the identical dispersion as in the case of the ITO devices at slightly different spin-coating parameters in order to result in layers of the same thickness (350 nm). The morphology study of the spin-coated ZnO NC layers is depicted in Figure 4.8 with (a) and (b) showing typical SEM-images of the NC layers on top of the FTO substrate. The resulting layers are densely packed and reveal a higher average surface roughness of 10 nm compared to the layers on smooth ITO substrates (7.6 nm), as shown in the AFM image of the layer in Figure 4.8 (c).

4.3.2 FTO-based archetype device characteristics

The 250 nm thick top Al electrode was thermally deposited through the shadow mask on top of the NC layer, as in case of ITO-based devices. A typical I-V behavior of the FTO-based archetype device is shown in Figure 4.9 (a). It is as well non-linear in both operation directions, with slightly higher currents under forward bias compared to reverse bias. This might be due to the higher barrier for the electron injection under

reverse bias, resulting from the higher work function of FTO (see Figure 4.1 (b)). Not only the electron injection barriers but also the charge transport properties of the active layer itself have a strong impact on the resulting I-V characteristics. The changed morphology of the nanocrystal layer with increased average roughness and incorporated spikes from the FTO, which might result in shortcuts, are expected to change the I-V-behavior of the device. Indeed, a significantly increased ohmic conduction in the low-voltage region could be observed in the FTO-based devices, as can be seen from Figure 4.9 (b) where typical FTO-based (blue) and ITO-based (black) I-V curves of the archetype devices are shown. The increase of the ohmic contribution is too dominant to allow a reasonable comparison of the I-V-behavior between the archetype devices and quantitative conclusions about the role of the modified work function. However, the EL behavior of the two archetype devices shows systematic differences.

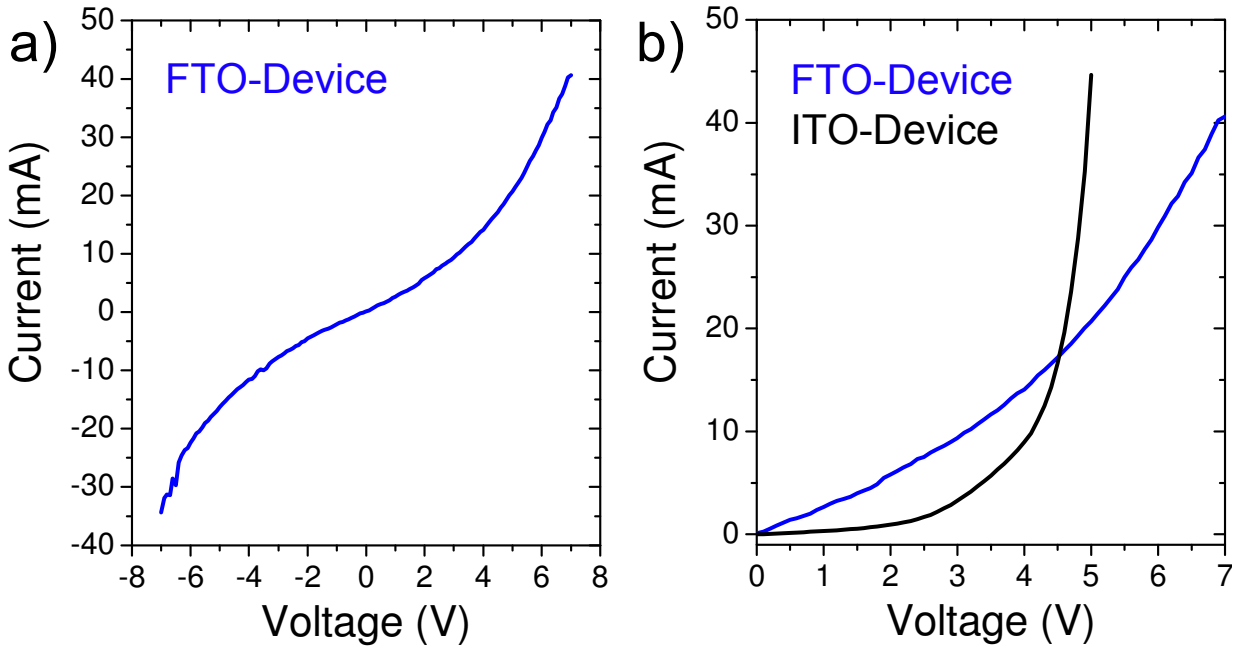

Figure 4.9: (a) I-V curve of the FTO-based archetype device under forward (positive) and reverse (negative) bias. (b) Typical I-V curves of the FTO- (blue) and ITO-based archetype devices under forward bias.

Figure 4.10 shows the typical EL spectra of the ITO- (black) and FTO-based (blue) ZnO archetype NC-devices under forward bias. Figure 4.10 (a) shows the first detectable EL spectra of the devices, which occurs in both cases at 4 V. Figure 4.10 (b) shows the EL spectra in the high voltage region (9V), where all the luminescent defect states as well as VB states can be accessed. In both cases the shape of the EL shows a clear trend: at the same applied bias (electrical field) as for FTO-based devices, the defect-related contribution in the green and blue spectral range is increased compared to ITO-based

archetype device. In addition, the FTO-based device shows a far more pronounced contribution in the UV range due to the NBR transitions. Therefore, it can be concluded that the efficiency of the electron extraction from the traps states responsible for green and blue emission as well as from the VB is higher than in ITO devices, in agreement with Parker et al.[292]

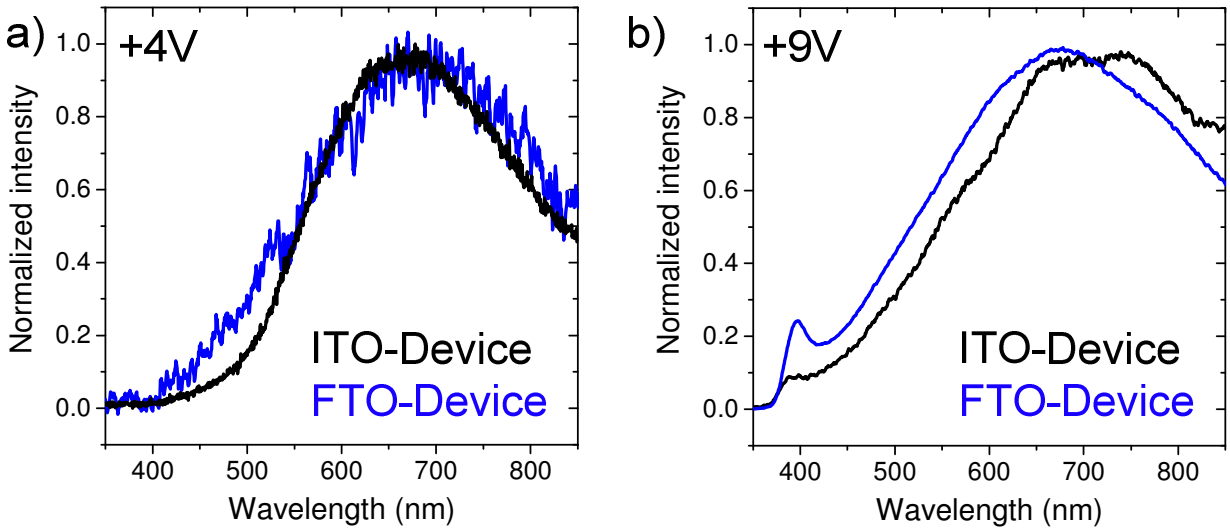

Figure 4.10: Normalized EL spectra of the ITO- (black) and FTO-based (blue) archetype ZnO NC-LEDs under forward bias of 4 V (a) and 9 V (b).

The overall EL emission intensity of the FTO-based devices was on average 3 times higher than the EL intensity of the ITO-devices at comparable current densities, which shows that the introduction of the FTO as a TCO in an archetype ZnO NC-LED structure clearly improves device performance. The main challenge still remains the high roughness of the FTO substrate.

4.3.3 Annealing of FTO-based archetype devices

Nanocrystalline layers annealed at moderate temperatures of about 200°C in different environments showed an increase in the total photoluminescence emission intensity, as was demonstrated in Chapter 3. Especially the contribution of the blue defect-related emission, resulting most probably from interstitial zinc defects, increased at annealing temperatures between 100°C and 200°C. Thus, an enhancement in the EL intensity can be expected due to the increase of the overall emission intensity by the moderate temperature treatment. The FTO-based archetype ZnO NC-LED design was chosen for the annealing studies due to the improved device performance, as demonstrated in Chapter 4.3.2. Another reason for choosing FTO as the TCO-substrate was its superior temperature stability, compared to ITO.[296, 297] While the sheet resistance of ITO can increase by more than 4 times within the studied temperature range, the sheet resistance of the FTO is expected to remain almost constant.[297]

350-nm thick ZnO NC layers were spin-coated on top of the cleaned, UVO-treated FTO substrates and afterwards annealed in a quartz tube furnace in ambient air at different temperatures (0°C to 600°C) for 30 minutes. The PL behavior of the layers was discussed in Chapter 3 (Figure 3.16). For the EL study, the annealed nanoparticle layers were further processed by evaporating Al contacts through a shadow mask, resulting in standard FTO-based archetype devices.

The ratio between the devices showing EL and the number of the overall fabricated devices, normalized to the typical yield in the untreated case, is shown in Figure 4.11 (a). It can be seen that the highest yield is obtained at the annealing temperature of 200°C, while none of the devices, annealed at higher temperatures, emitted any EL signal. It is interesting that all the devices exhibiting EL are characterized by a strongly non-linear I-V curve with a high resistance in the low voltage regime, as can be seen from Figure 4.11 (b).

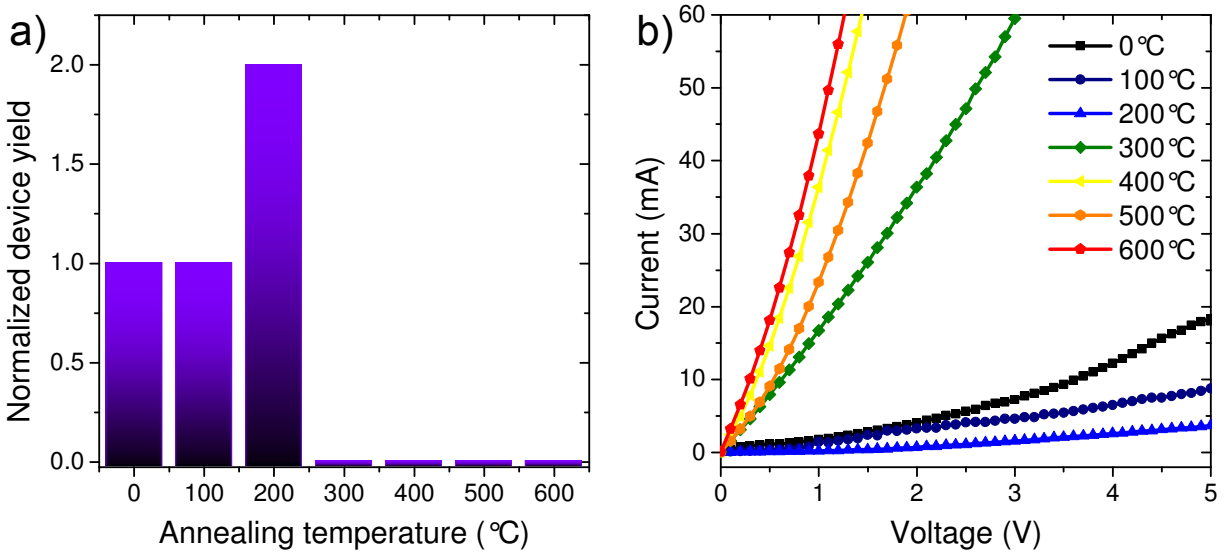

Figure 4.11: (a) Yield of the FTO-based EL devices as a function of the ZnO NC layer annealing temperature, normalized to the yield of the as-deposited ZnO NC-LEDs. (b) I-V behavior of the FTO-based devices in the low-voltage range as a function of ZnO NC annealing temperature.

The I-V-behavior of the NC layers annealed at different temperatures, shows basically two different temperature regimes: (i) a non-linear behavior with high resistance in the low voltage region, corresponding to the devices showing EL at voltages of 4 V and above, and (ii) an almost ohmic behavior with low resistance in the low-voltage range, without EL. Within the first temperature region, the resistance continuously increases with increasing temperature, improving the rectifying behavior of the device. At 300°C and higher annealing temperatures, the I-V characteristic becomes almost ohmic, with a decrease in resistance as the annealing temperature increases.

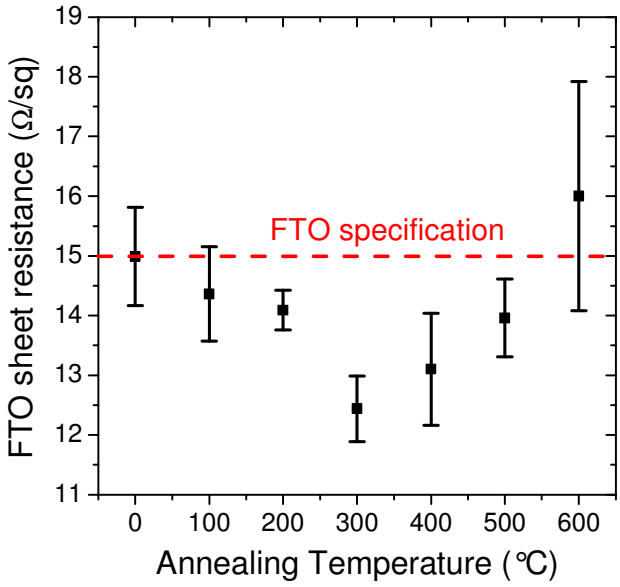

Figure 4.12: Sheet resistance of the FTO-coated substrates as a function of annealing temperature.

The changes in the I-V-behavior of the devices might be attributed to the changes of the FTO conductivity due to thermal treatment. To exclude this origin, the impact of the annealing step on the sheet resistance of the FTO substrates was measured on the reference FTO samples and is shown in Figure 4.12. In the temperature range below 300°C, when the resistance of the NC layers in the low-voltage regime increases, no increase of the FTO sheet resistance could be observed. On the contrary, the sheet resistance even slightly decreased and subsequently reached the nominal value of 15 Ω/sq during the annealing at temperatures above 300°C. Hence, the observed changes in the I-V-curves of the annealed devices can not be associated with temperature-induced changes within the FTO substrate.

Another reason for the changes in the I-V behavior can be morphological changes within the ZnO NC layer during the annealing step. SEM studies of the annealed layers could not reveal substantial changes in the structure of the layer itself and nanocrystals within the soft annealing regime (below 300°C). Annealing at higher temperatures (above 300°C) indeed changes the morphology of the NC layer, as can be seen in Figure 4.13, where the NC layer, annealed at 600°C (b) is compared to the typical SEM image of the layer annealed under temperatures below 300°C (a). As expected, the size of the particles increases during the high-temperature annealing.[174]

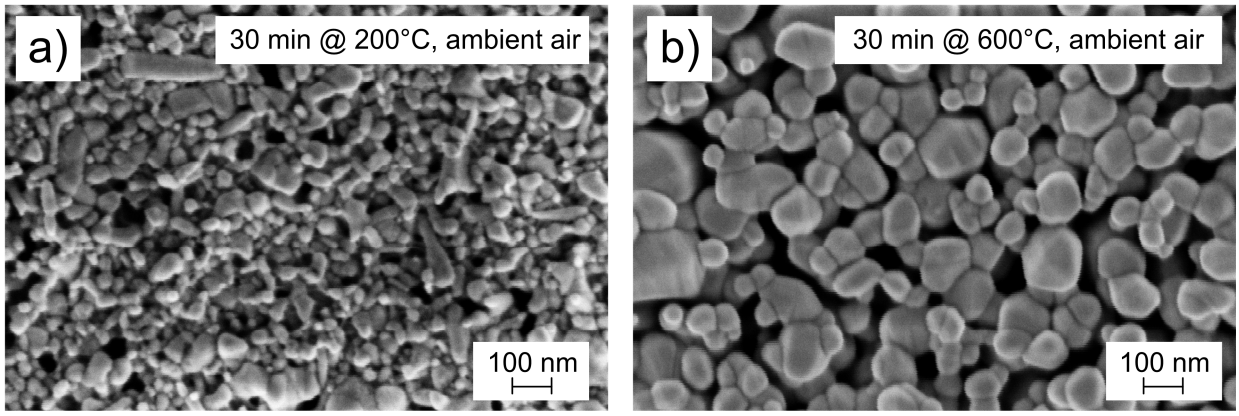

Figure 4.13: Typical SEM image of the ZnO NC-layers after the annealing at (a) 200°C and (b) 600°C.

The growth of the particles increases the layer porosity and possibly leads to the diffusion of the Al through the layer to the FTO during the evaporation, creating shortcuts. Another reason for the strong changes in the I-V-curves by high temperature annealing might be the increase of the layer conductivity, either by forming tight contact necks between the particles, by increasing the excess carrier density and thus the conductivity of the particles itself during annealing or by a decrease of the energy barrier of the contact boundaries between particles.

Obviously, an annealing step in ambient air at around 150-200°C increases the intensity of the luminescence (especially those of blue defects), the overall yield of the NC-LEDs and improves the rectification behavior. Therefore there seems to be an optimum process temperature between 100°C and 200°C for improving the device characteristics.

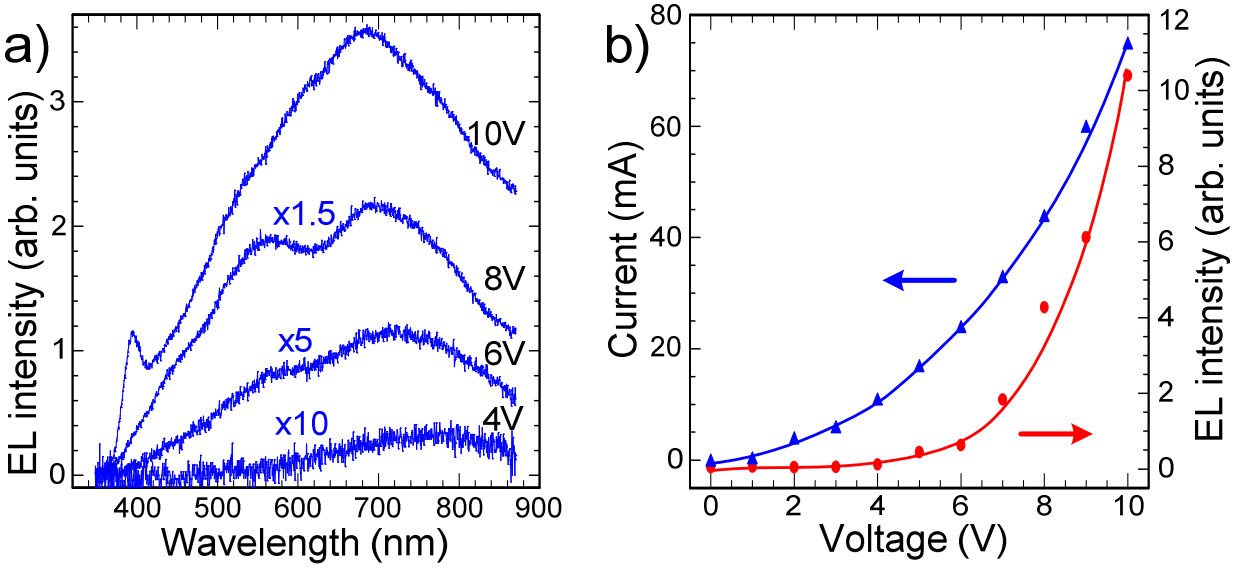

Figure 4.14: (a) EL spectra of the forward-biased FTO-archetype LED based on ZnO NC layer, annealed at 150°C for 30 min. (b) Corresponding EL intensity and current through the device as a function of the applied forward bias.

The optimum annealing temperature to retrieve archetype ZnO NC-LEDs with the best performance was found to be 150°C. Figure 4.14 (a) shows the EL spectra of a forward-biased NC-LED, prepared on a FTO substrate including an annealing step at 150°C on a hot plate for 30 minutes in ambient air. The observed EL behavior is quite similar to other archetype devices, as discussed above, starting at 4 V in the red and near-infrared spectral region. With increasing bias voltage, the device also shows components in the green and blue spectral range and exhibits a distinct UV peak from the near-band gap emission from 9 V on.[45] The overall intensity of the device increases with increasing voltage as shown in Figure 4.14 (a) (red dots), while the I-V-behavior of the device is non-linear with currents in the range of several tens of mA (blue triangles).

The all-inorganic device showed a stable operation under ambient air without any encapsulation during 3 hours of operation. Figure 4.15 shows the EL intensity of the device under reverse (red squares) and forward (blue triangles) bias as a function of the current through the device. The device shows higher external efficiency (i.e. ratio between the emitted photons and the injected electrons) compared to the ITO-based

NC-LED under forward bias due to the increased work function of the TCO-electrode. The efficiency under forward bias is roughly 2 times higher than under the reverse bias, which is a comparable value to NC-LEDs with a similar simple design.[111, 116]

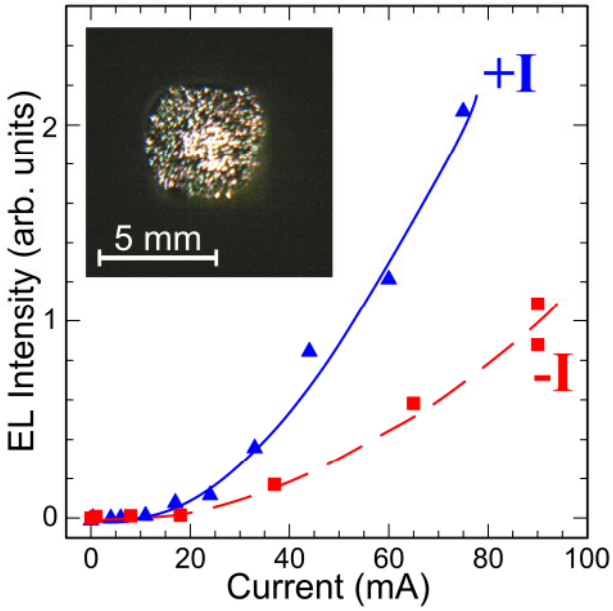

Figure 4.15: EL intensity of the FTO-based device, annealed at 150°C, as a function of the current in forward (blue) and reverse (red) directions. The inset shows a photograph of the emitting device at 8 V forward bias.[45]

The LED emission color was white and, starting from ~7 V, visible to the naked eye with high color rendering indices typically between 96 and 98 and a correlated color temperature between 3200 K and 3700 K. (see Appendix A1) The inset of Figure 4.15 shows an image of the device under operation of 8 V forward bias. Although the whole contacted area of the nanoparticle layer shows EL, the intensity over the emitting region remains inhomogeneous. Some of the possible reasons might be inhomogeneities of the active layer due to the wide size and shape distribution of the nanoparticles as well as high roughness of the FTO substrate.

4.3.4 FTO archetype devices based on aged nanocrystals

The archetype devices, fabricated from aged nanocrystals, showed very low emission intensity when annealed at 150°C and no EL without annealing. They also exhibited very low emission homogeneity with only few active emission centers over the electrode. The inset of the Figure 4.16 (b) shows a typical image of the active circular (diameter of 3 mm) electrode being under operation in forward direction. The EL

spectra, shown in Figure 4.16 (b), correspond to a FTO-based archetype ZnO LED with a ~500-nm thick annealed NC-layer. Such device types show a pronounced contribution in the UV-range and reduced defect-related EL intensity due to the substantial reduction in defect states, as showed by PL measurements in Figure 4.16 (a). At lower voltages, the spectra don't exhibit an UV contribution and show a similar voltage-dependent change of the defect-related EL spectra shape, as the devices fabricated from fresh nanocrystals, though with a very low intensity. At voltages around 8 V, the contribution in the UV range becomes measurable, and at 9 V and higher a pronounced UV peak dominates the EL spectrum. However, the origin of such an increased NBR contribution, compared to the emission in visible range, requires further clarification.

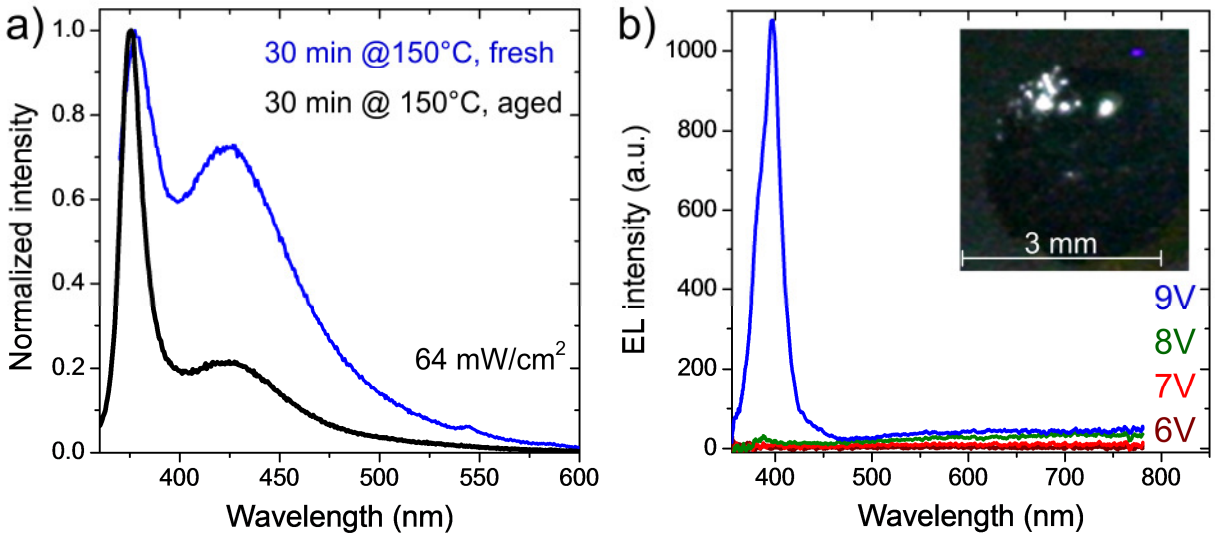

Figure 4.16: (a) PL spectra of NC layers annealed for 30 min at 150°C in air consisting of fresh (blue) and aged (black) nanocrystals. (b) Typical EL spectra of devices based on layers of aged NCs annealed at 150°C for 30 min.

The position of the UV-peak in both aged and fresh devices shows a considerable red shift of ca. 9 to 23 nm of the EL compared to PL. Such a significant red shift was also observed in other EL devices with active light emitting ZnO layers [64, 288, 298], nanowires and nanorods [50, 54, 56], and nanocrystals incorporated between organic support layers [29]. A red shift between EL and PL is also quite typical for QD-LEDs, but in this case, the shift is in the range of few nm.[16, 22, 101, 112, 299, 300] In QD-LEDs the red-shift of the EL emission with respect to PL is typically attributed to the energy transfer from smaller to larger QDs as well as the quantum confined Stark effect in QD ensembles.[16, 22, 25, 101] Both effects are not the issue for large (bulk) ZnO nanostructures.[54] Thermal shift due to the heat from the current can be one possible origin for the red-shift.[56, 301] Xi et al. presumed a possible influence of the defects

and surface states on the NBR emission contribution to the EL spectra of ZnO LEDs.[54] The aged ZnO nanocrystals and the archetype devices based on them, offer an excellent platform for such a study, since the NC themselves showed a very distinct defect-related excitonic contribution in the UV range (A-Line, Figure 3.12) even at room temperature, and the corresponding LEDs showed an exceptionally pronounced EL in the UV range without additional defect-related emission [29, 49, 50, 52, 58] and / or emission coming from additional organic [302]/ inorganic [303] support layers. Thereby the low- and room-temperature-PL as well as EL spectra of the ZnO nanostructures can be correlated.

For a closer study of the origin of the UV-contribution to the EL emission spectra in the ZnO-nanostructure-LEDs as well as its red-shift compared to the PL, a selected normalized EL spectrum of the aged FTO-based archetype ZnO NC-LEDs is plotted in Figure 4.17, together with the corresponding room temperature PL spectrum.

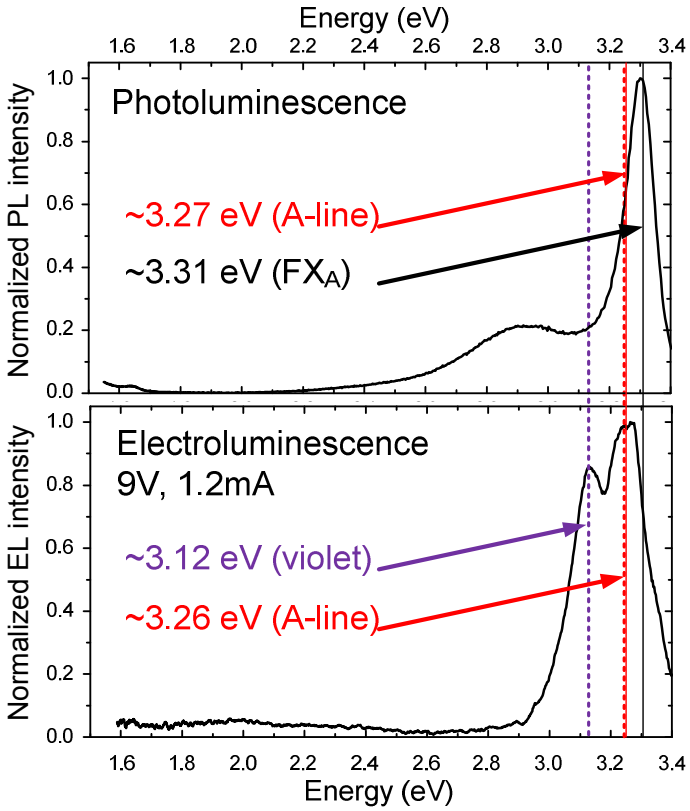

Figure 4.17: Comparison between the PL (upper part) and the EL spectra (lower part) of the NBR peak of the FTO-based archetype devices based on aged NCs.

Figure 4.17 (upper part) shows the PL spectrum of the aged annealed (30 min at 150°C) NCs. It was demonstrated by the low-temperature and temperature dependent measurements that the NBR peak is formed by two different excitonic contributions:

the free A-exciton at ~3.31 eV and the A-line at ~3.27 eV. The spectral position of these transitions is marked in Figure 4.17 by solid black and red lines, respectively. Figure 4.17 (lower part) clearly shows that the distinct EL contribution in the UV range mainly consists of two peaks at ~3.12 eV (398 nm) and 3.26 eV (381 nm), which positions are marked by dotted violet and red lines, respectively. The width of the high-energy peak at ~3.26 eV can be estimated to be ~100 meV, which is in very good agreement with the characteristics of the A-line (~3.27 eV, and width of ~95 meV), retrieved from the PL study of the particles in Chapter 3. The width of the low-energy side transition can be estimated to be ~150 meV. Both the position of the peak and its width are in excellent agreement with the values deduced from the fitting procedure of the PL spectra in Chapter 3 for the "violet" transition (~3.12 eV and ~120 meV respectively).

The observation of the pronounced "violet" transition supports the proposed defect structure, shown in Figure 3.20, whereby this transition is attributed to the initial Zn_i defect (shallow donor) states. The A-line was attributed to the A-exciton, bound to surface states or structural defects on the surface of the ZnO nanocrystals. The assignment of these transitions and their correlation to the PL show a possible explanation for the large energy shift between the PL and EL spectra of the ZnO LEDs observed in literature. While the excess-energy PL excitation usually favors the formation of free excitons in ZnO nanostructures, in case of the EL only the defect states and excitons bound to the defects can be predominantly successfully excited by the applied electrical field, so that the red-shifted emission, observed in the UV-range in ZnO-LED devices is actually defect related.

4.4 Study of the I-V Behavior

ZnO archetype NC-LEDs offer a good platform to study the current transport properties of ZnO NC layers, since the possible impact of additional charge injection, transport or blocking layers, typical for advanced NC-LEDs, is minimized. The I-V behavior of the archetype device is determined only by the properties of the ZnO NC layer itself as well as by the TCO and metallic contact layers. To minimize the impact of the TCO substrate roughness (e.g. possible shortcuts or locally increased electrical fields), the typical I-V curve of the ITO-based archetype LED (see Figure 4.6 (a)) was chosen for the analysis of the I-V behavior.

To demonstrate that the I-V-behavior of the archetype device is not purely controlled by drift and diffusion mechanisms, known from the conventional p-n semiconductor diodes (see Chapter 1.4), the forward branch of the I-V-curve (Figure 4.6 (a)) was plotted on a semi-logarithmic plot, shown in Figure 4.18 (b). Superficially, the curve shows indeed an almost linear characteristic in the high bias range. The derivative shows no saturation at a constant value, as expected from the Schockley equation. Instead, it shows two local minima and increases continuously in the high bias range, which is typical for the trap-charge-limited transport behavior (Figure 1.13).

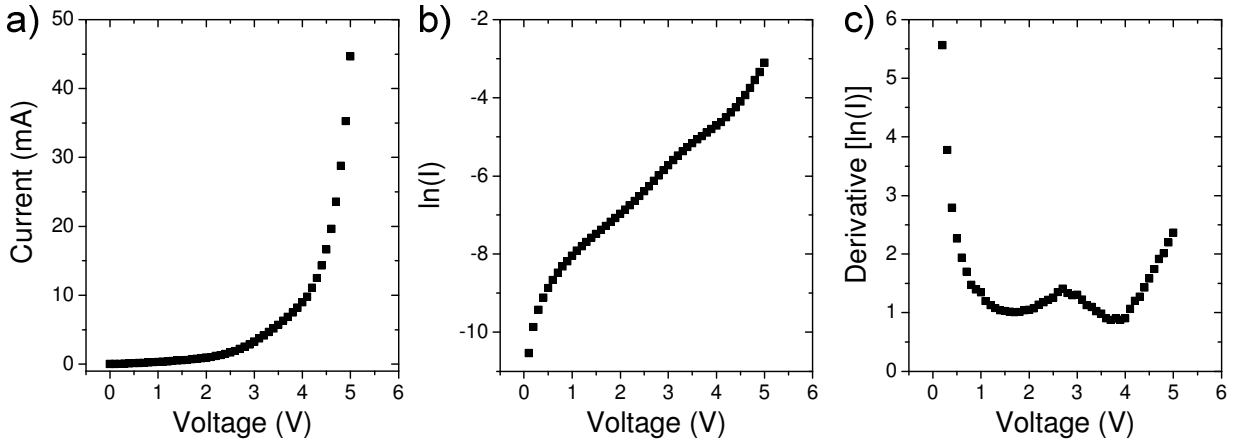

Figure 4.18: Typical forward bias I-V-behavior of the archetype ZnO NC-LED with ITO as a transparent electrode. (a) Semi-logarithmic plot (b) and its derivative as a function of applied voltage. (c)

Trap-charge- (TCL) and space-charge-limited (SCL) transport properties at high electric fields are frequently observed in nanocrystalline layers and networks as well as in isolators and wide-band-gap-semiconductors with a high amount of defects.[15, 16, 29, 60, 89, 100, 116, 137, 138, 258, 287, 289, 304, 305] To identify the effect of the space-

charge build-up on the transport properties of the ZnO NC layer, the I-V characteristic of the ITO archetype device under forward bias is plotted on a double-logarithmic scale in Figure 4.19 (a). The resulting curve can be approximated by a linear characteristic with a slope of 1 (green linear fit) in the low-voltage regime (below 1.3 V), indicating ohmic transport. At higher voltages, the power-law dependence due to the space-charge build-up in the NC-layer becomes dominant with an exponent of 4 (slope of the red line fit), changing to an exponent of above 11 at voltages above the onset of emission (4V).

According to the SCL conduction model (Chapter 1.4.2), an exponent above 2 identifies an exponential energy distribution of the trap states below the CB edge. The value of the exponent (reduced by 1) reflects the relation between the average energy of the corresponding traps and the thermal energy, thus the higher slope corresponds to the deeper traps (those energetically closer to the valence band) involved in the current transport. Similar behavior, i.e. a transition between multiple trap states, was also observed in ZnO nanocrystal LEDs with organic support layers.[29] The ohmic and TCL conduction regimes were also observed in ZnO NC-layers of the same material system from the identical nanocrystal batch in a different (planar) geometry, where the same exponent of 4 was correlated to traps with a density of ~10^{13} cm^{-3}, determining the conduction properties of the ZnO NC layers.[305] The first EL spectrum of the device was recorded in the transition region between "shallower" (slope of 4) and "deeper" traps.

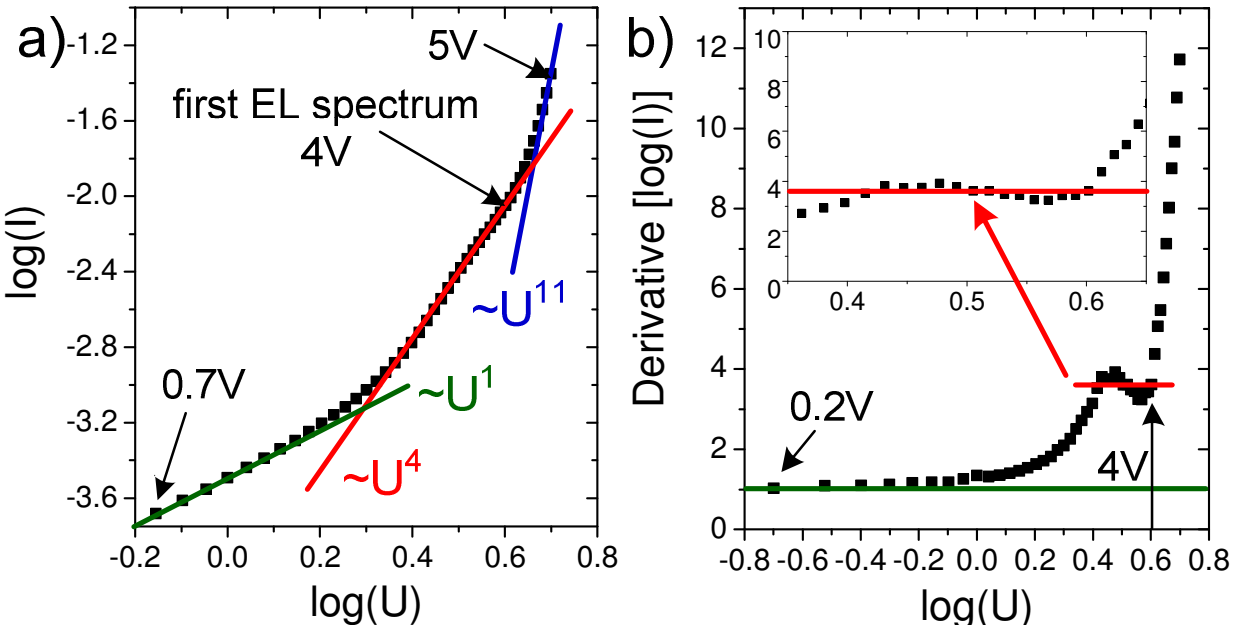

Figure 4.19: Double-logarithmic plot (a) and its derivative (b) of the typical I-V-behavior of the ITO archetype ZnO NC-LED under forward bias.

In order to confirm the contribution of at least two kinds of traps to the TCL behavior, the derivative of the double-logarithmic plot is shown in Figure 4.19 (b). The derivative shows a similar behavior as theoretically calculated for the case of "modeled" TCL ($I_{TCL}(U)$) with "shallower" (exponent of 4) and "deeper" (exponent >10) traps, determining the I-V-behavior (see Figure 1.11). The characteristic plateau in the transition range between both trap states is shown enlarged in the inset of Figure 4.19 (b). Besides, the derivative plot displays two interesting features. Firstly, the EL spectrum was detected at the beginning of the voltage range, when the contribution to the charge transport due to the "deeper" traps becomes significant. Also, in the transition (plateau) region the slope shows a clear decrease, while theoretically, based on solely TCL behavior, it should continuously increase, as can be seen in Figure 1.11. The only transport mechanism, which results in a continuous decrease in the I-V-slope on a double-logarithmic plot is tunneling, as can be seen from the theoretical plot of the different conduction mechanisms in Figure 1.15.

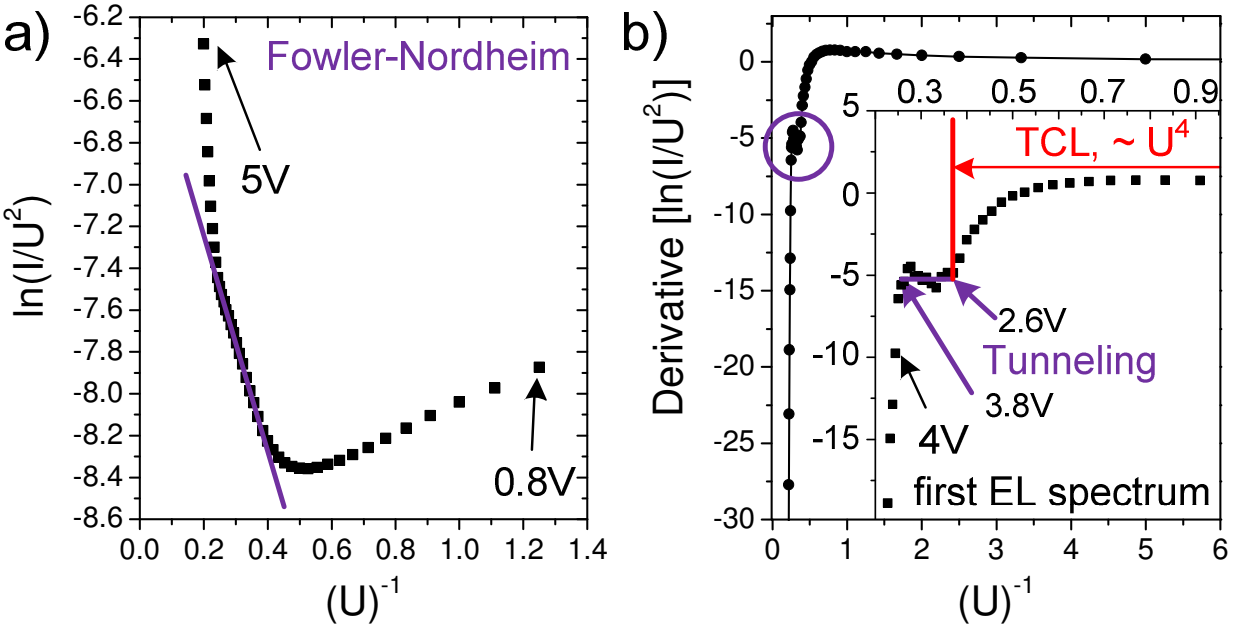

Figure 4.20: Fowler-Nordheim plot (a) of the typical I-V behavior of the ITO-based archetype ZnO NC-LED under forward bias, and its derivative (b,c,)

For a clear confirmation of the tunneling contribution to the I-V characteristics of the archetype device, the I-V curve is shown on a Fowler-Nordheim plot in Figure 4.20 (a) together with its derivative within the selected ranges (b). The shapes of the I-V curve on the FN-plot (Figure 4.20 (a)) as well as its derivative (Figure 4.20 (b)) are in general in agreement with the theoretically expected ones for TCL conduction (see Figure 1.16). Ohmic conduction, dominant at voltages below 1.3 V, can be confirmed by the increase of the derivative (see Figure 1.16). The steep decrease of the derivative at voltages

above 1.3 V is caused by TCL conduction ("shallower" traps, exponent of 4) dominating at voltages above 1.3 V over ohmic conduction, as shown in the inset of Figure 4.20 (b). A closer look at the region, marked in Figure 4.20 (b) by the violet circle and enlarged in the inset, reveals a clear constant derivative of the FN-plot in the range between 2.6 V and 3.8 V, which can only be explained by tunneling, dominating the I-V behavior in this range (see Figure 1.16), as already presumed from Figure 4.19 (b).

Tunneling arises in the voltage range where TCL current due to "shallower" traps is already very pronounced, so the tunneling through the possible energy barrier for the electron injection on the Al/ZnO interface (injection limited regime for the electrons from the Al electrode) can be disregarded. This assumption is realistic, since Al is experimentally known to form an ohmic contact to ZnO.[169, 306] Therefore, following origins of the tunneling contribution to the I-V behavior can be considered: tunneling through the double energy barrier at the NC boundaries (due to the formation of the depletion layer on the surface of ZnO NCs, see Figure 2.5 (b,c)) and tunneling of the electrons from the deep traps inside the ZnO band gap.

Tunneling through the double energy barrier at the NC boundaries would not explain the subsequent change back to the TCL behavior with a higher exponent and the onset of the defect-related emission as the applied voltage is increased. Instead, if the applied electrical field is sufficient enough for electrons in the conduction band to overcome the double barrier, a breakdown of the non-linear I-V characteristic with ohmic conduction through the CB can be expected.[235, 243]

On the other hand, the assumption of tunneling through the electron extraction barrier for the electrons from the deep traps is reasonable, since once the field is sufficiently high and the hole injection (electron extraction) limit is overcome, the first EL spectra can be detected and the dominating traps of TCL conduction change to the deeper ones (higher exponent). This can explain the significant rise in current at voltages below the actual emission onset, frequently observed in literature.[52, 281, 287–289] This possible origin is discussed within the following section in correlation with the electroluminescent properties of the archetype devices leading to the proposal of the possible emission mechanism.

4.5 Proposed Emission Mechanism

It is essential to understand the origin of the EL in a ZnO-only (single component) archetype device, as well as its electrical behavior and the correlation of both, to design efficient ZnO nanostructure LEDs. Despite some reports on EL in the visible and near-band-gap spectral range of different ZnO structures such as layers [287, 288], single crystals [289, 307], micropowders [308], microwire [281], nanowires [290], and nanotubes [52], all sandwiched between two electrodes, the emission mechanism of a ZnO-only (single component) device is still a puzzle.[281]

While for ZnO LEDs incorporating organic support layers, the direct electron and hole injection into ZnO is most frequently considered to be the origin of the EL, [58, 59, 29, 60] the role of this mechanism can be questioned in case of ZnO-only devices. In archetype devices, no other material is incorporated, except ZnO, to produce EL, and since ZnO is a naturally n-type semiconductor, [36, 37] there is also no other material to donate and transport holes as required for the conventional bipolar direct charge injection EL mechanism.[281] Few studies proposed the involvement of the ionization processes in the EL emission mechanism, such as impact excitation of electron-hole pairs by electrons injected from the electrode and accelerated by the applied electrical field.[281, 288, 289, 307, 309] However, electrical field strengths exceeding 10^6 V/cm are required for conventional ionization processes resulting in visible emission.[69] This condition is indeed fulfilled in case of some ZnO AC thin film EL-devices, [28] but when it comes to ZnO nanostructures under DC excitation, the average electrical fields are usually below 10^6 V/cm and still visible [279, 280, 310, 311] and UV [45, 52, 312] EL can be observed. The ZnO-only devices also have a non-linear I-V-characteristics under forward and reverse bias [281, 287–290] as well as a significant rise in current at voltages below the emission onset (significantly higher emission turn-on voltage than the electrical turn-on voltage of the device) [52, 281, 287–289] in common. In the following section a model explaining the observed electrical and emission properties is proposed by the correlation of the I-V- and voltage dependent EL behavior of the archetype ZnO NC-LED device, introduced in the previous sections.

In the model of rigid bands presented by Parker [292], the voltage drop across the active layer between the electrodes is assumed to be homogeneous. This assumption is a good approximation for isolating materials or semiconductors with a low doping

concentration. The photoluminescence and absorption measurements in Chapter 3 showed a strong evidence of high natural n-type doping of the order of 10^{19} cm^{-3} resulting from large amounts of shallow donor-type localized defect states close to the CB of ZnO. Ideally, such a high doping concentration would result in a predominantly ohmic behavior of the archetype devices under forward bias, which is not the case. This contradiction can be solved when the active ZnO layer is no longer approximated by the single crystal layer, but its nanocrystalline nature is also considered. As discussed in Chapter 2.2, a formation of a depletion layer on top of the ZnO nanocrystals within the active layer under ambient air conditions is very probable. The assumption of a typical energy barrier of ~1 eV [201, 236, 237] and a background doping concentration of 10^{19} cm^{-3} (as estimated by absorption measurements) would result in a depletion width of ~10 nm after equation (2.1.11), which is in good agreement with other estimated depletion widths in ZnO nanostructures.[41, 191, 201] Taking into account the average size of the ZnO NC of ~40 nm would mean that the NC is partly depleted, as sketched in the right part of Figure 2.5 (d). This would explain why the optical measurements show evidence of a high natural doping level (corresponding to the core of the NC) while the transport behavior is significantly influenced by depleted grain boundaries (TCL conduction).

The consideration of the depletion width leads to an inhomogeneous voltage drop within the NC layer, as schematically sketched in Figure 4.21. Thereby not only a voltage drop over the NC core has to be considered, but also an expected higher one over the grain boundaries between the NCs (as well as over the depletion layers).

Taking into account the model of Parker [292] and the field driven ionization mechanism of the EL emission in nanocrystals, introduced by Wood et al. [101, 124], and extending both to the simplified field distribution within the NC layer as well as the proposed defect structure of the ZnO nanoparticles, i.e. shallow and deep luminescent defect states within the band gap, the following origin of the EL emission in single-component ZnO devices can be suggested.

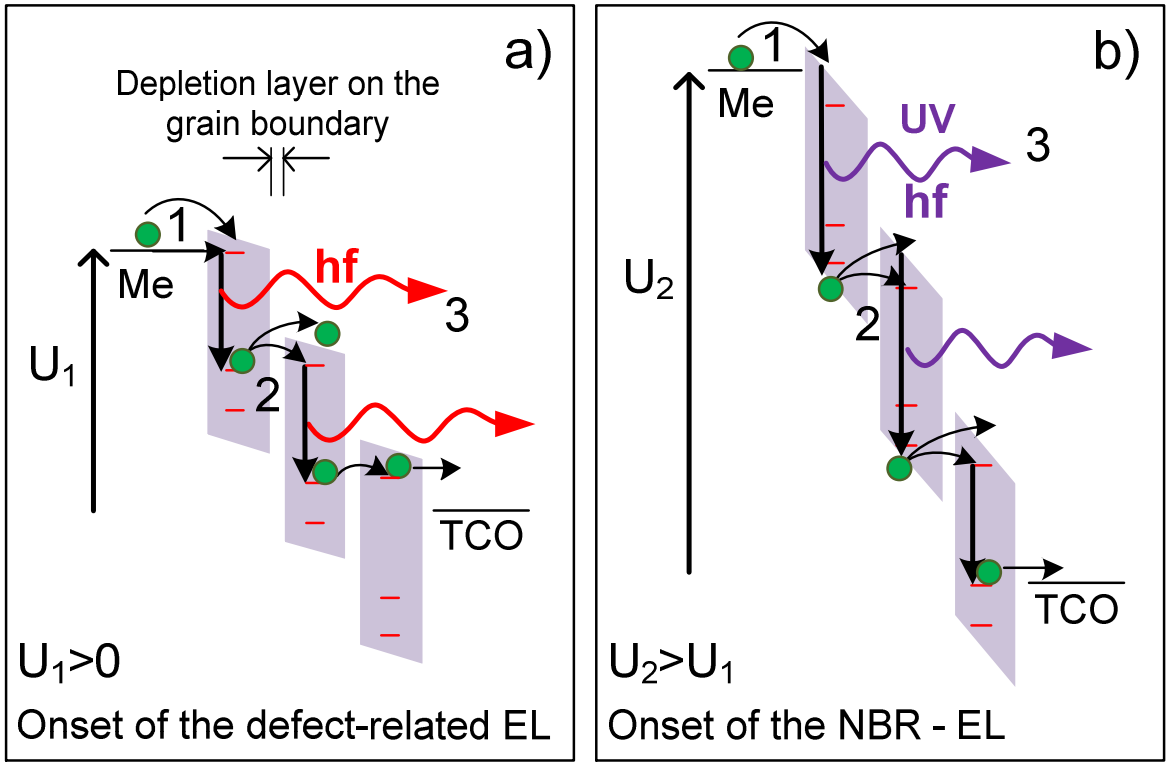

Figure 4.21: Simplified band energy diagram of the ZnO nanocrystal layer, sandwiched between a metallic (Me) and TCO electrode with the schematic of the shallow and deep traps of ZnO (a) under moderate forward bias indicating the defect-related emission onset, and (b) under high forward bias, showing schematically the emergence of the NBR-EL.

Under a moderate applied forward bias, electrons are first injected into the CB of ZnO or the available shallow trap states from the metallic (Me) electrode, as shown in Figure 4.21 (a), (1). In case of the Al electrode, the contact can be considered as ohmic, so a possible electron injection barrier can be neglected. The majority of the injected electrons are transported through the CB and the shallow traps to the TCO contact. Besides, electrons can be extracted from deep traps in ZnO to the shallow trap and free CB states (also those of the neighbor-particle) (2) by the applied field. The extracted electron leaves an unoccupied trap state behind (hole) which can be occupied by the electrons from the shallow traps or the conduction band. During this process a photon can be emitted (3), giving rise to defect-related EL emission. As the applied bias increases, the electrons from deeper defect states can be extracted, which enables the contribution of higher energy defect-related emission to the overall spectrum. At sufficiently high applied bias, electrons from the VB can also be extracted to the shallow trap states and the CB (Figure 4.21 (b), (2)), leaving a hole in the VB behind. The recombination of the (injected) electrons in the CB and shallow traps with the hole in the VB results in the near-band-gap contribution (3) in the UV spectral region. It should also be noted, that the defect and NBR EL due to impact ionization processes at

the grain boundaries can also principally contribute to the overall emission due to locally increased electrical fields.[236, 237, 243]

According to the suggested model, the electric field across the device also controls the emission color. Wood et al. demonstrated that a higher electric field needs to be applied across the device with green QDs to produce green EL compared to the device with red QDs.[124] Similarly higher field strength is required to extract electrons from the deeper traps and VB. From the proposed luminescent defect structure of the studied particles (Figure 3.20) the first emission that can be expected to appear under the applied voltage is in the red spectral range due to oxygen defects. As the voltage and consequently the strength of the applied electrical field increases, green and blue luminescent defects can be accessed as well as near-band-gap emission. The voltage dependent shape of the EL spectra, expected after the proposed model, was indeed observed, as shown in Figure 4.5 (a).

The extraction of electrons from the luminescent defect states and the VB is expected to take place predominantly via tunneling [101, 124, 292] and trap-assisted tunneling [313], whereby the current density equation for the latter is the same as FN tunneling with a height of the barrier ϕ_B corresponding to the trap barrier height.[313] Therefore, one can expect a linear I-V characteristic on the $\ln(I/U^2)$ vs. 1/U (Fowler-Nordheim, FN) plot. (see Chapter 1.4.1) On the other hand, the majority of injected electrons are transported by the CB and / or shallow traps over the ZnO NC layer without contributions to the EL of the device, determining decisively the I-V characteristics of the device.[292] In this case, the resulting I-V behavior is a superposition of the conduction properties of the active nanocrystal layer and the electron injection properties of the electrode (cathode).

Correlating the proposed defect structure (Figure 3.20), the EL emission (Figure 4.21) and the charge transport mechanisms of the device, it can be suggested that the electrons, injected under forward bias from the Al electrode travel through the ZnO NC layer over the CB states and shallow traps ($I \sim U^4$) to the TCO. At sufficiently high strength of the applied field across the NC layer, electrons can also be extracted by the conventional and trap-assisted tunneling from the deep traps and VB, giving a rise to the defect-related and near-band-gap EL of the device and changing the exponent of the TCL I-V curve ($I \sim U^{11}$).

Chapter 5

Si/ZnO Heterojunction NC-LEDs

In the previous chapter, first all-inorganic ZnO nanocrystal LED with low operation voltages and large-area white emission were demonstrated, emphasizing the potential of ZnO nanostructures for cost-effective ambient lighting applications. However, the fabrication of low-cost, inorganic LEDs based on ZnO nanocrystals remains ambitious mainly owing to its wide band gap and challenging hole injection.[49, 50, 58, 66, 45, 314] Analogously to QD-LEDs, the hole injection into ZnO nanocrystals can be realized by the incorporation of organic support layers.[50, 59, 60] These organic layers are usually sensitive toward oxygen and humidity, making an appropriate encapsulation essential for good device performance. A successful strategy to avoid encapsulation and produce air-stable devices is to combine ZnO with p-doped rigid substrates of, for example Si [64–66, 301, 315–317], GaN [53, 62, 63, 318–320], or NiO [54, 55, 309].

The utilization of rigid crystalline substrates significantly limits the device design and fabrication techniques. These limitations can be overcome by utilization of p-type nanocrystals. Here, all-inorganic and solution-processable p-Si / n-ZnO multiple-nanocrystal-layer LEDs are presented. They demonstrate warm white light with color rendering index (CRI) values up to 98. Boron-doped Si nanocrystals [321] were used as both hole injection and electron blocking layers while naturally n-doped ZnO nanoparticles [305] act as the active, light emissive layer. Efficiency enhancement was achieved by introducing a mixed p-Si / n-ZnO layer in the center of the active region in order to optimize the electron-hole balance. First proof-of-concept devices demonstrated good stability while being under constant operation for over two weeks in ambient air without any encapsulation.

The devices comprise multiple spin-coated nanocrystal layers, sandwiched between two conductive electrodes. A fluorine-doped tin oxide (FTO)-coated glass substrate serves as a transparent anode. The top evaporated Al contact is used as a cathode. The schematic of design A, where Si and ZnO layers are prepared one on top of the other forming separate layers is shown in Figure 5.1 (a).

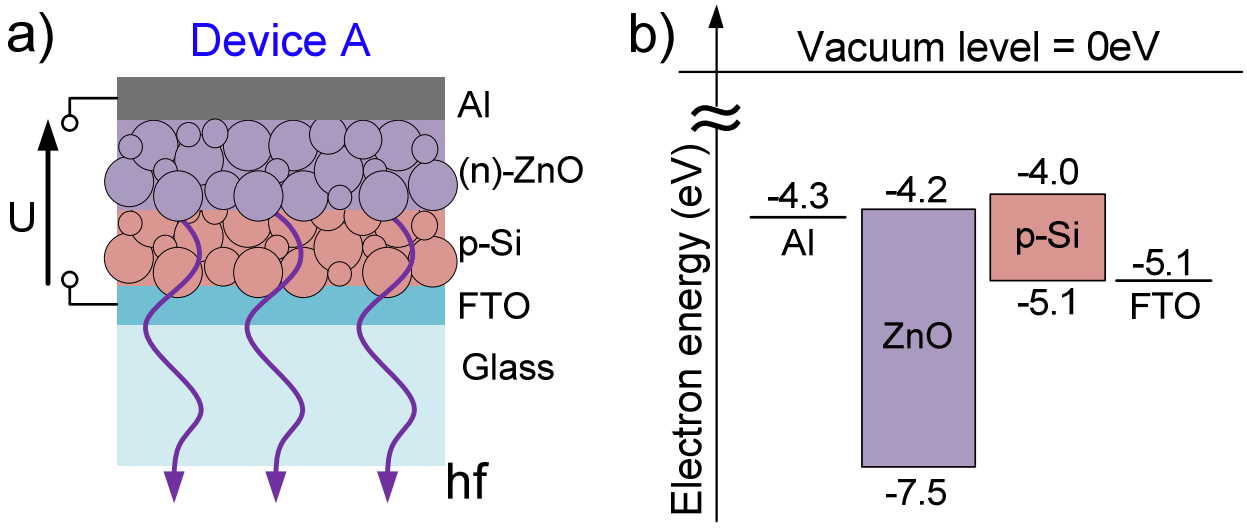

Figure 5.1: Schematic of the p-Si/(n)-ZnO NC double layer device design (device A) under forward bias.(a) Simplified energy band diagram of the involved materials.(b)

Figure 5.1 (b) shows the expected simplified energy band diagram of the involved materials based on the data from literature.[50, 322] Assuming direct charge injection under forward bias, electrons are predominantly injected into the ZnO conduction band, and the holes, via the FTO and the p-Si layer, into both valence band and defect states inside the band gap of ZnO. Afterwards, electrons and holes recombine resulting in band-gap and defect-related electroluminescence in the ZnO.[314]

5.1 Si Nanocrystal Layers

Boron-doped Si nanocrystals ($5 \cdot 10^{18}$ cm^{-3}) were fabricated by gas phase synthesis in a hot wall reactor.[323] Silane (SiH_4) was used as a precursor gas and diborane (B_2H_6) was added in the desired concentration as a dopant source. The resulting Si nanocrystals have a logarithmic-normal size distribution with a mean diameter of 20 nm, so that any luminescence of the Si nanocrystals due to quantum confinement effects can be excluded.[324] The overall doping concentration in the nanocrystals has been verified by glow discharge mass spectroscopy and inductively coupled plasma mass spectroscopy.[321] The nanocrystals were commercially dispersed and stabilized electrostatically in an ethanol solution without additives.

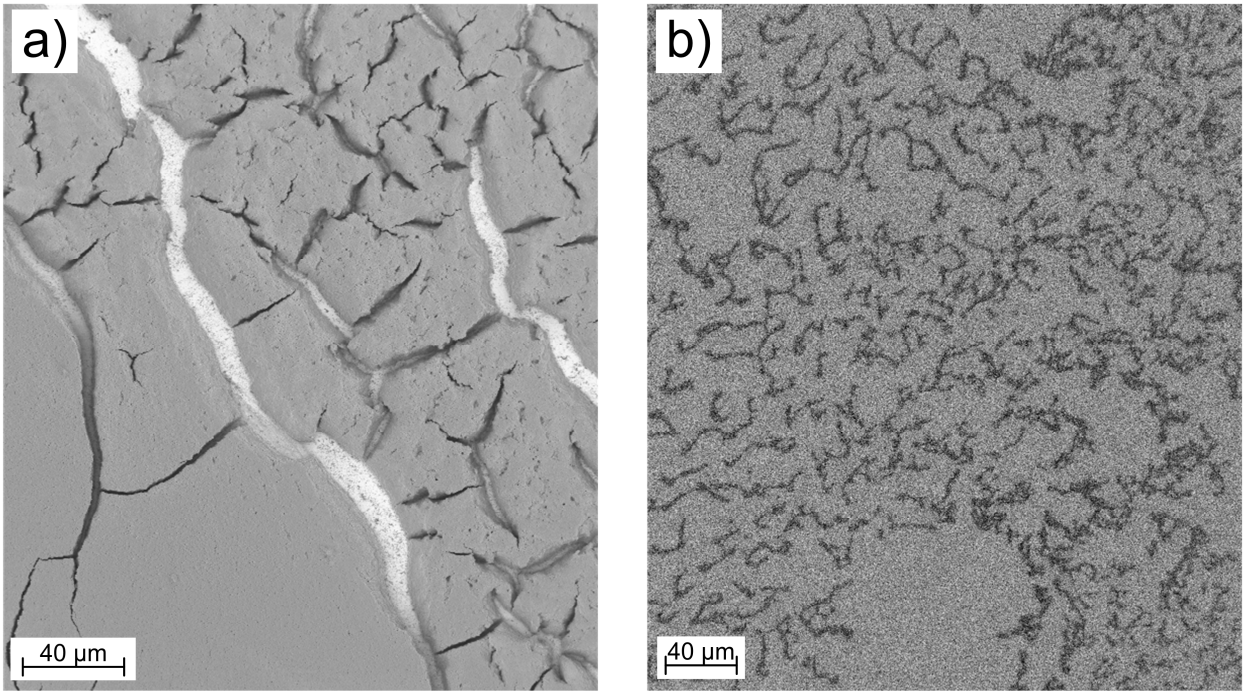

Figure 5.2: SEM images of the Si-NC layers from the as received ethanol dispersion (a) and a diluted ethanol dispersion (b).

Figure 5.2 (a) shows a typical SEM image of the Si-NC layers, spin-coated from the commercial dispersion. Due to high vapor pressure of the ethanol (compared to e.g. butyl acetate or water), the solvent evaporates very fast already during the drop-deposition of the dispersion and before the spin-coating procedure begins, leaving very little space for adjustment of layer thickness and morphology, compared to ZnO dispersions. To achieve smooth and dense Si-NC layers by spin-coating, the initial

dispersion needs to be modified. Figure 5.2 (b) shows a SEM image of the Si-NCs, spin-coated from a highly diluted (1/20) ethanol dispersion. Primary, as-synthesized particles are interconnected by solid sinter-bridges forming stable chains.[325] The formation of these sinter-bridges leads, despite high homogeneity and stability of the dispersions, to increased porosity and inhomogeneity of the spin-coated layers even if the NC-concentration and spin-coating parameters are optimized.

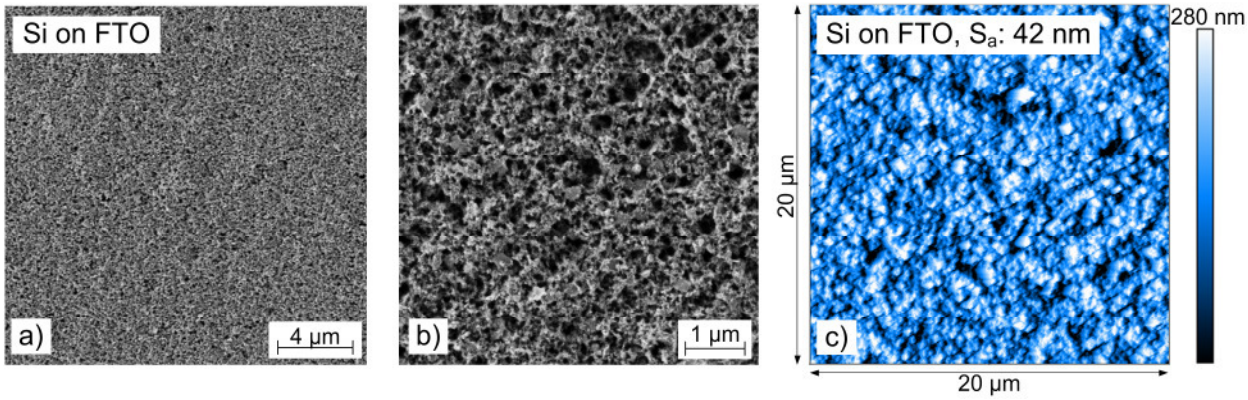

Figure 5.3: (a) SEM image of the Si NC layer on top of the FTO substrate, (b) close-up on the Si NC layer and (c) AFM image of the Si NC layer with the resulting average surface roughness of 42 nm.

Figure 5.3 (a) shows exemplarily a SEM image of the ~100 nm thick Si-NC layer spin-coated on top of the FTO substrate from the ethanol dispersion with an optimal NC load (dilution 1/3) at optimized spin-coating parameters of 10 s at 2000 rpm. A SEM close-up of the layer (Figure 5.3 (b)) shows the high porosity of the Si-NC layers, resulting in a high average roughness of ~42 nm, as measured by the AFM-scan (see Appendix A1) of the layer (Figure 5.3 (c)).

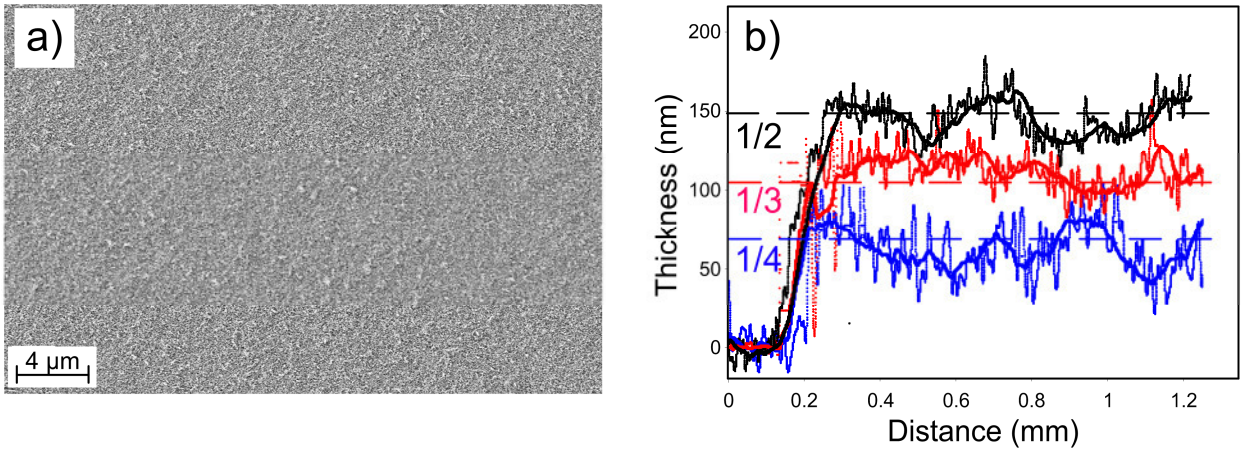

Figure 5.4: (a) SEM image of the spin-coated 100 nm thick Si NC layer on top of the FTO substrate. (b) Surface profiles of the Si NC layers spin-coated on top of the FTO substrate at identical parameters from the ethanol dispersions with low (1/2, black) middle (1/3, red) and high (1/4, blue) grade of dilution.

High porosity and roughness of the Si layers also limits the control of the thickness of uninterrupted layer down to ~100 nm (Figure 5.4 (a)). Although thinner layers can be fabricated by a careful adjustment of the Si-NC concentration, trench-free layers can be no longer guaranteed. Figure 5.4 (b) shows surface profiles of the three different Si-NC layers spin-coated at the same parameters from the diluted ethanol dispersion (see Appendix A2), whereby the dilution ratio of 1/2 corresponds to the thickest layer (black, ~150 nm) and the lowest NC load (dilution ratio of 1/4) to the thinnest one (blue, ~70 nm). The average thickness (solid line) varies significantly over the measured distance and, in the case of 70 nm layer due to the additional roughness of the FTO substrates, trenches through the nanocrystal layer can't be ruled out.

5.2 Si/ZnO Bilayer NC-LEDs

The fabrication of multiple nanocrystalline layers on top of each other, especially in a solution-based approach, introduces new challenges concerning the deposition techniques and, more importantly, the choice of the solvents.[326] For example, water-based ZnO dispersions completely dissolve the underlying Si-NC layer during the spin-coating step. Butyl acetate-based ZnO dispersions showed a good compatibility with Si-NC layers from the ethanol dispersions, so after the spin-coating parameter and NC load optimization (see Appendix A2), first nanocrystalline p-Si/(n)-ZnO multilayers could be realized. Thereby, the top ZnO-layer, exemplarily shown in Figure 5.5 (a), partly evens out the roughness of the underlying Si layer remaining homogeneous and densely packed, as known from ZnO-only devices.

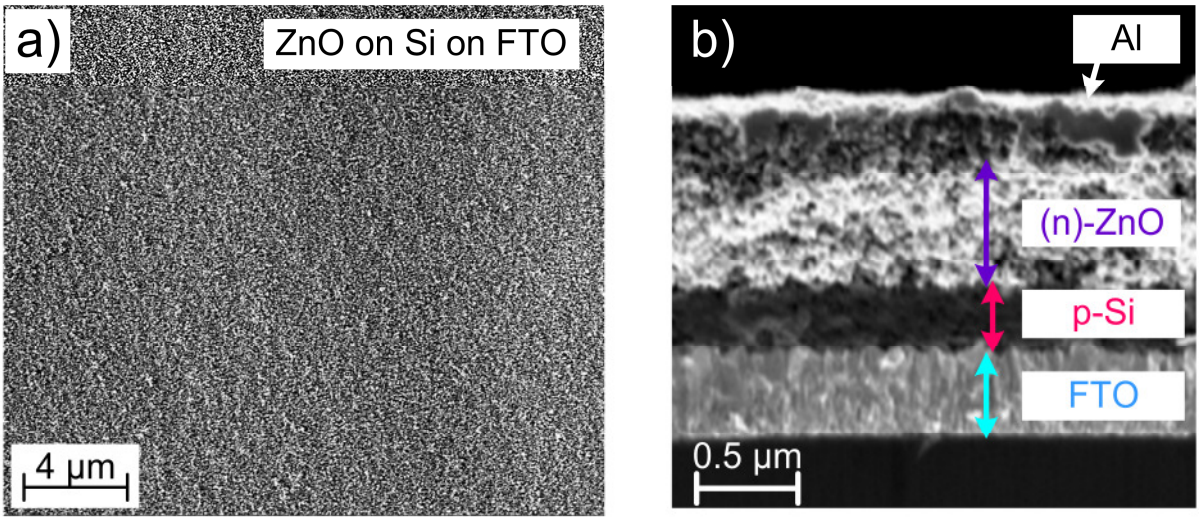

Figure 5.5: (a) SEM image of the ZnO NC layer on top of the spin-coated Si NC layer. (b) Cross-sectional SEM image of the device structure A.

p-Si/(n)-ZnO nanocrystal multilayers spin-coated on top of a cleaned, UVO-treated FTO-glass substrates were dried for 1 hour at 150°C under nitrogen flow to remove the solvent residues and improve the luminescent properties of ZnO nanocrystals. A nitrogen atmosphere was chosen in order to avoid the additional oxidation of Si nanocrystals, taking place in oxygen-containing atmospheres. After the soft annealing step, a 250 nm thick Al top-electrode was evaporated through a 3 mm round shadow mask. Figure 5.5 (b) shows an exemplary scanning electron microscopy (SEM) image of the layer stack of device design A. In this particular device, the thickness of the

nanoparticle layers was chosen to be slightly larger than that of the devices discussed below, for better contrast between the individual nanocrystal layers. It is obvious that the multilayer nanoparticle stack is well defined and has a low porosity and no obvious shortcuts or trenches. The thickness of the nanoparticle multilayers was measured with a surface profiler to 750 nm and confirmed from the cross-sectional SEM images of the layer stacks.

5.2.1 I-V behavior of the Si/ZnO bilayer devices

The I-V behavior of the multilayer devices is discussed in the following section based on 400 nm and 750 nm thick devices of type A, representing exemplarily the typical features of the I-V curves and correlating them to the emission properties. Similar results are also observed in all the other tested devices of type A. Especially devices with a total thickness below 600 nm show very unstable behavior under reverse bias with dielectric breakdown at low voltages. Therefore, only the forward-biased characteristics could be reliably studied in devices with different thicknesses. To exclude changes due to the self-annealing during operation or possible degradation of the devices, the I-V curves were measured on pristine devices with identical settings. The corresponding EL spectra were measured simultaneously.

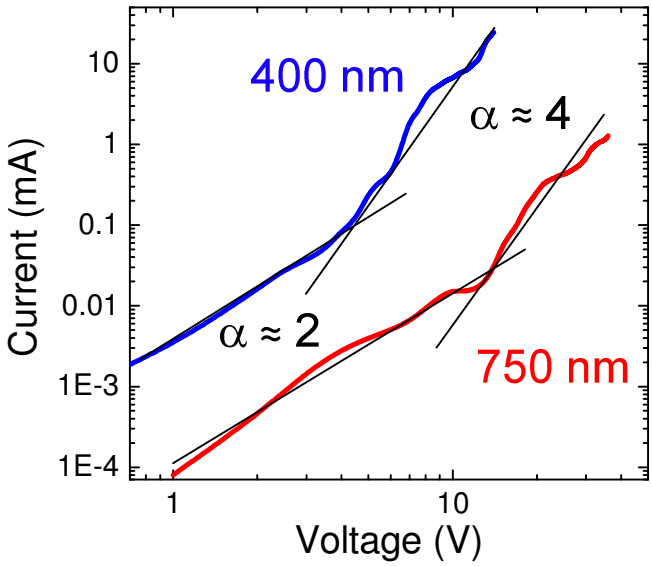

Figure 5.6: Double-logarithmic plot of the I-V curves of the 750 nm thick (red line) and 400 nm thick (blue line) pristine (n)-ZnO / p-Si NC multilayer devices.

Figure 5.6 shows typical I-V curves of the 750 nm (red) and 400 nm (blue) thick p-Si/(n)-ZnO NC heterojunction devices of type A on a double-logarithmic plot.

Superficially, both I-V curves show a typical TCL conduction behavior with higher currents through the device at comparable voltages, when the thickness of the layer stack is reduced. In the low-voltage regime, the I-V curves are quite well approximated by the power-law dependence with an exponent of 2. This can be an indication of shallow traps (that is traps, lying close enough to the CB to be in thermal equilibrium with electrons therein).[136] At higher voltages the behavior can be approximated by the TCL conduction with an exponent of 4. Similar behavior has been observed in other nanocrystal LEDs.[100, 116]

On the other hand, the two I-V curves show significant deviations, especially at higher voltages, from the corresponding asymptotes on the double-logarithmic plot, which was not observed that strongly in case of ZnO-only devices.(see Figure 4.19 (a)) The behavior at high electric fields shows multiple regions of fast increases in current ("steps"), followed by "plateaus" of almost ohmic to SCL conduction behavior with a slope between 0.7 and 2. Interestingly, both "steps" and "plateaus" occur at similar average field strength for both devices, indicating fundamental field-dependent mechanism influencing the device characteristics.

The experimental data could not be fitted by the thermionic emission model. For possible explanation of the I-V behavior at high voltages in terms of tunneling of charge carriers, the Fowler-Nordheim (FN) plot of the data was applied, as shown in Figure 5.7 (a). The I-V characteristics of both devices, plotted on the FN-plot over the inverse average electric field, show ranges of linear behavior (indicated by the green dotted lines), characteristic for tunneling of the charge carriers. Moreover, in case of both devices, one can clearly distinguish between two kinks (peaks, followed by plateaus or valleys) and a subsequent increase of the current, which can be fitted by a linear characteristic within the FN-plot. There is one recent report on similar behavior in NC / organic hybrid LED by Son et al. [89], whereby "plateaus" on the double-logarithmic plot, which show deviations from the TCL behavior, were observed as well. The possible proposed explanation for this phenomenon was the capturing of the charge carriers by the nanocrystals, which results in the reduction of the tunneling current.[89]

In the present case, the kinks occur at similar applied electric fields in devices with different layer thickness, indicating that the corresponding energy barriers are correlated with the choice of the material system. The slight deviations between the exact values of the field strength might be due to the average thickness deviations of +/- 50 nm within the nanocrystal layer stack due to e.g. absence or presence of an

additional nanoparticle with a wide size distribution between 10 and 100 nm as well due to the inhomogeneous field distribution within the NC layer.

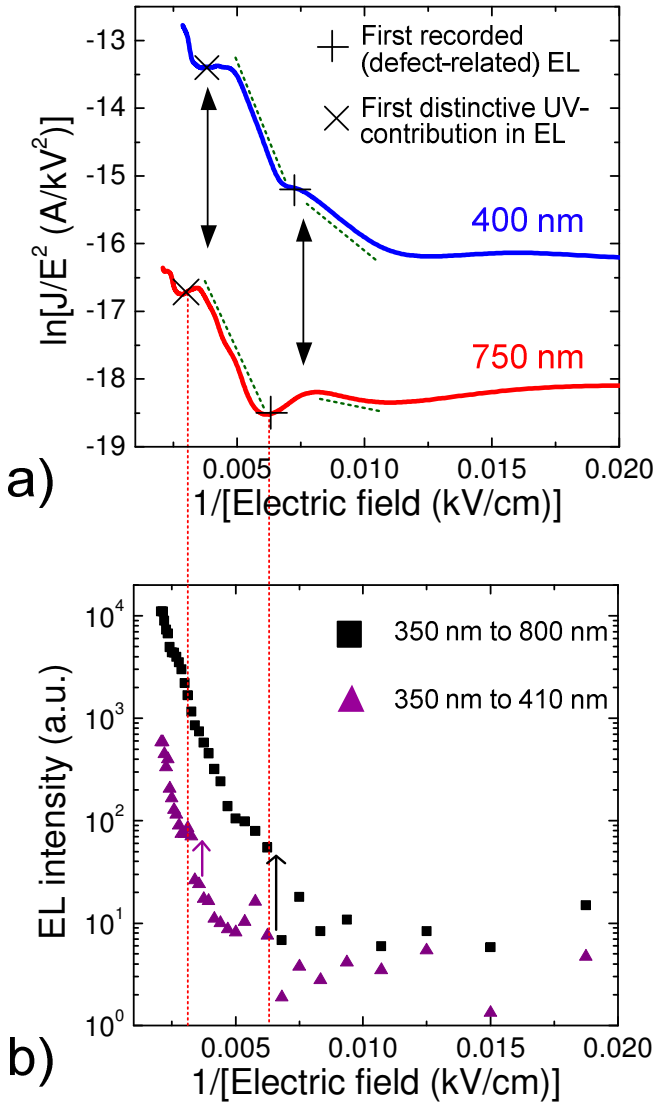

Figure 5.7: (a) Fowler-Nordheim plot of the I-V curves of the 750 nm (red line) and 400 nm (blue line) thick, pristine devices of type A. Onset of defect-related and UV EL in both devices are marked by "+" and "x" respectively. (b) Integrated EL intensity in UV (violet triangles) and UV and visible spectral range (black squares) of the pristine 750 nm thick device, plotted on a semi-logarithmic plot as a function of the inverse average applied electrical field.

In addition to the correlation of the kink position between the devices with different thickness, a correlation between the kinks and the EL properties of the devices was observed. Figure 5.7 (b) shows the overall EL intensity (black squares) and the intensity of the emission in the near-band gap range (violet triangles) on a semi-logarithmic plot as a function of the inverse average applied electric field for the case of 750 nm thick device. The first detected EL spectrum with an intensity significantly higher than the background noise, was detected right after the first pronounced kink. At higher

voltages, the emission intensity increased continuously, remaining defect-related with a negligible background contribution in the UV range. Right after the second pronounced kink the emission in the UV range showed a significant increase and the corresponding EL spectra showed a distinctive peak in the UV region, related to the NBR emission of ZnO nanocrystals. Analogously, the onset of the defect-related and UV emission were determined for the 400 nm thick device and the corresponding data of the I-V curves was marked for both devices as a "+" and a "x" on Figure 5.7 (a) respectively. Similar to the archetype-devices, a sufficient electrical field needs to be applied to extract the electrons from the defect states by tunneling. The emptied states can be populated, resulting in TCL conduction. The onset of defect-related as well as NBR EL always corresponds to the transition range between ohmic and TCL conduction (around the "peak" of the slope) and always takes place after the tunneling, as was the case for archetype devices (see Figure 4.20). The fact that this transition takes place at similar average applied fields once again supports the field-related origin of the emission.

5.2.1 Emission properties

The electroluminescence spectra of the ~750 nm thick spin-coated p-Si/(n)-ZnO heterojunction under forward bias are shown in Figure 5.8 (a). Pronounced EL spectra could be detected starting at ~10 V.

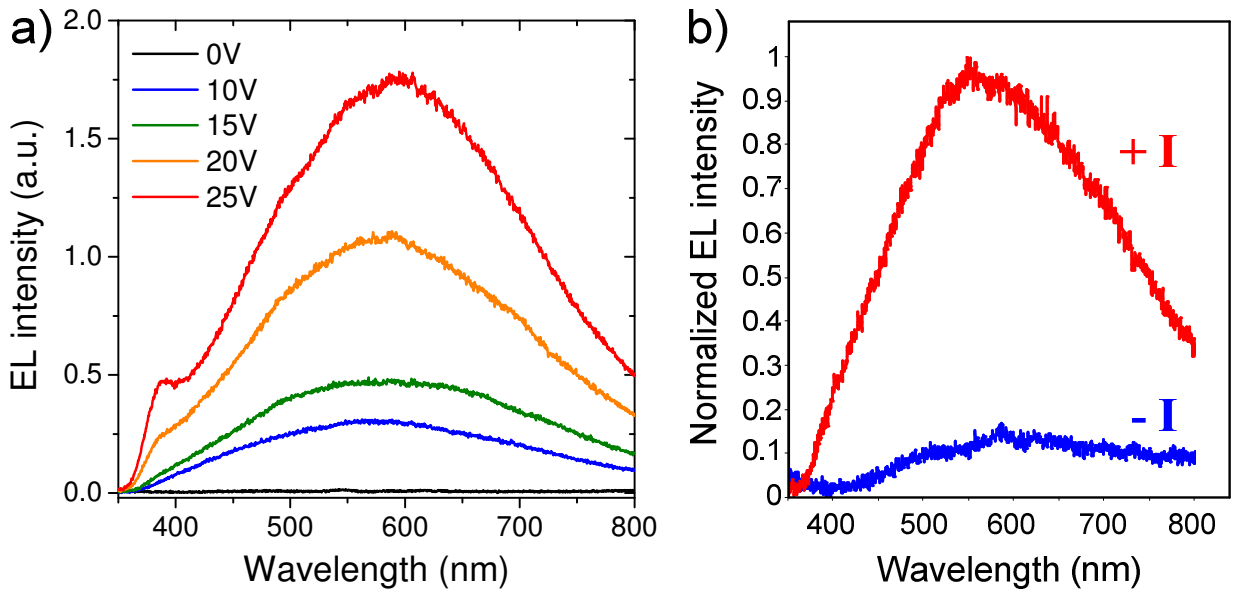

Figure 5.8: (a) EL spectra of the 750 nm thick Si/ZnO nanocrystal heterojunction LED of type A. (b) Exemplary plotted EL spectra of the device at the same operation current of 2.4 mA under forward (red, +I) and reverse (blue, -I) bias conditions.

The overall emission properties of the device are very similar to those of ZnO-only devices (see Chapter 4) with constant intensity increase and the relative increase of the contribution from the high energy transitions in blue and UV range as the applied voltage increases. The NBR-contribution in the UV range becomes distinct at voltages above 20 V. The device showed similar to ZnO-only devices, EL both under forward (+I) and reverse (-I) bias, as exemplarily shown in Figure 5.8 (b) whereby both spectra correspond to the injection current of 2.4 mA.

The integrated intensity of the EL emission under forward and reverse bias is shown in Figure 5.9 as a function of the current through the device (a) and as a function of the applied voltage (b). While in case of ITO-based ZnO-only archetype devices, no measurable difference was observed (see Figure 4.6 (b)) and FTO-based devices demonstrated twice as high ratio of the EL intensity under forward vs. reverse bias (see Figure 4.15), the introduction of the p-Si nanocrystal layer increased this ratio by about an order of magnitude. So, it can be concluded that the p-Si hole injection (electron extraction) layer significantly enhanced the efficiency of the device under forward bias, as compared to reverse. The overall reduction of the current through the device compared to archetype devices is attributed to the increased thickness of the overall nanocrystal layer stack and poor conductivity of the Si NC layer.[321]

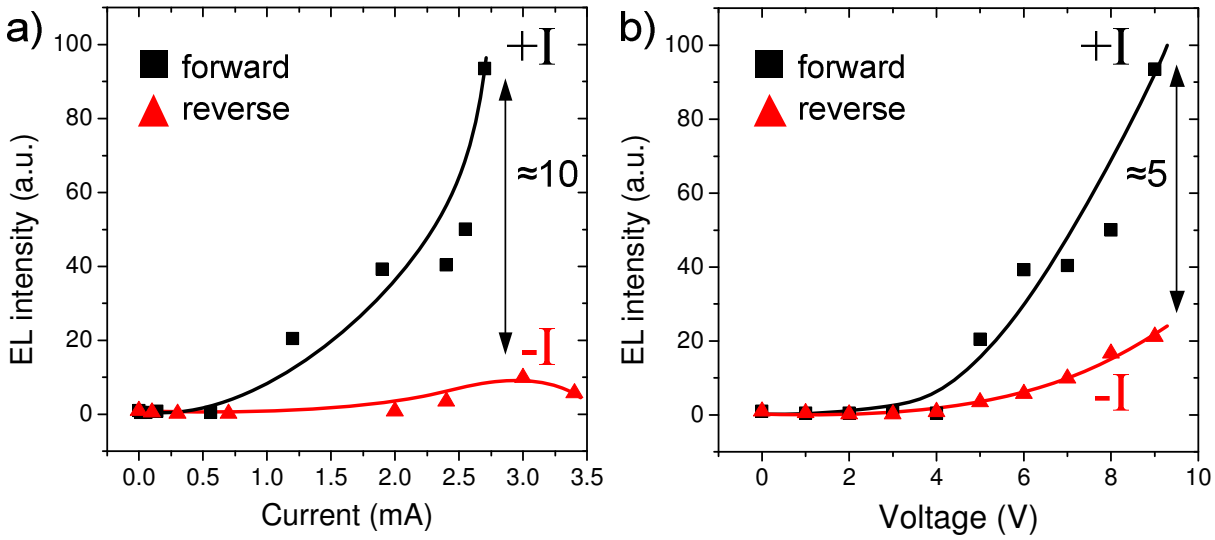

Figure 5.9: Integrated EL intensity of the 750 nm thick device type A forward-biased (black squares, +I) and reverse-biased (red triangles, -I) as a function of the injected current (a) and applied voltage (b).

The overall maximum emission intensity was ~1.5 times weaker than in the case of ZnO-only device at the same operation voltages. Mainly this can be attributed to the reduced current densities through the device due to the insufficient transport of the charge carriers through the nanocrystalline multilayers because of the high device

thickness. Another reason might be also the partial absorption of the emission through the Si layer. The thickness of the Si-layer was about 300 nm. Assuming a perfect 300 nm thick single Si crystal layer and literature data of the absorption coefficient (~$3 \cdot 10^4$ cm^{-1} and ~$3 \cdot 10^3$ cm^{-1} in the UV and visible spectral range, respectively) [125], about 10% of the emitted light would be absorbed in the visible range and about 60% in the UV range. Considering the porosity of the Si layer, about 40 % absorption in the UV and below 6 % in the visible spectral range can be expected.

To improve the device performance, the total thickness of the layer stack was reduced down to 400 nm with the Si layer being 100 to 150 nm thick. The device (further called "device A") showed very unstable behavior under reverse bias with a dielectric breakdown at very low voltages (~5 V), prohibiting systematic studies of the forward-reverse EL ratio behavior. However, the EL behavior under forward bias improved significantly.

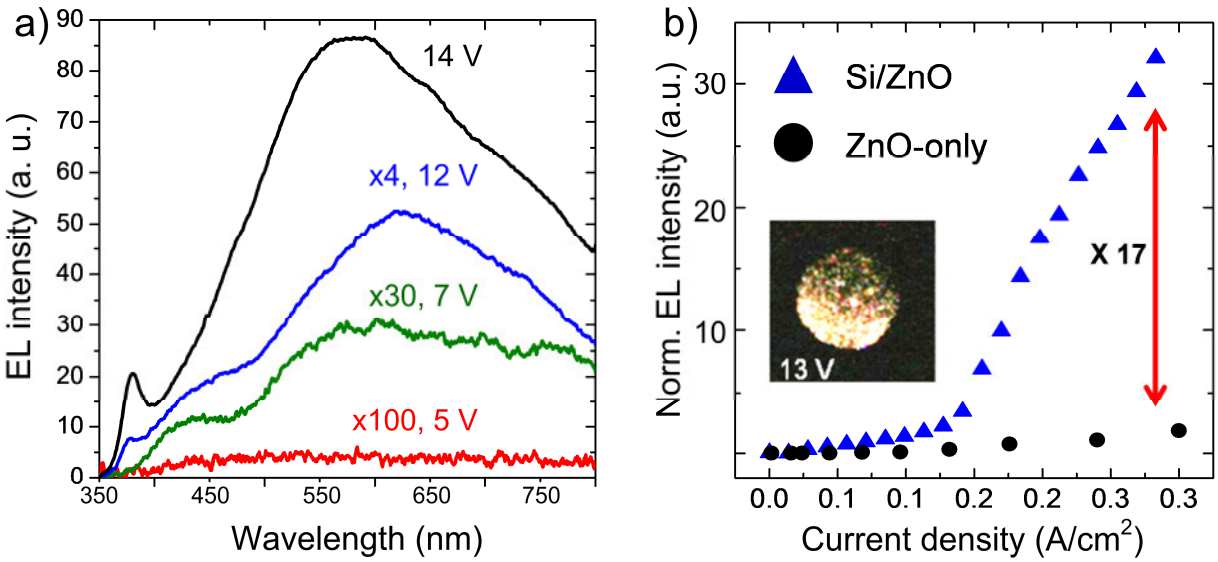

Figure 5.10: (a) EL spectra of the device A under forward bias of 5 V (magnified by a factor of 100), 7 V (magnified by a factor of 30), 12 V (magnified by a factor of 4), and 14 V with the corresponding current densities of 0.03, 0.05, 0.18, and 0.24 A/cm². (b) EL intensity of the ZnO-only device (black spots) and device A (blue triangles) as a function of the operation current density. The inset shows an EL image of the device A at 13 V operation voltage.

The turn-on voltage of the defect-related emission was reduced to ~5 V and the distinct NBR-peak in the UV range was observed at voltages of 12 V and above, as shown in Figure 5.10 (a). At low voltages, the EL mainly covers the red spectral range with slight contributions of the green and blue bands. This is attributed to an efficient extraction of electrons from the defect levels within the band gap, which facilitates defect-dominated EL, especially at low voltages. As the voltage increases, the overall

emission intensity is enhanced and the contribution of blue defects and near-band-gap emission increases. At 14 V, the contribution of the near-band-gap emission in the UV range becomes very pronounced. The overall emission from device A appears white, distributed over the whole electrode and visible to the naked eye, as shown in the inset of Figure 5.10 (b). The spectral characteristics of device A are very similar to those of reference devices without the p-Si layer.(see Figure 4.14 (a))

In Figure 5.10 (b), the spectrally and spatially integrated EL intensity is plotted as a function of the injection current density for the p-Si/n-ZnO heterojunction device (blue triangles) and a pure ZnO reference device (black spots), discussed in Chapter 4.3.3 (Figure 4.15). Impressively, the EL intensity of device A is about 17 times higher than that obtained for the reference ZnO nanocrystal LED at comparable current densities. Thus, it can be concluded that the introduction of the additional p-Si nanocrystalline layer significantly improved the device efficiency, emission intensity and homogeneity as well as the efficiency of the electron extraction from the deep defect states under the forward bias.

However, when discussing the clear role of the p-Si NC layer in the achieved LED improvements, the presence of the defect states within the Si NC-network and a possible formation of new defect states on the Si/ZnO interface should be considered. In addition, Si NCs are known to be covered by a few (typically 1 to 2) nm thick natural silicon oxide shell (SiO_x).[324, 325] This natural oxide shell is also present inside the multilayer devices, since their fabrication took place under ambient air conditions and the SiO_x shell was not removed by additional etching steps. Consequently, this oxide shell can also very likely act as a barrier for the charge carriers to pass the nanocrystal multilayer. The key importance of an insulating layer for the efficient generation of the EL in ZnO / p-Si LEDs was also demonstrated for ZnO film- [64, 316, 327, 328] and ZnO nanowire / nanorod- [56, 66, 314] LEDs.

The observed improvement of the asymmetry of the EL emission under forward vs. reverse bias is also in agreement with the presence of the SiO_x-blocking layer similarly to the observations for QD-LEDs, operated by field-driven ionization.[101] Under forward bias, the electrons are blocked after their injection into the active ZnO layer. Thereby, they are confined to the active layer and slowed down, so that the recombination probability with the holes, created by the electron extraction from the defect states and VB by high electric field across the interface, increases. Under the reverse bias, the extraction of the electrons from the VB and defect states by the Al electrode has the same efficiency as in case of reverse-biased archetype devices, while

the electron injection is hindered by the SiO_x layer. The electrons are blocked before they can enter the active layer.

Taking into consideration the electron blocking properties of the SiO_x shell, the efficient emission is expected to take place predominantly close to the interface between the ZnO and Si nanocrystals, which is only a small fraction of the ZnO NC layer. To improve the device performance by effective increase of the interaction area between Si and ZnO nanocrystals, an innovative design of interpenetrating nanocrystal layers was developed. This approach and the improved device performance are going to be introduced in Chapter 5.3

5.3 Si/ZnO Multilayer NC-LEDs

As in nanoparticle layers, limited charge transport is expected due to scattering at the interfaces and, in the case of p-Si, due to the isolating oxide shell, we adopted the design of interpenetrating n- and p-layers well-known from organic solar cells and photodiodes.[329] The idea behind was to increase the interaction area (active interface region) among n-ZnO and p-Si nanoparticles by inserting a nanocrystal mixed layer in between the thin p-Si and n-ZnO nanocrystal layers and thereby improve the device performance.

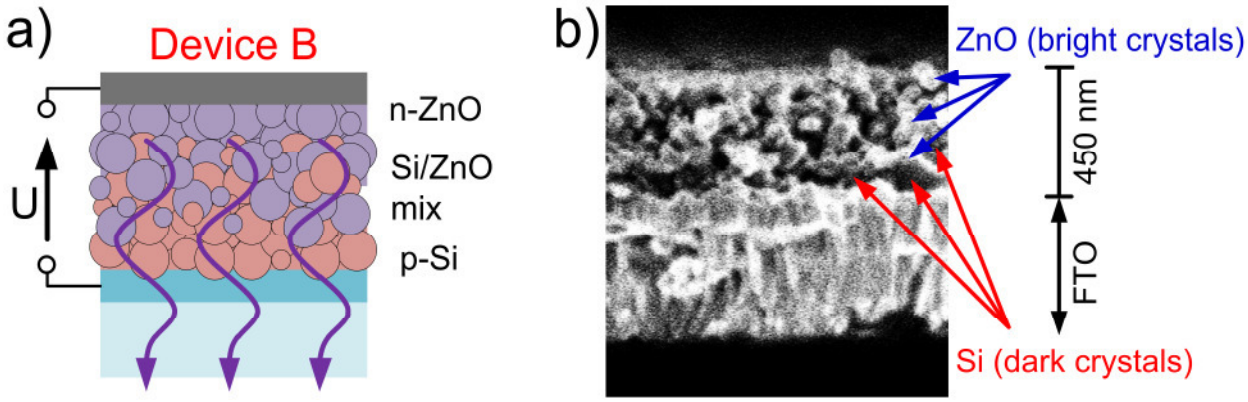

Figure 5.11: (a) Schematic of the device B under forward bias. (b) Cross-sectional SEM image of the NC layer stack of the device B.

The structure of the corresponding device B is schematically depicted in Figure 5.11 (a). The fabrication process of the device B, up to the deposition of the second nanocrystal layer, was the same as in case of device A. For the Si/ZnO mixed layer, a new dispersion was prepared (see Appendix A2). In a first step, ZnO powder (exactly the same as in the case of the butyl acetate dispersion) was dispersed in ethanol by ultra-sonication (Bandelin Sonopuls HD 2070, 6 h 70 % power and 70% cycle). This solution was mixed with the ethanolic Si nanocrystal dispersion and again sonicated for 1 hour. The resulting mixed dispersion was spin-coated on top of the Si nanoparticle layer at 2000 rpm, whereby a part of the Si-only layer was removed during the spin-coating. ZnO nanocrystals in butyl acetate at a slightly lower concentration as in case of device A were then spin-coated on top at 4000 rpm. The thickness of this nanocrystal layer stack was measured to be on average 450 nm. Figure 5.11 (b) shows the cross-sectional SEM image of the resulting layer stack. No clear contrast between dark Si and bright ZnO nanocrystals can be observed. This implies a good intermixing between

both nanocrystal species with bright spots coming from ZnO nanocrystals and dark ones from Si, respectively. After finishing the spin-coating steps, device B was treated in exactly the same way as device A: it was dried at 150°C for 1 hour under nitrogen flow to avoid additional oxidation of Si nanoparticles and finally, a 250 nm thick Al electrode was thermally deposited on top of the layer stack through a 3 mm pin-hole shadow mask.

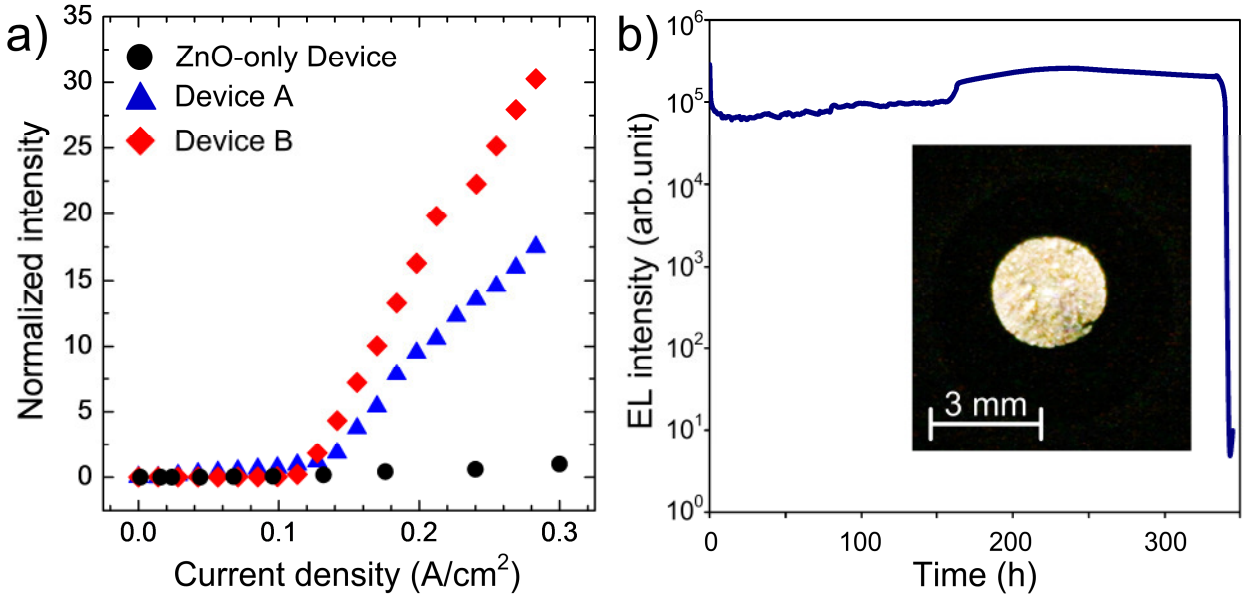

Figure 5.12: (a) EL intensity of the ZnO-only device (black spots) and devices A (blue triangles) and B (red diamonds) as a function of operation current density. (b) Plot of the integrated intensity of the device B as a function of time during the operation at constant 20 mA. The inset shows an EL image of the device B at a current density of 0.28 A/cm^2.

Figure 5.12 (a) shows the EL intensity of the device A (blue triangles) and the device B (red squares) as a function of current. Apparently, the ratio between emitted photons and the amount of charge carriers flowing through the device, i.e. the efficiency, almost doubled from device A to device B. Similar data obtained on further devices demonstrate an average 2- to 4-fold improvement in efficiency for the devices of design B as compared to design A. Also, the emission intensity of the devices of type B was strong enough to be monitored by a calibrated Si-photodiode (see Appendix A1), so that the external quantum efficiency (EQE) of the devices could be determined to be on average $1 \cdot 10^{-5}$%, which is already of a similar order of magnitude as white EL devices with comparable CRI values based on ultrasmall CdSe QDs [26], although low compared to state of the art OLEDs. Here, one has to keep in mind that no EQE values were so far reported for LEDs, where ZnO acts as the active material [68]. The measured EQE in type-B- devices can be party explained by the internal quantum efficiency of 0.2 % measured for the ZnO nanocrystals, used in the following work,

which is more than two orders of magnitude less than state-of-the-art CdSe/ZnS core-shell QDs. However, it should be noted that the defect related emission of ZnO-nanocrystals can be as efficient as 20% - 45% in optimized nanocrystals, which shows the potential for further improvements.[41, 42]

Interestingly, device B also demonstrated exceptional robustness without encapsulation in ambient air. Figure 5.12 (b) shows the room temperature EL intensity of device B at constant current of 20 mA over the time. Within the first 2 hours of operation, the EL intensity decreased slightly and then remained constant for the following 6.5 days. This decrease in intensity was correlated with a voltage drop from 19 V to 15 V. We attribute this behavior to the formation of local shortcuts, which lower the applied voltage and thereby reducing the emission intensity. After 6.5 days the device recovered almost to its primary intensity. The voltage also recovered to 19 V, therefore we believe that the local shortcut, responsible for the intensity drop, was annealed or interrupted after a while. After about 330 hours of operation, the intensity started to decrease and finally dropped down until the EL almost completely disappeared. The device showed at all times a large area EL emission over the 3 mm device. This can be seen in the inset of Figure 5.12 (b), where a photograph of the EL emission at 19.8 V and 20 mA is shown. Note that the slightly inhomogeneous emission observed is most probably caused by the roughness of our FTO substrate as well as size and shape variations of the used nanocrystals, thus causing local field inhomogeneities and consequently a local variation of the emission intensity.

The EL spectra of the device B showed a contribution in the UV range, comparable to device A, as can be seen from the Figure 5.13 (a). The defect-related emission, however, exhibited a red-shift, which might be an indication of additional defect states at the interface between ZnO and Si nanocrystals.

Since all the devices demonstrated white large area emission, Commission Internationale de l'Eclairage (CIE) color coordinates (see Appendix A2) of the EL spectra were evaluated to compare the emission color characteristics of the devices. The results are summarized in Figure 5.13 (b) with blue, red and black spots representing device A, device B and a reference ZnO-only device, respectively. The highest emission correlated color temperature (CCT) of 4570 K, which is close to daylight (5000 K), was achieved at 14 V with device A, which, however, exhibits the lowest corresponding color rendering index (CRI) of 92. The overall color characteristics of the device A is very similar to the reference ZnO-only device (black spot), as the EL emission stems from the ZnO layer only. The emission color characteristics of device B is slightly

different (red spots). We obtain CRI values up to 98, while the CCT matches very well the color temperature of standard light bulbs (2700 K to 3300 K), indicating "warm white" emission. This low CCT might be due to an enhanced hole injection into low energy defect states or due to additional luminescent low-energy defect states at the interface between p-Si and n-ZnO, as suggested by the EL spectra (Figure 5.13 (a)).

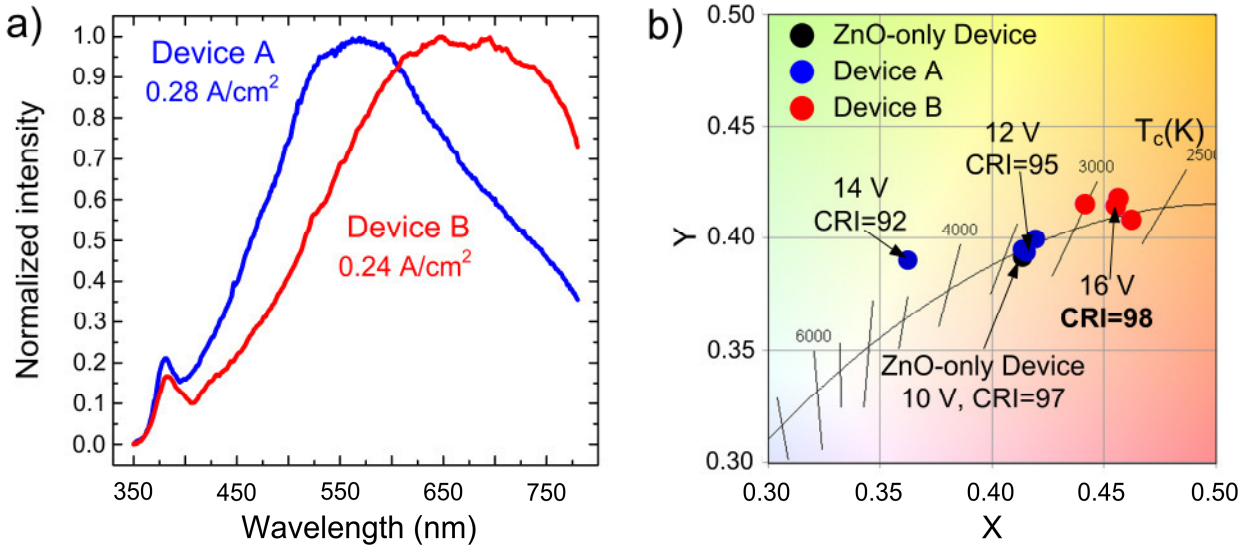

Figure 5.13: Normalized EL spectra of devices A (blue) and B (red) at the same current density of 0.28 A/cm². (a) Enlarged CIE color coordinates as well as CRI and CCT values of the EL from the devices A (blue spots, 11-14 V operating voltage) and B (red spots, 14-19 V operating voltage) in comparison to a ZnO-only device (black spot). (b)

In summary, all-inorganic large-area light emitting devices based on p-Si / n-ZnO nanocrystal multilayers were fabricated. Most importantly, the nanocrystal hetero-junction approach exhibits a significant efficiency enhancement as compared to a pure ZnO reference device, which is further improved by designing the active layer as an intermixed nanoparticle network. The devices showed correlated color temperatures between 2600 K and ~ 4600 K and a color rendering index of up to 98 is achieved. The exceptional robustness of the device, being under operation for more than 2 weeks under ambient air conditions without any encapsulation, can be attributed to the choice of the materials and all-inorganic approach. Besides, the involved materials are environmentally friendly and can be produced in large amounts at low costs and, in addition, the device fabrication is quite easy and can be adapted to large areas, thus making the findings interesting for future robust large-area and low-cost ambient lighting applications.[330]

Chapter 6

WO_3/ZnO Heterojunction NC-LEDs

Metal oxide materials and nanostructures have recently gained a lot of interest because of their unique properties envision a wide variety of potential applications.[68, 331, 332] These materials show not only superior chemical, thermal and morphological stability under ambient conditions, but they also can be synthesized and deposited at low costs.[68, 326] One of the main reasons for the high scientific attention is related to their tunable electronic properties. By additional doping or variation of synthesis conditions, these materials can cover the whole range from isolators over semiconductors to almost metallic conductors, retaining their transparency in the visible range.[68, 331] While transparent conductive oxides (e.g. In2O3 doped with Sn (ITO), F-doped SnO2 (FTO), Al-doped ZnO (AZO) etc) are widely commercially applied, e.g. in displays, solar cells etc. [331], the application of semiconducting oxides as active material in light emitters, solar cells or transistors is subject of intensive research.[68] Recently, an assembly of different metal oxide nanocrystals in a multilayer by a spin-coating approach was demonstrated, though without a functionality.[326]

In this chapter, a white light emitting device using an all-metal-oxide mixed nanocrystal multilayer approach is demonstrated. The robust oxide nanocrystal WLEDs are realized by combining naturally n-type luminescent ZnO nanocrystals with metal oxide nanocrystals acting as a natural electron extractor (hole generator) (here WO_3).[333] While sputtered WO_3 layers have already been demonstrated to be an efficient hole injector in green and blue quantum dot (QD) LEDs [113] and organic LEDs (OLEDs) [334, 335], it was not used in combination with ZnO so far. In order to optimize the electron-hole balance, the active layer was designed as an intermixed layer of WO_3 and ZnO nanocrystals as introduced in Chapter 5 (design B). The first devices

show highly uniform large-area white emission with color rendering index (CRI) of 92 and correlated color temperature (CCT) between 3700 K and 4200 K and an external quantum efficiency up to $2 \cdot 10^{-4}$ %.

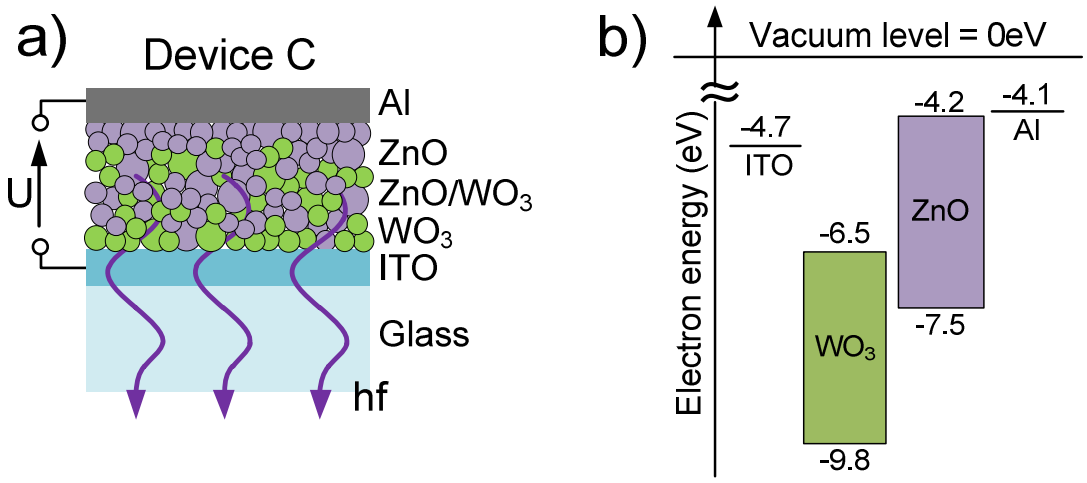

Figure 6.1: Schematic of the device design C. (a) Simplified band diagram of the device C, based on the values for the involved materials known from literature.[15, 108, 335]

In the chosen device architecture, shown in Figure 6.1 (a), the device consists of a stack of spin-coated nanoparticle layers embedded between ITO and Al electrodes. The underlying idea is that naturally n-type ZnO nanocrystals act both as electron transport [16] and luminescent [45] layer and WO_3 nanocrystals are used as a hole generation (electron extraction) and transport layer [68, 335]. WO_3 was demonstrated to be a naturally n-type semiconductor with a band gap of ~3.3 to 3.4 eV and an extremely high work function of ~6.27 to 6.5 eV.[113, 333, 335–337]. In the present device architecture, the deep-lying CB of WO_3 NCs is expected to extract electrons from the deep defect and VB states of ZnO, thereby creating a "local p-doping" of the ZnO NCs and hence improve the emission properties of ZnO NC-LED. To increase the electrical field across the device, the overall thickness of the NC layer stack was reduced from ~450 nm in case of Si/ZnO devices down to ~100 nm. Hence, ITO was chosen as a transparent electrode due to its low surface roughness compared to FTO.

6.1 Fabrication of a WO_3/ZnO Heterojunction

ZnO nanocrystals (VP AdNano ZnO 20) were used both as powder and butyl acetate dispersion. WO_3 nanocrystals, also synthesized in the gas phase, were purchased from SkySpring Nanomaterials Inc, (8010CN) in powder form. Figure 6.2 (a) shows a typical SEM figure of the as-purchased WO_3 NC powder. The NCs show quite wide size distribution with an average particle size of ~90 nm.

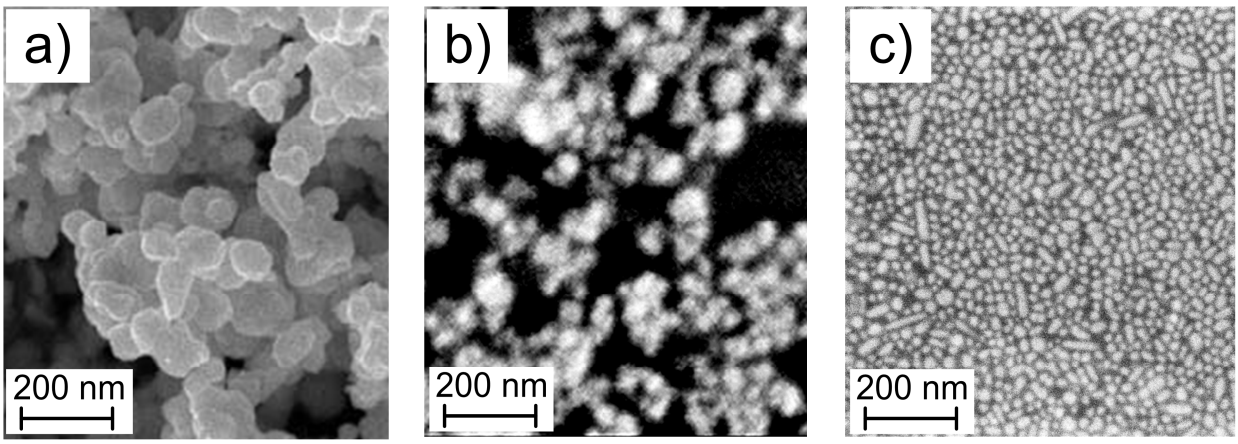

Figure 6.2: SEM images of the WO_3 NC as purchased (a) and WO_3 (b) and ZnO (c) NC layers, spin-coated from ethanol and butyl acetate dispersions respectively on the ITO substrates after the centrifuge step.

In order to reduce the total thickness of the NC layer stack, the average size of the WO_3 and ZnO nanocrystals should be significantly reduced from ~90 nm and ~40 nm, respectively. Smaller particles with a narrow size and shape distribution are expected to result in more homogeneous and densely packed layers. In Chapter 3.3.3, a successful approach to narrowing the size distribution and reduce the mean diameter of the nanocrystals synthesized in the gas phase by the centrifuge step was demonstrated. This technique was also applied to both NC types to fabricate a thin and homogeneous WO_3/ZnO NC layer stack.

For this purpose, in a first step, 6 wt% each of ZnO and WO_3 ethanol dispersions, were prepared by 7 hours sonication of the nanocrystal powder in ethanol. In the second step, both dispersions were centrifuged for 2 min at 10.000 rpm, resulting in Dispersions A (ZnO) and B (WO_3). During centrifugation, agglomerates and large nanocrystals were separated from small primary particles, resulting in a narrow size distribution with an average diameter of ~40 nm (WO_3) and ~20 nm (ZnO), respectively

(see Figure 6.2 (b, c) and Figure 3.9 (b)). Dispersions A and B were subsequently mixed in a 1:1 ratio by a short sonication, forming Dispersion AB. The commercial ZnO butyl acetate dispersion was also centrifuged at 20.000 rpm for 2 min resulting in Dispersion C. Please note that the luminescent properties of the active ZnO nanocrystals were also significantly improved by the centrifuge step as well as the ratio of the extended Zn_i states, as showed in Chapter 3.3.3.

For the fabrication of the WO_3/ZnO NC-LED, the cleaned ITO substrate (Thin Film Devices, 20 Ω/sq) was first treated in oxygen plasma for 5 minutes to further reduce its work function.[338, 339] In the first step, a WO_3 nanocrystal layer was spin-coated at 2.000 rpm on top of the ITO substrate from the ethanol-based Dispersion B. Figure 6.2 (b) shows the SEM image of the resulting layer, which is not dense showing high fraction of the uncovered ITO substrate (dark regions). In order to increase the interaction area between the ZnO and the WO_3 nanocrystals and thereby enhance the amount of holes generated in the ZnO, the second layer was fabricated from a mixed ethanol Dispersion AB containing both ZnO and WO_3 nanocrystals. The Dispersion AB was spin-coated at 2000 rpm on top of the first layer, partly dissolving it and thus creating a good intermixing. Finally the last ZnO nanocrystal layer from the butyl acetate Dispersion C was spin-coated at 4.000 rpm on top. In this case, a different solvent was used in order to prevent the mixed layer from being dissolved. Indeed, the last ZnO layer showed a complete coverage of the substrate, as shown on a reference layer in Figure 6.2 (c). The thickness of the resulting layer stack was measured to be as thin as ~80 to 100 nm over a 1 cm x 1 cm spin-coated layer. Finally, a 150 nm thick Al top electrode was deposited through the shadow mask, forming 2 mm x 2 mm electrodes. The whole fabrication process, except the top Al electrode deposition, was performed under ambient air conditions. The devices were stored and measured under ambient air conditions as well without any encapsulation.

.

6.2 WO_3/ZnO NC-Heterojunction LED

The devices were tested only under forward bias to prevent them from fast dielectric breakdown under reverse bias. The electroluminescence (EL) spectra of the device C at different applied forward voltages are shown in Figure 6.3 (b). No PL from WO_3 nanocrystals under the same and higher excitation conditions as in ZnO was observed. Therefore the EL of the device can be solely attributed to ZnO nanocrystals. First detectable EL with an almost negligible intensity starts at ~8 V with a contribution in the NIR spectral range. As the applied voltage increases, the charge injection into deeper trap states becomes possible resulting in increasing red and green emission, and at higher voltages also blue contributions. The characteristic ZnO near-band-gap emission (black arrow) below 400 nm is similar to ITO-archetype devices quite weak and less pronounced, compared to the emission in the visible range and can be observed at voltages above 12 V. Though all defect related transitions, identified by the PL measurements (marked by colored arrows in the Figure 6.3 (a)) can also be observed in EL, the intensity ratio among them is quite different, significantly changing the shape of the EL spectra. This voltage dependent behavior of the EL as well as the quite different emission spectrum, compared to PL (Figure 6.3 (a)) is quite common for ZnO LEDs and was observed earlier in layer [285, 286], nanowire [38, 44, 53, 54] and nanocrystal LEDs (see Chapter 4.2).

The Commission Internationale de l'Eclairage (CIE) 1931 color coordinates of the EL, shown in Figure 6.3 (d) were calculated from the corresponding EL spectra.(see Appendix A1) The position in the color space is very close to the back body curve. At all voltages, a high CRI of 92 was obtained, which is quite close to the CRI of incandescent lamps (100) and is significantly higher than the CRI of "cool white" fluorescent lamps (62). Furthermore, the correlated color temperature (CCT) of the emission shifts from 3700 K to 4200 K with the applied voltage, as can be seen in Figure 6.3 (c) and is in between a "warm white" of light bulbs (3200 K) and "daylight" imitation of fluorescent lamps (4500 K), which are the most popular emission colors for the ambient lightning applications.

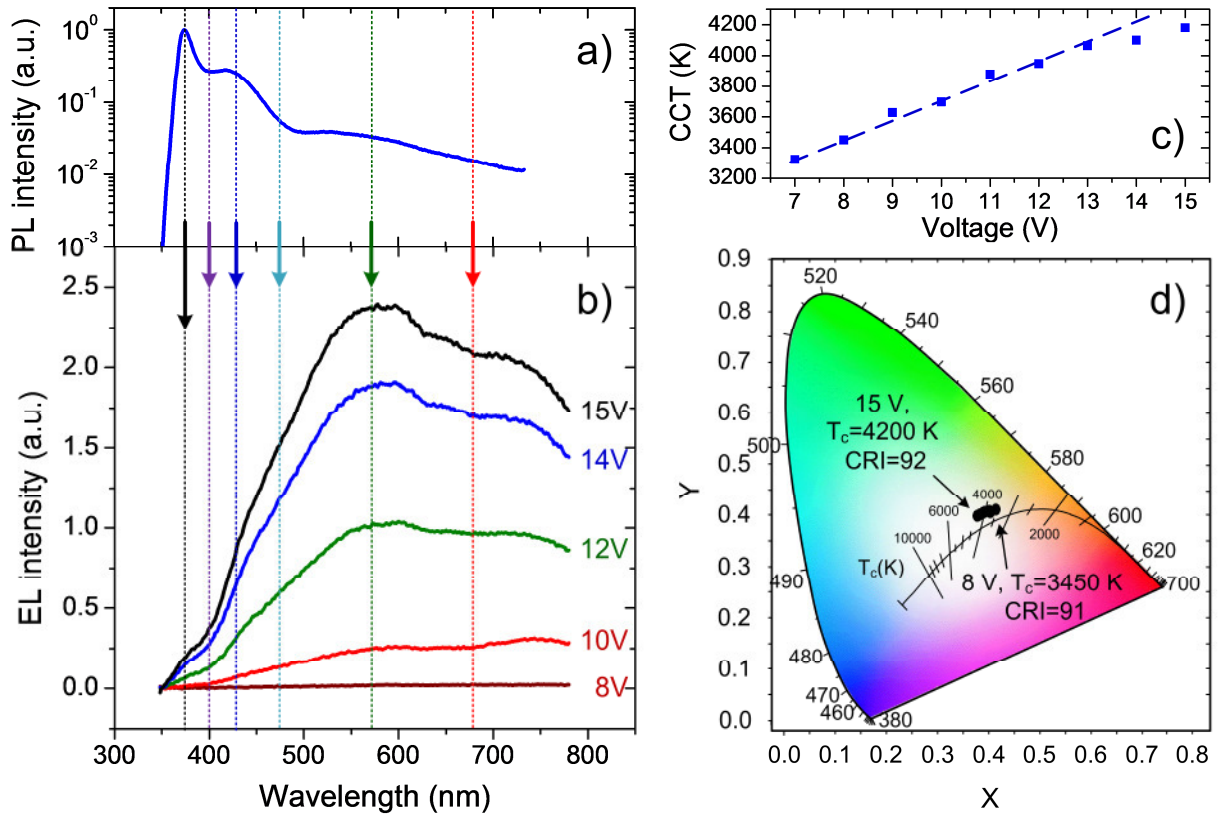

Figure 6.3: (a) PL spectrum normalized to the NBR emission peak of the centrifuged ZnO NC layer. (b) EL spectra of the device C at different driving voltages. (c) Correlated color temperature (CCT) of the EL as a function of the applied voltage. (d) Calculated position of the LED emission in the CIE color diagram at 8 to 15 V with corresponding CCT and CRI values.

The current density through the active device area (4 mm^2) versus the applied voltage is shown in Figure 6.4 (a). Figure 6.4 (b) shows a double logarithmic plot of the current density over the applied bias to demonstrate the trap limited conduction in the device. At voltages below the emission threshold (~8 V) the curve follows first the almost ohmic conduction with $J \sim V^{1.3}$, which is quite typical for nanocrystal devices.[15, 16, 100] As the voltage increases, the electron extraction from the defect states takes place and the emptied traps start to be filled by the injected electrons from the contact, resulting in a noisy behavior between 1.2 and 7 V. After the EL threshold (above 8 V) the current is proportional to V^{11}, which is a sign of trap limited conduction, similar to ITO-based archetype devices. The operating current densities are quite similar to other nanocrystal LEDs.[101, 109, 113]

The corresponding non-linear behavior of the EL intensity as a function of applied voltage is shown in Figure 6.4 (c). The onset voltage of the pronounced EL of the device was measured to be around 8.5 V by a calibrated Si photodiode.

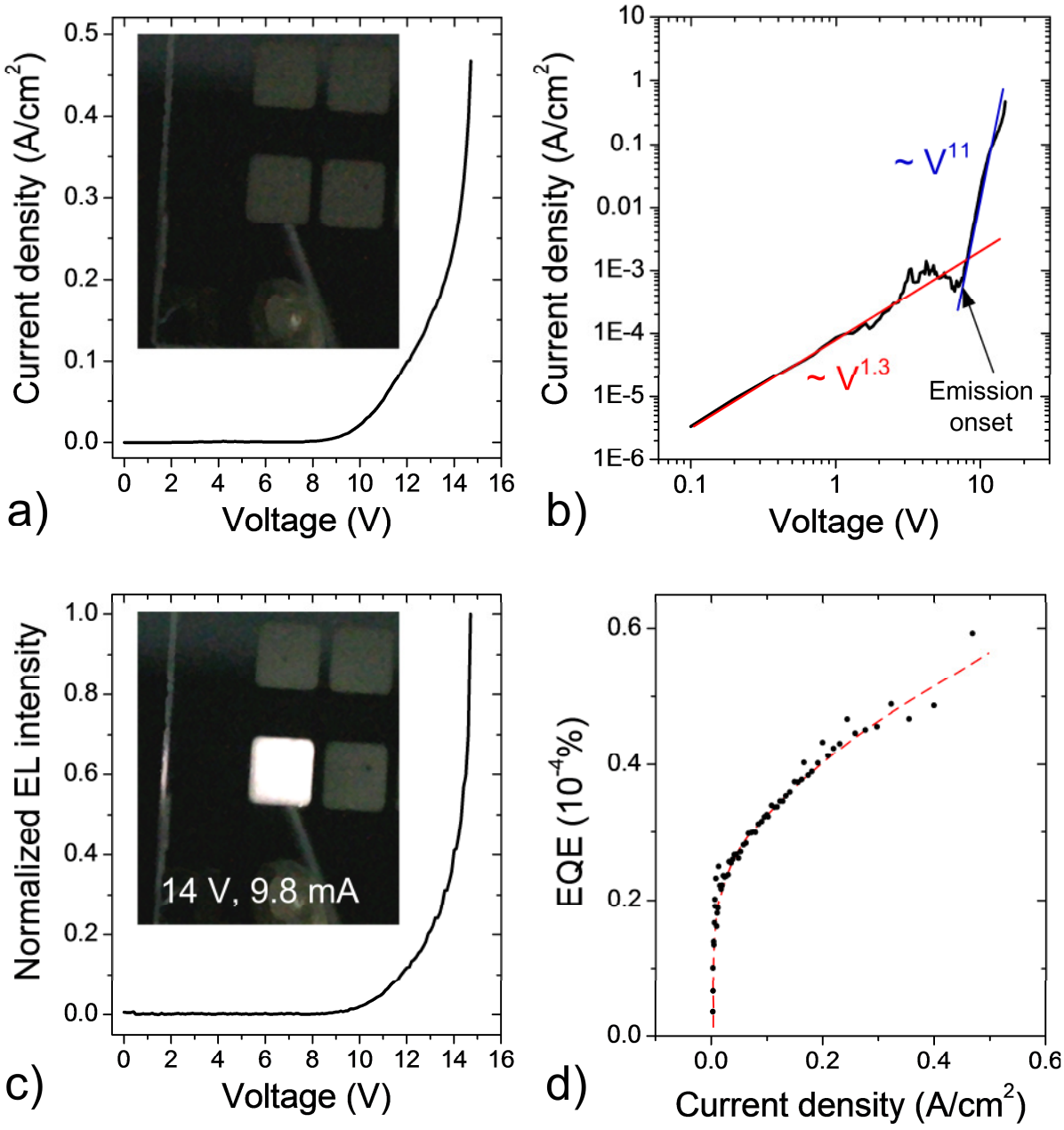

Figure 6.4: (a) Current density versus applied voltage characteristics of the device C. The inset shows a photograph of the device in an off-state (0 V). (b) Double-logarithmic plot of the current density versus the applied voltage. (c) Normalized EL intensity of the LED as a function of the applied voltage. The inset shows a photograph of the 2 mm x 2 mm active area of the device, operated at 14 V. (d) EQE as a function of the current density through the device C with dashed red line as a guide to the eye.

The inset in Figure 6.4 (a) shows a photograph of the 2 mm x 2 mm large device at moderate room illumination at 0 V bias. The inset of Figure 6.4 (c) shows the photograph of the same device under 14 V forward bias. The highly uniform white EL over the whole device area becomes clearly visible. The device showed stable operation under ambient air in constant bias mode as well as the same large-area emission characteristics after being stored in ambient air for almost two months.

Typically in NC-LEDs, their EQE first increases with increasing current density, reaches its maximum at current densities around 0.1 to 1 mA/cm² in case of hybrid QD-LEDs [300], 0.1 to 0.6 A/cm² for all-inorganic field-driven QD-LEDs [101], and 1 to 2.5 A/cm² for direct injection-type all-inorganic QD-LEDs [100, 113] and then shows saturation with subsequent decrease. Figure 6.4 (d) shows the measured external quantum efficiency (EQE, see Appendix A1) as a function of the current density through the device C. Obviously, the saturation point of the EQE is not yet reached at 0.5 A/cm², as indicated by the dashed red trend line and even higher EQE at higher current densities through the device can be expected. This result is comparable to sputtered oxide support layers [100, 113] and underlines the robustness of the devices.

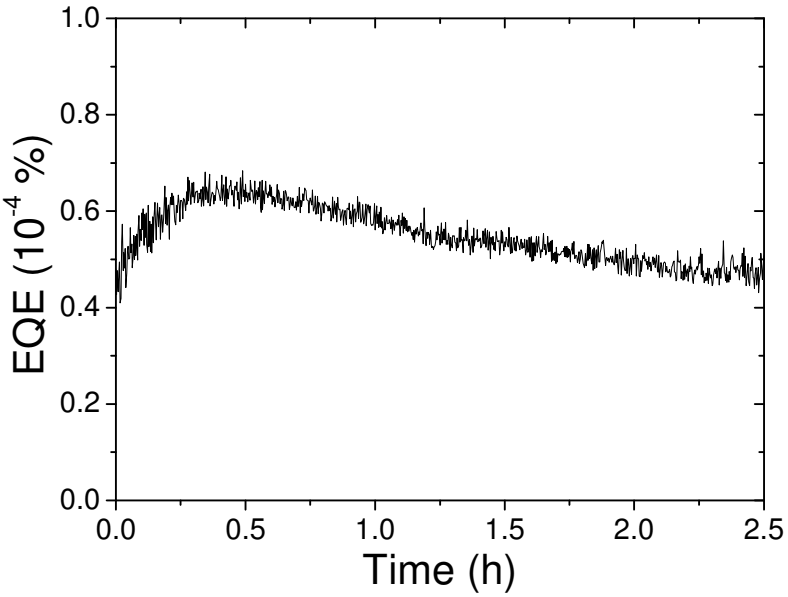

Figure 6.5: External quantum efficiency monitored over time at 13 V applied to device C.

Figure 6.5 emphasizes the robustness of the device concept and shows a long-term test of one of the contact pads of the device C at a constant bias of 13 V in ambient air without packaging. During the observation time no efficiency drop was registered. The efficiency increased slightly during first 30 minutes, then decreased slightly within the next 1.5 hours and remained constant for the rest of the experiment at a value slightly higher than in the beginning of the experiment.

Device C demonstrated the highest EQE of $0.6 \cdot 10^{-4}$ %, which is 6 times higher than the highest measured EQE of the Si/ZnO mixed multilayer NC-LEDs. The brightness was improved by a factor of 25 compared to Si/ZnO NC-LEDs and ~850 compared to the best ZnO-only archetype devices. In other devices of type C a maximum EQE of $2 \cdot 10^{-4}$% was achieved (at ~ half of the brightness of device C). The only "drawback" of the introduced design was the increased operation voltage of ~8 V, compared to 5 V for

Si/ZnO multilayer devices and 4 V for archetype ZnO-only devices. The possible reason for the increased turn-on voltage might be an additional voltage drop over the introduced WO_3 NCs.

It is quite interesting to discuss the external quantum efficiency (EQE) of the introduced devices with respect to literature data on nanocrystal WLEDs. The highest EQE values so far reported are in the range of 0.3 %, obtained for QD-WLEDs comprising a mix of red, green and blue emitting Cd-containing QDs.[25] Due to the monochromaticity of the involved QDs, however, the achieved CRI values are below 90. The strategy to combine broad band, defect-related emission in ultrasmall CdSe nanocrystals with blue emission of the organic support layer results in high CRI values of up to 96.6 [26], however, with a maximal EQE of $1.3 \cdot 10^{-4}$ %. The introduced oxide nanoparticle WLEDs showed a maximal EQE of $2 \cdot 10^{-4}$ %, but probably more important is the fact that the WLEDs are all-inorganic, free of toxic heavy metals like Cd, and their white emission stems from one and the same material (ZnO). Note that so far no EQE values for pure ZnO based LEDs were reported.[68] The still low EQE as compared e.g. to white OLEDs, is partly related to the limited internal quantum efficiency of the ZnO nanoparticles used here as active material. We measured a value of 0.2%, which is more than one order of magnitude lower than obtained for the white emitting ultrasmall CdSe nanocrystals (4%) mentioned above and even more than two orders of magnitude lower than state-of-the-art core-shell nanocrystals and organic emitters. This comparison underlines the potential of the WO_3 /ZnO device concept introduced here, in particular when considering that the synthesis of the ZnO nanocrystals used in this work was not optimized with respect to quantum yield and, in addition, quantum yields up to 20 % to 45% have already been reported for defect related emission of ZnO nanoparticles in literature.[41, 42]

In summary, all-inorganic, metal oxide nanocrystal multilayer WLEDs were developed. They combine optically active ZnO nanocrystals with WO_3 nanoparticles for electron extraction in an intermixed layer morphology. The implemented, Cd-free material systems are environmentally safe and highly available.[31, 36, 68, 326, 340] The resulting devices demonstrated highly uniform white light emission over the whole 4 mm^2 active area with voltage-controlled CCT values between 1600 and 4200 K and CRI between 92 and 96 while being fabricated, stored and measured under ambient air conditions without encapsulation. The introduced findings open a path towards low-cost, bio-safe, large-area white emitters with excellent color characteristics on flexible substrates.

Chapter 7

Summary and Conclusions

Semiconductor nanocrystals (NCs) are very promising candidates for lightweight large-area rollable displays and light emitting devices (LEDs). They are expected to combine the efficiency, robustness and color tunability of conventional semiconductor LEDs with the flexible fabrication techniques known from OLED technology, since the NCs are compatible with solution processing and therefore can be deposited on virtually any substrates including glass and plastic. Today, NC-LEDs consist of chemically synthesized QDs embedded in organic charge injection and transport layers. The organic layers limit the robustness of the NC-LEDs and result in significant constrictions within the device fabrication procedure, such as organic evaporation steps, inert (i.e. humidity and oxygen free) atmosphere and obligatory encapsulation. These limitations during the production process as well as complex chemical synthesis route of the implemented NCs and organic components lead to high fabrication costs and low turnover. So far, only prototype devices have been introduced by several research groups and industrial companies. Still, the main concern retarding NC-LEDs from market launch is the high content of toxic heavy metals like Cd in the active nanocrystalline light emitting material.

Within this work, possible environmentally safe and ambient-air-compatible alternatives to conventional QDs and organics were explored, with the main focus on design and fabrication of completely inorganic white NC-LEDs with commercial ZnO nanoparticles as an active light emitting material. While the electrical transport properties through the NC-network of the commercially available VP AdNano® ZnO20 particles were already to some extent explored, their optical properties and therefore suitability as an active light emitter in NC-LEDs were not studied so far.

In a first step, the optical quality of the nanocrystals was extensively studied by the means of absorption and photoluminescence (PL) spectroscopy. In agreement with high resolution transmission electron microscopy (HRTEM), the nanocrystals showed high crystalline quality without any line or plane defects resulting in a pronounced excitonic contribution to the absorption spectra at room temperature (RT). With supplementary temperature-dependent PL studies of the NCs, the near-band-gap-related excitonic emission was found to result from two transitions, assigned to the free A-exciton and the A-exciton bound to surface states or structural defects on the NC surface. This assignment of the transitions was also supported by size-selection experiments.

The studied nanocrystals demonstrated pronounced and stable bluish-white PL emission over the whole visible range. While the near-infrared, red, yellow and green defect-related contributions are quite frequently observed in different ZnO structures, the pronounced blue and violet emission is quite unusual and its origin in ZnO nanocrystals was not extensively studied previously. Based on the Zn-rich synthesis conditions of the crystals at high temperatures and the results of the PL studies of the NCs, annealed under ambient air and nitrogen, the origin of the blue and violet emission was assigned to neutral and ionized interstitial Zn defects, situated close to the surface of the crystals, in agreement with theoretical predictions. Annealing experiments demonstrated that the emission intensity of the particles can be increased by a soft annealing step at 150°C to 200°C by a factor of 1.3. Another elegant way to increase the defect-related emission intensity and simultaneously narrow the size and shape distribution of the NCs and thereby improve the homogeneity of the spin-coated layers, was found to be a size selection within the dispersion by a centrifuge step. The size-selection study also confirmed that most luminescent defect centers are situated on the surface of the nanocrystals, rather than the crystalline core, in agreement with other reports in literature. The comprehensive PL study of the luminescent properties of the commercially synthesized VP AdNano® ZnO20 particles resulted in a proposal of the energy diagram for the involved radiative transitions.

In the next step, a simple and straightforward design of all-inorganic ZnO NC-LEDs was developed and implemented. Thereby, dense ZnO NC layers were spin-coated on top of the transparent conductive oxide (TCO) substrates and covered by Al electrodes, evaporated through the shadow mask. First all-inorganic ZnO NC-LEDs operating at low voltages in the range typically between 4 V and 10 V were presented. The best devices showed large-area white electroluminescence (EL) with color rendering index (CRI) of ~97, and correlated color temperature (CCT) of ~3500K, visible to the naked

eye, as well as pronounced near-band-gap-related (NBR) emission with an operating lifetime of 3 hours in ambient air without any encapsulation.

The simple and robust archetype design of the devices enabled an extensive study of the EL and current/voltage (I-V) behavior and their direct correlation with the luminescent defect structure of ZnO nanostructures. A model was proposed to explain the observed behavior of the devices, which is not only consistent with the experiments showed here, but also with typical features of ZnO-based LEDs observed in literature, which remained a puzzle up to date. The light emission within the ZnO NC-network was assigned to a field driven ionization mechanism, whereby electrons from deep trap states and valence band (VB) states are extracted by the applied electrical field through conventional and trap-assisted tunneling to the conduction band (CB) and shallow trap states of the neighbor NC. The extracted electrons leave a hole behind, which can radiatively recombine with the electrons from the CB or shallow trap states, injected from the cathode. The efficiency of the electron extraction (hole injection into ZnO) by the electrical field determines the efficiency of the device, while the I-V behavior is dominated by the electron transport through the NC network, which can be basically characterized by space charge and trap charge limited conduction mechanisms.

From the starting point of these archetype devices and the proposed operation mechanism, the device design was systematically advanced. For the first time, p-doped NCs were utilized as a hole injection layer in a ZnO NC-LED. To abide the cost-effective all-inorganic approach, boron-doped Si NC, synthesized as well in the gas phase, were implemented within a NC double-layer solution processed LED approach. Due to the introduction of the p-Si NC layer, an “emission rectification ratio” of 10 under forward bias was achieved. More importantly, the overall emission intensity was increased by a factor of more than 15 compared to the archetype devices at similar current densities. This efficiency enhancement could be further improved by designing the active layer as an intermixed nanoparticle network. This nanocrystal intermixing approach was not introduced in any other type of NC devices before. The resulting devices showed improved homogeneity of the large-area white emission with CCT between ~2600 K and ~4600 K and CRIs up to 98. The devices also showed exceptional robustness, being operated for more than 2 weeks under ambient air conditions without any encapsulation, which can be attributed to the choice of the involved materials and the all-inorganic approach.

The intermixed NC approach was pursued in an all-inorganic, metal oxide nanocrystal multilayer design of the ZnO WLED. Optically active ZnO nanocrystals

were combined with WO_3 nanoparticles in an intermixed layer morphology. WO_3 NCs are expected to act as a local electron extractor for the ZnO NCs and thereby improve the efficiency of the NC-LED. Though the intriguing nature of the electron extraction properties of WO_3 in combination with ZnO is not yet completely understood, the emission properties of the WO_3/ZnO NC-LEDs are significantly improved. The resulting devices demonstrated highly uniform white light emission over the whole 4 mm^2 active area with voltage-controlled CCT values between 1600 and 4200 K and CRI between 92 and 96 while being fabricated, stored and measured under ambient air conditions without encapsulation. Compared to the best p-Si/ZnO NC-LEDs, the device brightness was increased by the factor of ~25 and the external quantum efficiency (EQE) by one order of magnitude up to $2 \cdot 10^{-4}$%, which is the highest so far reported EQE value for all-inorganic ZnO NC-LED.

Throughout the whole work the initial brightness of the first large-area all-inorganic white ZnO NC-LEDs was increased by the factor of ~850 and the EQE was improved by the factor of ~680. Yet the overall device performance requires further improvements to become comparable to the state-of-the-art lighting technology. Therefore the efficiency of the light generation within the ZnO NCs needs to be improved by the factor of at least ~100 by e.g. enhancing the electron extraction from ZnO and improving the charge carrier balance within the active layer. However, the most obvious improvement can be achieved by the utilization of the ZnO NCs, which luminescent properties are optimized for the LED applications. A more than 200 times EQE improvement is expected comparing the commercial ZnO NCs (luminescent quantum yield of 0.2%) studied here with chemically “souped-up" ZnO NCs with luminescent quantum yields of 45% and higher. Thus, there is quite a potential for further improvements left. Nevertheless, the introduced concept of the white all-inorganic NC-LEDs is very promising, since the implemented Cd-free material systems are environmentally safe, highly available and can be produced in large amounts at low costs. Therefore, the introduced findings open a path towards low-cost, bio-safe, large-area white ambient lighting applications with excellent color characteristics on flexible substrates.

Bibliography

1. Maier M: *Atalanta Fugiens*. Frankfurt: 1618.
2. Held G: *Introduction to light emitting diode technology and applications*. Boca Raton: CRC Press; 2009.
3. Jain S: *Conducting organic materials and devices*. 1st ed. Amsterdam ;;Boston: Elsevier/Academic Press; 2007.
4. Li Z: *Organic light-emitting materials and devices*. Boca Raton: CRC/Taylor & Francis; 2007.
5. Müllen K: *Organic light-emitting devices : synthesis, properties, and applications*. Weinheim: Wiley-VCH; 2006.
6. Mottier P: *LEDs for lighting applications*. London ;Hoboken NJ: ISTE ;;Wiley; 2009.
7. Burnham G, Society of Photo-optical Instrumentation Engineers.: *Laser diodes and LEDs in industrial, measurement, imaging, and sensors applications II : Testing, packaging, and reliability of semiconductor lasers V : 26-26[sic], January, 2000, San Jose, California*. Bellingham Wash.: SPIE; 2000.
8. Colvin VL, Schlamp MC, Alivisatos AP: **Light-emitting diodes made from cadmium selenide nanocrystals and a semiconducting polymer**. *Nature* 1994, **370**:354.
9. Efros AL, Efros AL: **Interband absorption of light in a semiconductor sphere**. *Sov. Phys. Semicond.* 1982, **16**:772.
10. Brus L: **Quantum crystallites and nonlinear optics**. *Appl. Phys. A* 1991, **53**:465.
11. Jang E, Jun S, Jang H, Lim J, Kim B, Kim Y: **White-Light-Emitting Diodes with Quantum Dot Color Converters for Display Backlights**. *Advanced Materials* 2010, **22**:3076.
12. Anikeeva PO, Halpert JE, Bawendi MG, Bulović V: **Quantum Dot Light-Emitting Devices with Electroluminescence Tunable over the Entire Visible Spectrum**. *Nano Lett.* 2009, **9**:2532.
13. Lim J, Bae WK, Kwak J, Lee S, Lee C, Char K: **Perspective on synthesis, device structures, and printing processes for quantum dot displays**. *Optical Materials Express* 2012, **2**:594.
14. Sun Q, Wang YA, Li LS, Wang D, Zhu T, Xu J, Yang C, Li Y: **Bright, multicoloured light-emitting diodes based on quantum dots**. *Nature Photonics* 2007, **1**:717.
15. Caruge J-M, Halpert JE, Bulović V, Bawendi MG: **NiO as an Inorganic Hole-Transporting Layer in Quantum-Dot Light-Emitting Devices**. *Nano Lett.* 2006, **6**:2991.
16. Stouwdam JW, Janssen RAJ: **Red, green, and blue quantum dot LEDs with solution processable ZnO nanocrystal electron injection layers**. *J. Mater. Chem.* 2008, **18**:1889.
17. Cho K-S, Lee EK, Joo W-J, Jang E, Kim T-H, Lee SJ, Kwon S-J, Han JY, Kim B-K, Choi BL, Kim JM: **High-performance crosslinked colloidal quantum-dot light-emitting diodes**. *Nature Photonics* 2009, **3**:341.
18. Kim T-H, Cho K-S, Lee EK, Lee SJ, Chae J, Kim JW, Kim DH, Kwon J-Y, Amaratunga G, Lee SY, Choi BL, Kuk Y, Kim JM, Kim K: **Full-colour quantum dot displays fabricated by transfer printing**. *Nature Photonics* 2011, **5**:176.
19. Qian L, Zheng Y, Xue J, Holloway PH: **Stable and efficient quantum-dot light-emitting diodes based on solution-processed multilayer structures**. *Nature Photonics* 2011, **5**:543.
20. Kwak J, Bae WK, Lee D, Park I, Lim J, Park M, Cho H, Woo H, Yoon DY, Char K, Lee S, Lee C: **Bright and Efficient Full-Color Colloidal Quantum Dot Light-Emitting Diodes Using an Inverted Device Structure**. *Nano Letters* 2012, **12**:2362.
21. Kim L, Anikeeva PO, Coe-Sullivan SA, Steckel JS, Bawendi MG, Bulović V: **Contact**

Printing of Quantum Dot Light-Emitting Devices. *Nano Lett.* 2008, **8**:4513.
22. Rizzo A, Mazzeo M, Palumbo M, Lerario G, D'Amone S, Cingolani R, Gigli G: **Hybrid Light-Emitting Diodes from Microcontact-Printing Double-Transfer of Colloidal Semiconductor CdSe/ZnS Quantum Dots onto Organic Layers**. *Adv. Mater.* 2008, **20**:1886.
23. Haverinen HM, Myllylä RA, Jabbour GE: **Inkjet printing of light emitting quantum dots**. *Appl. Phys. Lett.* 2009, **94**:073108.
24. Li YQ, Rizzo A, Cingolani R, Gigli G: **Bright White-Light-Emitting Device from Ternary Nanocrystal Composites**. *Adv. Mater.* 2006, **18**:2545.
25. Anikeeva PO, Halpert JE, Bawendi MG, Bulović V: **Electroluminescence from a Mixed Red−Green−Blue Colloidal Quantum Dot Monolayer**. *Nano Lett.* 2007, **7**:2196.
26. Schreuder MA, Xiao K, Ivanov IN, Weiss SM, Rosenthal SJ: **White Light-Emitting Diodes Based on Ultrasmall CdSe Nanocrystal Electroluminescence**. *Nano Lett.* 2010, **10**:573.
27. Özgür U, Alivov YI, Liu C, Teke A, Reshchikov MA, Doğan S, Avrutin V, Cho S-J, Morkoç H: **A comprehensive review of ZnO materials and devices**. *J. Appl. Phys.* 2005, **98**:041301.
28. Omata T, Tani Y, Kobayashi S, Takahashi K, Miyanaga A, Maeda Y, Otsuka-Yao-Matsuo S: **Ultraviolet electroluminescence from colloidal ZnO quantum dots in an all-inorganic multilayer light-emitting device**. *Applied Physics Letters* 2012, **100**:061104.
29. Toyama T, Takeuchi H, Yamaguchi D, Kawasaki H, Itatani K, Okamoto H: **Solution-processed ZnO nanocrystals in thin-film light-emitting diodes for printed electronics**. *Journal of Applied Physics* 2010, **108**:084302.
30. Djurišić AB, Leung YH: **Optical Properties of ZnO Nanostructures**. *Small* 2006, **2**:944.
31. Bacsa R, Kihn Y, Verelst M, Dexpert J, Bacsa W, Serp P: **Large scale synthesis of zinc oxide nanorods by homogeneous chemical vapour deposition and their characterisation**. *Surface and Coatings Technology* 2007, **201**:9200.
32. Beeckmans JM, Brown JR: **Toxicity of catalytically active zinc oxides.** *Arch. Environ. Health* 1963, **7**:346.
33. Schilling K, Bradford B, Castelli D, Dufour E, Nash JF, Pape W, Schulte S, Tooley I, van den Bosch J, Schellauf F: **Human safety review of "nano" titanium dioxide and zinc oxide**. *Photochem. Photobiol. Sci.* 2010, **9**:495.
34. Tang ZK, Wong GKL, Yu P, Kawasaki M, Ohtomo A, Koinuma H, Segawa Y: **Room-temperature ultraviolet laser emission from self-assembled ZnO microcrystallite thin films**. *Appl. Phys. Lett.* 1998, **72**:3270.
35. Tsukazaki A, Ohtomo A, Onuma T, Ohtani M, Makino T, Sumiya M, Ohtani K, Chichibu SF, Fuke S, Segawa Y, Ohno H, Koinuma H, Kawasaki M: **Repeated temperature modulation epitaxy for p-type doping and light-emitting diode based on ZnO**. *Nat Mater* 2004, **4**:42.
36. Morkoç H, Özgür Ü: *Zinc oxide : fundamentals, materials and device technology*. Weinheim: Wiley-VCH; 2009.
37. Klingshirn C: *Zinc Oxide : from fundamental properties towards novel applications*. Berlin ;;Heidelberg: Springer; 2010.
38. Djurišić AB, Ng AMC, Chen XY: **ZnO nanostructures for optoelectronics: Material properties and device applications**. *Progress in Quantum Electronics* 2010, **34**:191.
39. van Dijken A, Makkinje J, Meijerink A: **The influence of particle size on the luminescence quantum efficiency of nanocrystalline ZnO particles**. *Journal of Luminescence* 2001, **92**:323.
40. Zeng H, Duan G, Li Y, Yang S, Xu X, Cai W: **Blue Luminescence of ZnO Nanoparticles Based on Non-Equilibrium Processes: Defect Origins and Emission Controls**. *Adv. Funct. Mater.* 2010, **20**:561.
41. van Dijken A, Makkinje J, Meijerink A: **The influence of particle size on the**

luminescence quantum efficiency of nanocrystalline ZnO particles. *J. Lumin.* 2000, **92**:323.
42. Yue Q, Cheng J, Li G, Zhang K, Zhai Y, Wang L, Liu J: **Fluorescence Property of ZnO Nanoparticles and the Interaction with Bromothymol Blue**. *J Fluoresc* 2010, **21**:1131.
43. Sun L-W, Shi H-Q, Li W-N, Xiao H-M, Fu S-Y, Cao X-Z, Li Z-X: **Lanthanum-doped ZnO quantum dots with greatly enhanced fluorescent quantum yield**. *Journal of Materials Chemistry* 2012, **22**:8221.
44. Willander M, Nur O, Zhao QX, Yang LL, Lorenz M, Cao BQ, Zúñiga Pérez J, Czekalla C, Zimmermann G, Grundmann M, Bakin A, Behrends A, Al-Suleiman M, El-Shaer A, Che Mofor A, Postels B, Waag A, Boukos N, Travlos A, Kwack HS, Guinard J, Le Si Dang D: **Zinc oxide nanorod based photonic devices: recent progress in growth, light emitting diodes and lasers**. *Nanotechnology* 2009, **20**:332001.
45. Neshataeva E, Kümmell T, Bacher G, Ebbers A: **All-inorganic light emitting device based on ZnO nanoparticles**. *Appl. Phys. Lett.* 2009, **94**:091115.
46. Willander M, Nur O, Bano N, Sultana K: **Zinc oxide nanorod-based heterostructures on solid and soft substrates for white-light-emitting diode applications**. *New J. Phys.* 2009, **11**:125020.
47. Bano N, Zaman S, Zainelabdin A, Hussain S, Hussain I, Nur O, Willander M: **ZnO-organic hybrid white light emitting diodes grown on flexible plastic using low temperature aqueous chemical method**. *J. Appl. Phys.* 2010, **108**:043103.
48. Zhang S, Wei S-H, Zunger A: **Intrinsic n-type versus p-type doping asymmetry and the defect physics of ZnO**. *Phys. Rev. B* 2001, **63**:075205.
49. Könenkamp R, Word RC, Schlegel C: **Vertical nanowire light-emitting diode**. *Appl. Phys. Lett.* 2004, **85**:6004.
50. Könenkamp R, Word RC, Godinez M: **Ultraviolet Electroluminescence from ZnO/Polymer Heterojunction Light-Emitting Diodes**. *Nano Lett.* 2005, **5**:2005.
51. Ling B, Zhao JL, Sun XW, Tan ST, Kyaw AKK, Divayana Y, Dong ZL: **Color tunable light-emitting diodes based on p-Si/p-$CuAlO_2$/n-ZnO nanorod array heterojunctions**. *Appl. Phys. Lett.* 2010, **97**:013101.
52. Guo H, Lin Z, Feng Z, Lin L, Zhou J: **White-Light-Emitting Diode Based on ZnO Nanotubes**. *The Journal of Physical Chemistry C* 2009, **113**:12546.
53. Park WI, Yi G-C: **Electroluminescence in n-ZnO Nanorod Arrays Vertically Grown on p-GaN**. *Adv. Mater.* 2004, **16**:87.
54. Xi YY, Hsu YF, Djurišić AB, Ng AMC, Chan WK, Tam HL, Cheah KW: **NiO/ZnO light emitting diodes by solution-based growth**. *Appl. Phys. Lett.* 2008, **92**:113505.
55. Wang J-Y, Lee C-Y, Chen Y-T, Chen C-T, Chen Y-L, Lin C-F, Chen Y-F: **Double side electroluminescence from p-NiO/n-ZnO nanowire heterojunctions**. *Appl. Phys. Lett.* 2009, **95**:131117.
56. Zimmler MA, Voss T, Ronning C, Capasso F: **Exciton-related electroluminescence from ZnO nanowire light-emitting diodes**. *Appl. Phys. Lett.* 2009, **94**:241120.
57. Katusic S, Michael G, Kress P, Varga GJ, Staab E, Weber W: **Nanoscale zinc oxide, process for its production and use**. 2005.
58. Lee C-Y, Haung Y-T, Su W-F, Lin C-F: **Electroluminescence from ZnO nanoparticles/organic nanocomposites**. *Appl. Phys. Lett.* 2006, **89**:231116.
59. Lee C-Y, Hui Y-Y, Su W-F, Lin C-F: **Electroluminescence from monolayer ZnO nanoparticles using dry coating technique**. *Appl. Phys. Lett.* 2008, **92**:261107.
60. Toyama T, Kawasaki H, Itatani K, Okamoto H: **Top-Emission Ultraviolet-Light-Emitting Diodes Containing Solution-Processed ZnO Nanocrystals**. *Applied Physics Express* 2011, **4**:065005.
61. Park WI, Yi G-C: **Electroluminescence in n-ZnO Nanorod Arrays Vertically Grown on**

p-GaN. *Adv. Mater.* 2004, **16**:87.
62. Jeong M-C, Oh B-Y, Ham M-H, Lee S-W, Myoung J-M: **ZnO-Nanowire-Inserted GaN/ZnO Heterojunction Light-Emitting Diodes**. *Small* 2007, **3**:568.
63. Jha S, Qian J-C, Kutsay O, Kovac Jr J, Luan C-Y, Zapien JA, Zhang W, Lee S-T, Bello I: **Violet-blue LEDs based on p-GaN/n-ZnO nanorods and their stability**. *Nanotechnology* 2011, **22**:245202.
64. Tan ST, Sun XW, Zhao JL, Iwan S, Cen ZH, Chen TP, Ye JD, Lo GQ, Kwong DL, Teo KL: **Ultraviolet and visible electroluminescence from n-ZnO/SiO_X/(n,p)-Si heterostructured light-emitting diodes**. *Appl. Phys. Lett.* 2008, **93**:013506.
65. Bao J, Zimmler MA, Capasso F, Wang X, Ren ZF: **Broadband ZnO Single-Nanowire Light-Emitting Diode**. *Nano Lett.* 2006, **6**:1719.
66. Zimmler MA, Stichtenoth D, Ronning C, Yi W, Narayanamurti V, Voss T, Capasso F: **Scalable Fabrication of Nanowire Photonic and Electronic Circuits Using Spin-on Glass**. *Nano Letters* 2008, **8**:1695.
67. Ohta H, Kawamura K, Orita M, Hirano M, Sarukura N, Hosono H: **Current injection emission from a transparent p–n junction composed of p-$SrCu_2O_2$/n-ZnO**. *Appl. Phys. Lett.* 2000, **77**:475.
68. Sessolo M, Bolink HJ: **Hybrid Organic-Inorganic Light-Emitting Diodes**. *Adv. Mater.* 2011, **23**:1829.
69. Yen W: *Phosphor handbook.* 2nd ed. /. Boca Raton FL: CRC Press/Taylor and Francis; 2007.
70. Ono Y: *Electroluminescent displays*. Singapore; River Edge NJ: World Scientific; 1995.
71. Manzoor K, Vadera SR, Kumar N, Kutty TRN: **Multicolor electroluminescent devices using doped ZnS nanocrystals**. *Appl. Phys. Lett.* 2004, **84**:284.
72. Adachi D, Hama T, Toyama T, Okamoto H: **Electroluminescent properties of chemically synthesized zinc sulfide nanocrystals doped with manganese**. *J Mater Sci: Mater Electron* 2007, **20**:130.
73. Toyama T, Hama T, Adachi D, Nakashizu Y, Okamoto H: **An electroluminescence device for printable electronics using coprecipitated ZnS:Mn nanocrystal ink**. *Nanotechnology* 2009, **20**:055203.
74. Wood V, Halpert JE, Panzer MJ, Bawendi MG, Bulović V: **Alternating Current Driven Electroluminescence from ZnSe/ZnS:Mn/ZnS Nanocrystals**. *Nano Lett.* 2009, **9**:2367.
75. Vanessa Claire Wood: **Electrical excitation of colloidally synthesized quantum dots in metal oxide structures**. *Ph.D. Thesis*, Massachusetts Institute of Technology, 2010.
76. Bach U, Lupo D, Comte P, Moser JE, Weissortel F, Salbeck J, Spreitzer H, Gratzel M: **Solid-state dye-sensitized mesoporous TiO_2 solar cells with high photon-to-electron conversion efficiencies**. *Nature* 1998, **395**:583.
77. Vossen JL: **Transparent conducting films**. *Phys. Thin Films* 1977, **9**:1.
78. Chopra K, Major S, Pandya D: **Transparent conductors—A status review**. *Thin Solid Films* 1983, **102**:1.
79. Minami T: **Substitution of transparent conducting oxide thin films for indium tin oxide transparent electrode applications**. *Thin Solid Films* 2008, **516**:1314.
80. Minami T: **Present status of transparent conducting oxide thin-film development for Indium-Tin-Oxide (ITO) substitutes**. *Thin Solid Films* 2008, **516**:5822.
81. Raniero L, Ferreira I, Pimentel A, Goncalves A, Canhola P, Fortunato E, Martins R: **Role of hydrogen plasma on electrical and optical properties of ZGO, ITO and IZO transparent and conductive coatings**. *Thin Solid Films* 2006, **511-512**:295.
82. Dabbousi BO, Bawendi MG, Onitsuka O, Rubner MF: **Electroluminescence from CdSe quantum-dot/polymer composites**. *Appl. Phys. Lett.* 1995, **66**:1316.

83. Gaponik NP, Talapin DV, Rogach AL, Eychmüller A: **Electrochemical synthesis of CdTe nanocrystal/polypyrrole composites for optoelectronic applications**. *J. Mater. Chem.* 2000, **10**:2163.
84. Tessler N: **Efficient Near-Infrared Polymer Nanocrystal Light-Emitting Diodes**. *Science* 2002, **295**:1506.
85. Zhao J, Zhang J, Jiang C, Bohnenberger J, Basché T, Mews A: **Electroluminescence from isolated CdSe⁄ZnS quantum dots in multilayered light-emitting diodes**. *J. Appl. Phys.* 2004, **96**:3206.
86. Lee C-Y, Hui Y-Y, Su W-F, Lin C-F: **Electroluminescence from monolayer ZnO nanoparticles using dry coating technique**. *Appl. Phys. Lett.* 2008, **92**:261107.
87. Yang H, Holloway PH, Ratna BB: **Photoluminescent and electroluminescent properties of Mn-doped ZnS nanocrystals**. *J. Appl. Phys.* 2003, **93**:586.
88. Sundar Manoharan S, Mohammad Q: **White light electroluminescence in zinc sulfide: polyflourene blends**. *phys. stat. sol. (a)* 2005, **202**:1124.
89. Son D-I, Park D-H, Choi WK, Kim TW: **Electroluminescence of a single active layer polymer–nanocrystal hybrid light-emitting diode with inversion symmetry**. *Nanotechnology* 2009, **20**:275205.
90. Tessler N, Solomeshch O, Kigel A, Saschiuk A, Medvedev V, Aharoni A, Razin A, Eichen Y, Banin U, Lifshitz E: **Optoelectronic properties of polymer-nanocrystal composites active at near-infrared wavelengths**. *J. Appl. Phys.* 2005, **98**:074310.
91. Mattoussi H, Radzilowski LH, Dabbousi BO, Fogg DE, Schrock RR, Thomas EL, Rubner MF, Bawendi MG: **Composite thin films of CdSe nanocrystals and a surface passivating/electron transporting block copolymer: Correlations between film microstructure by transmission electron microscopy and electroluminescence**. *J. Appl. Phys.* 1999, **86**:4390.
92. Gao M, Richter B, Kirstein S, Möhwald H: **Electroluminescence Studies on Self-Assembled Films of PPV and CdSe Nanoparticles**. *J. Phys. Chem. B* 1998, **102**:4096.
93. Huang J, Yang Y, Xue S, Yang B, Liu S, Shen J: **Photoluminescence and electroluminescence of ZnS:Cu nanocrystals in polymeric networks**. *Appl. Phys. Lett.* 1997, **70**:2335.
94. Que W, Zhou Y, Lam YL, Chan YC, Kam CH, Liu B, Gan LM, Chew CH, Xu GQ, Chua SJ, Xu SJ, Mendis FVC: **Photoluminescence and electroluminescence from copper doped zinc sulphide nanocrystals/polymer composite**. *Appl. Phys. Lett.* 1998, **73**:2727.
95. Gaponik NP, Talapin DV, Rogach AL: **A light-emitting device based on a CdTe nanocrystal/polyaniline composite**. *Phys. Chem. Chem. Phys.* 1999, **1**:1787.
96. Bakueva L, Konstantatos G, Levina L, Musikhin S, Sargent EH: **Luminescence from processible quantum dot-polymer light emitters 1100–1600 nm: Tailoring spectral width and shape**. *Appl. Phys. Lett.* 2004, **84**:3459.
97. Larkin IA, Stockman MI, Achermann M, Klimov VI: **Dipolar emitters at nanoscale proximity of metal surfaces: Giant enhancement of relaxation in microscopic theory**. *Phys. Rev. B* 2004, **69**:121403(R).
98. Schlamp MC, Peng X, Alivisatos AP: **Improved efficiencies in light emitting diodes made with CdSe(CdS) core/shell type nanocrystals and a semiconducting polymer**. *J. Appl. Phys.* 1997, **82**:5837.
99. Coe-Sullivan S, Steckel JS, Woo W-K, Bawendi MG, Bulović V: **Large-Area Ordered Quantum-Dot Monolayers via Phase Separation During Spin-Casting**. *Adv. Funct. Mater.* 2005, **15**:1117.
100. Caruge JM, Halpert JE, Wood V, Bulović V, Bawendi MG: **Colloidal quantum-dot light-emitting diodes with metal-oxide charge transport layers**. *Nature Photon* 2008, **2**:247.

101. Wood V, Panzer MJ, Caruge J-M, Halpert JE, Bawendi MG, Bulović V: **Air-Stable Operation of Transparent, Colloidal Quantum Dot Based LEDs with a Unipolar Device Architecture**. *Nano Lett.* 2010, **10**:24.
102. Li Y, Rizzo A, Mazzeo M, Carbone L, Manna L, Cingolani R, Gigli G: **White organic light-emitting devices with CdSe/ZnS quantum dots as a red emitter**. *J. Appl. Phys.* 2005, **97**:113501.
103. Jing-hua N, Rui-nian H, Wen-lian L, Ming-tao L, Tian-zhi Y: **Electroluminescent properties of a device based on terbium-doped ZnS nanocrystals**. *J. Phys. D: Appl. Phys.* 2006, **39**:2357.
104. Rizzo A, Li Y, Kudera S, Della Sala F, Zanella M, Parak WJ, Cingolani R, Manna L, Gigli G: **Blue light emitting diodes based on fluorescent CdSe/ZnS nanocrystals**. *Appl. Phys. Lett.* 2007, **90**:051106.
105. Anikeeva PO, Madigan CF, Halpert JE, Bawendi MG, Bulović V: **Electronic and excitonic processes in light-emitting devices based on organic materials and colloidal quantum dots**. *Phys. Rev. B* 2008, **78**:085434.
106. Artemyev MV, Sperling V, Woggon U: **Electroluminescence in thin solid films of closely packed CdS nanocrystals**. *J. Appl. Phys.* 1997, **81**:6975.
107. Mahalingam V, Tan M, Munusamy P, Gilroy JB, Raudsepp M, van Veggel FCJM: **Bright Blue Photo- and Electroluminescence from Eu^{2+}-Doped GaN/SiO_2 Nanocomposites**. *Adv. Funct. Mater.* 2007, **17**:3462.
108. Neshataeva E, Kümmell T, Bacher G, Ebbers A: **All-inorganic light emitting device based on ZnO nanoparticles**. *Appl. Phys. Lett.* 2009, **94**:091115.
109. Anikeeva PO, Halpert JE, Bawendi MG, Bulović V: **Quantum Dot Light-Emitting Devices with Electroluminescence Tunable over the Entire Visible Spectrum**. *Nano Lett.* 2009, **9**:2532.
110. Coe S, Woo W-K, Bawendi M, Bulović V: **Electroluminescence from single monolayers of nanocrystals in molecular organic devices**. *Nature* 2002, **420**:800.
111. O'Connor E, O'Riordan A, Doyle H, Moynihan S, Cuddihy A, Redmond G: **Near-infrared electroluminescent devices based on colloidal HgTe quantum dot arrays**. *Appl. Phys. Lett.* 2005, **86**:201114.
112. Gopal A, Hoshino K, Kim S, Zhang X: **Multi-color colloidal quantum dot based light emitting diodes micropatterned on silicon hole transporting layers**. *Nanotechnology* 2009, **20**:235201.
113. Wood V, Panzer MJ, Halpert JE, Caruge J-M, Bawendi MG, Bulović V: **Selection of Metal Oxide Charge Transport Layers for Colloidal Quantum Dot LEDs**. *ACS Nano* 2009, **3**:3581.
114. Niu J, Hua R, Li W, Li M, Tian-zhi Y: **Electroluminescent properties of a device based on terbium-doped ZnS nanocrystals**. *J. Phys. D: Appl. Phys.* 2006, **39**:2357.
115. Lee C-Y, Haung Y-T, Su W-F, Lin C-F: **Electroluminescence from ZnO nanoparticles/organic nanocomposites**. *Appl. Phys. Lett.* 2006, **89**:231116.
116. Hikmet RAM, Talapin DV, Weller H: **Study of conduction mechanism and electroluminescence in CdSe/ZnS quantum dot composites**. *J. Appl. Phys.* 2003, **93**:3509.
117. Tan Z, Xu J, Zhang C, Zhu T, Zhang F, Hedrick B, Pickering S, Wu J, Su H, Gao S, Wang AY, Kimball B, Ruzyllo J, Dellas NS, Mohney SE: **Colloidal nanocrystal-based light-emitting diodes fabricated on plastic toward flexible quantum dot optoelectronics**. *J. Appl. Phys.* 2009, **105**:034312.
118. Anikeeva PO: **Physical properties and design of light-emitting devices based on organic materials and nanoparticles**. *Ph.D. Thesis*, Massachusetts Institute of Technology, 2009.

119. Förster T: **Zwischenmolekulare Energiewanderung und Fluoreszenz**. *Ann. Phys.* 1948, **437**:55.
120. Andrews D: **A unified theory of radiative and radiationless molecular energy transfer**. *Chemical Physics* 1989, **135**:195.
121. Andrews DL, Bradshaw DS: **Virtual photons, dipole fields and energy transfer: a quantum electrodynamical approach**. *Eur. J. Phys.* 2004, **25**:845.
122. Haugland RP, Yguerabide J, Stryer L: **Dependence of the kinetics of singlet-singlet energy transfer on spectral overlap**. *Proc. Natl. Acad. Sci. U.S.A* 1969, **63**:23.
123. Mach R, Müller GO: **Physical Concepts of High-Field, Thin-Film Electroluminescence Devices**. *phys. stat. sol. (a)* 1982, **69**:11.
124. Wood V, Panzer MJ, Bozyigit D, Shirasaki Y, Rousseau I, Geyer S, Bawendi MG, Bulović V: **Electroluminescence from Nanoscale Materials via Field-Driven Ionization**. *Nano Letters* 2011, **11**:2927.
125. Sze SM, Ng KK: *Physics of semiconductor devices*. Hoboken, N.J.: Wiley-Interscience; 2007.
126. Geyer S, Porter V, Halpert J, Mentzel T, Kastner M, Bawendi M: **Charge transport in mixed CdSe and CdTe colloidal nanocrystal films**. *Phys. Rev. B* 2010, **82**: 155201.
127. Wang ZB, Helander MG, Greiner MT, Qiu J, Lu ZH: **Analysis of charge-injection characteristics at electrode-organic interfaces: Case study of transition-metal oxides**. *Phys. Rev. B* 2009, **80**:235325.
128. Woellner CF, Freire JA: **Reformulated space-charge-limited current model and its application to disordered organic systems**. *J. Chem. Phys.* 2011, **134**:084112.
129. Burrows PE, Shen Z, Bulovic V, McCarty DM, Forrest SR, Cronin JA, Thompson ME: **Relationship between electroluminescence and current transport in organic heterojunction light-emitting devices**. *J. Appl. Phys.* 1996:7991.
130. Groß M: **Poly(4,4'-dimethoxybithiophen)-Filme als polymere Anoden mit variabler Austrittsarbeit**. *Ph.D. Thesis,* Ludwig-Maximilians-Universität München, 2000.
131. Kao K-C: *Electrical transport in solids : with particular reference to organic semiconductors*. 1st ed. Oxford ;;New York: Pergamon Press; 1981.
132. Fowler RH, Nordheim L: **Electron Emission in Intense Electric Fields**. *Proceedings of the Royal Society A: Mathematical, Physical and Engineering Sciences* 1928, **119**:173.
133. Koehler M, Hümmelgen IA: **Temperature dependent tunnelling current at metal/polymer interfaces—potential barrier height determination**. *Appl. Phys. Lett.* 1997, **70**:3254.
134. Lampert M, Mark P: *Current injection in solids*. New York: Academic Press; 1970.
135. Mott NF, Gurney RW: *Electronic Progress in Ionic Crystals*. New York: Oxford University Press; 1940.
136. Rose A: **Space-Charge-Limited Currents in Solids**. *Phys. Rev.* 1955, **97**:1538.
137. Smith R, Rose A: **Space-Charge-Limited Currents in Single Crystals of Cadmium Sulfide**. *Phys. Rev.* 1955, **97**:1531.
138. Lampert M: **Simplified Theory of Space-Charge-Limited Currents in an Insulator with Traps**. *Phys. Rev.* 1956, **103**:1648.
139. Nespurek S, Zmeskal O, Sworakowski J: **Space-charge-limited currents in organic films: Some open problems**. *Thin Solid Films* 2008, **516**:8949.
140. Gao M, Richter B, Kirstein S: **Electroluminescence and photoluminescence in CdSe/poly (p-phenylene vinylene) composite films**. *Synthetic Metals* 1999, **102**:1213.
141. Khan MT, Kaur A, Dhawan SK, Chand S: **Hole transport mechanism in organic/inorganic hybrid system based on in-situ grown cadmium telluride nanocrystals in poly(3-hexylthiophene)**. *J. Appl. Phys.* 2011, **109**:114509.

142. Gao M, Lesser C, Kirstein S, Möhwald H, Rogach AL, Weller H: **Electroluminescence of different colors from polycation/CdTe nanocrystal self-assembled films**. *Journal of Applied Physics* 2000, **87**:2297.
143. Mark P, Helfrich W: **Space-Charge-Limited Currents in Organic Crystals**. *J. Appl. Phys.* 1962, **33**:205.
144. Burrows PE, Forrest SR: **Electroluminescence from trap-limited current transport in vacuum deposited organic light emitting devices**. *Appl. Phys. Lett.* 1994, **64**:2285.
145. Gao M, Richter B, Kirstein S: **White-light electroluminescence from self-assembled Q-CdSe/PPV multilayer structures**. *Adv. Mater.* 1997, **9**:802.
146. Mattoussi H, Radzilowski LH, Dabbousi BO, Thomas EL, Bawendi MG, Rubner MF: **Electroluminescence from heterostructures of poly(phenylene vinylene) and inorganic CdSe nanocrystals**. *J. Appl. Phys.* 1998, **83**:7965.
147. Klingshirn C: **ZnO: Material, Physics and Applications**. *ChemPhysChem* 2007, **8**:782.
148. Ashrafi ABMA, Ueta A, Avramescu A, Kumano H, Suemune I, Ok Y-W, Seong T-Y: **Growth and characterization of hypothetical zinc-blende ZnO films on GaAs(001) substrates with ZnS buffer layers**. *Appl. Phys. Lett.* 2000, **76**:550.
149. Bates CH, White WB, Roy R: **New High-Pressure Polymorph of Zinc Oxide**. *Science* 1962, **137**:993.
150. Desgreniers S: **High-density phases of ZnO: Structural and compressive parameters**. *Phys. Rev. B* 1998, **58**:14102.
151. Kim S-K, Jeong S-Y, Cho C-R: **Structural reconstruction of hexagonal to cubic ZnO films on Pt/Ti/SiO_2/Si substrate by annealing**. *Appl. Phys. Lett.* 2003, **82**:562.
152. Phillips J: *Bonds and bands in semiconductors,*. New York: Academic Press; 1973.
153. Meyer BK, Alves H, Hofmann DM, Kriegseis W, Forster D, Bertram F, Christen J, Hoffmann A, Straßburg M, Dworzak M, Haboeck U, Rodina AV: **Bound exciton and donor–acceptor pair recombinations in ZnO**. *phys. stat. sol. (b)* 2004, **241**:231.
154. Jagadish C, Pearton S: *Zinc oxide bulk, thin films and nanostructures : processing, properties and applications*. Amsterdam; London: Elsevier; 2006.
155. Varshni Y: **Temperature dependence of the energy gap in semiconductors**. *Physica* 1967, **34**:149.
156. Meyer BK, Alves H, Hofmann DM, Kriegseis W, Forster D, Bertram F, Christen J, Hoffmann A, Straßburg M, Dworzak M, Haboeck U, Rodina AV: **Bound exciton and donor–acceptor pair recombinations in ZnO**. *phys. stat. sol. (b)* 2004, **241**:231.
157. Kumar B, Gong H, Vicknesh S, Chua SJ, Tripathy S: **Luminescence properties of ZnO layers grown on Si-on-insulator substrates**. *Appl. Phys. Lett.* 2006, **89**:141901.
158. Liao Z-M, Zhang H-Z, Zhou Y-B, Xu J, Zhang J-M, Yu D-P: **Surface effects on photoluminescence of single ZnO nanowires**. *Physics Letters A* 2008, **372**:4505.
159. Fonoberov V, Alim K, Balandin A, Xiu F, Liu J: **Photoluminescence investigation of the carrier recombination processes in ZnO quantum dots and nanocrystals**. *Phys. Rev. B* 2006, **73**:165317.
160. Schneider L: **Optische Kurzzeitspektroskopie an magnetisch dotierten Halbleiter-Nanopartikeln**. *Ph.D. Thesis*, Universität Duisburg-Essen, 2010.
161. Qiu J, Li X, He W, Park S-J, Kim H-K, Hwang Y-H, Lee J-H, Kim Y-D: **The growth mechanism and optical properties of ultralong ZnO nanorod arrays with a high aspect ratio by a preheating hydrothermal method**. *Nanotechnology* 2009, **20**:155603.
162. Kurbanov S, Panin G, Kim TW, Kang TW: **Thermo- and Photo-annealing of ZnO Nanocrystals**. *Jpn. J. Appl. Phys.* 2007, **46**:4172.
163. Zhang L, Yin L, Wang C, lun N, Qi Y, Xiang D: **Origin of Visible Photoluminescence of ZnO Quantum Dots: Defect-Dependent and Size-Dependent**. *J. Phys. Chem. C* 2010,

114:9651.
164. Mollwo E: **Das ultraviolette Absorptionsspektrum der Sulfide und Oxyde von Zink und Kadmium**. *Reichsberichte für Physik* 1944, **1**.
165. Cao B, Cai W, Zeng H: **Temperature-dependent shifts of three emission bands for ZnO nanoneedle arrays**. *Appl. Phys. Lett.* 2006, **88**:161101.
166. Thomas D: **The exciton spectrum of zinc oxide**. *Journal of Physics and Chemistry of Solids* 1960, **15**:86.
167. Djurišić AB, Leung YH: **Optical Properties of ZnO Nanostructures**. *Small* 2006, **2**:944.
168. Djurišić AB, Ng AMC, Chen XY: **ZnO nanostructures for optoelectronics: Material properties and device applications**. *Progress in Quantum Electronics* 2010, **34**:191.
169. Litton C: *Zinc oxide materials for electronic and optoelectronic device applications*. Chichester West Sussex: Wiley; 2011.
170. Klingshirn C, Fallert J, Gogolin O, Wissinger M, Hauschild R, Hauser M, Kalt H, Zhou H: **Linear and nonlinear optics, dynamics, and lasing in ZnO bulk and nanostructures**. *Journal of Luminescence* 2008, **128**:792.
171. Teke A, Özgür ü., Doğan S, Gu X, Morkoç H, Nemeth B, Nause J, Everitt H: **Excitonic fine structure and recombination dynamics in single-crystalline ZnO**. *Phys. Rev. B* 2004, **70**:195207.
172. Zeuner A, Alves H, Hofmann DM, Meyer BK, Heuken M, Bläsing J, Krost A: **Structural and optical properties of epitaxial and bulk ZnO**. *Appl. Phys. Lett.* 2002, **80**:2078.
173. Djurišić AB, Leung YH, Tam KH, Hsu YF, Ding L, Ge WK, Zhong YC, Wong KS, Chan WK, Tam HL, Cheah KW, Kwok WM, Phillips DL: **Defect emissions in ZnO nanostructures**. *Nanotechnology* 2007, **18**:095702.
174. Schneider L, Zaitsev SV, Bacher G, Jin W, Winterer M: **Recombination dynamics in ZnO nanoparticles produced by chemical vapor synthesis**. *J. Appl. Phys.* 2007, **102**:023524.
175. Fallert J, Hauschild R, Stelzl F, Urban A, Wissinger M, Zhou H, Klingshirn C, Kalt H: **Surface-state related luminescence in ZnO nanocrystals**. *J. Appl. Phys.* 2007, **101**:073506.
176. Bekeny C, Voss T, Hilker B, Gutowski J, Hauschild R, Kalt H, Postels B, Bakin A, Waag A: **Influence of ZnO seed crystals and annealing on the optical quality of low-temperature grown ZnO nanorods**. *J. Appl. Phys.* 2007, **102**:044908.
177. Wischmeier L, Voss T, Rückmann I, Gutowski J: **Correlations between surface-excitonic emission bands in ZnO nanowires**. *Nanotechnology* 2008, **19**:135705.
178. Wagner M, Callsen G, Reparaz J, Schulze J-H, Kirste R, Cobet M, Ostapenko I, Rodt S, Nenstiel C, Kaiser M, Hoffmann A, Rodina A, Phillips M, Lautenschläger S, Eisermann S, Meyer B: **Bound excitons in ZnO: Structural defect complexes versus shallow impurity centers**. *Physical Review B* 2011, **84**:035313.
179. Ozaki S, Tsuchiya T, Inokuchi Y, Adachi S: **Photoluminescence and photomodulated transmittance spectroscopy of ZnO nanowires**. *physica status solidi (a)* 2005, **202**:1325.
180. Pankove J: *Optical processes in semiconductors*. New York: Dover; 1975.
181. Willardson RK, Beer AC: *Transport and optical phenomena*. New York: Academic Press; 1972.
182. Dean PJ: **Inter-impurity recombinations in semiconductors**. *Progress in Solid State Chemistry* 1973, **8**:1.
183. Makino T, Tsukazaki A, Ohtomo A, Kawasaki M, Koinuma H: **Shifting Donor-Acceptor Photoluminescence in N-doped ZnO**. *Journal of the Physics Society Japan* 2006, **75**:073701.
184. Bacewicz R, Zuk P, Trykozko R: **Photoluminescence study of ZnO/CdS/Cu(In,Ga)Se2 solar cells**. *Opto-electronics review* 2003, **11**:277.
185. Dingle R: **Radiative Lifetimes of Donor-Acceptor Pairs in p-Type Gallium Arsenide**. *Physical Review* 1969, **184**:788.

186. Dean P, Merz J: **Pair Spectra and "Edge Emission" in Zinc Selenide**. *Physical Review* 1969, **178**:1310.
187. Kaufmann U, Kunzer M, Obloh H, Maier M, Manz C, Ramakrishnan A, Santic B: **Origin of defect-related photoluminescence bands in doped and nominally undoped GaN**. *Physical Review B* 1999, **59**:5561.
188. Thomas D, Hopfield J, Augustyniak W: **Kinetics of Radiative Recombination at Randomly Distributed Donors and Acceptors**. *Physical Review* 1965, **140**:A202.
189. Irimpan L, Nampoori VPN, Radhakrishnan P, Deepthy A, Krishnan B: **Size dependent fluorescence spectroscopy of nanocolloids of ZnO**. *J. Appl. Phys.* 2007, **102**:063524.
190. Zeng H, Duan G, Li Y, Yang S, Xu X, Cai W: **Blue Luminescence of ZnO Nanoparticles Based on Non-Equilibrium Processes: Defect Origins and Emission Controls**. *Adv. Funct. Mater.* 2010, **20**:561.
191. Ghosh M, Raychaudhuri AK: **Shape transition in ZnO nanostructures and its effect on blue-green photoluminescence**. *Nanotechnology* 2008, **19**:445704.
192. Zhang DH, Xue ZY, Wang QP: **The mechanisms of blue emission from ZnO films deposited on glass substrate by r.f. magnetron sputtering**. *J. Phys. D: Appl. Phys.* 2002, **35**:2837.
193. Sarkar A, Chakrabarti M, Ray SK, Bhowmick D, Sanyal D: **Positron annihilation lifetime and photoluminescence studies on single crystalline ZnO**. *J. Phys.: Condens. Matter* 2011, **23**:155801.
194. Wu J-J, Liu S-C: **Low-Temperature Growth of Well-Aligned ZnO Nanorods by Chemical Vapor Deposition**. *Adv. Mater.* 2002, **14**:215.
195. Zhang X-H, Xie S-Y, Jiang Z-Y, Zhang X, Tian Z-Q, Xie Z-X, Huang R-B, Zheng L-S: **Rational Design and Fabrication of ZnO Nanotubes from Nanowire Templates in a Microwave Plasma System**. *J. Phys. Chem. B* 2003, **107**:10114.
196. Zhao L-H, Sun S-Q: **Synthesis of water-soluble ZnO nanocrystals with strong blue emission via a polyol hydrolysis route**. *CrystEngComm* 2011, **13**:1864.
197. Ou Q, Matsuda T, Mesko M, Ogino A, Nagatsu M: **Cathodoluminescence Property of ZnO Nanophosphors Prepared by Laser Ablation**. *Jpn. J. Appl. Phys.* 2008, **47**:389.
198. Patra MK, Manzoor K, Manoth M, Vadera SR, Kumar N: **Studies of luminescence properties of ZnO and ZnO:Zn nanorods prepared by solution growth technique**. *Journal of Luminescence* 2008, **128**:267.
199. Studenikin SA, Cocivera M: **Time-resolved luminescence and photoconductivity of polycrystalline ZnO films**. *J. Appl. Phys.* 2002, **91**:5060.
200. Shan FK, Liu GX, Lee WJ, Lee GH, Kim IS, Shin BC: **Aging effect and origin of deep-level emission in ZnO thin film deposited by pulsed laser deposition**. *Appl. Phys. Lett.* 2005, **86**:221910.
201. Vanheusden K, Warren WL, Seager CH, Tallant DR, Voigt JA, Gnade BE: **Mechanisms behind green photoluminescence in ZnO phosphor powders**. *J. Appl. Phys.* 1996, **79**:7983.
202. Lin Y-J, Tsai C-L: **Changes in surface band bending, surface work function, and sheet resistance of undoped ZnO films due to $(NH_4)_2S_x$ treatment**. *J. Appl. Phys.* 2006, **100**:113721.
203. Ye JD, Gu SL, Qin F, Zhu SM, Liu SM, Zhou X, Liu W, Hu LQ, Zhang R, Shi Y, Zheng YD: **Correlation between green luminescence and morphology evolution of ZnO films**. *Appl. Phys. A* 2004, **81**:759.
204. Guo B, Qiu ZR, Wong KS: **Intensity dependence and transient dynamics of donor–acceptor pair recombination in ZnO thin films grown on (001) silicon**. *Applied Physics Letters* 2003, **82**:2290.
205. Djurišić AB, Choy WCH, Roy VAL, Leung YH, Kwong CY, Cheah KW, Gundu Rao TK,

Chan WK, Fei Lui H, Surya C: **Photoluminescence and Electron Paramagnetic Resonance of ZnO Tetrapod Structures**. *Adv. Funct. Mater.* 2004, **14**:856.
206. Ling B, Zhao JL, Sun XW, Tan ST, Yang Y, Dong ZL: **Electroluminescence From Ferromagnetic Fe-Doped ZnO Nanorod Arrays on p-Si**. *IEEE Trans. Electron Devices* 2010, **57**:1948.
207. Gruzintsev AN, Yakimov EE: **Annealing Effect on the Luminescent Properties and Native Defects of ZnO**. *Inorg Mater* 2005, **41**:725.
208. Kang HS: **Annealing effect on the property of ultraviolet and green emissions of ZnO thin films**. *J. Appl. Phys.* 2004, **95**:1246.
209. Yang CL, Wang JN, Ge WK, Guo L, Yang SH, Shen DZ: **Enhanced ultraviolet emission and optical properties in polyvinyl pyrrolidone surface modified ZnO quantum dots**. *J. Appl. Phys.* 2001, **90**:4489.
210. Liu X, Wu X, Cao H, Chang RPH: **Growth mechanism and properties of ZnO nanorods synthesized by plasma-enhanced chemical vapor deposition**. *J. Appl. Phys.* 2004, **95**:3141.
211. Lin B, Fu Z, Jia Y: **Green luminescent center in undoped zinc oxide films deposited on silicon substrates**. *Appl. Phys. Lett.* 2001, **79**:943.
212. Djurišić AB, Leung YH, Tam KH, Ding L, Ge WK, Chen HY, Gwo S: **Green, yellow, and orange defect emission from ZnO nanostructures: Influence of excitation wavelength**. *Appl. Phys. Lett.* 2006, **88**:103107.
213. van Dijken A, Meulenkamp EA, Vanmaekelbergh D, Meijerink A: **The Kinetics of the Radiative and Nonradiative Processes in Nanocrystalline ZnO Particles upon Photoexcitation**. *J. Phys. Chem. B* 2000, **104**:1715.
214. Shalish I, Temkin H, Narayanamurti V: **Size-dependent surface luminescence in ZnO nanowires**. *Phys. Rev. B* 2004, **69**:245401.
215. van Dijken A, Meulenkamp E, Vanmaekelbergh D, Meijerink A: **Identification of the transition responsible for the visible emission in ZnO using quantum size effects**. *Journal of Luminescence* 2000, **90**:123.
216. Janotti A, Van de Walle CG: **Oxygen vacancies in ZnO**. *Appl. Phys. Lett.* 2005, **87**:122102.
217. Zhou H, Alves H, Hofmann DM, Kriegseis W, Meyer BK, Kaczmarczyk G, Hoffmann A: **Behind the weak excitonic emission of ZnO quantum dots: ZnO/Zn(OH)[sub 2] core-shell structure**. *Appl. Phys. Lett.* 2002, **80**:210.
218. Cross RBM, Souza MMD, Narayanan EMS: **A low temperature combination method for the production of ZnO nanowires**. *Nanotechnology* 2005, **16**:2188.
219. Lauer R: **The I.R. photoluminescence emission band in ZnO**. *Journal of Physics and Chemistry of Solids* 1973, **34**:249.
220. Zhang S, Wei S-H, Zunger A: **Intrinsic n-type versus p-type doping asymmetry and the defect physics of ZnO**. *Phys. Rev. B* 2001, **63**:075205.
221. Chiu S-P, Lin Y-H, Lin J-J: **Electrical conduction mechanisms in natively doped ZnO nanowires**. *Nanotechnology* 2009, **20**:015203.
222. Tsai L-T, Chiu S-P, Lu JG, Lin J-J: **Electrical conduction mechanisms in natively doped ZnO nanowires (II)**. *Nanotechnology* 2010, **21**:145202.
223. Kim Y-S, Park C: **Rich Variety of Defects in ZnO via an Attractive Interaction between O Vacancies and Zn Interstitials: Origin of n-Type Doping**. *Phys. Rev. Lett.* 2009, **102**:086403.
224. Vidya R, Ravindran P, Fjellvåg H, Svensson B, Monakhov E, Ganchenkova M, Nieminen R: **Energetics of intrinsic defects and their complexes in ZnO investigated by density functional calculations**. *Phys. Rev. B* 2011, **83**:045206.
225. Janotti A, Van de Walle CG: **Native point defects in ZnO**. *Phys. Rev. B* 2007, **76**:165202.

226. Bubel S, Mechau N, Schmechel R: **Electronic properties of polyvinylpyrrolidone at the zinc oxide nanoparticle surface**. *J Mater Sci* 2011, **46**:7776.
227. Lu JG, Fujita S, Kawaharamura T, Nishinaka H, Kamada Y, Ohshima T, Ye ZZ, Zeng YJ, Zhang YZ, Zhu LP, He HP, Zhao BH: **Carrier concentration dependence of band gap shift in n-type ZnO:Al films**. *Journal of Applied Physics* 2007, **101**:083705.
228. Tampo H, Yamada A, Fons P, Shibata H, Matsubara K, Iwata K, Niki S, Nakahara K, Takasu H: **Degenerate layers in epitaxial ZnO films grown on sapphire substrates**. *Applied Physics Letters* 2004, **84**:4412.
229. Schleife A, Rödl C, Fuchs F, Hannewald K, Bechstedt F: **Optical Absorption in Degenerately Doped Semiconductors: Mott Transition or Mahan Excitons?** *Physical Review Letters* 2011, **107**:236405.
230. Klingshirn C, Hauschild R, Fallert J, Kalt H: **Room-temperature stimulated emission of ZnO: Alternatives to excitonic lasing**. *Physical Review B* 2007, **75**:115203.
231. Burstein E: **Anomalous Optical Absorption Limit in InSb**. *Phys. Rev.* 1954, **93**:632.
232. Jain SC, McGregor JM, Roulston DJ: **Band-gap narrowing in novel III-V semiconductors**. *J. Appl. Phys.* 1990, **68**:3747.
233. Wang R, King LLH, Sleight AW: **Highly conducting transparent thin films based on zinc oxide**. *J. Mater. Res.* 1996, **11**:1659.
234. Sakai K, Kakeno T, Ikari T, Shirakata S, Sakemi T, Awai K, Yamamoto T: **Defect centers and optical absorption edge of degenerated semiconductor ZnO thin films grown by a reactive plasma deposition by means of piezoelectric photothermal spectroscopy**. *J. Appl. Phys.* 2006, **99**:043508.
235. Gupta TK: **Application of Zinc Oxide Varistors**. *Journal of the American Ceramic Society* 1990, **73**:1817.
236. Greuter F, Blatter G: **Electrical properties of grain boundaries in polycrystalline compound semiconductors**. *Semiconductor Science and Technology* 1990, **5**:111.
237. Greuter F: **Electrically active interfaces in ZnO varistors**. *Solid State Ionics* 1995, **75**:67.
238. Mahan GD, Levinson LM, Philipp HR: **Theory of conduction in ZnO varistors**. *Journal of Applied Physics* 1979, **50**:2799.
239. He J, Zeng R, Chen Q, Chen S, Guan Z, Han S-W, Cho H-G: **Nonuniformity of Electrical Characteristics in Microstructures of ZnO Surge Varistors**. *IEEE Transactions on Power Delivery* 2004, **19**:138.
240. Grovenor CRM: **Grain boundaries in semiconductors**. *Journal of Physics C: Solid State Physics* 1985, **18**:4079.
241. Ghosh M, Ningthoujam RS, Vatsa RK, Das D, Nataraju V, Gadkari SC, Gupta SK, Bahadur D: **Role of ambient air on photoluminescence and electrical conductivity of assembly of ZnO nanoparticles**. *Journal of Applied Physics* 2011, **110**:054309.
242. Li CC, Du ZF, Li LM, Yu HC, Wan Q, Wang TH: **Surface-depletion controlled gas sensing of ZnO nanorods grown at room temperature**. *Applied Physics Letters* 2007, **91**:032101.
243. Glot AB: **A model of non-Ohmic conduction in ZnO varistors**. *Journal of Materials Science: Materials in Electronics* 2006, **17**:755.
244. Yan W, Mechau N, Hahn H, Krupke R: **Ultraviolet photodetector arrays assembled by dielectrophoresis of ZnO nanoparticles**. *Nanotechnology* 2010, **21**:115501.
245. Wang JX, Sun XW, Yang Y, Huang H, Lee YC, Tan OK, Vayssieres L: **Hydrothermally grown oriented ZnO nanorod arrays for gas sensing applications**. *Nanotechnology* 2006, **17**:4995.
246. van Dijken A, Meulenkamp EA, Vanmaekelbergh D, Meijerink A: **Influence of Adsorbed Oxygen on the Emission Properties of Nanocrystalline ZnO Particles**. *The Journal of*

Physical Chemistry B 2000, **104**:4355.
247. Osterwalder N, Capello C, Hungerbühler K, Stark WJ: **Energy Consumption During Nanoparticle Production: How Economic is Dry Synthesis?** *J Nanopart Res* 2006, **8**:1.
248. Athanassiou EK, Grass RN, Stark WJ: **Chemical Aerosol Engineering as a Novel Tool for Material Science: From Oxides to Salt and Metal Nanoparticles**. *Aerosol Science and Technology* 2009, **44**:161.
249. Ali M: **Chemical Vapor Synthesis and Characterization of Undoped, Doped and Functionalized ZnO Nanoparticles**. *Ph.D. Thesis*, Universität Duisburg-Essen, 2009.
250. Polarz S, Roy A, Merz M, Halm S, Schröder D, Schneider L, Bacher G, Kruis F, Driess M: **Chemical Vapor Synthesis of Size-Selected Zinc Oxide Nanoparticles**. *Small* 2005, **1**:540.
251. Kleinwechter H, Janzen C, Knipping J, Wiggers H, Roth P: **Formation and properties of ZnO nano-particles from gas phase synthesis processes**. *J Mater Sci* 2002, **37**:4349.
252. Katusic S, Kröll M, Kress P, Zimmermann G: **Silica coated zinc oxide particles obtainable by a flame pyrolysis process**. *Patent* WO 2008/019905 A1, 2008.
253. Granqvist CG, Buhrman RA: **Ultrafine metal particles**. *J. Appl. Phys.* 1976, **47**:2200.
254. Muth JF, Kolbas RM, Sharma AK, Oktyabrsky S, Narayan J: **Excitonic structure and absorption coefficient measurements of ZnO single crystal epitaxial films deposited by pulsed laser deposition**. *J. Appl. Phys.* 1999, **85**:7884.
255. Tan ST, Chen BJ, Sun XW, Fan WJ, Kwok HS, Zhang XH, Chua SJ: **Blueshift of optical band gap in ZnO thin films grown by metal-organic chemical-vapor deposition**. *J. Appl. Phys.* 2005, **98**:013505.
256. Lin Y-J, Tsai C-L, Lu Y-M, Liu C-J: **Optical and electrical properties of undoped ZnO films**. *J. Appl. Phys.* 2006, **99**:093501.
257. Dutta S, Chattopadhyay S, Sutradhar M, Sarkar A, Chakrabarti M, Sanyal D, Jana D: **Defects and the optical absorption in nanocrystalline ZnO**. *J. Phys.: Condens. Matter* 2007, **19**:236218.
258. Bubel S: **Feldeffekttransistoren aus nanopartikulärem Zinkoxid**. *Ph.D. Thesis*, Technische Universität Darmstadt, 2009.
259. Dasgupta S, Gottschalk S, Kruk R, Hahn H: **A nanoparticulate indium tin oxide field-effect transistor with solid electrolyte gating**. *Nanotechnology* 2008, **19**:435203.
260. Zhang XQ, Yao ZG, Huang SH, Suemune I, Kumano H: **Intrinsic exciton transitions in high-quality ZnO thin films grown by plasma-enhanced molecular-beam epitaxy on sapphire substrates**. *J. Appl. Phys.* 2006, **99**:063709.
261. Tan ST, Chen BJ, Sun XW, Fan WJ, Kwok HS, Zhang XH, Chua SJ: **Blueshift of optical band gap in ZnO thin films grown by metal-organic chemical-vapor deposition**. *Journal of Applied Physics* 2005, **98**:013505.
262. Shi WS, Cheng B, Zhang L, Samulski ET: **Influence of excitation density on photoluminescence of zinc oxide with different morphologies and dimensions**. *Journal of Applied Physics* 2005, **98**:083502.
263. Foreman JV, Everitt HO, Yang J, McNicholas T, Liu J: **Effects of reabsorption and spatial trap distributions on the radiative quantum efficiencies of ZnO**. *Physical Review B* 2010, **81**:115318.
264. Ali M, Winterer M: **ZnO Nanocrystals: Surprisingly "Alive."***Chemistry of Materials* 2010, **22**:85.
265. Zacks E, Halperin A: **Dependence of the Peak Energy of the Pair-Photoluminescence Band on Excitation Intensity**. *Physical Review B* 1972, **6**:3072.
266. Cooper DE, Bajaj J, Newman PR: **Photoluminescence spectroscopy of excitons for evaluation of high-quality CdTe crystals**. *Journal of Crystal Growth* 1990, **86**:544.
267. Schmidt T, Lischka K, Zulehner W: **Excitation-power dependence of the near-band-**

edge photoluminescence of semiconductors. *Physical Review B* 1992, **45**:8989.
268. Wang L, Giles NC: **Temperature dependence of the free-exciton transition energy in zinc oxide by photoluminescence excitation spectroscopy**. *J. Appl. Phys.* 2003, **94**:973.
269. Ashrafi ABMA: **Temperature-dependent photoluminescence of ZnO layers grown on 6H-SiC substrates**. *J. Appl. Phys.* 2004, **95**:7738.
270. Eliseev PG: **The red σ^2/kT spectral shift in partially disordered semiconductors**. *Journal of Applied Physics* 2003, **93**:5404.
271. Bell A: **Exciton freeze-out and thermally activated relaxation at local potential fluctuations in thick $Al_xGa_{1-x}N$ layers**. *Journal of Applied Physics* 2004, **95**:4670.
272. Li Q, Xu SJ, Xie MH, Tong SY: **Origin of the "S-shaped" temperature dependence of luminescent peaks from semiconductors**. *Journal of Physics: Condensed Matter* 2005, **17**:4853.
273. Liu B, Zhang Z, Zhang R, Fu DY, Xie ZL, Lu H, Schaff WJ, Song LH, Cui YC, Hua XM, Han P, Zheng YD, Chen YH, Wang ZG: **Electron concentration dependence of exciton localization and freeze-out at local potential fluctuations in InN films**. *Applied Physics A* 2010, **99**:139.
274. Kim MS, Yim KG, Jeon SM, Lee D-Y, Kim JS, Kim JS, Son J-S, Leem J-Y: **Photoluminescence Studies of Porous ZnO Nanorods**. *Japanese Journal of Applied Physics* 2011, **50**:035003.
275. Arnaudov B, Paskova T, Paskov P, Magnusson B, Valcheva E, Monemar B, Lu H, Schaff W, Amano H, Akasaki I: **Energy position of near-band-edge emission spectra of InN epitaxial layers with different doping levels**. *Physical Review B* 2004, **69**:115216.
276. Gu Y, Kuskovsky IL, Yin M, O'Brien S, Neumark GF: **Quantum confinement in ZnO nanorods**. *Applied Physics Letters* 2004, **85**:3833.
277. Kaufmann U, Kunzer M, Obloh H, Maier M, Manz C, Ramakrishnan A, Santic B: **Origin of defect-related photoluminescence bands in doped and nominally undoped GaN**. *Physical Review B* 1999, **59**:5561.
278. Halliburton LE, Giles NC, Garces NY, Luo M, Xu C, Bai L, Boatner LA: **Production of native donors in ZnO by annealing at high temperature in Zn vapor**. *Applied Physics Letters* 2005, **87**:172108.
279. Li J, Zhao X, Yan C, Yijing L: **Electroluminescence of ZnO nanocrystalline particles annealed from mesoporous precursors**. *Materials Chemistry and Physics* 2008, **107**:177.
280. Ning G, Zhao X, Li J, Zhang C: **Hugely enhanced electroluminescence from mesoporous ZnO particles**. *Optical Materials* 2006, **28**:385.
281. Ding M, Zhao D, Yao B, Li B, Zhang Z, Shan C, Shen D: **The surface defect-related electroluminescence from the ZnO microwire**. *Journal of Physics D: Applied Physics* 2011, **44**:075104.
282. Helander MG, Greiner MT, Wang ZB, Tang WM, Lu ZH: **Work function of fluorine doped tin oxide**. *J. Vac. Sci. Technol. A* 2011, **29**:011019.
283. King PDC, Veal TD: **Conductivity in transparent oxide semiconductors**. *Journal of Physics: Condensed Matter* 2011, **23**:334214.
284. Latz R, Michael K, Scherer M: **High Conducting Large Area Indium Tin Oxide Electrodes for Displays Prepared by DC Magnetron Sputtering**. *Japanese Journal of Applied Physics* 1991, **30**:L149.
285. Lim J-H, Kang C-K, Kim K-K, Park I-K, Hwang D-K, Park S-J: **UV Electroluminescence Emission from ZnO Light-Emitting Diodes Grown by High-Temperature Radiofrequency Sputtering**. *Adv. Mater.* 2006, **18**:2720.
286. Wei ZP, Lu YM, Shen DZ, Zhang ZZ, Yao B, Li BH, Zhang JY, Zhao DX, Fan XW, Tang ZK: **Room temperature p-n ZnO blue-violet light-emitting diodes**. *Appl. Phys. Lett.* 2007,

90:042113.
287. Shimizu A, Kanbara M, Hada M, Kasuga M: **ZnO Green Light Emitting Diode**. *Japanese Journal of Applied Physics* 1978, **17**:1435.
288. Wang H-T, Kang BS, Chen J-J, Anderson T, Jang S, Ren F, Kim HS, Li YJ, Norton DP, Pearton SJ: **Band-edge electroluminescence from N^+-implanted bulk ZnO**. *Applied Physics Letters* 2006, **88**:102107.
289. Minami T, Takata S, Yamanishi M, Kawamura T: **Metal-Semiconductor Electroluminescent Diodes in ZnO Single Crystal**. *Japanese Journal of Applied Physics* 1979, **18**:1617.
290. Lee C-Y, Huang J-S, Lin C-F: **White Light Electroluminescence from Zinc Oxide Nanowire Composites**. In IEEE; 2008:120.
291. Dabbousi BO, Bawendi MG, Onitsuka O, Rubner MF: **Electroluminescence from CdSe quantum-dot/polymer composites**. *Appl. Phys. Lett.* 1995, **66**:1316.
292. Parker ID: **Carrier tunneling and device characteristics in polymer light-emitting diodes**. *J. Appl. Phys.* 1994, **75**:1656.
293. Qiao Q, Beck J, Lumpkin R, Pretko J, Mcleskeyjr J: **A comparison of fluorine tin oxide and indium tin oxide as the transparent electrode for P3HT/TiO2 solar cells**. *Solar Energy Materials and Solar Cells* 2006, **90**:1034.
294. Gläser HJ: *Large area glass coating*. Dresden: Von Ardenne Anlagentechnik; 2000.
295. Szyszka B, Ulrich S: **Transparent leitfähige Oxide - Materialübersicht**. OTTI 2008.
296. Kawashima T, Ezure T, Okada K, Matsui H, Goto K, Tanabe N: **FTO/ITO double-layered transparent conductive oxide for dye-sensitized solar cells**. *Journal of Photochemistry and Photobiology A: Chemistry* 2004, **164**:199.
297. Baek W-H, Choi M, Yoon T-S, Lee HH, Kim Y-S: **Use of fluorine-doped tin oxide instead of indium tin oxide in highly efficient air-fabricated inverted polymer solar cells**. *Applied Physics Letters* 2010, **96**:133506.
298. Thomas BW, Walsh D: **Metal-insulator-semiconductor electroluminescent diodes in single-crystal zinc oxide**. *Electronics Letters* 1973, **9**:362.
299. Chin PTK, Stouwdam JW, van Bavel SS, Janssen RAJ: **Cluster synthesis of branched CdTe nanocrystals for use in light-emitting diodes**. *Nanotechnology* 2008, **19**:205602.
300. Anikeeva PO, Halpert JE, Bawendi MG, Bulović V: **Quantum Dot Light-Emitting Devices with Electroluminescence Tunable over the Entire Visible Spectrum**. *Nano Lett.* 2009, **9**:2532.
301. Chen P, Ma X, Yang D: **Ultraviolet electroluminescence from ZnO/p-Si heterojunctions**. *J. Appl. Phys.* 2007, **101**:053103.
302. Wadeasa A, Beegum SL, Raja S, Nur O, Willander M: **The demonstration of hybrid n-ZnO nanorod/p-polymer heterojunction light emitting diodes on glass substrates**. *Applied Physics A* 2009, **95**:807.
303. Gopal A, Hoshino K, Kim S, Zhang X: **Multi-color colloidal quantum dot based light emitting diodes micropatterned on silicon hole transporting layers**. *Nanotechnology* 2009, **20**:235201.
304. Son D-I, Park D-H, Choi WK, Cho S-H, Kim W-T, Kim TW: **Carrier transport in flexible organic bistable devices of ZnO nanoparticles embedded in an insulating poly(methyl methacrylate) polymer layer**. *Nanotechnology* 2009, **20**:195203.
305. Bubel S, Mechau N, Hahn H, Schmechel R: **Trap states and space charge limited current in dispersion processed zinc oxide thin films**. *J. Appl. Phys.* 2010, **108**:124502.
306. Gu QL, Ling CC, Brauer G, Anwand W, Skorupa W, Hsu YF, Djurišić AB, Zhu CY, Fung S, Lu LW: **Deep level defects in a nitrogen-implanted ZnO homogeneous p-n junction**. *Appl. Phys. Lett.* 2008, **92**:222109.

307. Takata S, Minami T, Nanto H, Kawamura T: **Temperature dependence of electro- and photoluminescence in ZnO single crystals**. *Physica Status Solidi (a)* 1981, **65**:K83.
308. Pike GE, Kurtz SR, Gourley PL, Philipp HR, Levinson LM: **Electroluminescence in ZnO varistors: Evidence for hole contributions to the breakdown mechanism**. *Journal of Applied Physics* 1985, **57**:5512.
309. Hwang D-K, Oh M-S, Lim J-H, Choi Y-S, Park S-J: **ZnO-based light-emitting metal-insulator-semiconductor diodes**. *Applied Physics Letters* 2007, **91**:121113.
310. Yan C, Chen Z, Zhao X: **Enhanced electroluminescence of ZnO nanocrystalline annealing from mesoporous precursors**. *Solid State Communications* 2006, **140**:18.
311. Seo K, Lim T, Kim S, Park H-L, Ju S: **Tunable-white-light-emitting nanowire sources**. *Nanotechnology* 2010, **21**:255201.
312. Neshataeva E, Kümmell T, Ebbers A, Bacher G: **Electrically driven ZnO nanoparticle light emitting device**. *Electron. Lett.* 2008, **44**:1485.
313. Qu TL, Li J, Zhao YG, Mei JW, Liu X, Tian HF, Shi JP, Guo SM, Li J, Zheng DN, Li JQ: **Nonlinear current-voltage behavior and giant positive magnetoresistance in nonmagnetic Au/Yttria-stabilized zirconia/Si heterostructures**. *Applied Physics Letters* 2009, **95**:242113.
314. Lee SW, Cho HD, Panin G, Won Kang T: **Vertical ZnO nanorod/Si contact light-emitting diode**. *Applied Physics Letters* 2011, **98**:093110.
315. Ye JD, Gu SL, Zhu SM, Liu W, Liu SM, Zhang R, Shi Y, Zheng YD: **Electroluminescent and transport mechanisms of n-ZnO/p-Si heterojunctions**. *Appl. Phys. Lett.* 2006, **88**:182112.
316. Zhao JL, Sun XW, Tan ST, Lo GQ, Kwong DL, Cen ZH: **Realization of n-$Zn_{1-x}Mg_xO$/i-ZnO/SiO_x/n^+-Si heterostructured n-i-n light-emitting diodes by low-cost ultrasonic spray pyrolysis**. *Applied Physics Letters* 2007, **91**:263501.
317. Lee SW, Cho HD, Panin G, Won Kang T: **Vertical ZnO nanorod/Si contact light-emitting diode**. *Applied Physics Letters* 2011, **98**:093110.
318. Ng AMC, Xi YY, Hsu YF, Djurišić AB, Chan WK, Gwo S, Tam HL, Cheah KW, Fong PWK, Lui HF, Surya C: **GaN/ZnO nanorod light emitting diodes with different emission spectra**. *Nanotechnology* 2009, **20**:445201.
319. Hwang D-K, Kang S-H, Lim J-H, Yang E-J, Oh J-Y, Yang J-H, Park S-J: **p-ZnO/n-GaN heterostructure ZnO light-emitting diodes**. *Appl. Phys. Lett.* 2005, **86**:222101.
320. Sadaf JR, Israr MQ, Kishwar S, Nur O, Willander M: **White Electroluminescence Using ZnO Nanotubes/GaN Heterostructure Light-Emitting Diode**. *Nanoscale Res Lett* 2010, **5**:957.
321. Lechner R, Stegner AR, Pereira RN, Dietmueller R, Brandt MS, Ebbers A, Trocha M, Wiggers H, Stutzmann M: **Electronic properties of doped silicon nanocrystal films**. *J. Appl. Phys.* 2008, **104**:053701.
322. Dietmueller R, Stegner AR, Lechner R, Niesar S, Pereira RN, Brandt MS, Ebbers A, Trocha M, Wiggers H, Stutzmann M: **Light-induced charge transfer in hybrid composites of organic semiconductors and silicon nanocrystals**. *Appl. Phys. Lett.* 2009, **94**:113301.
323. Wiggers H, Starke R, Roth P: **Silicon Particle Formation by Pyrolysis of Silane in a Hot Wall Gasphase Reactor**. *Chem. Eng. Technol.* 2001, **24**:261.
324. Gupta A, Swihart MT, Wiggers H: **Luminescent Colloidal Dispersion of Silicon Quantum Dots from Microwave Plasma Synthesis: Exploring the Photoluminescence Behavior Across the Visible Spectrum**. *Adv. Funct. Mater.* 2009, **19**:696.
325. Reindl A: **Dispersing and Stabilizing Semiconducting Nanoparticles for Application in Printable Electronics**. *Ph.D. Thesis*, Universität Erlangen-Nürnberg, 2009.
326. Redel E, Petrov S, Dag Ö, Moir J, Huai C, Mirtchev P, Ozin GA: **Green Nanochemistry: Metal Oxide Nanoparticles and Porous Thin Films from Bare Metal Powders**. *Small* 2012,

8:68.
327. Chen P, Ma X, Yang D: **Fairly pure ultraviolet electroluminescence from ZnO-based light-emitting devices**. *Applied Physics Letters* 2006, **89**:111112.
328. Ma X, Chen P, Li D, Zhang Y, Yang D: **Electrophotoluminescence of ZnO film**. *Applied Physics Letters* 2007, **91**:021105.
329. Halls JJM, Walsh CA, Greenham NC, Marseglia EA, Friend RH, Moratti SC, Holmes AB: **Efficient photodiodes from interpenetrating polymer networks**. *Nature* 1995, **376**:498.
330. Nannen E, Kümmell T, Ebbers A, Bacher G: **p-Si/n-ZnO Nanocrystal Heterojunction Light Emitting Device**. *Applied Physics Express* 2012, **5**:035001.
331. *Handbook of Transparent Conductors*. Boston, MA: Springer US; 2010.
332. Ramanathan S: *Thin film metal-oxides : fundamentals and applications in electronics and energy*. New York: Springer; 2010.
333. Meyer J, Kröger M, Hamwi S, Gnam F, Riedl T, Kowalsky W, Kahn A: **Charge generation layers comprising transition metal-oxide/organic interfaces: Electronic structure and charge generation mechanism**. *Appl. Phys. Lett.* 2010, **96**:193302.
334. Meyer J, Winkler T, Hamwi S, Schmale S, Johannes H-H, Weimann T, Hinze P, Kowalsky W, Riedl T: **Transparent Inverted Organic Light-Emitting Diodes with a Tungsten Oxide Buffer Layer**. *Adv. Mater.* 2008, **20**:3839.
335. Hamwi S, Meyer J, Kröger M, Winkler T, Witte M, Riedl T, Kahn A, Kowalsky W: **The Role of Transition Metal Oxides in Charge-Generation Layers for Stacked Organic Light-Emitting Diodes**. *Adv. Funct. Mater.* 2010, **20**:1762.
336. Meyer J, Hamwi S, Bülow T, Johannes H-H, Riedl T, Kowalsky W: **Highly efficient simplified organic light emitting diodes**. *Appl. Phys. Lett.* 2007, **91**:113506.
337. Kröger M, Hamwi S, Meyer J, Riedl T, Kowalsky W, Kahn A: **Role of the deep-lying electronic states of MoO_3 in the enhancement of hole-injection in organic thin films**. *Appl. Phys. Lett.* 2009, **95**:123301.
338. Sharma A, Hotchkiss PJ, Marder SR, Kippelen B: **Tailoring the work function of indium tin oxide electrodes in electrophosphorescent organic light-emitting diodes**. *Journal of Applied Physics* 2009, **105**:084507.
339. Brown PR, Lunt RR, Zhao N, Osedach TP, Wanger DD, Chang L-Y, Bawendi MG, Bulović V: **Improved Current Extraction from ZnO/PbS Quantum Dot Heterojunction Photovoltaics Using a MoO_3 Interfacial Layer**. *Nano Letters* 2011, **11**:2955.
340. Fierro JLG: *Metal oxides : chemistry and applications*. Boca Raton, FL: Taylor & Francis; 2006.

Appendix

A1 Characterization Techniques

In the following, the details on the characterization techniques, used within this work, are briefly introduced.

Electron Microscopy and Size Distribution Statistics

The top and cross-sectional scanning electron microscopy (SEM) images were taken using a Zeiss-Gemini Supra 25 SEM-system. The TCO-coated glasses, used as the substrates, were thereby grounded by the conductive silver paste and double-sided conductive carbon tabs, to reduce the charging effects and thereby significantly improve the image quality. For cross-sectional images the samples were first scratched on the backside (middle of the glass substrate) by the diamond scriber, subsequently carefully broken and built into the SEM system under 90° tilt of the stage.

Size and shape distribution statistics were collected by an SEM analysis of the size and the shape of the ZnO nanocrystals, spin-coated on top of a Si substrate from the butyl acetate dispersions. For each figure over 1600 nanocrystals were analyzed.

The high-resolution transmission electron microscopy (HR-TEM) of the ZnO nanocrystals was performed by Dr. Ralf Theissmann (Institute of for Nano Structures and Technology, University Duisburg-Essen and CeNIDE).

Layer Morphology

The layer thickness measurements were performed using a KLA-Tencor P15 and an Ambios XP-200 surface profiler. The topography study of the TCO surfaces and the resulting spin-coated nanocrystal layers as well as study of their roughness were performed using a Nanosurf Easyscan 2 atomic force microscopy system. The average surface roughness S_a was thereby calculated by the software from the collected data according to the following formula:

$$S_a = \frac{1}{MN}\sum_{k=0}^{M-1}\sum_{l=0}^{N-1}\left|z\left(x_k, y_l\right)\right|, \text{ (A1.1)}$$

with z being the measured height value at the local (x, y) lateral point of the surface.

Absorption Spectroscopy

The absorption measurements of ZnO layers and the TCO substrates were performed with double channel Cary 5000 UV-Vis and Shimadzu UV-2700 spectrometers. The studied ZnO layer (Chapter 3.2) was spin-coated from the aged butyl acetate ZnO dispersion on top of the cleaned and oxygen-plasma-treated quartz substrate at 4000 rpm, resulting in approximately 300 nm thick nanocrystal layer, as measured by the surface profiler. An equally treated quartz substrate without the ZnO layer was used as a reference in the second channel. No reference was used for the measurement of the TCO substrates: the resulting transparency values correspond to the transparency through both the TCO coating and the glass substrate.

Photoluminescence / Electroluminescence Spectroscopy

For the photoluminescence (PL) spectroscopy, the nanocrystal layers were excited either by the 334.5 nm line of the Ar^+-laser (Coherent Sabre Innova DBW25/5) or by the 325 nm line of a HeCd- laser (Kimmon IK5451R-E). The PL was measured in a standard two-lens macro-PL setup using a combination of Horiba Jobin Yvon iHR 320 (150 mm^{-1} grating if not otherwise stated) spectrometer with the Symphony liquid nitrogen cooled CCD camera. The atmosphere and temperature dependent PL measurements were

performed with the same setup in a PT403 Oxford Instruments closed-cycle cryostat. All the detected spectra were corrected for the spectral sensitivity of both spectrometer and CCD. No PL was detected in reference measurements for all the substrates (ITO, FTO, quartz-glass, Si wafers) as well as in case of p-Si and WO_3 nanocrystal layers.

The same setup was used to detect the spectral characteristics of the electroluminescence (EL). The overall EL emission intensity was determined by analyzing the CCD image intensity of each pixel within the device after the subtraction of the background noise. For the determination of the external quantum efficiency (EQE) of the Si/ZnO devices (Chapter 5) as well as all intensity and EQE measurements of the WO_3/ZnO devices (Chapter 6), a calibrated Si-photodetector (Newport UV-818) was used.

Electrical Characterization

The contacts to the TCO and metal electrodes were realized by spring contact probes with a thin layer of conductive silver paste in between. The device was electrically contacted and monitored by a LabVIEW-controlled Keithley 2601 source meter.

External Quantum Efficiency Measurements

The External quantum Efficiency (EQE) is a measure of how efficiently the LED transforms charge carriers (electrons) into photons and is defined as the ratio between the number of photons emitted per second and the number of electrons passing through the device per second. The light output of the devices here was measured by a calibrated Si-photodetector as a photocurrent I_{ph}, which is subsequently converted into power P (in Watts) using the responsivity R_{ph} of the detector at the particular wavelength λ under the consideration of the dark current I_d from the photodetector:

$$P(\lambda) = \frac{I_{ph} - I_d}{R_{ph}(\lambda)}. \quad \text{(A1.1)}$$

The number of photons, detected per second can be calculated by

$$N_{hf} = \frac{P(\lambda)}{E_{hf}(\lambda)} = \frac{P(\lambda) \cdot \lambda}{h \cdot c}. \quad \text{(A1.2)}$$

Finally the EQE can be calculated by

$$EQE = \frac{N_{hf}}{I/e} \cdot g \cdot 100\% = \frac{P(\lambda)}{E_{hf}(\lambda)} = \frac{\left(I_{ph} - I_d\right) \cdot \lambda}{R(\lambda) \cdot h \cdot c} \cdot \frac{e}{I} \cdot g \cdot 100\% \text{ , (A1.3)}$$

where I is the current through the device, h is the Planck's constant, c is the light velocity and g is a configuration factor, which accounts for the losses due to the geometry of the light collection. Under the assumption of the Lambertian emission profile from the NC-LED surface, the intensity changes with $I = I_0 \cos(\theta)$ as a function of the solid angle θ. The ratio of total emitted power to the power, detected by the photodetector, represented by the factor g, can be calculated by

$$g = \frac{R^2 + a^2}{a^2} \text{ (A1.4)}$$

with R being the perpendicular distance between the photodetector and the LED and a being the radius of the photodetector. The reduction of the outcoupling efficiency due to the high refractive indices of the metal oxides inside the devices and thereby induced optical wave-guiding was not considered for the EQE calculations.

CIE Characteristics

The color of the EL with a spectrum of EL(λ) can be transformed into the color coordinates x and y on the two-dimensional color space, defined by the International 1931 Convention on Illumination (Commission Internationale de l'Eclairage, CIE) by the following procedure. First, the tristimulus values X, Y and Z are calculated with the help of standard observer matching functions $\bar{x}$, $\bar{y}$ and $\bar{z}$ (see Figure A1.1 (a)) by

$$\begin{aligned} X &= \int EL(\lambda) \cdot \bar{x}(\lambda) d\lambda \\ Y &= \int EL(\lambda) \cdot \bar{y}(\lambda) d\lambda \\ Z &= \int EL(\lambda) \cdot \bar{z}(\lambda) d\lambda \end{aligned} \text{ (A1.5)}$$

The tristimulus values describe the perception of the emission color by a standard human observer, evoked by the excitation of the three different receptor types in the human eye. The responsivity of these receptors (in the case of the defined standard observer's eye) to the light of different wavelength is represented by the standard observer matching function, shown in Figure A1.1 (a).

To bring the three-dimensional color and intensity EL impression, defined by the tristimulus values, into a two-dimensional color chart independent of the emission intensity, the sum of the coordinates is normalized to 1. The coordinates x and y in the two-dimensional color space, showed in Figure A1.1 (b) are calculated by

$$x = \frac{X}{X+Y+Z} \qquad y = \frac{Y}{X+Y+Z} \tag{A1.6}$$

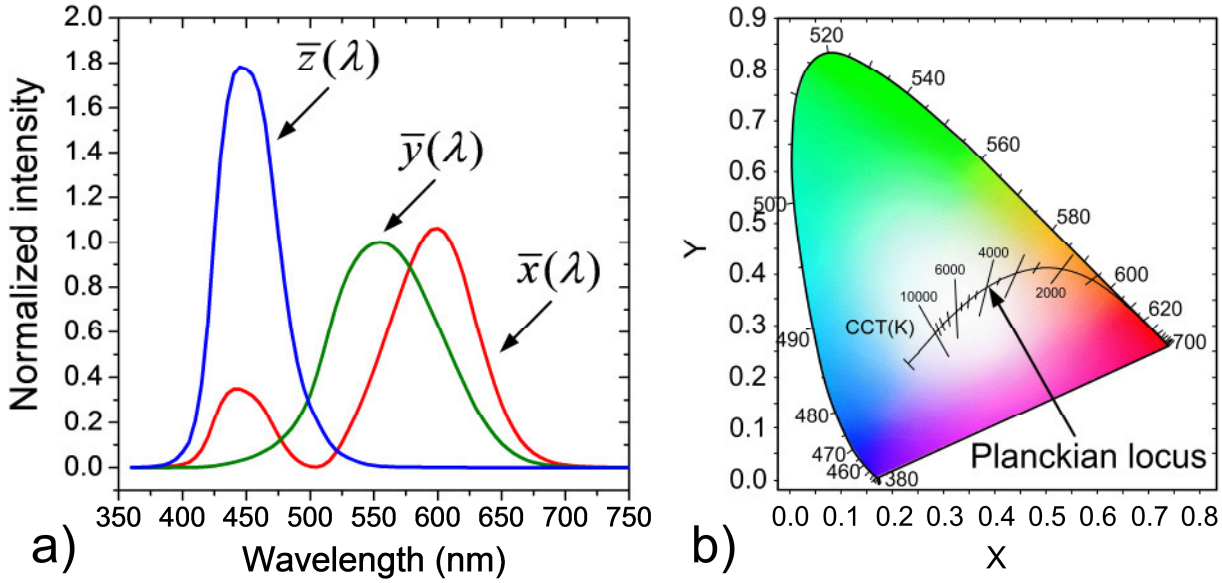

Figure A1.1: Standard observer color matching functions. (a) CIE 1931 color space with the curve of the Planckian locus with the color temperature and correlated color temperature marked on the locus. (b)

The boundary line of the color space defines the coordinates of the spectrally pure (monochromatic) colors, which can be detected by the human eye. All the points, which lie within the boundary line correspond to the mix of the different colors with the white point in the middle of the color chart with the coordinates of x=y=0.33.

Planckian locus, situated in the "white" region of the color chart represents the color coordinates of natural light sources like sun or fire. Their spectral response is approximated by the black body radiator, and it depends of the temperature of the black body radiator. Traditionally, the impression of the white emission from the black body radiator is described by the corresponding color temperature (CT). Paradoxialy, the white emission from the blackbody radiator with lower temperature (e.g. candles CT=1900 K, light bulb CT=2800 K, etc) is called "warm white" due to the higher fraction of red light and psychological impression of fire, and the emission from higher temperatures (e.g. north sky light CT=7500 K) is called "cold white" due to the higher

fraction of blue light. For the light sources emitting white light with the color lying close to the locus, but not directly on it, a correlated color temperature (CCT) is defined as the temperature of the black body radiator at point of the locus having the closest distance to the color coordinates of the studied white light source.

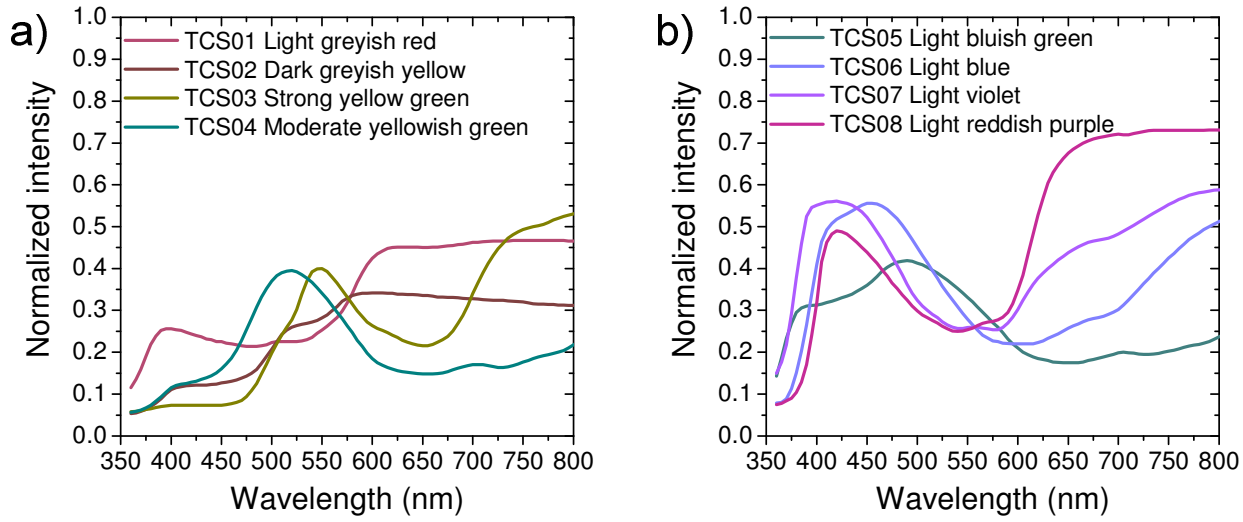

Figure A1.2: Absorption spectra of the 8 test color samples (1 to 4 in (a), 5 to 8 in (b)), used to determine the general color rendering index (CRI) of the studies light sources.

Another important value is the color rendering index (CRI), which describes "how natural" different colors are rendered while being illuminated by the studied light source. The color rendering index of the black body radiator is defined to be 100. The general color rendering of a light source is determined by the average deviation of the rendering of 8 defined test color samples (TCS), showed in Figure A1.2, from the rendering of the same samples by the black body light source with the same color temperature as the studied light source.

Practically, the calculation of the color coordinates, CCT and CRI from the detected EL spectra was performed with the ColorCalculator software. Prior the calculation, all the EL spectra were corrected by the spectral response of both the CCD and Spectrometer.

A2 Fabrication Details

In the following section, some practical details concerning the cleaning procedure of the substrates, treatment of the dispersions and their spin-coating, as well as the top-electrode deposition are given.

Cleaning Procedure

All of the used substrates were cleaned the same way according to the following procedure. First, 80 ml of deionized water (DI) is mixed with 6 drops of the conventional washing-up liquid and stir-mixed for 2 minutes. Subsequently, the substrates are sonicated within this solution for 5 minutes to remove possible residues and splinters from the substrate dicing procedure. Afterwards, the soap residues are removed by DI-rinsing step, followed by a second 5 min sonication step in clear DI water. In the next step, the substrates are boiled in acetone on a hot plate for 2 min and afterwards sonicated inside the same hot acetone beaker for 2 min. This step is followed by the second boiling step inside the new acetone beaker for 2 min. Afterwards, the same procedure is repeated with 2 beakers of isopropyl alcohol, instead of acetone. This step is important to remove the acetone residues from the substrate surface. After the second boiling step in isopropyl alcohol, the substrates are carefully removed from the beaker and dry-blown by nitrogen. During the whole liquid cleaning steps, it is important to hold the substrates with the active (to be coated) surface down in order to avoid re-deposition of the dirt particles on the active surface. The custom-made TCO substrate holder, which vertically fixes the TCO sheets, demonstrated a good alternative to tweezers during the cleaning step, when it comes to cleaning of multiple substrates at the same time.

An additional 30 min UV ozone (UVO) cleaning step just prior the spin-coating of the dispersions turned out to be essentially in order to achieve reproducible smooth layers. This UVO-cleaning step not only removes the organic residues from the substrate, it also modifies the surface energy of the substrate (interfacial tension, IFT).[117, 282, 338] Usually, dispersions show good wetting of the substrate surface if the IFT of the dispersion is equal or smaller than the IFT of the substrate. The IFT of the ZnO dispersions was measured by goniometer to be around 60 mN/m, which is a typical

value for hydrophilic dispersions. The IFT value of the ITO and FTO substrates before the UVO-treatment was calculated from the contact angle measurements of the 3 known fluids to be 31 mN/m and 36 mN/m respectively. After the UVO-treatment, the IFT values of the ITO and FTO substrates increased to 61 mN/m and 65 mN/m respectively, resulting in a good wetting of the TCO substrate surface by the dispersions during the spin-coating step and resulting in smooth and homogeneous layers.

Dispersions and Spin-Coating Procedure

ZnO butyl acetate-based dispersions.

The commercial butyl acetate-based ZnO NC dispersions were used as delivered without additional chemical modifications. Prior to the spin-coating step, the dispersions were filtered by 0.45 μm Millipore hydrophilic filter to avoid large agglomerates within the layers. The butyl acetate vapor pressure of ~3.3 kPa at 20°C leaves enough time for the processing before the solvent evaporates. Therefore a 40 to 60 μl drop (depending on the substrate size) is first deposited and homogeneously distributed over the substrate surface, before the actual spin-coating process is started.

Rotation speed (rpm)	1000	2000	4000	6000	8000
Layer thickness (nm)	1030 ± 160	700 ± 90	590 ± 60	470 ± 70	320 ± 70

Table A2.1: Thickness of the ZnO NC layers, spin-coated on FTO substrates from the identical butyl acetate dispersion at different rotation speed.

The thickness of the ZnO NC layers, spin-coated from the butyl acetate dispersions, can in general be controlled by the final rotation speed of the spin-coater, as shown in Table A2.1. Practically, the dispersion itself as well as the NC concentration change with time due to e.g. solvent evaporation, hard agglomeration of the NCs and their irreversible sedimentation. The layers deposited from the aged dispersions, in case they were shaken and sonicated to re-disperse the sediments, demonstrated to result in layers approximately twice as thick, as in case of the fresh dispersions spin-coated at the same parameters. In case the part of the aged dispersion from the top was used (without re-dispersion), the layer thickness could be reduced by the factor of 2 or even

3, compared to the layers from the fresh dispersion. Therefore the thickness of the layers, spin-coated at the same parameters from the butyl acetate dispersions, was controlled by the slight variation of the concentration followed by the "calibrating" thickness measurements by the surface profiler. Afterwards only the layers with the desired thickness were used for the further device fabrication. The optimal spin-coating parameters for all the different concentrations were found to be 60 s at the rotation speed of 4000 rpm with the acceleration from 0 rpm to 4000 rpm within the first 10 s.

p-Si ethanol-based dispersions.

The commercial ethanol-based p-Si NC dispersions were used as delivered without additional chemical modifications. Due to the high vapor pressure of ethanol (~9 kPa at 20°C), the solvent evaporated very fast from as-delivered dispersion. In order to maintain round about the as-delivered concentration, ethanol was continuously added to the dispersion, followed by the sonication step. The high vapor pressure also led to a very fast evaporation of the solvent during the first seconds of the spin-coating procedure, prohibiting the reliable control of the layer thickness by the rotation speed, contrary to the butyl acetate dispersions. Hence, the thickness of the layers was controlled by the dilution of the original dispersion by ethanol with subsequent 5 min sonication step prior the spin-coating. Table A2.2 shows the thickness of the Si NC layers, spin-coated from the original dispersion on top of the cleaned FTO substrates at the identical spin-coating parameters, whereby the concentration of the Si NC in the original dispersion was stepwise reduced by the dilution with ethanol.

Dilution ratio	1/4	1/3	1/2	2/3	3/4
Layer thickness (nm)	70 ± 25	100 ± 25	150 ± 30	200 ± 30	300 ± 30

Table A2.2: Thickness of the p-Si NC layers, spin-coated on FTO substrates from the original dispersion, diluted by ethanol, at the identical spin-coating parameters.

In case of the ethanol-based p-Si dispersions, the optimal spin-coating parameters were found to be 10 s at the rotation speed of 2000 rpm with the acceleration from 0 rpm to 2000 rpm within the first 5 s.

Self-mixed p-Si, ZnO and WO_3 ethanol-based dispersions.

To achieve Si/ZnO (Chapter 5) and WO_3/ZnO mixed layers as well as WO_3 layers (Chapter 6), ethanol dispersions from the dry powders were prepared. For the Si/ZnO dispersion in the first step 6 wt% ZnO nanopowder (VP AdNano® ZnO 20) dispersion in ethanol was prepared by 6 h sonication (Bandelin Sonoplus HD 2070, 70% power, 70% cycle). Afterwards it was filtered by a 0.45 μm Millipore hydrophilic filter to avoid large agglomerates and mixed in the ratio 3:1 with the 1/3 diluted p-Si ethanol dispersion and again sonicated for 1 h before the spin-coating step.

For the WO_3 and WO_3/ZnO dispersions, the ZnO and WO_3 (SkySpring Nanomaterials Inc, 8010CN) were each first sonicated in ethanol at 6 wt%. Afterwards they were both centrifuged for 2 min at 10000 rpm. Afterwards WO_3 dispersion was directly used for the layer deposition, while the WO_3/ZnO dispersion was formed by mixing of the centrifuged ZnO and WO_3 dispersions in the 1:1 ratio, followed by additional 1 h sonication step and subsequent spin-coating.

In case of the self-mixed ethanol-based NC dispersions, the optimal spin-coating parameters were found to be the same as in case of Si dispersions: 10 s at the rotation speed of 2000 rpm with the acceleration from 0 rpm to 2000 rpm within the first 5 s.

Top-Electrode Deposition Procedure

During the present work, Al was used as a top-electrode due to its ohmic contact to ZnO.[306] Al is by far not as reactive as e.g. Ba or Ca, which are frequently used as low work function cathodes in OLEDs and QD-LEDs, still Al is quite sensitive towards the ambient conditions and tends to oxidize during the deposition. To avoid the oxidation and assure a good quality of Al some preconditions need to be considered during the deposition. First, it is reasonable to avoid any noble metals (e.g. Au, Ag) inside the chamber, since they may catalyze the oxidation of the Al during the deposition. This can be reached by either the cleaning the chamber and covering it with Al foil or the pre-deposition step of ~50-100 nm Al inside the chamber without the sample. Second, it is important to take care of the atmosphere inside the chamber: as less oxygen (air) as possible. For vacuum deposition chambers (e-beam or thermal evaporation systems) this means that the vacuum inside the chamber should be as good as possible, empirically at least below $6 \cdot 10^{-6}$ mbar. For sputtering systems, the chamber should be

purged with inert gas (e.g. N_2 or Ar) and subsequently evacuated for at least 3 times after the chamber was exposed to air or oxygen. Third, to assure high quality of the deposited Al, the target should first be degased and subsequently 20 to 50 nm should be deposited at a stable rate inside the chamber before the shutter in front of the sample is opened and the actual electrode deposition begins. The top electrodes of the devices, discussed in Chapter 4 and 5 were thermally evaporated and in Chapter 6 sputter-deposited at the rates of 5 Å/s and 0.3 Å/s respectively.

A3 Contributions Associated with the Thesis

Books / Journals

0. **E. Nannen**, G. Bacher, V. Bulovic, "*White metal oxide nanocrystal multilayer light emitting device",* to be published

1. **E. Nannen**, T. Kümmell, A. Ebbers, G. Bacher "*p-Si / n-ZnO nanocrystal heterojunction light emitting device",* Appl. Phys. Express 2012; 5:035001.

2. **E. Neshataeva**, T. Kuemmell, G. Bacher, "*Light emitting devices based on direct band gap semiconductor nanoparticles*". (invited book chapter) In: "*Inorganic Nanoparticles - New Frontiers of Research: Synthesis, Applications and Perspectives*", book edited by Dr. Altavilla, CRC Press, ISBN: 97814398176122011 (2011)

3. **E. Neshataeva**, T. Kuemmell, A. Ebbers, G. Bacher, "*All-inorganic light emitting devices based on semiconducting nanoparticles*". In: MRS Proceedings; 2010:1260-T09-02.

4. **E. Neshataeva**, T. Kuemmell, A. Ebbers, G. Bacher, "*Low operation voltage UV-light emitting device based on ZnO nanoparticles*". In: Proceedings of SPIE. San Jose, CA, USA; 2009:721707-721707-10.

5. **E. Neshataeva**, T. Kümmell, G. Bacher, A. Ebbers, "*All-inorganic light emitting device based on ZnO nanoparticles*". Appl. Phys. Lett. 2009; 94(9):091115.

6. **E. Neshataeva**, T. Kümmell, A. Ebbers, G. Bacher, "*Electrically driven ZnO nanoparticle light emitting device*". Electron. Lett. 2008; 44(25):1485.

Selected Talks

7. **E. Neshataeva**, T. Kümmell, A. Ebbers and G. Bacher, *„White light emitting devices based on nanoparticle multilayers"*, (talk) E-MRS 2011, 09. - 13.5.2011, Strasbourg, France

8. G. Bacher, T. Kümmell, **E. Neshataeva**, *„Nanocrystal light emitting diodes"*, (invited talk) 6. International Korean-German Workshop on Nanophotonics, 03. - 06.10.2010, Baekdam-sa temple, Korea,

9. **E. Neshataeva**, T. Kümmell, A. Ebbers and G. Bacher, "*All-inorganic light emitting devices based on nanoparticles*" at Symposium T "Photovoltaics and optoelectronics from nanoparticles" (talk) MRS spring meeting 05.04. – 09.04. 2010, San Francisco, USA

10. **E. Neshataeva**, T. Kümmell, A. Ebbers and G. Bacher, *"Inorganic light emitting devices based on ZnO nanoparticles"*, (invited talk) Opto'10 at PhotonicsWest'10, 25. - 30.1.2010, San Francisco, USA

11. **E. Neshataeva**, T. Kümmell, A. Ebbers and G. Bacher, *"Low operation voltage light emitting devices based on ZnO nanoparticles"*, (talk) DPG-Spring Meeting, 22. - 27.3.2009, Dresden, Germany.

12. **E. Neshataeva**, T. Kümmell, A. Ebbers and G. Bacher, *"Low operation voltage light emitting devices based on ZnO nanoparticles"*, (talk) Opto'09 at PhotonicsWest'09, 24. - 29.1.2009, San Jose, USA

13. **E. Neshataeva**, T. Kümmell, A. Ebbers and G. Bacher, *„Low operation voltage light emitting device based on inorganic nanoscaled materials"*, (talk) E-MRS 2008, 26. - 30.5.2008, Strasbourg, France

A4 Further Contributions

14. Y.S. Chen, S. Halm, **E. Neshataeva**, T. Kümmell, G. Bacher, M. Wiater, T. Wojtowicz, G. Karczewski, "*Local control of spin polarization in a semiconductor by microscale current loops*". Appl. Phys. Lett. 2008; 93(14):141902.

15. S. Halm, P. E. Hohage, J. Nannen, **E. Neshataeva**, L. Schneider, G. Bacher, Y.H. Fan, J. Puls, F. Henneberger, "*Manipulation of spin states in a semiconductor by microscale magnets*". J. Phys. D: Appl. Phys. 2008; 41(16):164007.

16. S. Halm, **E. Neshataeva**, F. Seifert, T. Kümmell, E. Schuster, W. Keune, J. Puls, F. Henneberger, G. Bacher, "*Local Control of Carrier Spin States in a Semiconductor by Microscale Ferromagnetic Wires*". In: AIP Conference Proceedings. Vienna (Austria); 2007:1355-1356.

17. S. Halm, P.E. Hohage, **E. Neshataeva**, F. Seifert, T. Kümmell, E. Schuster, W. Keune, M. Sperl, Y.H. Fan, J. Puls, F. Henneberger, G. Bacher, "*Incoherent and coherent spin manipulation in ferromagnet-dilute magnetic semiconductor hybrids*". phys. stat. sol. (a). 2007; 204(1):191-201.

18. S. Halm, **E. Neshataeva**, F. Seifert, T. Kümmell, E. Schuster, W. Keune, M. Sperl, J. Puls, F. Henneberger, G. Bacher, "*Fe/Tb multilayer ferromagnets for local semiconductor spin control*". phys. stat. sol. (c). 2006; 3(12):4359-4363.

Acknowledgment

First of all I would like to thank my advisor, Prof. Gerd Bacher, for his guidance, criticism and encouragement. He gave me the opportunity and resources to develop as a scientist and realize my sometimes crazy ideas. He showed tremendous patience and supported me greatly, especially during the final thesis phase rush.

I am very grateful to my co-advisor Dr. André Ebbers for his enthusiasm, mentoring, and valuable advices. I would also like to gratefully acknowledge the support of the whole Creavis-Team of Evonik Degussa GmbH for open-minded research approach, great collaboration and experimental support during the work. I also thank Evonik Degussa GmbH for supply of ZnO and Si nanocrystals and dispersions, used in this work.

I would like to acknowledge the support of all of my collaborators within the Research Training Group GRK 1240 "Nanotronics" and especially the enthusiasm and commitment of its speaker Prof. Markus Winterer. The financial support from the Deutsche Forschungsgemeinschaft (DFG, German Research Foundation) and the Center for Nano Integration Duisburg-Essen (CeNIDE) University Duisburg-Essen are gratefully acknowledged.

My very special thanks go to Prof. Vladimir Bulović for giving me a priceless opportunity to work in ONE Lab during the research stay at the MIT. Thank you very much for being a wonderful host, an inspiring mentor and a critical advisor, pushing me to the limits and giving me probably one of the toughest and exciting research experiences, which will surely influence my future scientific life. Huge thanks to everyone in ONE Lab for their great collaborative support and patience with me during this few months. Especially Geoffrey, Yasu, Jill, Patrick, Tim, Ni and Apoorva who gave me not only very valuable advices, trained me on the lab equipment and showed me around, but were also responsible for the incredible amount of fun inside and outside the MIT walls! Without your help, guys, the results of Chapter 6 would not be possible.

It is my pleasure to thank my thesis committee members, Prof. Vogt, Prof. Erni, and Prof. Ding for accepting and evaluating my thesis as well as for their time and valuable comments, and Prof. Schmechel for his support and advice, encouraging smile during various talks and collaborative attitude. Also giant thanks to the whole NST group and

especially to Gabi Schierning for training me and letting me use the lab equipment. Also big thanks to Ralf Theissmann for the HR-TEM-images of the ZnO nanocrystals.

I would like to gratefully acknowledge the experimental support of Daniel Sager (spin-coating, evaporation), Dennis Vietz (spin-coating, SEM-images, NC-statistics), Kai Blekker (evaporation), Sven Eliasson (AFM-images), Franziska Muckel (annealing, PL quantum yield measurements) and Dino Iavarone (spin-coating, SEM-images, NC-statistics, long-term measurements). Thank you, guys, very much for your great job and your incredible patience with me and my "realistic" time schedule. It's always been a pleasure and fun to work with you!

I am very thankful to Ingeborg Schäl and Marion Bröckels for providing indispensable support with many administrative hurdles as well as with private issues.

Thank you everyone in the WET (swinging big band) group for your support, understanding, great working atmosphere, for making WET my second home and of course for wonderful memories from the legendary WET-seminars. Especially to my "roommates" Simon, Patric, Lars, Jörg and Rachel. Thanks for "epic moments" in BA 117, for your advices and support, for all the fun we had together and all the sorrows we shared. Thanks for being (and staying) true friends! Special thanks to O. Fox for fruitful discussions. ;-)

Giant thanks to my big family ("Neshes" and "Nannens") and my friends for their great support and understanding during the tough Ph.D.–time. Special thanks to my parents for the "engineer blood", my grandmother for the right cheers at the right time and my brother Ivan for taking care of Parasyonka and me, and housekeeping. Thanks also to Parasyonka for forcing me into (more or less) healthy and regulated way of life.

Finally, I'm enormously indebted to the single most influential and important person in my life, Ingo Nannen, whose technical knowledge, insight into electrical engineering, programming skills, advices, humor, optimism and support contributed in some way to every single page of this thesis. Thank you very much for the ATLAS simulation of the devices. Though at the end the results were not included, they invaluably contributed to the understanding of the operation mechanisms behind the LEDs. Thanks for pushing me forward and giving me great support when I was in doubt. Thanks for believing in me and my skills at times when I already gave up. Thanks for warm meals, for taking care of me, for all of your endless patience and love. Thanks for always being the person to rely on and my knight in shining armor. ☺